FORSCHUNGSZENTRUM JÜLICH GmbH

Institut für Plasmaphysik
Association EURATOM-KFA

Dynamic Ergodic Divertor (DED) for TEXTOR-94

Editor: K.H. Finken

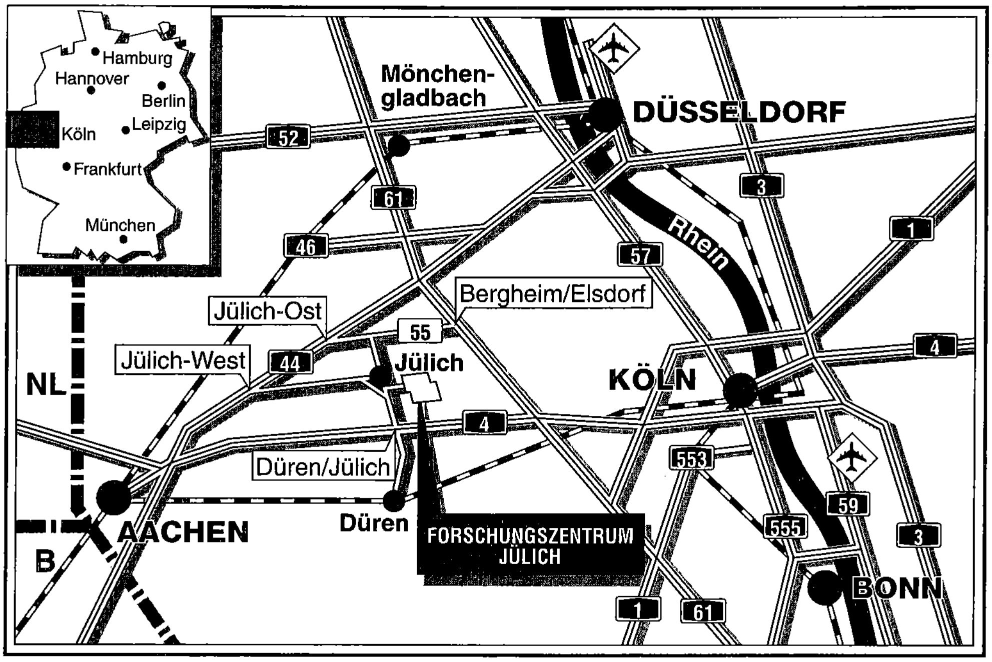

Berichte des Forschungszentrums Jülich ; 3285
ISSN 0944-2952
Institut für Plasmaphysik Jül-3285
Association EURATOM-KFA

Zu beziehen durch: Forschungszentrum Jülich GmbH · Zentralbibliothek
D-52425 Jülich · Bundesrepublik Deutschland
Telefon: 02461/61-6102 · Telefax: 02461/61-6103 · Telex: 833556-70 kfa d

Dynamic Ergodic Divertor (DED) for TEXTOR-94

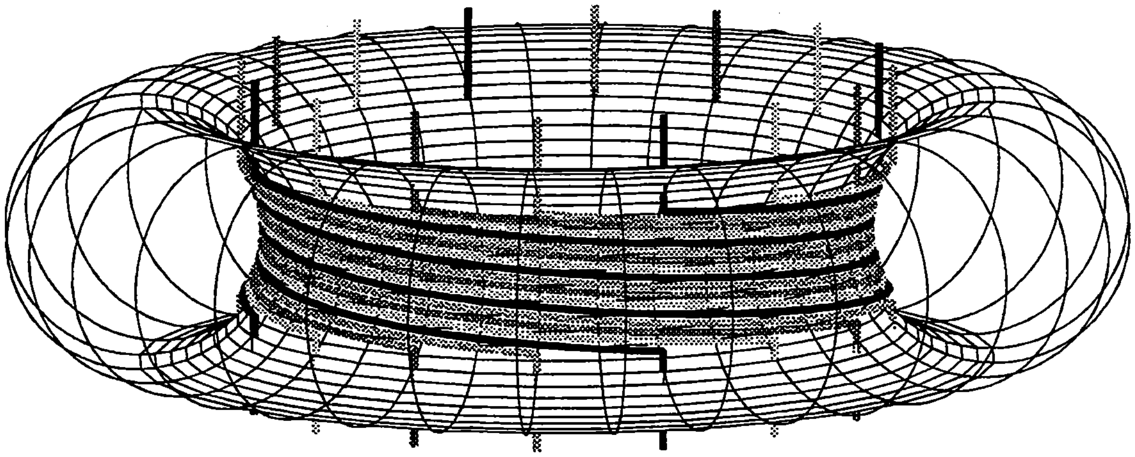

Association EURATOM-KFA Jülich
Partner in the Trilateral Euregio Cluster

1996

Editor: K.H. Finken

Contributors :

M. Baelmans[1*], P. Börner[1], T. Evans[4], D. Faulconer[2], K.H. Finken[1], B. Giesen[1], M. Haßler[1], T.H. Jensen[4], A. Kaleck[1], R. Koch[2], B. Küppers[1], A. Montvai[3], A. Nicolai[1], D. Reiter[1], A. Rogister[1], U. Samm[1], M. Tokar[1], G. Van Oost[2], G.H. Wolf[1]

[1] Institut für Plasmaphysik, Forschungszentrum Jülich,
Association EURATOM-KFA

[2] Laboratoire de Physique des Plasmas – Laboratorium voor Plasmafysica
Ecole Royale Militaire– Koninklijke Militaire School
Bruxelles – Brussel
Association EURATOM-Belgian State

[3] FOM Instituut voor Plasmafysica 'Rijnhuizen', Nieuwegein
Association EURATOM-FOM

[4] General Atomics, San Diego, USA

[*] Supported by EURATOM in the frame of ist fellowship scheme

Contents

Executive Summary

I Introduction

1. Background, Motivation, Concept and Scientific Aims 7
(K.H. Finken, G.H. Wolf, Institut für Plasmaphysik Forschungszentrum Jülich, Association EURATOM-KFA)

2. Technical Lay-out 12
(B. Giesen, Institut für Plasmaphysik Forschungszentrum Jülich, Association EURATOM-KFA)

II Features of the Perturbed Magnetic Field

3. Characteristic Parameters of the Ergodized Magnetic Field 24
(A. Nicolai, Institut für Plasmaphysik Forschungszentrum Jülich, Association EURATOM-KFA)

4. Ergodization of the Magnetic Field at the Plasma Edge 38
(M. Haßler, A. Kaleck, Institut für Plasmaphysik Forschungszentrum Jülich, Association EURATOM-KFA,
T. Evans, General Atomics, San Diego, USA)

5. Near Field Structure of the Magnetic Field 60
(K.H. Finken, Institut für Plasmaphysik Forschungszentrum Jülich, Association EURATOM-KFA

6. Physics Considerations for the TEXTOR in-vessel High Field Side (HFS) Perturbation Coils 72
(T. Evans, General Atomics, San Diego, USA)

III Specific Aspects

7. Parametric Variation of the Inboard Field Line Pitch Angle 77
(A. Rogister, Institut für Plasmaphysik Forschungszentrum Jülich, Association EURATOM-KFA)

8. Penetration of the Rotating Magnetic Field into the Plasma 86
(D. Faulconer, R. Koch,
Laboratoire de Physique des Plasmas - Laboratorium voor Plasmafysica, Association "Euratom - Belgian State", Ecole Royale Militaire - Koninklijke Militaire School, Brussels)

9. Considerations on Diagnostics during Operation with the Dynamic Ergodic Divertor on TEXTOR-94 106
(K.H. Finken, G. Van Oost
Institut für Plasmaphysik Forschungszentrum Jülich, Association EURATOM-KFA
Laboratoire de Physique des Plasmas - Laboratorium voor Plasmafysica, Association "Euratom - Belgian State", Ecole Royale Militaire - Koninklijke Militaire School, Brussels)

IV Modelling - Results and Development

10. Modelling of Plasma and Impurity Behaviour in a Tokamak with a Stochastic Layer 114
(M. Tokar', Institut für Plasmaphysik Forschungszentrum Jülich, Association EURATOM-KFA)

11. 2D Plasma Edge Transport Modelling of the DED Operation 131
(M. Baelmans, P. Börner, B. Küppers, D. Reiter, Institut für Plasmaphysik Forschungszentrum Jülich, Association EURATOM-KFA,*
**Supported by EURATOM in the frame of its fellowship scheme)*

12. Particle Drift-Trajectories in the Rotating Field of the Dynamic Ergodic Divertor in the TEXTOR Tokamak - a Monte-Carlo Study 172
(A. Montvai, FOM Instituut voor Plasmafysica 'Rijnhuizen', Association EURATOM - FOM, Nieuwegein)

13. Model for a Plasma Response for a Finite Relative Velocity between Plasma and the Magnetic Perturbation 187
(T. Jensen, General Atomics, San Diego, USA)

V Special Applications to the TEXTOR Programme

14. The Optimization of a Radiative Plasma Mantle 195
(U. Samm, Institut für Plasmaphysik Forschungszentrum Jülich, Association EURATOM-KFA)

15. Particle, in Particular Helium Removal Experiments 197
(K.H. Finken, Institut für Plasmaphysik Forschungszentrum Jülich, Association EURATOM-KFA)

Executive Summary

One of the essential problems for the successful operation of a fusion burner is to arrange for the exhaust of heat and particles in such a way that the following requirements are met:

(1) the materials and components of the inner wall are not overheated or unduly eroded

(2) the pumping system and the geometrical arrangement of the wall components allow sufficient helium removal

(3) only limited amounts of wall-released impurities, recycled helium and injected impurities (for edge radiation cooling) are able to penetrate the boundary layer into the plasma core

(4) the methods used to satisfy the above requirements are compatible with a high energy confinement and a practical fuelling scheme.

For the Next Step – ITER, the poloidal divertor is being developed to meet these requirements. Both for widening the understanding of the physics involved in the exhaust issue and for exploring possible alternative or complementing methods of exhausting particle and power, studies are also being undertaken on other concepts, in particular limiter concepts, the ergodic divertor, and the island divertor foreseen for Stellarators (see e.g. W7-X). An additional advantage of this programme strategy is the fact that (i) synergisms exist between different approaches and concepts and (ii) most methods and processes (like diagnostics, wall treatment, modelling, heating) which are developed on one system can be transferred to the others.

The stimulating results from the **Ergodic Divertor (ED)** of TORE SUPRA (Association EURATOM-CEA Cadarache), as well as the ideas and experiments of Takamura et al. have inspired KFA-Jülich and its partners to develop the concept of the **Dynamic Ergodic Divertor (DED)**. The Association EURATOM-KFA Jülich, therefore, proposes to build and install such a system in TEXTOR-94 as an integral part of the research programme of the Trilateral Euregio Cluster (TEC).

The beneficial effects of an **ED**, among which improved radiation efficiency of impurities and better impurity screening (TORE SUPRA) are the most significant ones, are due to the combined effects of increased electron density and decreased electron temperature at the plasma boundary in conjunction with enhanced radial transport and reduced sputtering of impurities. In the "near field" region of the helical coils (creating the multipolar perturbation field) the magnetic field lines are displaced radially even without resonances and ergodization. As a consequence, the magnetic field lines can intersect the target plates which cover the helical coils, resulting in high particle and heat fluxes there and establishing a **multipolar helical divertor** localized in front of the perturbation coils.

The **DED** introduces a new element into the concept of the ED, namely a magnetic perturbation with a phase velocity relative to the surrounding material structures as well as to the plasma. This opens up a new experimental dimension of unexplored physics, but allows also operation as an ED (i.e. DC-mode). Therefore, this approach is also of relevance for Stellarators, for which island divertors and edge ergodization are preferred means of solving the exhaust problem. Since the physics involved is complicated and only partly understood, a major part of the proposed effort will be aimed at understanding the underlying physics and experimentally assessing the potential of the proposed scheme.

The coil arrangement of the proposed DED consists of a quadruple set of four helical conductors, installed on the inboard side of the TEXTOR vessel and aligned parallel to the magnetic field lines (for $\beta_{pol} \approx 1$) at the nearby q=3 surface. Taking into account the available space, the technical constraints (such as current density, skin effect, heat capacity, cooling aspects, etc.) and the physics requirements, an m = 12, n = 4 perturbation field structure has been selected. This can be achieved by using coils which cover about 30 % of the inboard vessel surface on the high field side and which will be energized by a 4-phase current (up to 15 kA) at selected frequencies (DC, 50 Hz, 1 kHz and in a band between 1 kHz and10 kHz). These frequencies correspond to phase velocities projected on the poloidal coordinate of v_{ph} = 12 m/s, 240 m/s, 2400 m/s respectively. The coils can be connected in several ways allowing a certain range of different mode structures such as the m=6, n=2 and m=3, n=1 modes. The poloidal velocities will then be higher by a factor of two or 4 respectively.

Application of a low frequency (50 Hz) is aimed at avoiding hot spots by spreading the heat load evenly, either over the protection tiles of the helical divertor located at the high field side or over the pump limiter located at the low field side. It is expected that the particle removal rate at the pump limiter increases with an ergodic layer, as was found in calculations with the B2-EIRENE code.

The medium frequency of 1 kHz opens experimental access to the question whether a rotation of the perturbation pattern which is faster than the transit time of recycling particles in the boundary layer will affect particle transport and in consequence also the recycling process and the screening efficiency.

By applying the upper frequency band of 1-10 kHz – the velocity of perturbation is then of the same order as the natural diamagnetic drift velocity of the plasma – one can investigate whether the rotating field will induce an angular momentum in the plasma and whether the resulting torque will affect confinement and stability properties. A particularly interesting case may occur when the plasma rotation coincides with the rotation of the applied perturbation field. In this context, the DED also directly addresses questions of plasma confinement and stability.

It has been found (e.g. experimental tests on the linear PISCES device) that, for the proposed frequencies and the relevant plasma parameters, the perturbation field penetrates nearly undamped to the resonance layer where it couples to the plasma. Field line tracing studies (using the IPP-Garching version of the "Gourdon-Code") show that sufficient ergodization will be achieved with the planned coil currents and that TEXTOR-94 can operate either in the "island" or in the "ergodic" regime.

The proposed DED will be an integral part of the overall research programme of the TEC aiming at coherent concepts for energy and particle transport and exhaust.

The technical solution has been chosen to provide a wide range of experimental possibilities with a limited investment, the aim being the exploration of the potential and the limits of the DED as a means to influence and control plasma wall interaction. It is not expected that this solution could be directly applied to future larger devices. Rather the primary benefit of the intended studies is seen in the improvement in understanding of edge transport, island formation, effects of ergodicity etc. which may lead to the incorporation of some features of the TEXTOR DED into other exhaust concepts and may also stimulate the search for novel concepts and technical solutions which would have potential for development towards ultimate application on a burning fusion plasma. The planning of the dynamic ergodic divertor will considerably enhance the capabilities of the TEC within its plasma-wall and exhaust oriented programme.

I. Introduction

1. Background, Motivation, Concept and Scientific Aims

K.H. Finken, G.H. Wolf,
Institut für Plasmaphysik, Forschungszentrum Jülich, Association EURATOM-KFA, 52425 Jülich

One of the essential problems for the successful operation of a fusion burner is to arrange for the exhaust of heat and particles in such a way that the following requirements are met,

(1) the materials and components of the inner wall are not overheated or unduly eroded
(2) the pumping system and the geometrical arrangement of the wall components allow sufficient helium removal
(3) only limited amounts of wall-released impurities, recycled helium and injected impurities (for edge radiation cooling) are able to penetrate the boundary layer into the plasma core
(4) the methods used to satisfy the above requirements are compatible with a high energy confinement and a practical fuelling scheme.

For the Next Step – ITER, the poloidal divertor is being developed to meet these requirements. Both for widening the understanding of the physics involved in the exhaust issue and for exploring possible alternative or complementing methods of exhausting particle and power, studies are also being undertaken on other concepts, in particular limiter concepts, the ergodic divertor, and the island divertor foreseen for Stellarators. An additional advantage of this programme strategy is the fact that (i) synergisms exist between different approaches and concepts and (ii) most methods and processes (like diagnostics, wall treatment, modelling, heating) which are developed on one system can be transferred to the others.

Within this programme framework, and benefitting from fruitful partnerships – in particular with ERM/KMS and the IEA-partners –, TEXTOR has contributed to the field of plasma wall interaction and related confinement aspects, in particular to wall conditioning, particle – specifically helium – removal and power exhaust by edge radiation cooling. Instrumental for these contributions was a reproducibly operating tokamak system – equipped with a toroidal pump-limiter – which has been specifically designed for these tasks and which includes powerful heating devices (ICRH and NI), refined capabilities for plasma positioning and versatile diagnostic equipment. In its recently upgraded version, TEXTOR-94 is the central facility for the joint research programme of the Trilateral Euregio Cluster (TEC).

Juxtaposed on this background, the stimulating results from the **Ergodic Divertor (ED)** of TORE SUPRA, as well as the ideas and experiments of Takamura et al. have inspired KFA-Jülich and its partners to develop the concept of the **Dynamic Ergodic Divertor (DED)**. The Association EURATOM-KFA Jülich, therefore, proposes to build and install such a system in TEXTOR-94 as an integral part of the research programme of the Trilateral Euregio Cluster (TEC).

The **DED** introduces a new element into the concept of the ED, namely a magnetic perturbation with a phase velocity relative to the surrounding material structures as well as to the plasma. This opens up a new experimental dimension of unexplored physics, but allows also operation as an ED (i.e. DC-mode). This approach is also of relevance for Stellarators, for which island divertors and edge ergodization are preferred means of solving the exhaust problem. Since the physics involved is complicated and only partly understood, a major part of the proposed effort will be aimed at understanding the underlying physics and experimentally assessing the potential of the proposed scheme.

The principle of the **Ergodic Divertor** can be approximately described by the following cycle of particle transport: The open field lines near the plasma periphery guide the ionized particles of the plasma (hydrogen, impurities and helium ash) to the wall where they are neutralized. There – no longer coupled to the magnetic field lines – they may be scattered back into the plasma. If the ergodic layer is thick enough, the backscattered neutral particles will be re-ionized before entering the bulk plasma and – by collisions with the plasma flow from the confinement zone and as a result of increased radial transport caused by the ergodization – they will be swept back to the wall. This results in an enhanced density near the wall. In addition to the cooling of electrons by ionization and radiation, the electron temperature is lowered by the enhanced heat conductivity along the field lines in the ergodic zone; the ionization and excitation zones are broadened and shifted inward. Moreover, impurity release due to energy dependend processes (e.g. sputtering) can be reduced significantly. Thus, the combined effects of increased electron density and decreased electron temperature at the plasma boundary in conjunction with enhanced radial transport are responsible for the beneficial effects of an ED, among which improved radiation efficiency of impurities and better impurity screening are significant (TORE SUPRA).

In the "near field" region of the helical coils (creating the multipolar perturbation field) the magnetic field lines are displaced radially even without resonances and ergodization. This deflection depends on the specific configuration and on the amplitude of the perturbation field. As a consequence, the magnetic field lines can intersect the target plates which cover the helical coils with resultant high particle and heat fluxes there, establishing a multipolar helical divertor localized in front of the perturbation coils.

The distinguishing feature of the **Dynamic Ergodic Divertor**, however, is the establishment of a rotation of the applied magnetic perturbation pattern. This is motivated by a variety of applications which are related to the frequency range of the applied rotation.

The coil arrangement of the proposed DED consists of a quadruple set of four helical conductors, installed on the inboard side of the TEXTOR vessel and aligned parallel to the magnetic field lines (for $\beta_{pol} \approx 1$) at the nearby q=3 surface. Taking into account the available space, the technical constraints (such as current density, skin effect, heat capacity, cooling aspects, etc.) and the physics requirements, an m = 12, n = 4 perturbation field structure has been selected. This can be achieved by using coils which cover about 30 % of the inboard vessel surface on the high field side and which will be energized by a 4-phase current (up to 15 kA) at selected frequencies (DC, 50 Hz, 1 kHz and a band of 1 kHz to 10 kHz). These frequencies correspond to phase velocities projected on the poloidal coordinate of v_{ph} = 12 m/s, 240 m/s, 2400 m/s respectively. The coils can be connected in several ways allowing a certain range of different mode structures such as the m=6, n=2 and m=3, n=1 modes. The poloidal velocities will then be higher by a factor of two or 4 respectively.

Application of a low frequency – 50 Hz (v_{ph} = 12 m/s) is proposed for technical convenience – is aimed at spreading the heat load evenly either over the protection tiles of the helical divertor located at the high field side or over the pump limiter located at the low field side. Shifting the plasma position and/or changing the plasma aperture allows control of the relative distribution of the total heat and particle flux between these two main plasma facing components. This puts the proposed **DED** programme in a unique position to answer a number of critical questions which address the physics of mixed ergodic-island layers and how they can be used as an adaptive interface between hot, well-confined plasmas and plasma facing components.

In contrast to the 50 Hz case, the medium frequency of 1 kHz (v_{ph} = 240 m/s) opens experimental access to the interesting question of whether a rotation of the perturbation pattern which is faster than the transit time of recycling particles – penetrating the boundary layer – will affect particle transport and in consquence also the recycling process and the screening efficiency.

Last but not least, by applying the upper frequency band of 1 kHz to 10 kHz ($v_{ph} \leq 2400$ m/s) – the velocity of the perturbation is then of the same order as the natural diamagnetic drift velocity of the plasma – one can investigate whether the rotating field will induce an angular momentum in the plasma and whether the resulting torque will affect confinement and stability properties. A particularly interesting case may occur when the plasma rotation coincides with the rotation of the applied perturbation field. Moreover, the currents induced in the plasma by the rotating field pattern and their feedback on the resulting structure of the ergodized layer may become relevant at higher frequencies. Thus, besides the issues of particle and heat exhaust, the DED also directly addresses questions of plasma confinement and stability including locked modes and their interaction.

The technical solution for the DED on TEXTOR-94 has been chosen to provide a wide range of experimental possibilities with a limited investment, the aim being the exploration of the potential and the limits of the DED as a means to influence and control plasma wall interaction. It is not expected that this solution could be directly applied to future larger devices. Rather the primary benefit of the intended studies is seen in the improvement of the understanding of edge transport, island formation, effects of ergodicity etc. which may lead to the incorporation of some features of the TEXTOR DED into other exhaust concepts and may also stimulate the search for novel concepts and technical solutions which would have potential for development towards ultimate application on a burning fusion plasma.

The proposed DED will be an integral part of the overall research programme of the TEC aiming for coherent concepts for energy and particle transport and exhaust.

The scientific aims of the proposed Dynamic Ergodic Divertor are summarized as follows:

- *Study the effect of dynamic helical magnetic perturbation patterns on plasma-wall-interaction and on plasma confinement; compare the DC operation with other ergodisation experiments*

- *Improve and optimise the exhaust of particles, in particular of Helium and of seeded impurities*

- *Study and optimise the concept of edge radiation cooling, particularly in view of the demands for low* Z_{eff} *and good confinement*

- *Distribute the remaining convective heat load on larger areas of the plasma facing components*

- *Study the effect of different (higher) phase velocities, in particular on the resulting pattern of islands and ergodization, on particle screening, on (shear-) rotation and confinement, and on possible interactions between these processes*

- *Study the effect of different mode structures of the perturbation pattern, such as* $m=3$

- *Develop and evaluate analytical and numerical models necessary for extrapolation to larger devices or for general use in other configurations (e.g. stellarators)*

- *Improve and refine diagnostic methods for plasma parameters in ergodic layers and within islands or island divertors*

2. Technical Lay-out

B. Giesen,
Institut für Plasmaphysik, Forschungszentrum Jülich, Association EURATOM-KFA

Table I (General features of TEXTOR-94)

Major Radius	$R_0 = 1.75$ m
Minor Plasma Radius	$a \leq 0.48$ m (circular cross-section
Toroidal Magnetic Field	$B_t \leq 3$ T
Plasma Current	$I_p \leq 0.8$ MA
Long Pulse Capability	$\Delta t \leq 10$ s ($\Phi \leq 9$ Vs)
Exchangeable Liner	$T_{liner} \leq 500$ °C
Toroidal Pump Limiter ALT-II	8 adjustable blades; 8 ports
ICRH	2 antenna pairs; 4 MW, 25-28 MHz for > 10 s
NBI	2 injectors, 1 co, 1 counter; 4 MW, 60 kV for 10 s
Multi Pellet Injector	up to 9 H_2 or D_2 pellets

2.1 General Design Features

A set of 16 helical coils will be installed on the inboard side of the vacuum vessel of TEXTOR 94 covering about 30 % of the inboard vessel surface (Fig. 1). The inboard side has been chosen mainly because it implies minimum interference with diagnostic systems. The coils are aligned in parallel to the magnetic field lines at the nearby q=3 surface; they follow the torus on the high field side for one complete turn in toroidal direction. Two more coils will be installed for compensation of the stray field generated by the feeders and the star point connectors. These compensation coils are located inside the vessel above and below the set of ergodization coils, running in parallel to them. They are connected in series but their currents are flowing in opposite direction.

All 18 coils (16 ergodization coils, 2 compensation coils) are mounted on an array of poloidal belt segments (symmetric to the z=o plane). The belt segments are supported by the vacuum vessel. To accommodate the coils and their support segments, the corresponding area of the TEXTOR-liner will be removed. The edges of the remaining part of the liner will be reinforced and also supported by the vacuum vessel. For protection from contact with the plasma, the coils will be covered by graphite tiles which act as divertor target plates and/or bumper limiter. Each individual coil is enclosed in a stainless steel bellow. The coils are gas cooled at a pressure of 3.0 MPa to limit the temperature in the coils to 200 °C during operation and during baking of the liner and the target tiles.

Table II (Main characteristics and parameters)

Coils:				
number of coils	18 (2 for field compensation)			
turns per coil	1			
conductor	twisted copper wires			
wires per conductor	42			
diameter of wire	2.8 mm			
current density	5.8 kA/cm^2			
thickness of wire insulation	0.1 mm			
insulation material	polyimide			
Coil cooling:				
coolant	nitrogen gas			
pressure	3.0 MPa			
pressure drop	0.6 MPa			
max. temperature	200°C			
Electrical coil parameters				
inductivity	6.6 μH			
resistivity	1 mΩ			
time on/off	10 s / 360 s			
kind of current	DC and 4 phase current			
frequency	DC	50 Hz	1 kHz - 5 kHz	5 kHz - 10 kHz
current (peak)	15 kA	15 kA	10 kA	7.5 kA
voltage (peak)	30 V	69 V	830 V-4.1 kV	3.1 kV-6.2 kV
voltage to ground	15 V	34.5 V	415 V-2.1 kV	1.5kV-3.1 kV
Power Supply				
number of units	9			
voltage (peak)	600 V			
current per unit (peak)	1.5 kA			
transformer	600 V/60 V			
total peak power	8.1 MW			

In the standard set-up, four neighboring coils form one quartet. The whole divertor magnet consists of four of these quartets. Each of them will be fed by a 4-phase rotating current and has a star point connection; this makes also a symmetrical DC operation possible. The current in the individual coils will be limited to a peak value of 15 kA for a duration of 10 s. The system is designed for the application of the following frequencies: DC, 50 Hz and 1 kHz, and for a frequency-band from

1 kHz to 10 kHz (see extension). In the band 5 kHz to 10 kHz the maximum design current is only 7.5 kA.

A set of 9 identical frequency convertor units adjustable for the selected frequencies with a total power of 8.1 MW will be used. Four pairs of them will energize the four quadruple sets of the ergodization coils and one unit will be used to energize the two compensation coils.

2.2 Coil Design

In order to cope with the eddy currents and skineffects, to fulfill the cooling requirements and to limit the temperature rise for pulse durations of up to 10 s, and to make optimal use of the available space, a special conductor has been developed for the coils. It consists of six bundles of insulated twisted copper wires. The bundles are also twisted and act like a spring which tolerates thermal expansion of the interior parts. A glass fibre bundle supports the copper bundles from the inside. (Fig. 2) Each copper wire (diameter 2.8 mm) is insulated. The insulation material (thickness 0.1 mm) is polyimide (max. working temperature 250 °C) which resists voltages of up to 10 kV. The cable is wrapped in a woven glass fiber tube which protects from mechanical damage, this is enclosed in a waved stainless steel tube (bellows) of 0.2 mm thickness. In longitudinal direction the waved tube can handle expansions of 0.5 % and the twisted cable of 1 %. A test cable with a length of 100 m has been produced and has successfully passed the relevant electrical tests.

The forces on the coils from electromagnetic interactions amount to 3.5 kN/m. The coils are mounted to the poloidal belt segments by clamps which are also used as support for the target plates (Fig. 3). The toroidal distance between these clamps is 244 mm. In close neighbourhood of the feedthroughs, the coils are running perpendicular to the toroidal field. The magnetic forces there amount to 45 kN/m which requires the coils to be clamped every 100 mm.

The lay-out of the system takes into account heating by eddy-currents (at high frequencies), especially inside the vacuum vessel and in the feedthroughs where high uncompensated currents unavoidably flow close to the support structure. The vacuum-feedthroughs insulate the conductor of the coils and the tube from the vessel and give access to the cooling gas. The present design of a coaxial feedthrough (for two „in phase currents“ of opposite direction) is shown in Fig. 4.

The magnetic field of the coils has to penetrate the stainless steel tube (0.2 mm) and the carbon tiles (12 mm) also at high frequencies. Table II shows that the skindepths of both materials are much larger than the thickness of the relevant components (tube: 0.2 mm << 4.9 mm / tiles: 12 mm << 33 mm) and that consequently the magnetic field reaches the plasma mainly undamped.

Table III (Skindepth)

at frequency	copper	stainless steel	carbon
DC	∞	∞	∞
50 Hz	10 mm	74 mm	500 mm
1 kHz	2.1 mm	15.6 mm	1005 mm
10 kHz	0.66 mm	4.9 mm	33 mm

2.3 Cooling System

The coils will be cooled by nitrogen gas. The gas pressure is 3.0 MPa and the pressure drop is about 0.6 MPa. Table III shows the adiabatic temperature rise of the conductor and the pulse duration at the four selected frequencies.

Table IV (Coil temperature and pulse duration)

f	peak current	ΔT_{copper}	Δt
DC	15 kA	160 K	7.0 s
50 kHz	15 kA	120 K	10.0 s
1 kHz	15 kA	120 K	10.0 s
10 kHz	7,5 kA	30 K	10.0 s

The average power of the cooling system is 70 KW. An external heat exchanger transfers the energy to a water cooling system. The cool down time from 200 °C to 50 °C is about 6 min. A compressor with a power of 110 kW increases the pressure from 2.4 to 3.0 MPa after the expansion of the gas. Specific tests are in preparation.

2.4 Lay-out of the Power Supply Systems

The required 4-phase current system consists of two power units with a 90° phase shift (Fig. 5). The ends of four coils are connected by a common star point. The star point is grounded by a 10 Ω resistor which reduces the voltage to ground by a factor of two. The voltage to ground limits the current in the band 5 kHz to 10 kHz to 7.5 kA. For reactive power compensation, capacitors are connected in series to each coil. To comply with the voltage limitation of the power supply units, all L-C-branches have to be tuned to the same resonance frequency. In order to minimize cost, the coil parameters (high current, low voltage) are adapted by transformers to the convertor parameters (600 V, low current). For the power connections coaxial cables of low inductivity and high current will be used. For DC operation, diode rectifiers will be installed between the 1:10 transformer and the ergodization coils. The 9 convertor units will be supplied from the existing 21 kV station of TEXTOR-94 by one power transformer 21 kV / 400 V and 9 rectifier transformer 400 V / 568 V (Fig. 6).

2.5 Frequency Convertor Units

Nine identical frequency convertor units are required. The output voltage of one unit is 600 V and the peak current is 1.5 kA for 50 Hz and 1 kHz and 0.75 kA for 10 kHz. The driving voltage of 600 V has been chosen to minimize the cost of the power supply system (recommendation by industry).

A rectifier transformer and a controlled rectifier supplies the DC intermediate circuit of the convertor units (Fig. 7), and a 4-quadrant bridge with IGBT's produces the AC output voltage of 600 V (peak). The pulse duty cycle is 10s/360s.

The phase shift between the two power units is 90° to form a 4-phase (rotating) current system. In order to change the direction of rotation, the phase shift of the power units have to be changed from +90° to -90° in relation to the 0°- power units. One power unit with a phase shift of 45° feeds the compensation coils.

The required frequency-synchronization of all power units will be enforced by one central control unit. In order to compensate differences in the impedance of the individual loads, the current of each unit can be controlled separately in a close feed back loop.

2.6 Extension of the Dynamic Ergodic Divertor (DED) on TEXTOR 94 for Operation at more Frequencies

An extension of the DED for the operation of at least 5 additional frequencies in the range of 1 kHz to 10 kHz has been suggested by the Ad-Hoc group. A solution has been found, which covers the entire range of frequency from 1 kHz to 10 kHz.

For this purpose the capacitor banks originally foreseen for an operation at fixed frequencies of 1 kHz and 10 kHz will be subdivided in 14 groups with binary steps. For the frequency range from 2 kHz to 5 kHz and 5 kHz to 8 kHz two matching transformers per power circuit (altogether 18) are necessary. In the range of frequencies from 1 kHz to 5 kHz the max. current is 10 kA and from 5 kHz to 10 kHz the max. current is 7.5 kA. With this extended system all frequencies between 1 kHz and 10 kHz can be selected additional to the four frequencies DC/15 kA; 50 Hz/15 kA; 1 kHz/15 kA; and 10 kHz/7.5 kA.

At currents higher than 1,5 kA, the power supply circuits have to be operated as oscillator circuits . Therefore capacitors have to be switched in series to the coil inductivities. Because of the narrow range of frequencies all 9 circuits have to be tuned to the same resonant frequency.

On service days this tuning can be done in advance for a set of selected frequencies. On operational days the switch over to one of these frequencies will then be possible within 15 to 30 minutes. Shortening of that time seems to be possible if the operation on certain frequencies will be repeated. The binary subdivision in 14 steps of the capacitance makes a precise tuning of the oscillating circuits to the same frequency possible. This is necessary because of the narrow frequency range of 40 Hz to 160 Hz at currents of 15 kA to 7.5 kA.

For detection of resonant effects in low power operation a tuning at the range of frequency from 0 Hz to 5 kHz at a maximum current of 1.5 kA and from 5 kHz to 10 kHz at a decreasing current from 1.5 kA to 0.72 kA is still possible and can be done infinitely variable from discharge to discharge and if necessary during one discharge.

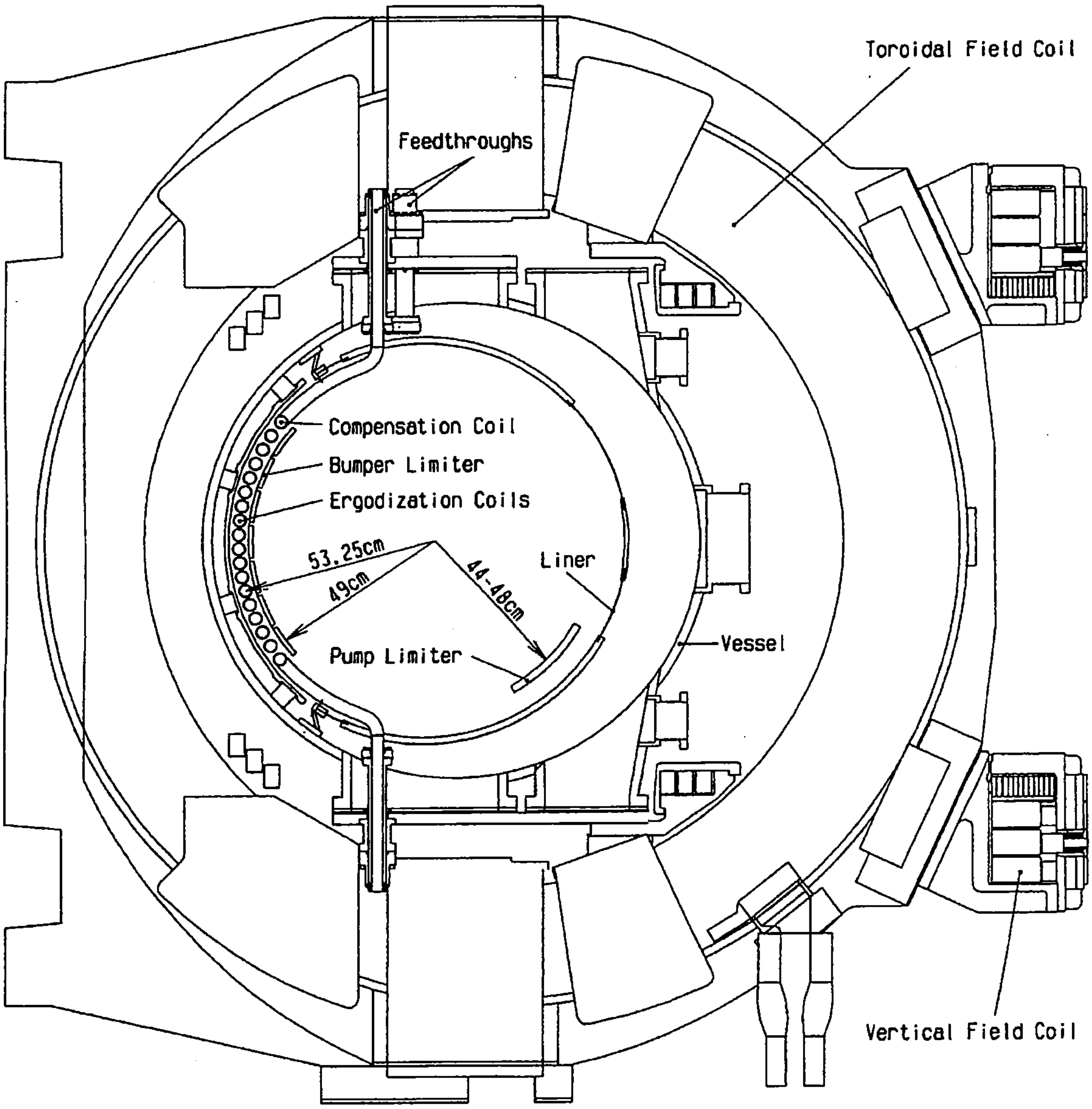

Fig. 1 Ergodization Coil Arrangement

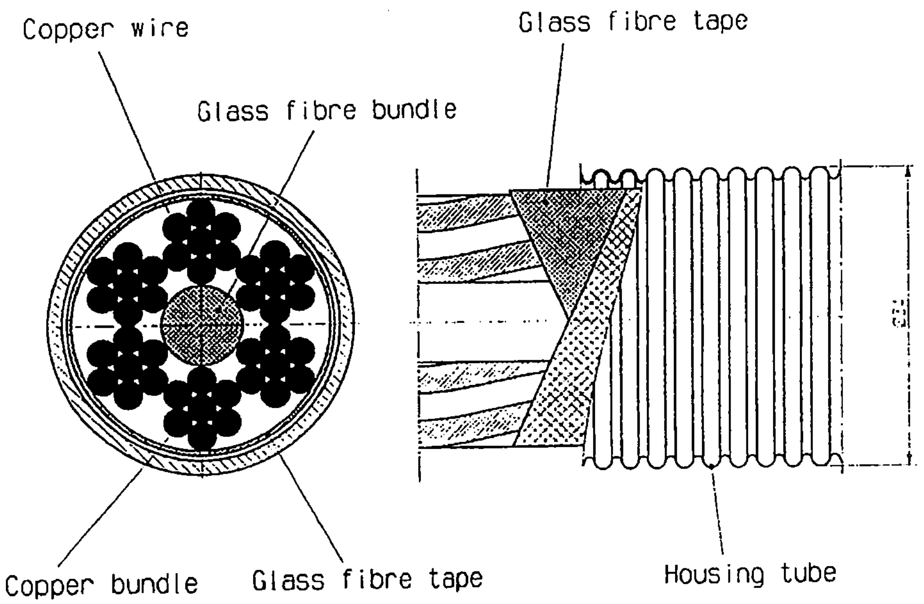

Fig. 2 Cable Coil

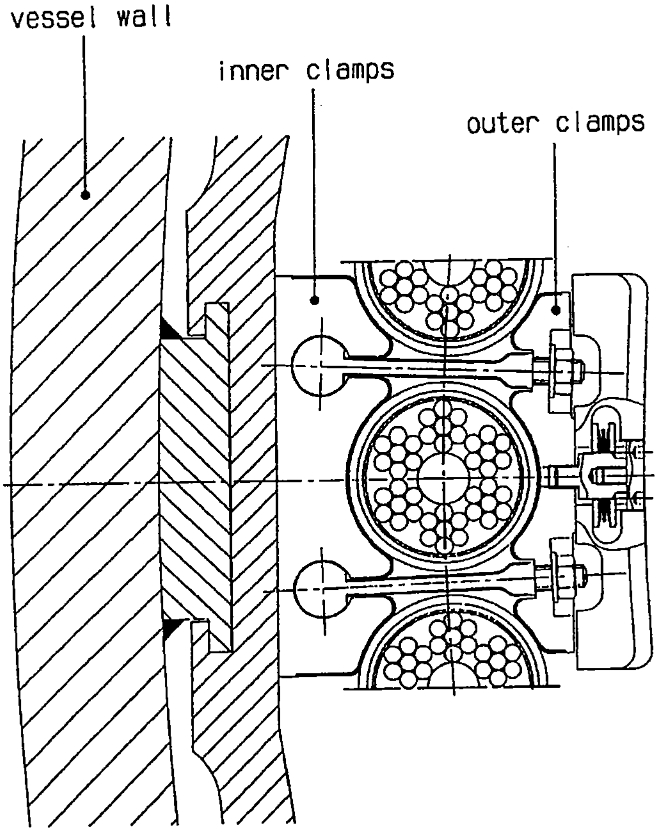

Fig. 3 Coil Support and Target Plates

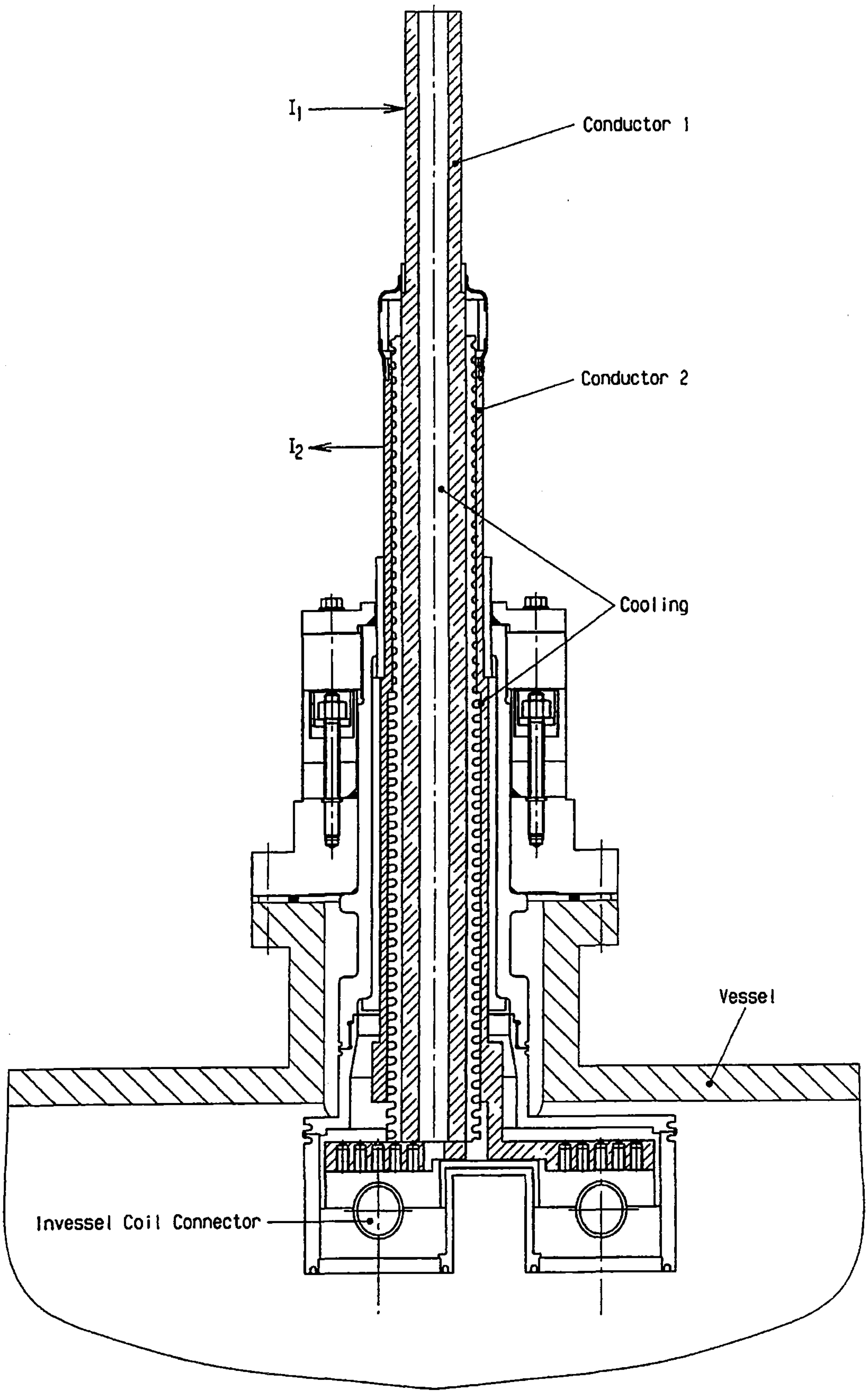

Fig. 4 Coaxial Feedthrough

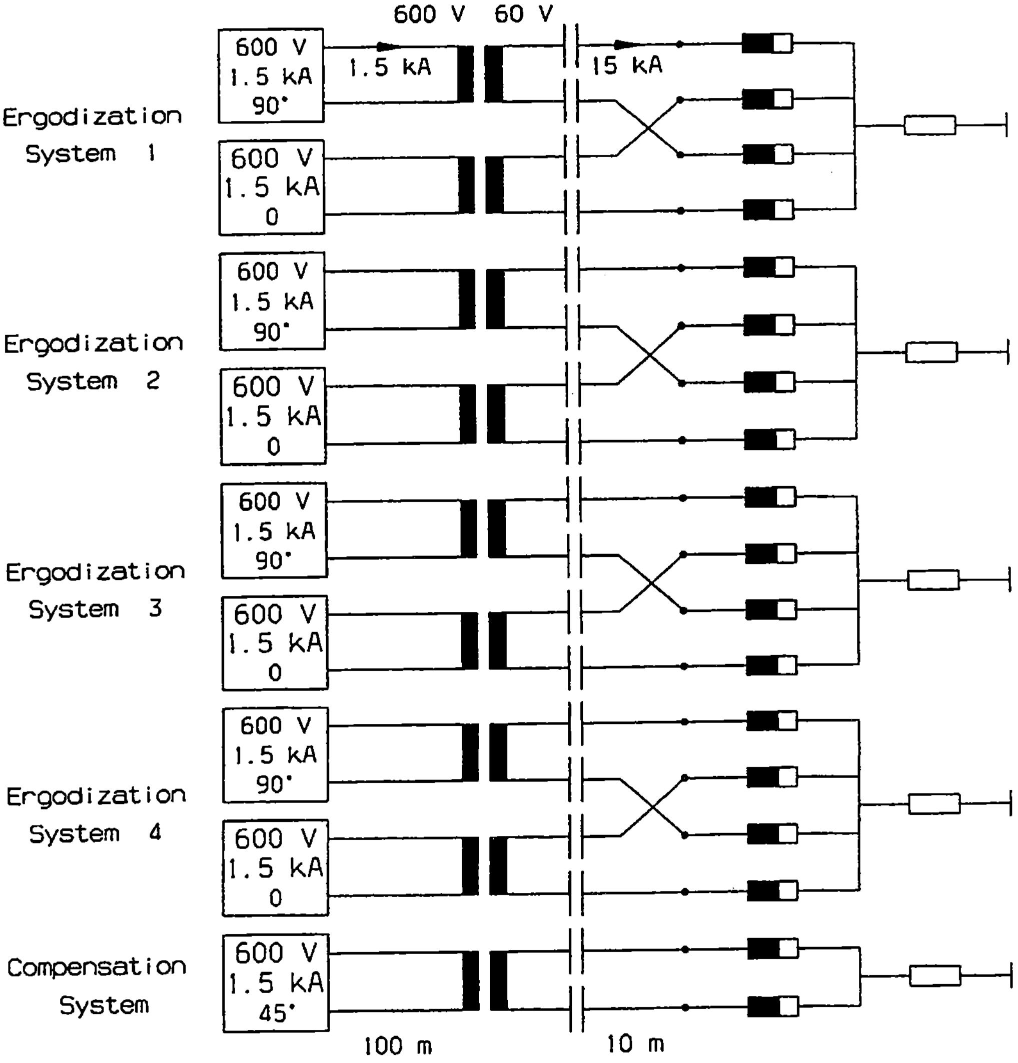

Fig 5 Power Supply Circuit

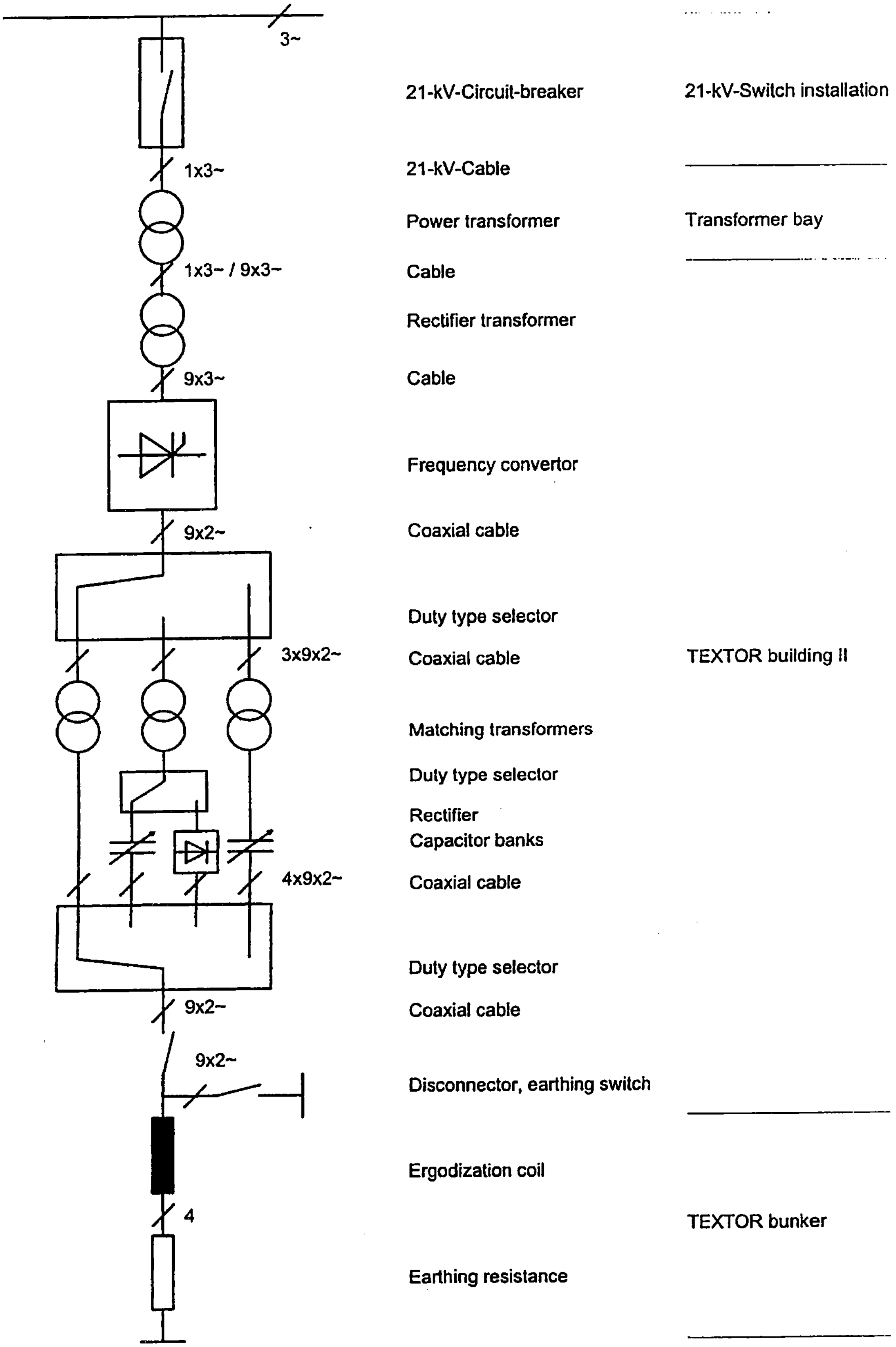

Fig 6 Power Supply Components

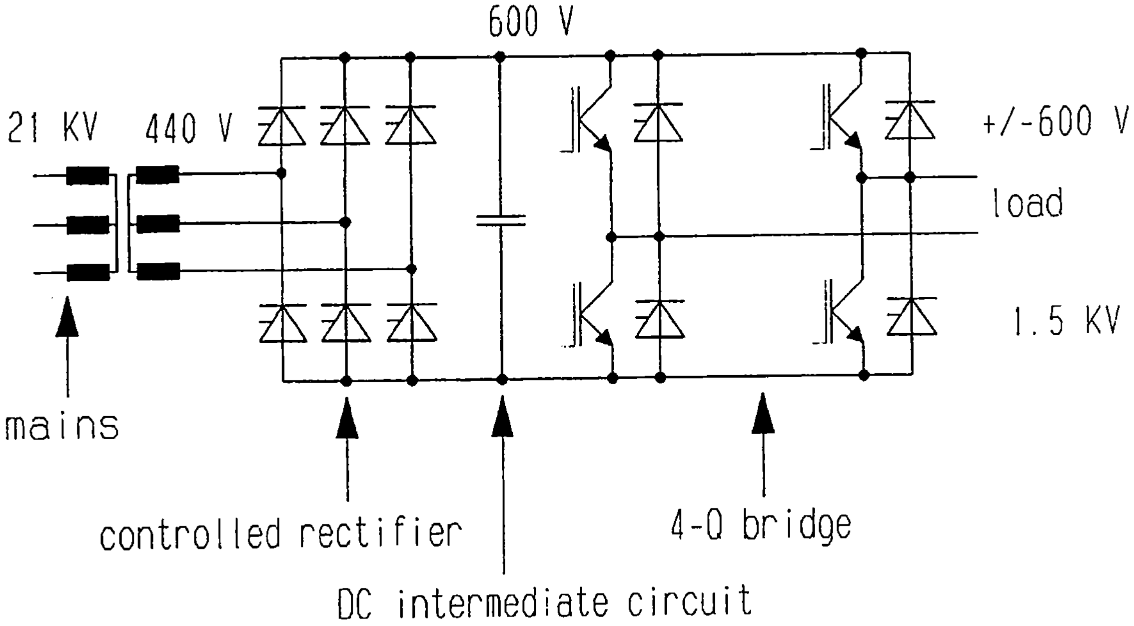

Fig. 7 Switch Mode Frequency Convertor Units with IGBT's

Part II: Features of the Perturbed Magnetic Field

3. Characteristic Parameters of the Ergodized Magnetic Field

A. Nicolai,
Institut für Plasmaphysik, Forschungszentrum Jülich, Association EURATOM-KFA

The mode structure of the radial field component generated by the coil currents of the windings allows computation of the characteristic parameters of the ergodized magnetic field namely the Chirikov - parameter, the Kolmogorov length and the quasilinear diffusion coefficient; from these parameters essential transport properties of the ergodic layer are derived. For these calculations it is assumed that the currents induced in the plasma by the perturbation field may be ignored. This assumption may be valid when the wave phase velocity is close or equal to the plasma flow velocity. When there is a significant difference between these velocities it is believed that the assumpion becomes invalid.

The Fourier components scale linearly with the coil current, which must be large to obtain a significantly enhanced diffusion coefficient. The currents in the coils of the dynamic ergodic divertor (DED) are assumed to control the transport properties of the plasma in the scrape off layer and the loading of the first wall. The perturbation field generates an ergodic and a laminar edge region with rather different properties; in this Section only the ergodic edge region is regarded.

In Hamada[1] and in 'intrinsic' coordinates[2] the equilibrium magnetic field lines are represented by straight lines. Both coordinate systems are based on axisymmetric equilibria. The latter system is more convenient for the perturbation coil configurations; in this representation the toroidal coordinates have their ordinary meaning ($\Phi^* = \Phi$). The poloidal coordinate Θ^* is modified in such a way that the magnetic field lines in the (Φ^*,Θ^*) representation are straight. To derive the transformation from Θ to Θ^* the Grad - Shafranov equation is considered for the poloidal flux function Ψ[3]

$$R^2\,\Delta\left(\frac{1}{R^2}\Delta\Psi\right) = \left[\frac{\partial^2}{\partial R^2} + \frac{\partial^2}{\partial z^2} - \frac{1}{R}\frac{\partial}{\partial R}\right]\Psi = -m\mu_o\,R\,j_\Phi$$

R and z are the distances from the axis of symmetry and the equatorial plane, respectively. The toroidal current density j_Φ is given by

$$j_\Phi = R \cdot \frac{dp}{d\Psi} + \frac{f}{m\mu_o R} \cdot \frac{df}{d\Psi}$$

The f - function is closely related to the toroidal flux function χ and is given by

$$f(\Psi) = R_o \cdot B_T$$

$p(\Psi)$ is the pressure profile and R_o the radius of the magnetic axis and B_T the toroidal field.

The dependence of $\Theta^* = \Theta^*(\Theta)$ is derived from relations concerning the field line pitch in general toroidal coordinates[4], intrinsic coordinates and ordinary toroidal coordinates (r,Θ,Φ)[5]. The thus obtained equation

$$\frac{d\Theta^*}{d\Theta} = \frac{1}{q} \cdot \frac{B_T}{B_p} \cdot \frac{r}{R}$$

can be integrated numerically.

$$B_p = \frac{|\Delta\Psi|}{R}$$

is the poloidal field and

$$q = \frac{d\chi}{d\Psi}$$

the safety factor. In the limit of a large aspect ratio plasma with circular cross-section an analytical relation may be used[4].

3.1 Fourier Components of the Radial Perturbation Field

The Fourier decomposition of the radial component and of the perturbation field at the radii of different Ψ - functions is performed within the intrinsic coordinates. By this choice the magnetic field lines are optimally traced and some toroidal effects leading to additional Fourier components can be minimized. These effects are mainly due to the local inclination of the magnetic field lines on the β_p-value. On the high field side the slope is shallower than on the low field side and the difference in slope increases with β_p.

Instead of labeling the Fourier components with Ψ, the safety factor q is selected as label. The sine- and cosine-components show a non trivial internal q-dependence and become:

$$b_{mn_s}(q) = \int d\Theta^*(q) \int d\Phi \; B_r(\Theta(\Theta^*(q)),\Phi) \cdot \sin(m\Theta^*(q) - n\Phi)$$
$$b_{mn_c}(q) = \int d\Theta^*(q) \int d\Phi \; B_r(\Theta(\Theta^*(q)),\Phi) \cdot \cos(m\Theta^*(q) - n\Phi)$$

and

$$b^2_{mn} = b^2_{mn_s} + b^2_{mn_c}$$

The calculations had been based on the following TEXTOR data[6]: minor radius a = 46 cm, major radius R = 175 cm, plasma current I_p = 420 kA, radius of the ergodization coils is assumed here to be r_e = 51 cm. This value is an older design value and not always consistent with other data in this proposal; the new coil radius is at 53.25 cm and therefore the actual characteristic parameters are overestimated by about a factor of 1.6 in the field amplitude in this Section. It is assumed that the current is distributed parabolically to the plasma edge (a = 46 cm); this is a limiting assumption because in general it has to be assumed - and has been measured[7] - that the electrical current is excluded from the ergodized layer with increasing ergodicity. The current in each conductor of I_e = 10 kA was assumed as a reference case. The resonant (q = 3) flux surface is then located at r_f = 42 cm. Here and at the neighboring flux surfaces for q = m/n (m = 10, ..., 14; n = 4) the Fourier analysis was performed.

Fig. 1 shows the case of the four phase helical windings at the inboard side of TEXTOR. They are parallel to the field lines at the q=3 surface for $\beta_p = 1$ and $l_i/2 = 0.7$ (typical value for TEXTOR). The winding covers 1\5 of the poloidal circumference at the inboard side of TEXTOR, thus entailing a rather broad Fourier spectrum in m. It contains four quadruplets (16 conductors). Each conductor is approximated by 75 straight pieces, the endpoints of which are located on the model helices. These helices are given (in intrinsic - coordinates) by

$$\Phi^* - \Phi^*_{oj} = q \cdot (\Theta^* - \Theta^*_{oj})$$

The starting points of the conductors are assumed to be distributed uniformly along the toroidal circumference. Thus we get in ordinary space $\phi_{oj} = (2\pi/12)\times(j-1)$, $\theta_{oj} = (4\pi/5)$, j = 1,...,16. The endpoints of the helical conductors are obtained by cutting the helices with the line $\theta = \{6\pi/5\}$. The arrows indicate the direction of the electrical current in the individual coils; those without arrows are current free for the phase considered here.

Fig. 2 shows the radial component of the magnetic field in the resonant flux surface q=3. This field can be described in good approximation by the sinusoidal waveform near the high field side but vanishes poloidally away from the perturbation coils. In the case of the four -phase AC - operation the currents $I_j = I_e \times \sin((2\pi/4)j + \alpha_p)$, j = 1,2,3,4 in each conductor quadruple depend on the phase α_p which in Fig. 1 is chosen to be zero. This can be done without loss of generality because it turns out that the impact of the phase on the Fourier amplitude is negligible.

The Fourier power spectra for the q-values 2.75, 3.0, 3.25 and 3.5 are plotted in Fig. 3a - 3e. The dominant Fourier component has the mode numbers n = 4 and m = 12, however, the m = 11 and m = 13 components are comparable in size. At the q = 2.75 surface the (m/n)-mode (11/4) will be resonating, at q = 3 the (12/4)-mode, at q = 3.25 the (13/4)-mode and at q = 3.5 the (14/4) mode and those mode amplitudes determine the island widths. The resonant modes reach values of about 2 - 30 Gauss for the perturbation current of 10 kA. In detail the mode spectrum is even more complex and higher modes like the (25/8) and even the (38/12) will be found back as will be described in the next Section.

3.2 Island width, Chirikov Parameter and Kolmogorov Length

The characteristic parameters for the ergodicity of a magnetic field are the island width, the Chirikov parameter and the Kolmogorov length. In a first approximation a single island forms not yet an ergodic field structure but a subtorus winding around the primary plasma-torus. If several small, radially distributed island chains are present in a tokamak the magnetic flux surfaces stay still intact and the different islands form chains of subtori. If the island size grows such that different islands start to overlap, the picture changes and flux surfaces get destroyed. The island get in addition destroyed from the inside because higher order island chains develop inside a primary island. The magnetic field becomes ergodized[8,9].

According to the standard theory, the width of an unperturbed island is given by

$$\Delta_{mn} = \sqrt{\frac{16r\,\varepsilon_{mn}}{m} \cdot L_{SH}}$$

The dimensionless quantity ε_{mn} stands mainly for the Fourier component of the radial field:

$$\varepsilon_{mn} = \frac{b_{mn}}{B_T}$$

The shear length L_{SH} depends mainly on the profile of the safety factor q :

$$L_{SH} = \frac{q^2 R_o}{r} \cdot \frac{1}{\frac{dq}{dr}}$$

The Chirikov parameter σ^{10} characterizes the ergodic structure due to overlapping islands and is given by

$$\sigma(r)^2 = \frac{8r(\varepsilon_{mn} + \varepsilon_{m'n'})}{m|L_{SH}|} \cdot (\frac{mqR}{r})^2$$

where (m,n) and (m',n') are the mode numbers of neighboring Fourier components. To derive the Chirikov parameter in the following $\Delta m = 1$ and n'= n are regarded. This choice overemphasizes possibly the role of the dominant Fourier modes and underestimates the influence of mode combinations like (12/4) - (25/8) - (38/12) -(13,4) as will be discussed in the next Section.

The separation of initially adjacent field lines is characterized by the Kolmogorov length L_k:

$$L_k = 2\pi q R_o \cdot \sigma^{-\frac{4}{3}}$$

Within the ergodic approximation, the particle transport is described by the quasilinear diffusion coefficient

$$D_Q = 2\pi q R_o \cdot |\varepsilon_{mn}|^2 \cdot v_{//}$$

where $v_{//}$ is the thermal particle (ion) velocity parallel to the field lines.

q	m/n	r(q)	B_{mn}	D_{mn}
2.5	10/4	38.7 cm	5.3 G	1.6 cm
2.75	11/4	40.6 cm	16 G	2.7 cm
3.0	12/4	42 cm	30 G	3.6 cm
3.25	13/4	43.9 cm	30 G	3.5 cm
3.5	14/4	45.1 cm	25 G	3.2 cm

From the shear length - assuming a parabolic current profile ($L_{SH} = 260$ cm) -, a B_T value of 2.25 T and the amplitude of the Fourier components treated above follows an unperturbed island width of $\Delta_{12,4} = 6.8$ cm at q = 3. The Fourier amplitude at the other resonant surfaces, the radial location, and the island widths are summarized in the table:

The Chirikov parameters and the Kolmogorov lengths are calculated for the locations in between two islands and are:

q	r	$\sigma_{mm',n}$	L_K
2.625	39.7 cm	1.60	1551 cm
2.875	41.6 cm	2.61	877 cm
3.125	43.2 cm	3.31	695 cm
3.375	44.5 cm	3.50	696 cm

The Kolmogorov length for q=3.125 is about 4 m long and this means that the correlation of the field lines is destroyed before they finish encircling the axis of symmetry one time. The quasilinear diffusion coefficient becomes about $D_q = 2\ m^2/s$ for $T_i = 100$eV and r = 43 cm. The particle diffusion due to the here considered ergodization is around one order of magnitude larger than the (anomalous) diffusion coefficient D_a without ergodization ($D_a \cong 1\ m^2/s$). Here the validity of the diffusion model is assumed.

Figure captions:

Fig. 1: Perturbation coil and current distribution used for the mode analysis.

Fig. 2: Perturbation field at the q=3 surface in the (Θ^*,Φ) plane.

Fig. 3 a-e: Fourier modes on different q-surfaces. The resonant modes are marked.

Fig. 4: Chirikov parameter as a function of the radius

References

- S. Hamada, Nucl. Fusion, **2** (1962) 23
- A. Samain, T. Blenski, Ph. Ghendrih et al. Contrib. Plasma Phys. **30** (1990) 157
- J.T. Hogan, Nucl. Fusion **19** (1979) 753
- Frédéric Nguyen, "Transport dans un plasma de fusion en présence d'un champ magnétique chaotique", Report EUR - CEA - FC - 1471 (1992)
- Ph. Ghendrih, H. Capes, J. Nguyen, A. Samain. Contributions to Plasma Physics, **32** (1992) 179
- K.H. Finken, G. Fuchs, B. Giesen et al, J. Nucl. Mater. **220 - 222** (1995) 448
- C. de Michelis, A. Grosman, X. Garbet et al., Nucl. Fusion, **35** (1995) 1133
- J.A. Lichtenberg, M.A. Liebermann, "Regular and Stochastic Motion", in Applied Mathematical Sciences 38, Springer Verlag, New Yorg, Heidelberg, Berlin, 1983
- M.C. Gutzwiller, "Chaos in Classical and Quantum Mechanics", in Interdisciplinary Applied Mathematics, Springer Verlag, New York, Heidelberg, Berlin,...1990
- B.V. Chirikov, Phys. Reports, **52** (1979) 265

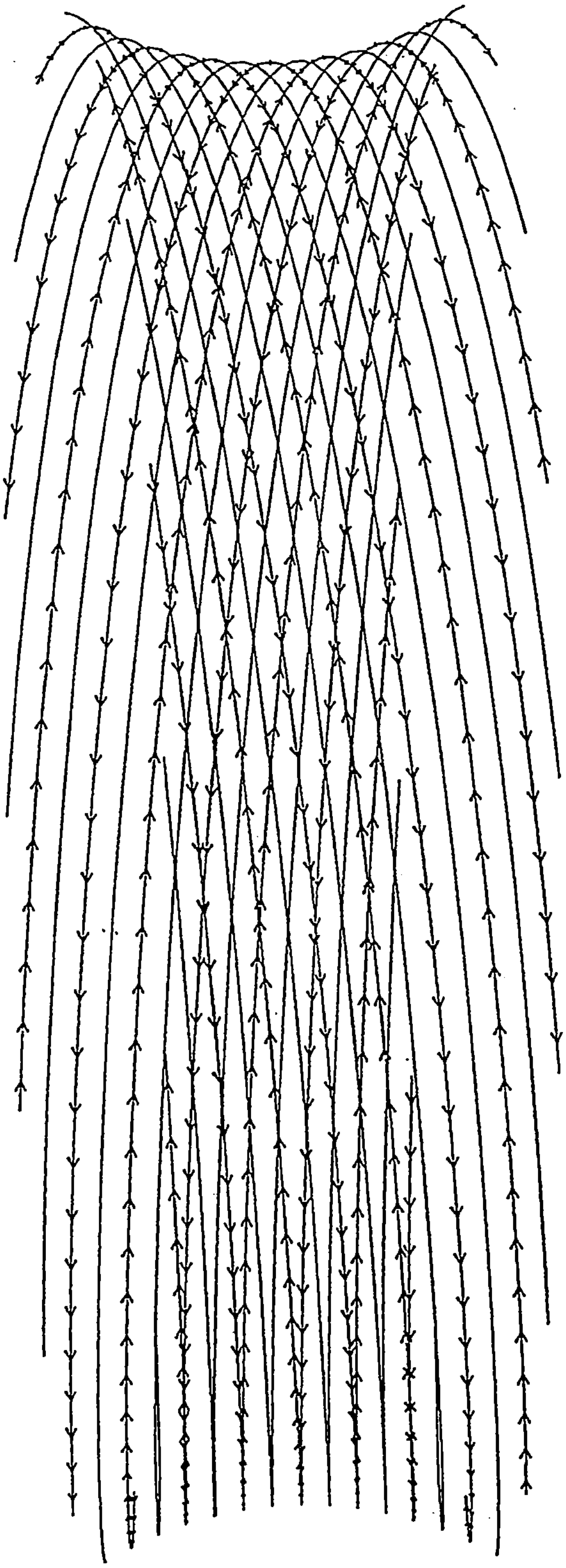

Fig. 1

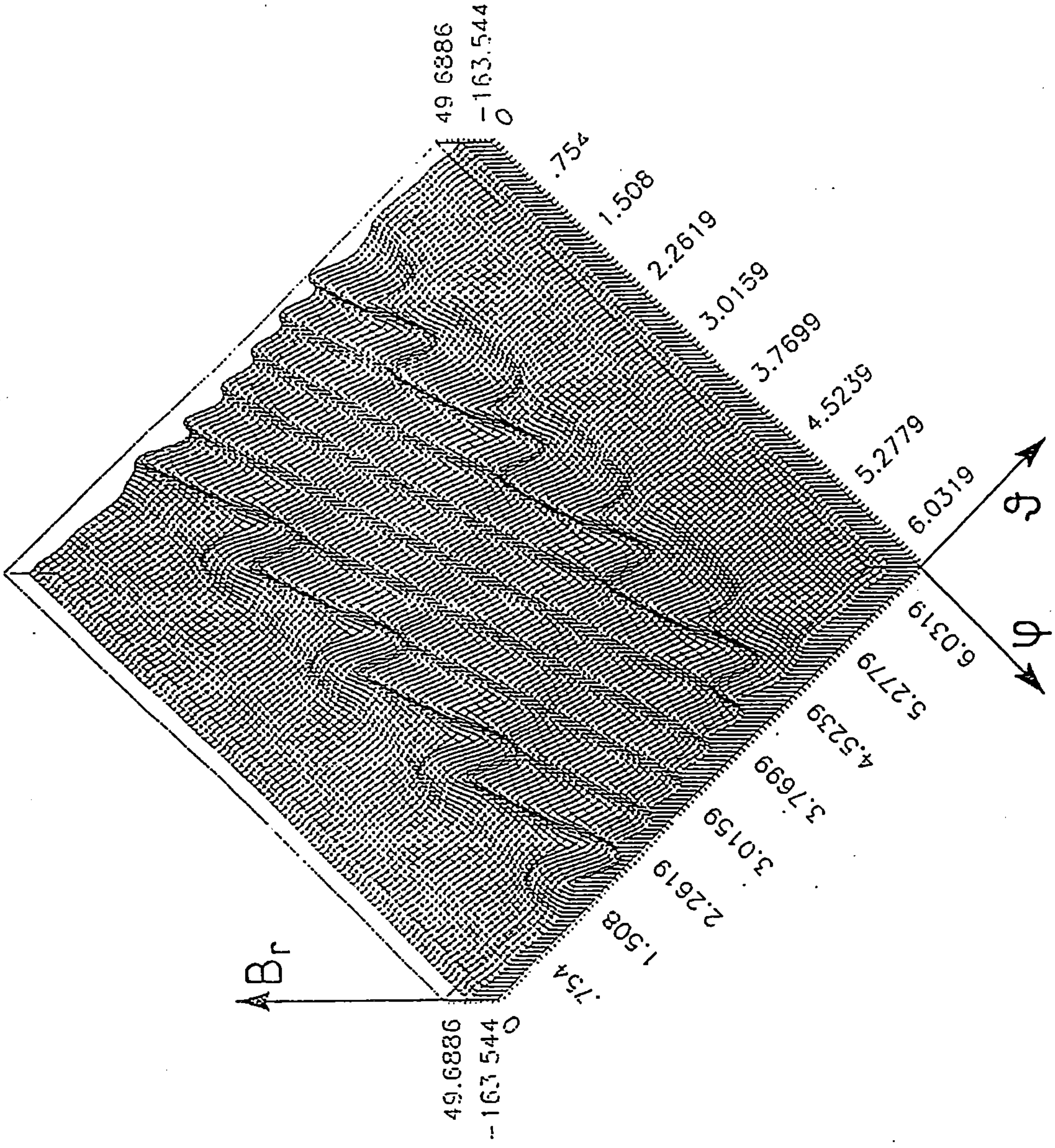
49.6886
-163.544
0
.754
1.508
2.2619
3.0159
3.7699
4.5239
5.2779
6.0319
ϑ
φ
6.0319
5.2779
4.5239
3.7699
3.0159
2.2619
1.508
.754
B_r
49.6886
-163.544
0

Fig. 2

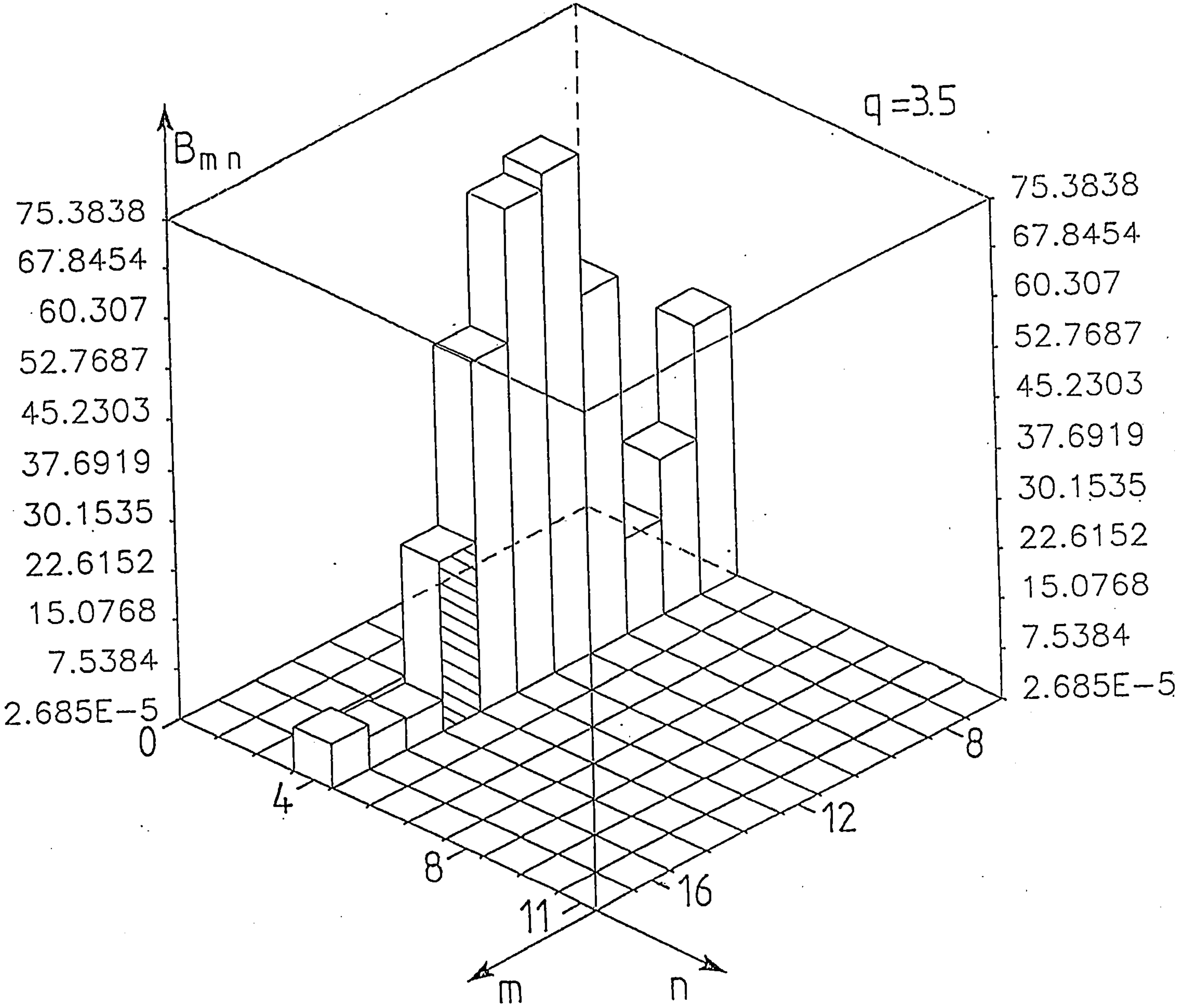
B_mn
q =3.5
75.3838
67.8454
60.307
52.7687
45.2303
37.6919
30.1535
22.6152
15.0768
7.5384
2.685E-5
0
4
8
11
8
12
16
m
n

Fig. 3a

Fig. 3b

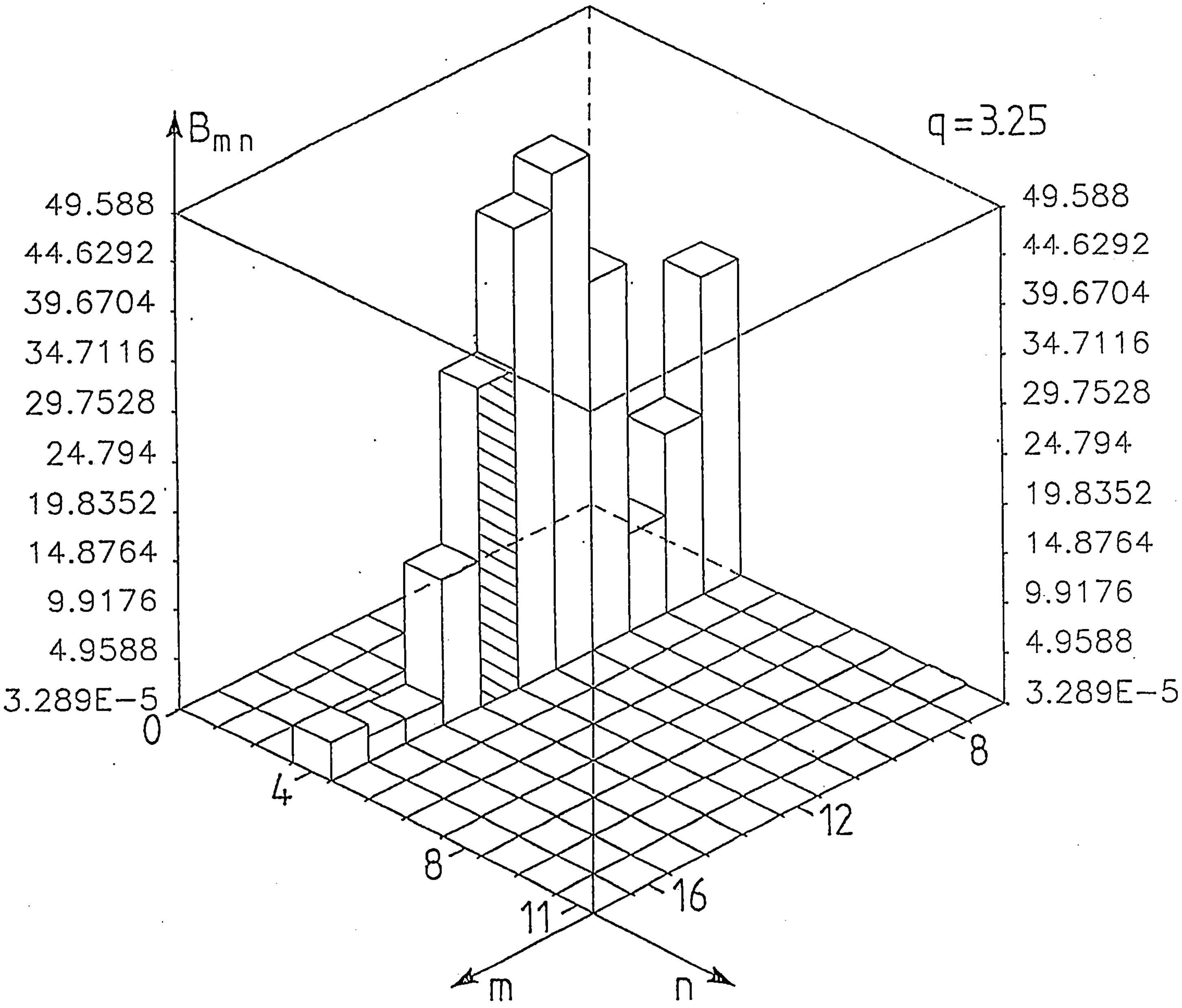
B$_{mn}$
q=3.25
49.588
44.6292
39.6704
34.7116
29.7528
24.794
19.8352
14.8764
9.9176
4.9588
3.289E-5
0
4
8
11
8
12
16
m
n

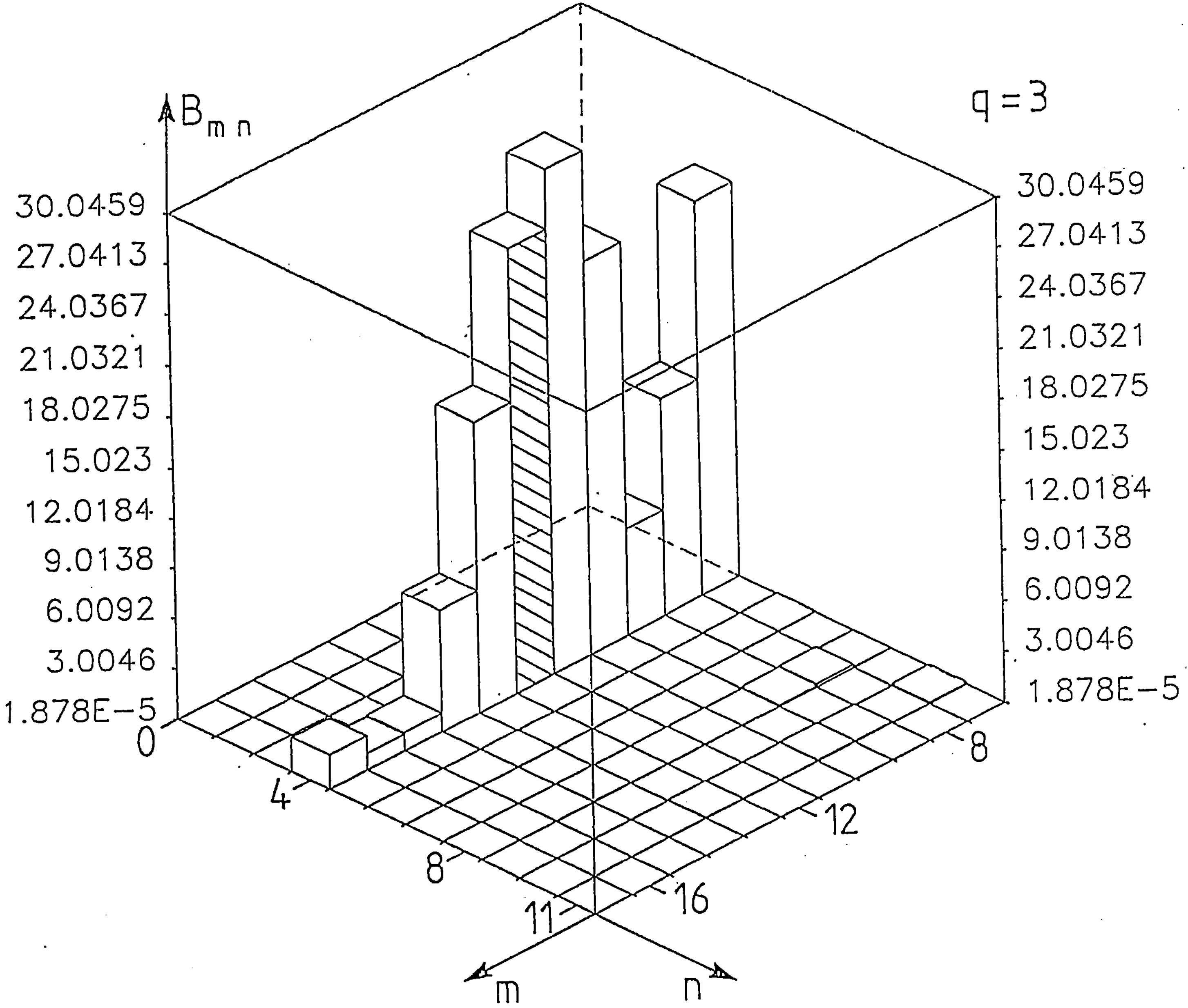
B_mn
q = 3
30.0459
27.0413
24.0367
21.0321
18.0275
15.023
12.0184
9.0138
6.0092
3.0046
1.878E-5
0
4
8
11
m
8
12
16
n

Fig. 3c

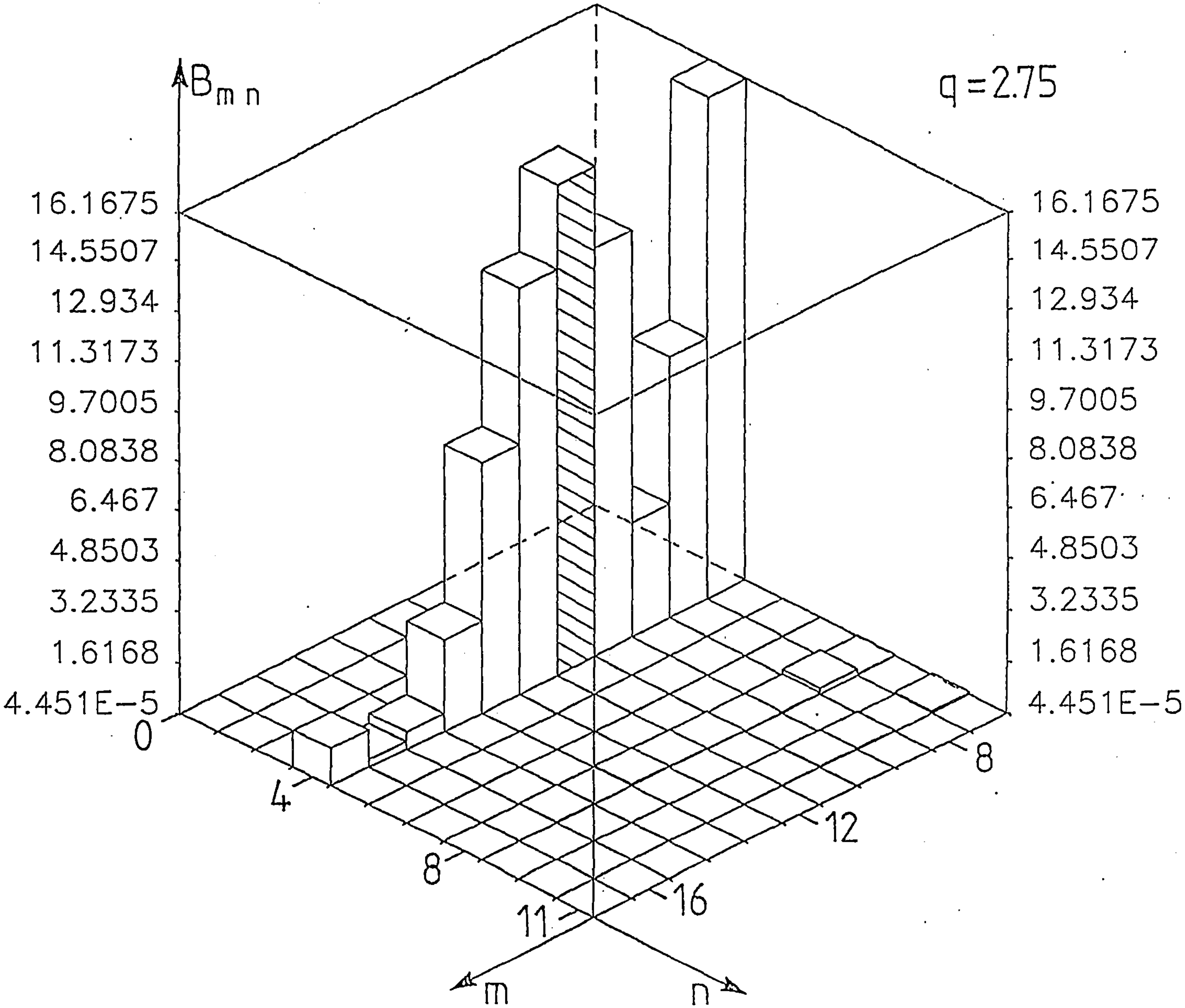
B_{mn}
q=2.75
16.1675
14.5507
12.934
11.3173
9.7005
8.0838
6.467
4.8503
3.2335
1.6168
4.451E-5
0
16.1675
14.5507
12.934
11.3173
9.7005
8.0838
6.467
4.8503
3.2335
1.6168
4.451E-5
4
8
11
8
12
16
m
n

Fig. 3d

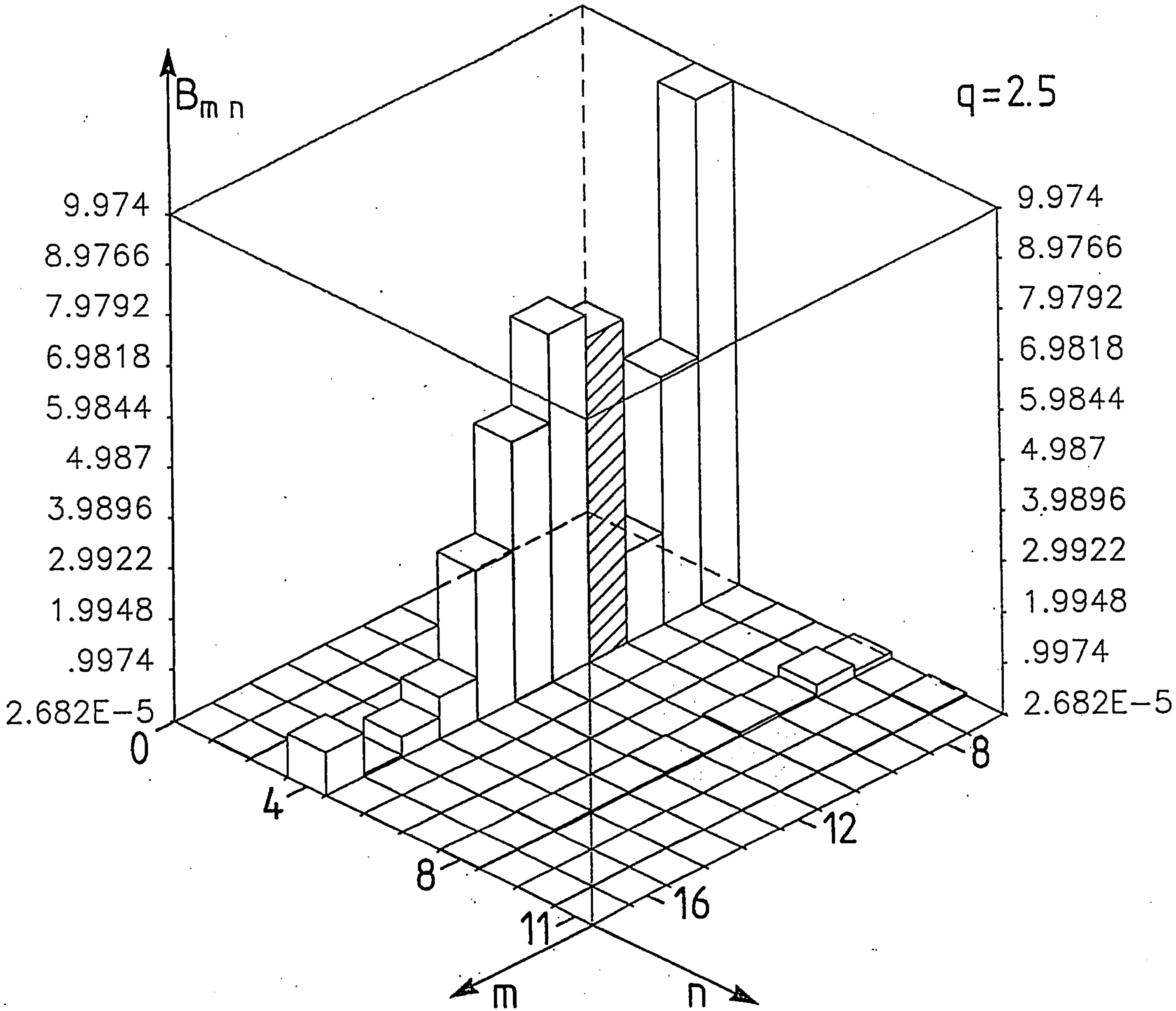
Bmn
q=2.5
9.974
8.9766
7.9792
6.9818
5.9844
4.987
3.9896
2.9922
1.9948
.9974
2.682E-5
0
4
8
11
m
16
12
8
n

Fig. 3e

4. Ergodization of the Magnetic Field at the Plasma Edge

*A. Kaleck**, *M. Haßler**, *T. Evans***

* Institut für Plasmaphysik, Forschungszentrum Jülich GmbH

** General Atomics, San Diego, CA

4.1 Introduction

This part contains the field line tracing calculations. In subsection 4.2 the numerical tool that has been used and an analysis of the magnetic field system will be shortly presented. The technical realization of the connections of the helical perturbation coil system to the power supply differs from the ideal configuration shown at the cover of this report. Additional coils are needed to compensate a net poloidal field.

In subsection 4.3 the evolution of the stochastization of the magnetic field at the plasma edge with increasing perturbation current will be demonstrated by Poincaré plots. It has been found that it is not the CHIRIKOV parameter for the main islands which describes the stochastization but the higher harmonics of the perturbation field dissolve the islands and cause the stochastization.

Some effects of the dynamical phases are shortly shown, and some preliminary attempts to obtain the limiter load and magnetic diffusion are reported. The results clearly show the local effect of the perturbation field and it is demonstrated that the usual theory which describes the magnetic diffusion by the KOLMOGOROV length has to be reconsidered carefully. Since the enhanced diffusion by the stochastization of the magnetic field has to be described in 2D by the behavior of the magnetic field lines at the plasma edge, one has to take into account that there are confinement regions, bounded island regions and a stochastic region. In the near future a model has to be developed as an input for fluid codes.

4.2 Description of Tools and Configuration

4.2.1 Numerical Tool – the Gourdon Code

For our calculations, the Gourdon Code was used which is described elsewhere. This version of the code was provided by the IPP Garching with the kindly support of J. Kisslinger. It has been adapted to standard UNIX systems.

This code integrates the ordinary differential equations for a magnetic field line with the ADAM integration method:

$$\frac{\partial R}{R\partial\phi}=\frac{B_R}{B_\phi};\ \frac{\partial z}{R\partial\phi}=\frac{B_z}{B_\phi} \tag{1}$$

with the toroidal coordinate ϕ, and R, z the coordinates in the poloidal plane.

The magnetic field for line currents is calculated by the BIOT-SAVART formula . For the plasma equilibrium field the ψ function was calculated by the DIVA equilibrium code.[1]

To save computer time, the magnetic field for a coil system is calculated once and stored on a spatial mesh. During the field line tracing, the actual field is interpolated.

For the Poincaré plot of the Gourdon code the θ, r representation (θ is the poloidal angle, and r is the minor radius around the plasma center at $R_0 = 175$ cm) is used. The structure is very detailed in r direction; by stretching the r dimension and retaining the full poloidal extension the harmonic structure is well visible.

Accuracy tests are described in appendix 4.4.1.

4.2.2 The Magnetic Field System

4.2.2.1 The plasma equilibrium

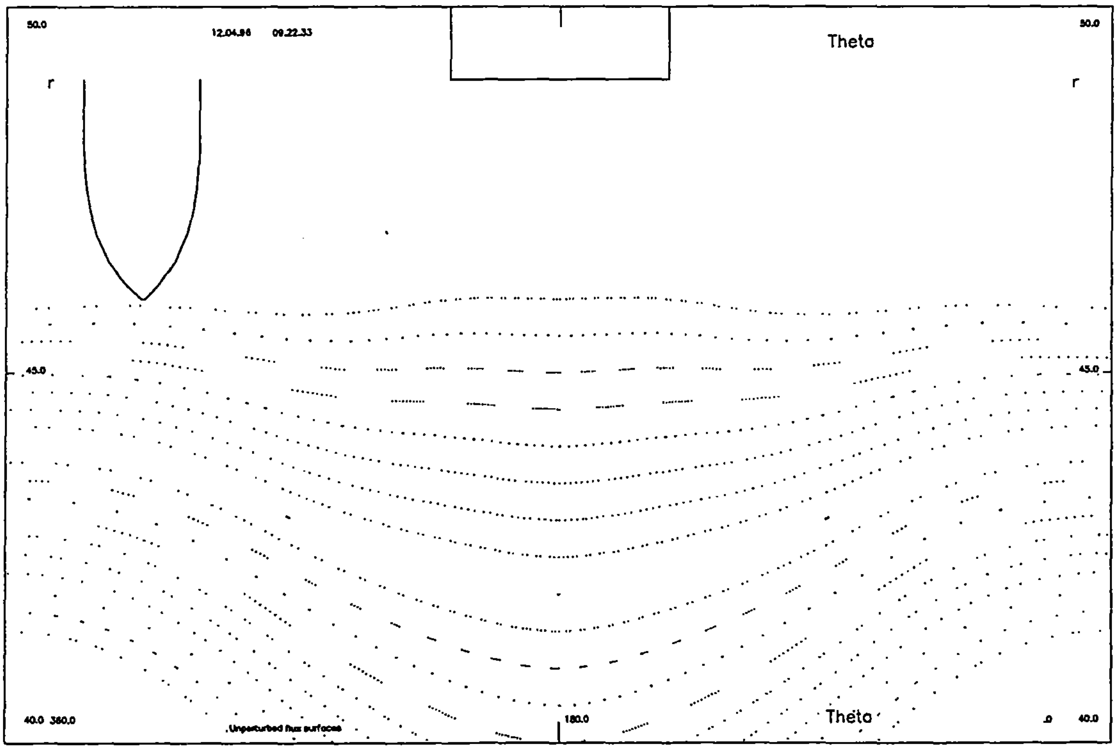

Fig. 1: Poincaré plot of the unperturbed flux surfaces. The uppermost line is the plasma boundary. The $q = 3$ surface is represented by the three points. (The pump limiter is sketched in the top left corner and the divertor target plate on the top.)

The ψ function of the unperturbed plasma equilibrium calculated by the DIVA equilibrium code from the IPP Garching[1] has been used. Fictive vertical field coils (the real TEXTOR vertical field system was not used since TEXTOR has an iron core transformer and the DIVA code works for vacuum field only) were designed ensuring a circular cross section of the plasma boundary ($R_0 = 175$ cm, $a = 46$ cm) and for a $\beta_{\text{pol}} = 1$ plasma. A parabolic plasma current distribution was chosen with zero current outside the $q = 3$ surface. The toroidal field is created by an axial current $I_{B\text{tor}} = 1.675 \cdot 10^7$ A to have the $q = 3$ surface at $R = 176$ cm and $r = 43$ cm.

Fig. 1 shows the plot of the unperturbed flux surfaces. The plasma boundary (the uppermost line) is an almost straight line with deviations less than 2 mm. $\theta = 180°$ corresponds to the high field side, and the poloidal angle is from right to left.

4.2.2.2 The perturbation coil system

The perturbation system is designed to create a resonance at the $q = 3$ surface. It is shown in fig. 2 and on the cover page of this report).

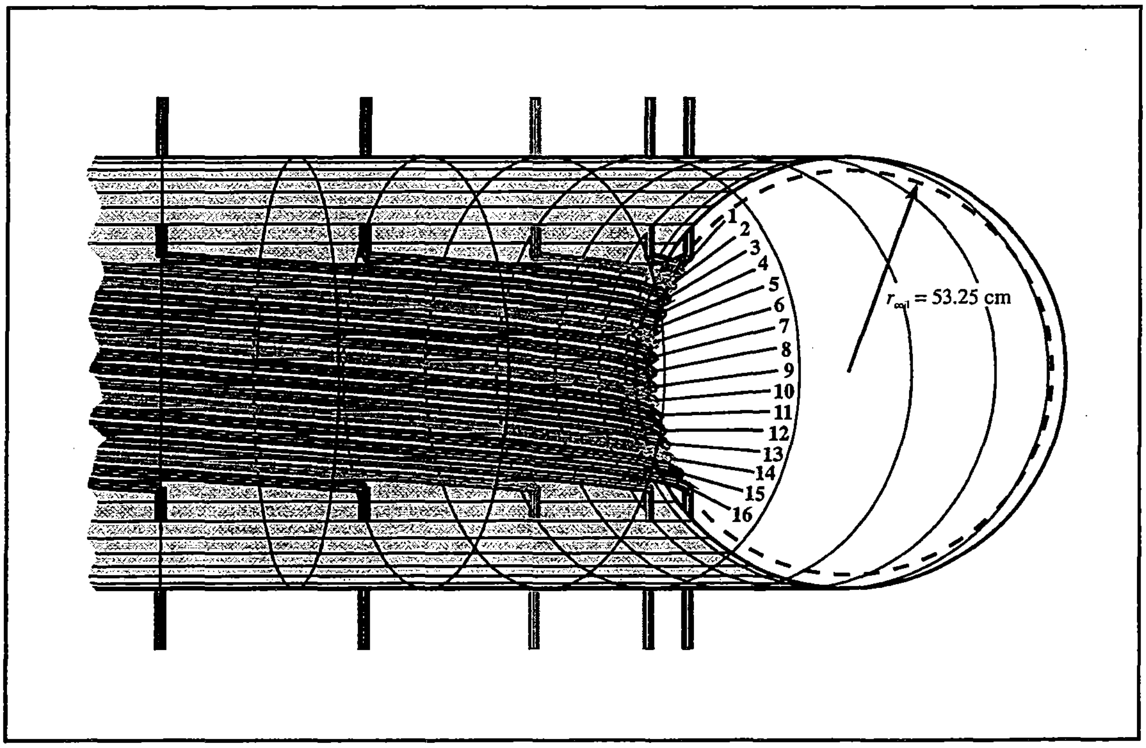

Fig. 2: Schematic view of the "ideal" coils.

The current distribution in the coils is

$$I_j = I_0 \cdot cc \cdot \sin\left((j-1)\frac{\pi}{2} + \omega t\right) \qquad j = 1...16 \qquad (2)$$

(I_0 = 15 kA is the maximum designed current and $0 \le cc \le 1$ a current control factor.)

This creates an $m = 12$, $n = 4$ structure. ($m = 6$, $n = 2$ and $m = 3$, $n = 1$ structures will be shown in appendix 4.4.4.)

Ideally the 16 helices are identical, starting and ending at a toroidal angle $\phi_j = (j-1)\cdot(\pi/8)$.

To minimize the forces and the number of necessary vessel ports, the feeding conductors of one quartet will be bundled in coaxial conductors as shown in fig. 3.

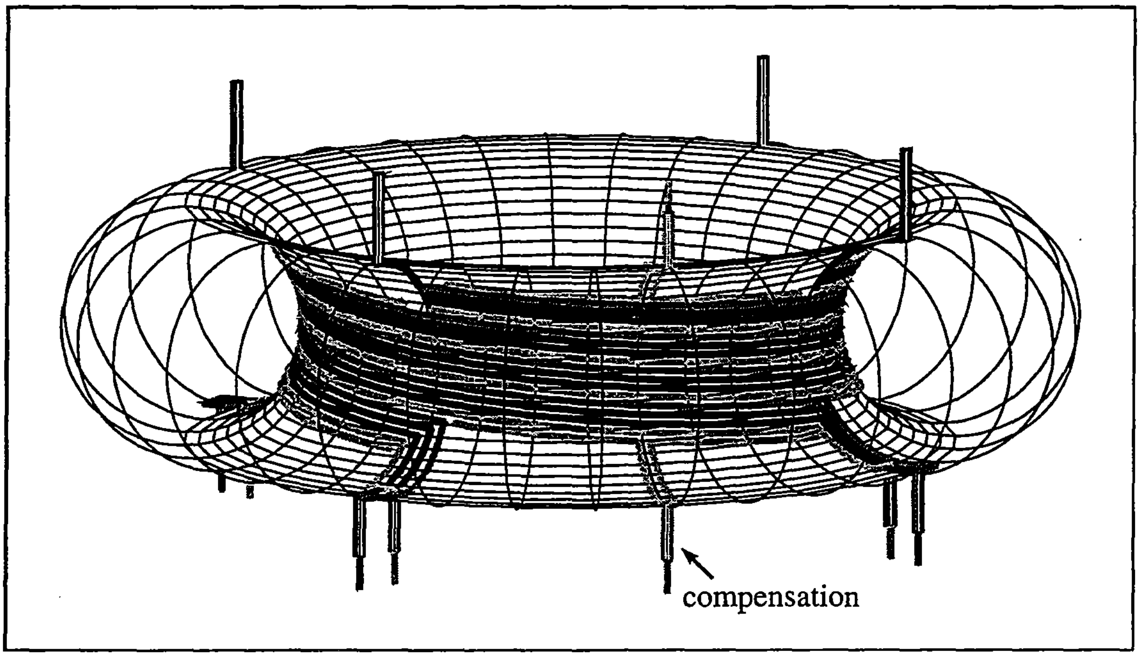

Fig. 3: Schematic view of the coil system. The four coils of one current system are bundled to a quartet. Only four flanges on top and on bottom are needed for the coil system. There are two additional compensation coils which need another flange on top and on bottom.

This setup causes a net poloidal field ($B_{n=0} \neq 0$, n is the toroidal mode number) which may affect the equilibrium. The reason for this net field is the asymmetry of the poloidal phase distribution which creates a unidirectional B_r field on the whole toroidal circumference. Two additional segmented helical coils (also shown in fig. 3) on top and on bottom compensate the net poloidal field. The currents in the compensation coils are

$$I_{\mathrm{comp}} = \mp \frac{I_0}{\sqrt{2}} \cdot cc \cdot \sin\left(\frac{\pi}{4} + \omega t\right) \tag{3}$$

(see fig. 4)

For the following calculations the poloidal connectors were left out. (They produce a localized B_r field which seems to be intolerable. A technical solution which avoids this disadvantage has to be found.) Usually the phase $\omega t = \pi/4$ was selected.

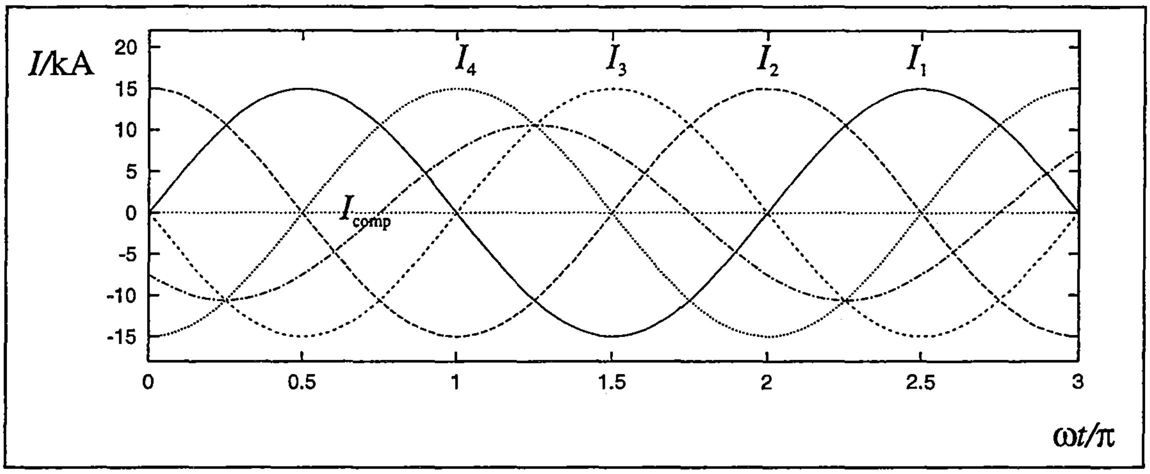

Fig. 4: Current distribution in the first four coils and the upper compensation coil.

The Poincaré plots for the compensated and the uncompensated field are shown in appendix 4.4.2.

4.2.2.3 The perturbation field

The perturbation field has an $n \geq 4$ structure and should have an $m \geq 12$ structure at the $q = 3$ surface. The perturbation field normal to three different surfaces is plotted in figures 5a to c.

Near the plasma edge, the resonant structure of the field is well seen, but farther away from the coils the higher harmonics decay rapidly.

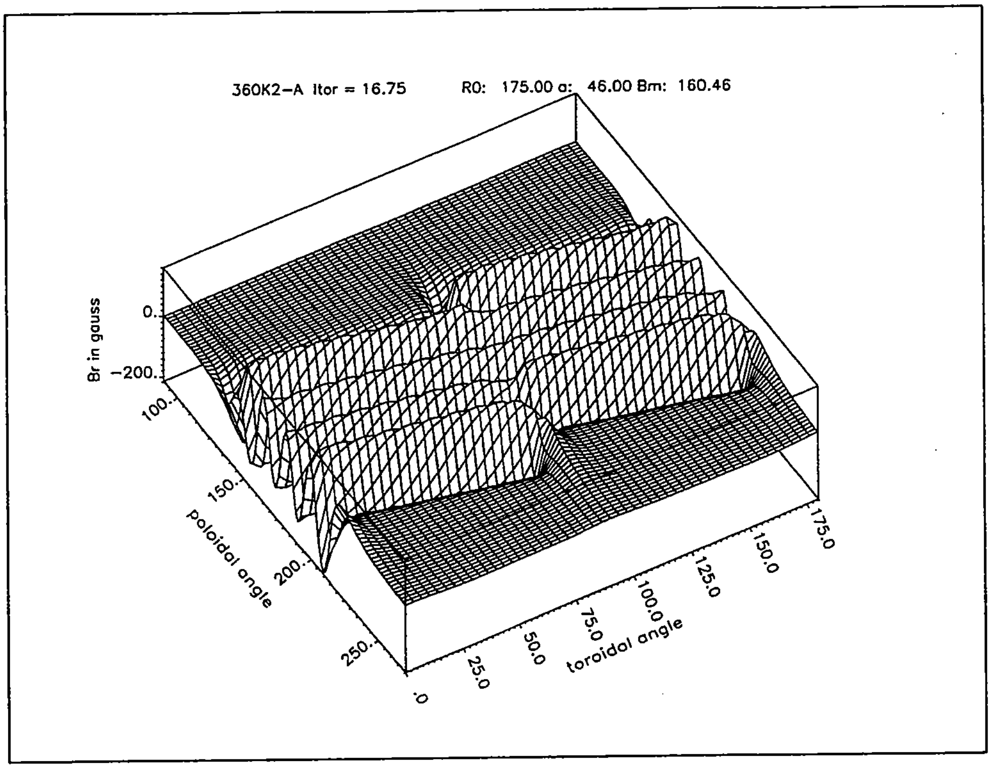

Fig. 5a: Perturbation field perpendicular to the plasma boundary at $r = 46$ cm.

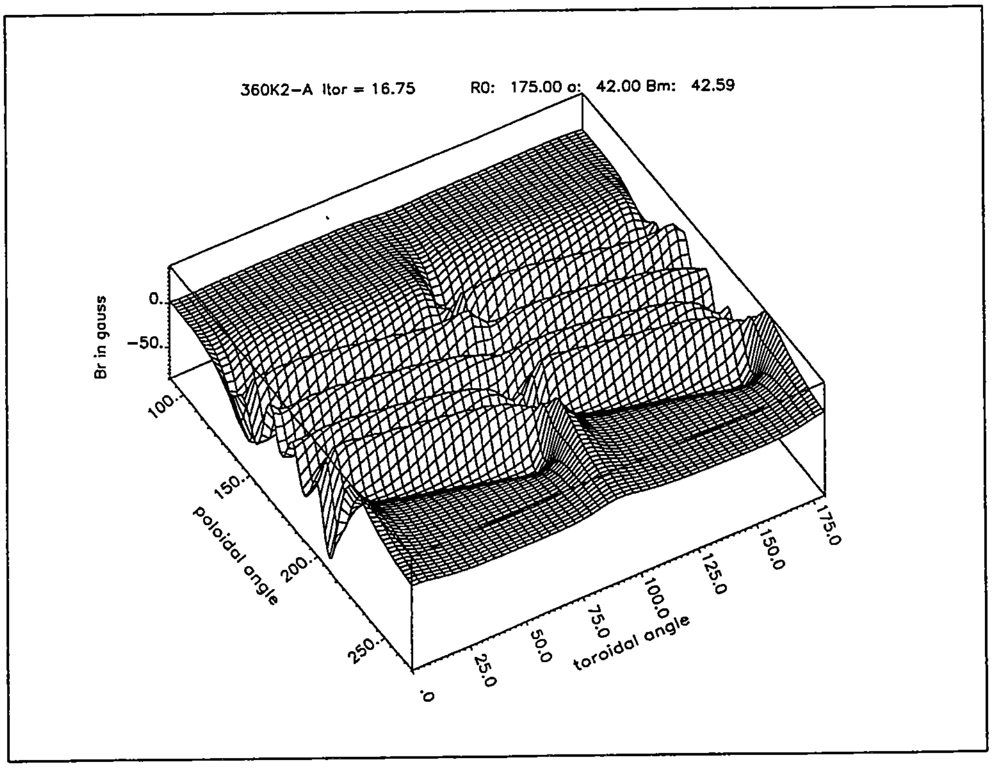

Fig. 5b: Perturbation field perpendicular to the unperturbed flux surface $r = 42$ cm ($q = 3$).

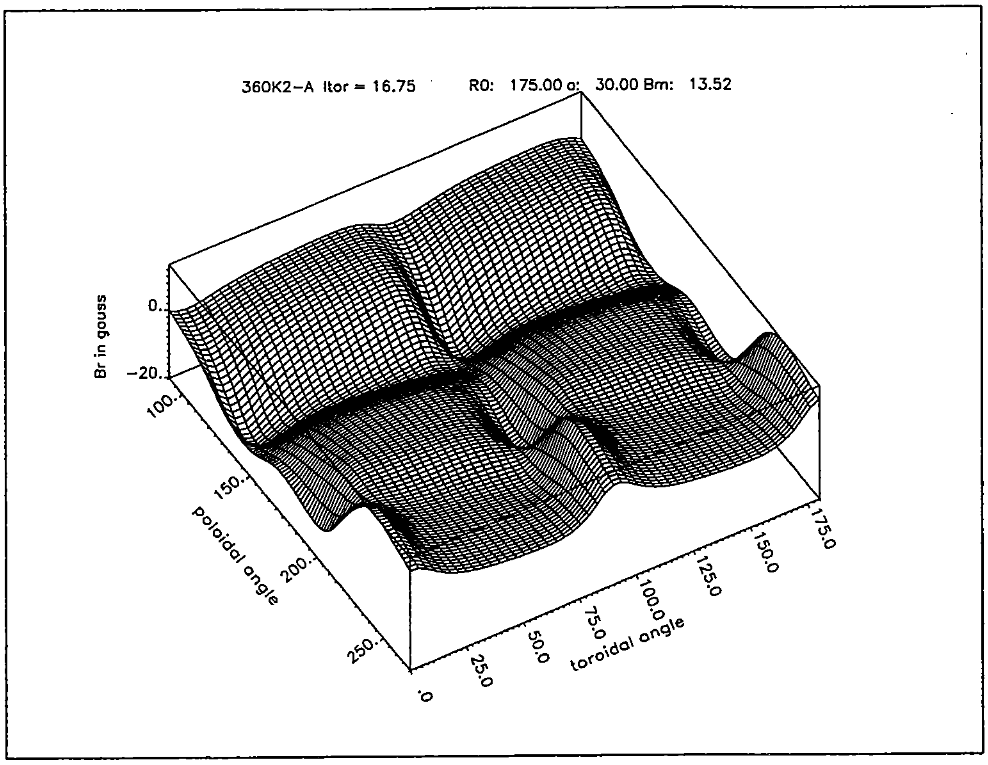

Fig. 5c: Perturbation field perpendicular to a surface $R_0 = 175$ cm, $r = 30$ cm.

4.3 Results of Field Line Tracing

Figures 6a to d demonstrate the evolution of the stochastization of the magnetic field at the plasma edge with increasing perturbation current.

At the $q = 3$ surface the $m = 12$, $n = 4$ islands appear as well as the 11/4 mode below and the 13/4 and 14/4 modes above. Between the 11/4 and the 12/4 modes the 23/8 mode appears and between the 12/4 and the 13/4 modes the 25/8 and the 37/12 modes are visible.

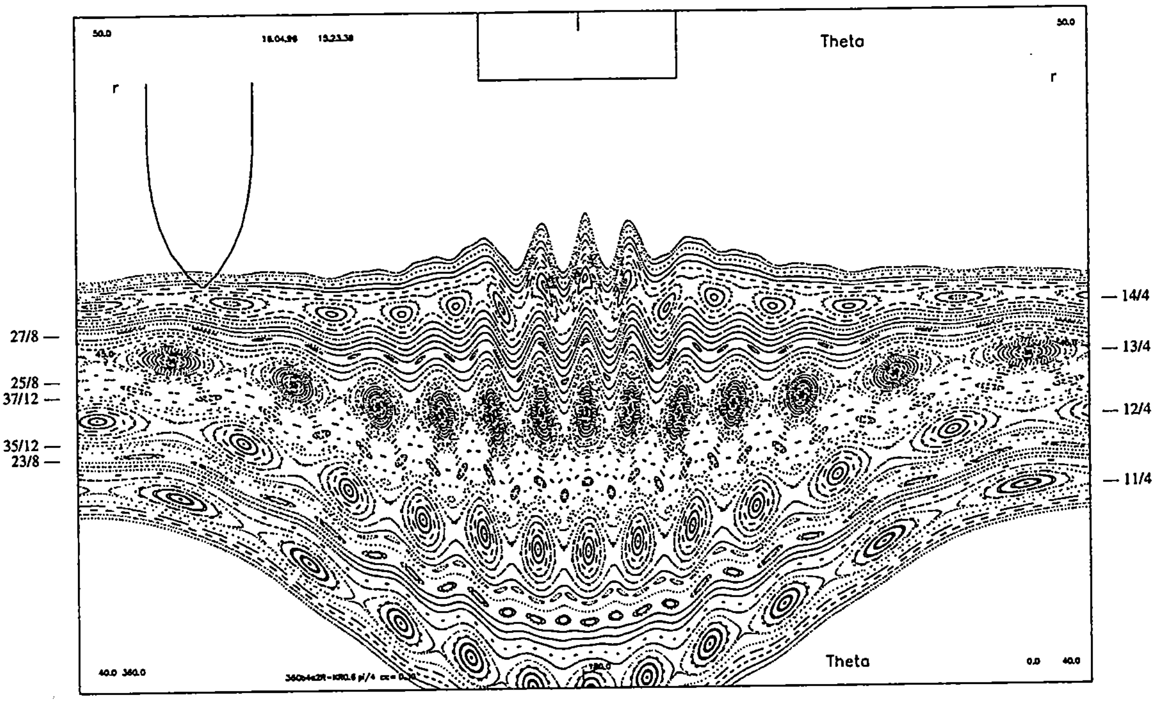

Fig. 6a: Evolution of stochastization (*cc* = 0.3; *cc* is the current control factor, see equation (2); *cc* = 1 is the maximum designed current). At the margin, the *m*/*n* mode numbers are indicated. (continued next page)

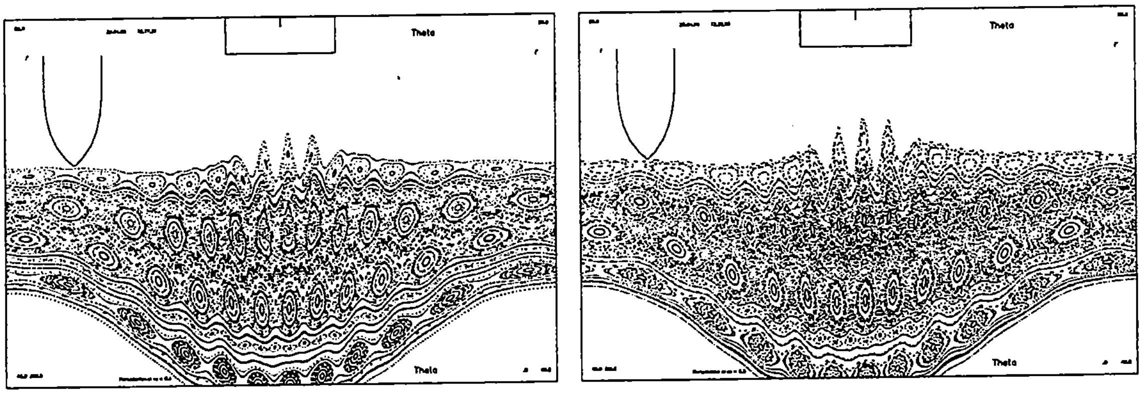

Fig. 6b – c: Evolution of stochastization (**b:** *cc* = 0.4, **c:** *cc* = 0.5).

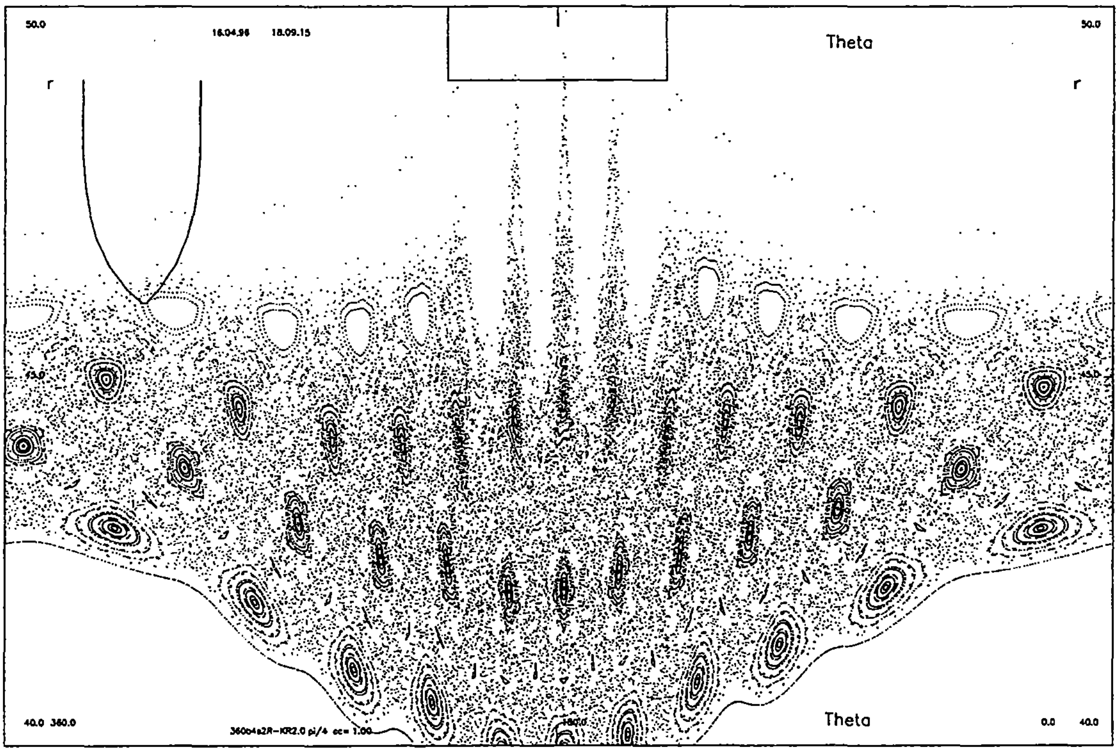

Fig. 6d: Evolution of stochastization (*cc* = 1.0).

4.3.1 Island Growth at Lower Perturbation Currents

The distance between the $m = 12$ and the $m = 13$ resonant surfaces is 2 cm at the high field side (see fig. 6a). Fig. 7 is a plot of the $m = 12$ island radial diameter as a function of the perturbation current. As expected, the island diameter grows proportional to $cc^{1/2}$.

Extrapolation to the full perturbation current ($cc = 1.0$) leads to an island diameter of $d = 2$ cm, i. e. the so defined CHIRIKOV parameter is equal to about unity and the main islands should then start to overlap.

Following the standard formula (used by A. NICOLAI in section 3) one would expect an extrapolated island diameter at the high field side of 3.4 cm ($B_{12,4} = 4$ G, $L_{\mathrm{SH}} = 260$ cm, $r = 43$ cm). In appendix 4.4.3 the deviation from the standard theory is worked out and it is shown that there is an effect of the location of the perturbation coils at the high field side.

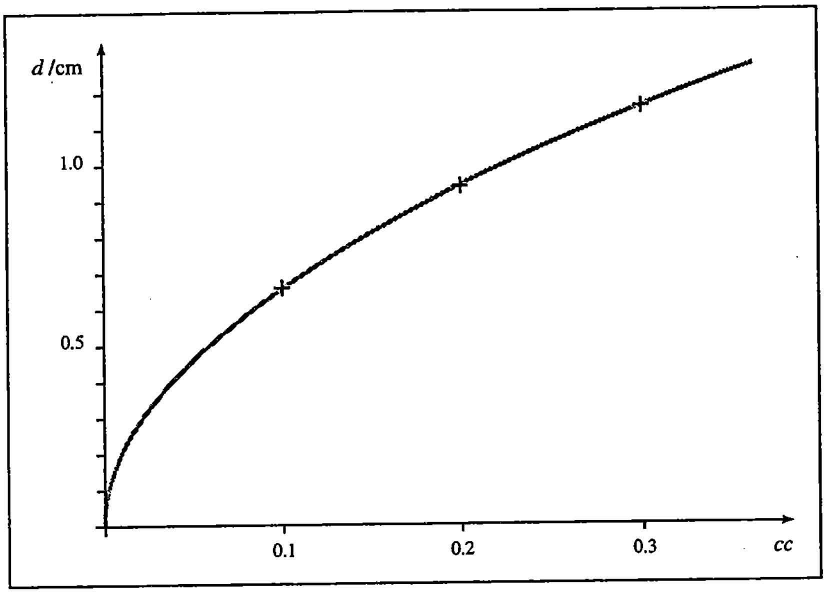

Fig. 7: Width of the $m = 12$ islands in r direction.

4.3.2 Onset of Stochastization

Since the CHIRIKOV parameter is just about unity for the maximum perturbation current, the main islands will touch but not overlap. This will not lead to satisfying stochastization. But the figures 6a, b and c and in detail figures 8a, b and c show for increasing perturbation current ($cc = 0.2, 0.4, 0.5$) the dissolution of the $m = 12$ islands by higher harmonics.[2,3]

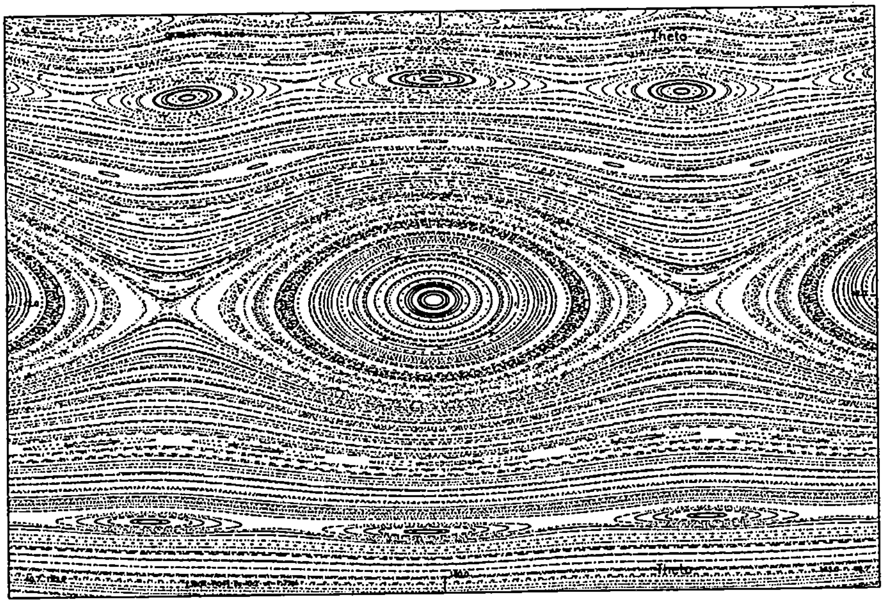

Fig. 8a: Dissolution of the $m = 12$ islands by higher harmonics ($cc = 0.2$). The separatrix is almost intact.

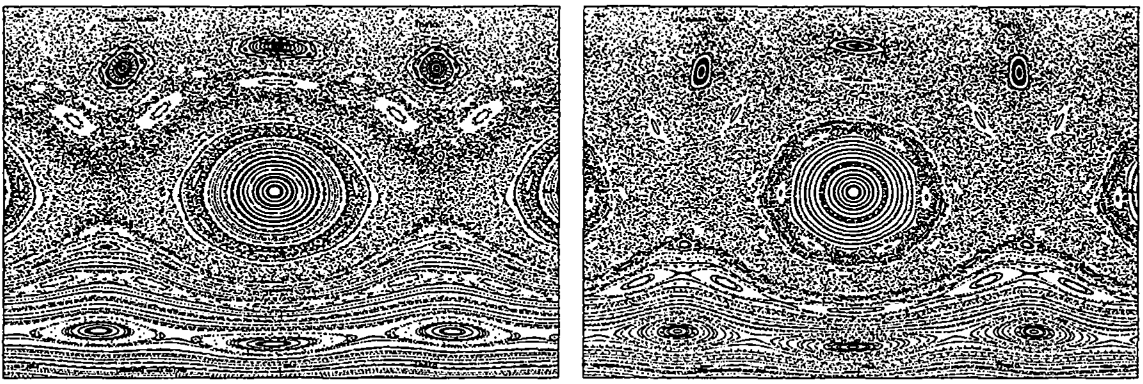

Fig. 8b – c: Dissolution of the $m = 12$ islands (**b:** $cc = 0.4$, **c:** $cc = 0.5$).

Also satellite islands occur (fig. 9).

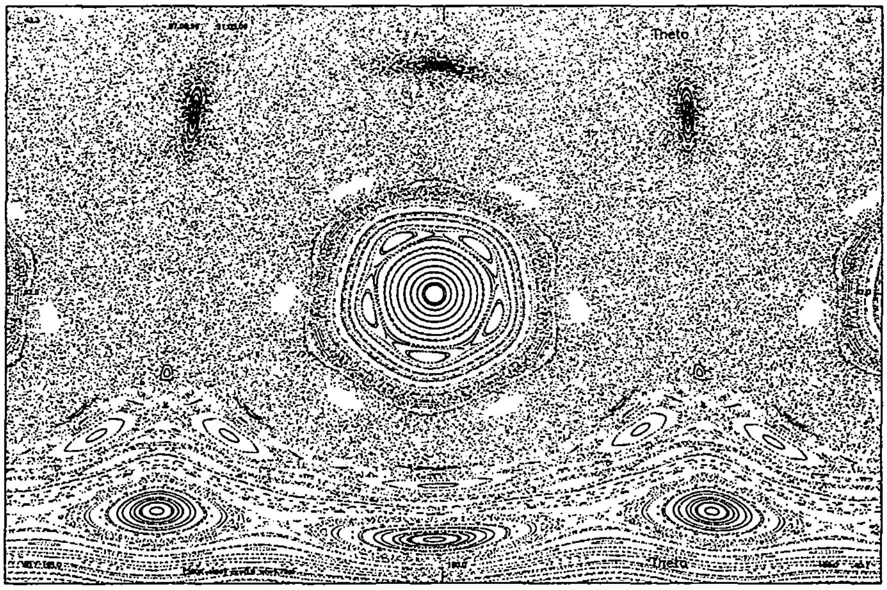

Fig. 9: An $m = 12$ satellite island system ($cc = 0.6$).

4.3.3 Ergodization at Full Perturbation Current

Fig. 6d shows the Poincaré plot for the maximum perturbation current at the phase $\omega t = \pi/4$ (i. e. $I_1, I_2 = 10.6$ kA, $I_3, I_4 = -10.6$ kA).

The main islands still persist. Their width decreased only moderately and even the 23/8 mode still exists. The $m = 12$ islands show four pronounced satellite islands, the five satellite islands structure of fig. 9 disappeared. There is a closed field line interior to the

$m = 11$ islands chain. Exterior to this, there seems to be an almost complete ergodization (except the four island chains). But there exist some "sticky regions" e. g. near the 23/8 mode and around the 14/4 mode where field lines may see a barrier. The situation is quite complicated and not yet well understood. More detailed calculations and accuracy tests have to be done.

The same holds for the region outside the plasma. The motion of the field lines is very turbulent because of the near field perturbations. More about this in the section "Limiter Load".

4.3.4 Sweeping of the Perturbation Pattern

Figures 10a and b show for two different phases of the dynamical operation the clockwise motion of the islands. In fig. 10a ($\omega t = 0$) the pump limiter points into a gap between two islands and in fig. 10b ($\omega t = \pi$) the pump limiter dips into an island. The spikes of the $m = 14$ islands by this way sweep along the divertor target plate and so the particle load is considered to be smeared out on its surface.

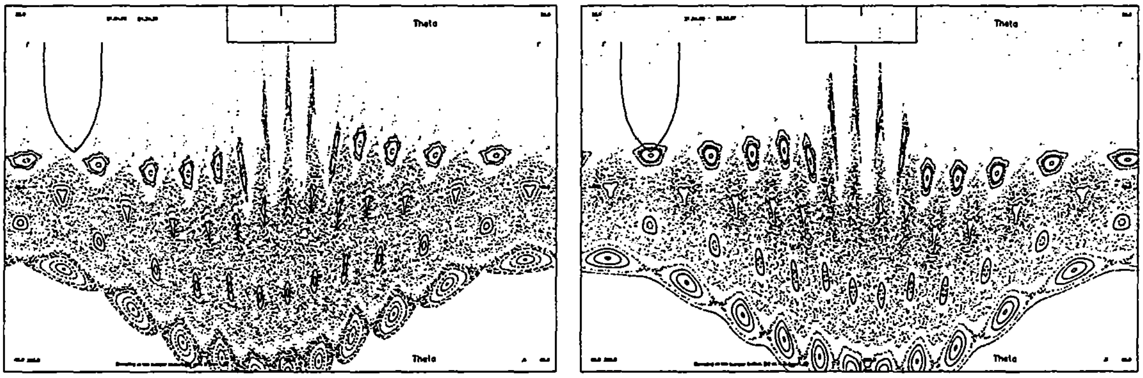

Fig. 10a – b: Two phases of the DED.

a: ($\omega t = 0$) The pump limiter points in between two $m = 14$ islands.

b: ($\omega t = \pi$) The island chains moved half a period from right to left.

4.3.5 Limiter Load

Fig. 6d reflects only field lines from inside the plasma. By physical diffusion particles will occupy field lines from outside which have a very turbulent behavior and there is no simple correlation between the Poincaré plot and the limiter load. Further detailed discussions and calculations are necessary.

So far it has been tried to get an image of the limiter load by starting field lines at circles around the plasma edge and tracing them until they hit one of the limiters. As starting points the plasma boundary (usually $R = 175$ cm, $r = 46$ cm) and a circle 1 cm outside the plasma ($r = 47$ cm) has been chosen. Table 1 is a list of the results.

	Starting points		$r_{q=3}$	plasma center	field lines hitting		
	R_0	r			target pl.	pump lim.	Liner
1	175.0 cm	46.0 cm	42.0 cm	175.0 cm	4 %	96 %	–
2	175.0 cm	47.0 cm	42.0 cm	175.0 cm	35 %	65 %	–
3	175.0 cm	46.0 cm	43.0 cm	175.0 cm	22 %	78 %	–
4	175.0 cm	47.0 cm	43.0 cm	175.0 cm	39 %	61 %	–
5	174.5 cm	46.0 cm	42.0 cm	174.5 cm	91 %	8 %	1 %
6	174.5 cm	47.0 cm	42.0 cm	174.5 cm	63 %	27 %	10 %

Table 1: Limiter load

For the standard case the field lines starting from the plasma boundary all hit the pump limiter (row 1). Those from farther outward split to 35 % to the divertor target plate (row 2). Shifting the $q = 3$ surface farther to the plasma boundary $r_{q=3} = 43$ cm (usually $r_{q=3} = 42$ cm) is seen to be a tool of slightly controlling the limiter load (row 3 and 4). Shifting the plasma 0.5 cm toward the divertor target plate shows an expected enhanced loading of this limiter and therefore is a sensitive control of the distribution between the two limiters (row 5 and 6). But shifting the plasma to the divertor target plate means shifting it nearer to the perturbation coils. This will enhance the ergodization drastically as one can imagine looking at fig. 11e and f.

Figures 11a to f are the poloidal projections of the field lines described in table 1. To identify spots at the limiter surface detailed considerations are necessary as well as taking into account the dynamical phases.

Figures 12a and b show for the standard and the inward shifted plasma position the trace of field lines starting at the surface of the divertor target plate. This gives an image of where the field lines hitting this limiter do come from. Some field lines are bended back to the surface after less than 1 cm radial excursion, but there seems to be no regularity since the region is stochastic.

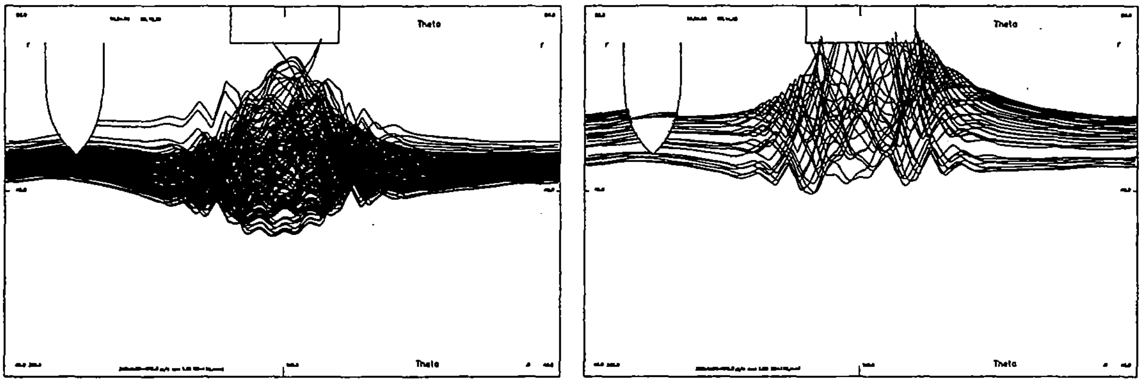

a, b: Standard plasma position.

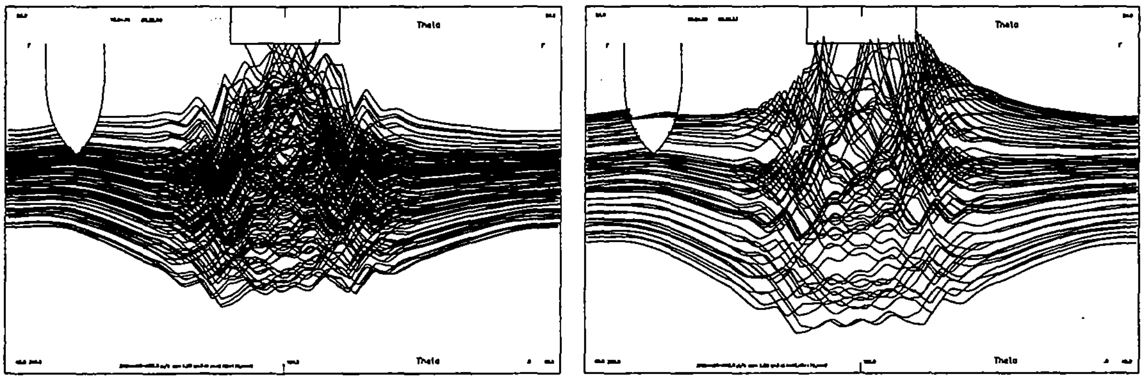

c, d: $q = 3$ surface at $r = 43$ cm.

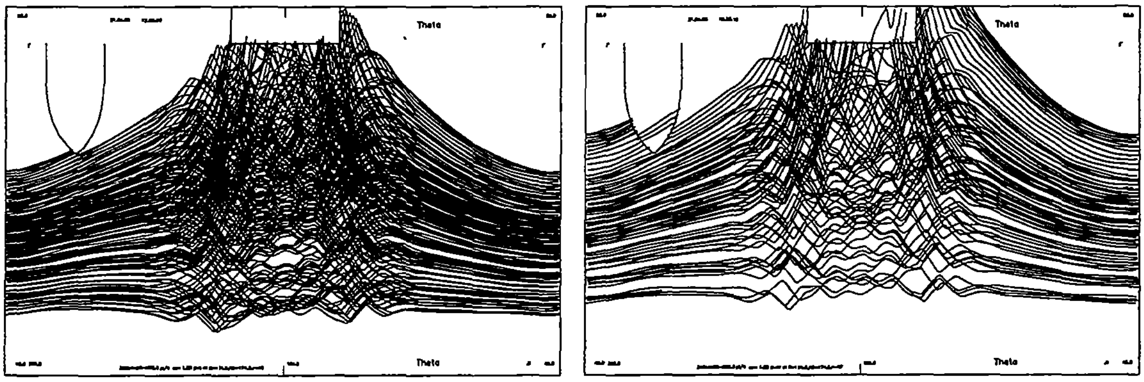

e, f: Plasma shifted inward 0.5 cm.

Fig. 11a – f: Poloidal projection of field lines starting on circles at the plasma boundary for different plasma conditions (see table 1).

a, c, e: Starting points at plasma boundary.

b, d, f: Starting points 1 cm outside plasma boundary.

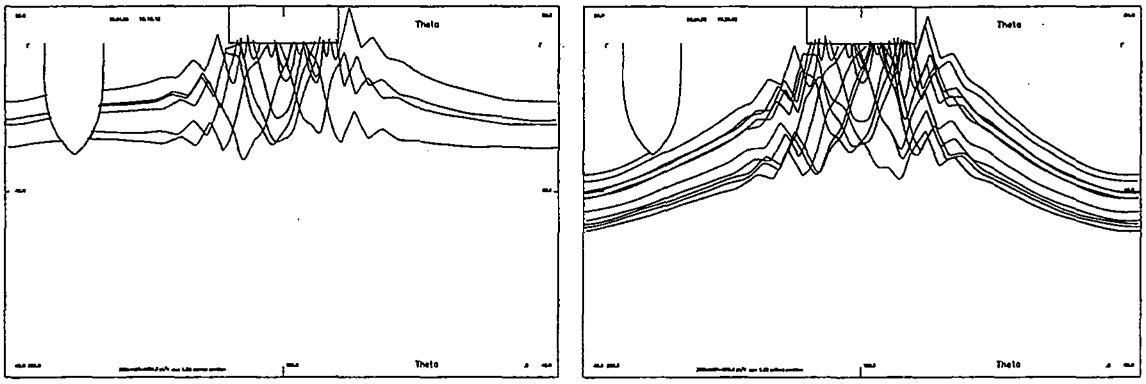

Fig. 12a – b: Poloidal projection of field lines starting from the limiter surface. **a:** standard plasma position, **b:** inward shifted plasma.

4.3.6 Diffusion of Field Lines

Usually the diffusion of field lines in an ergodic region is described by the KOLMOGOROV length. This linear model has to be reconsidered for the case when – roughly speaking – the longitudinal path of a particle between two collisions is larger than the KOLMOGOROV length.

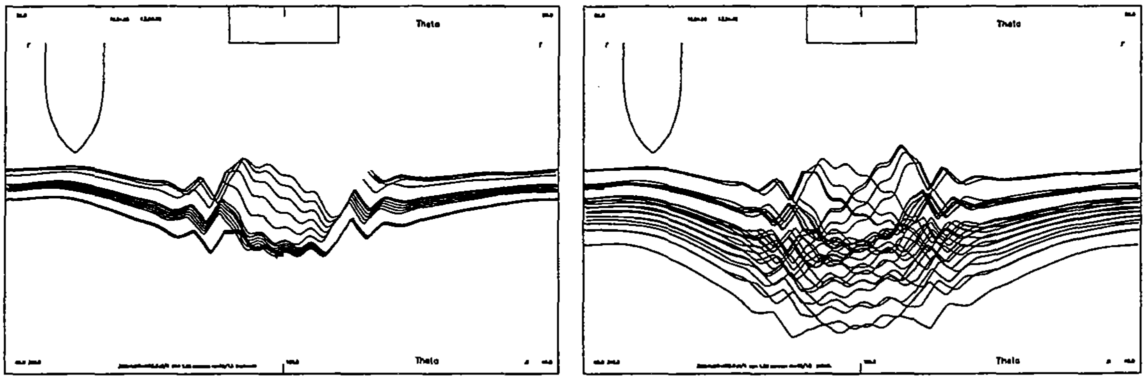

Fig. 13a – b: Traces of field lines of the main stochastic region (poloidal projection).

a: A bundle of field lines widens during 9 toroidal (i. e. 3 poloidal) turns, starting point is at $\theta = 180°$. Field lines go from right to left.

b: One field line during 100 toroidal turns.

Fig. 13a traces a bundle of field lines starting at the high field side in the stochastic region for 9 toroidal (i. e. about 3 poloidal) turns. The expansion of the bundle strictly happens in the bounded area in the vicinity of the perturbation coils.* (Due to the SHAVRANOV shift the bundle converges at the low field side.) Once passing through the perturbation zone the bundle is widened by more than a factor e, i. e. the KOLMOGOROV length is less than one toroidal turn and the model mentioned above is questionable. Fig. 13b shows the trace of one field line of the bundle for 100 toroidal turns. The field line covers a part of the stochastic domain discussed in section 4.3.3.

A bundle remains tight when started in an island region (fig. 14a) and a single field line during 100 turns covers a region which corresponds to the width of the islands (fig. 14b).

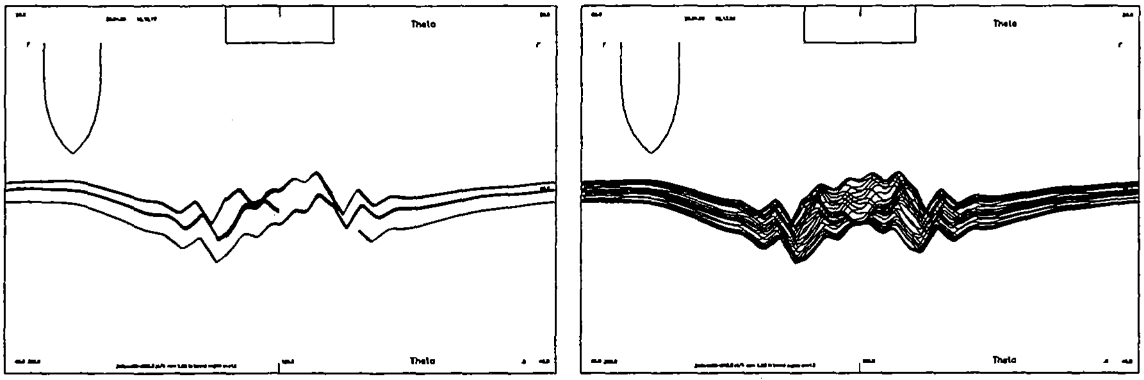

Fig. 14a – b: As fig. 13, the field lines start and remain inside the $m = 13$ islands region.

The main stochastic region has two "de facto" barriers (as one can imagine from fig. 13b). The lower barrier is located at the 23/8 mode and the upper one at the $m = 14$ mode (see fig. 15).

Our conclusions from these calculations are that for this experiment the recent model of magnetic diffusion has to be reconsidered and a model has to be elaborated which takes into account the division of the plasma edge into three parts: the strong local stochastization part, the bounded island zones and the confinement region at the low field side.

---

* One should notice that tracing back the bundle leads to exactly the same plot.

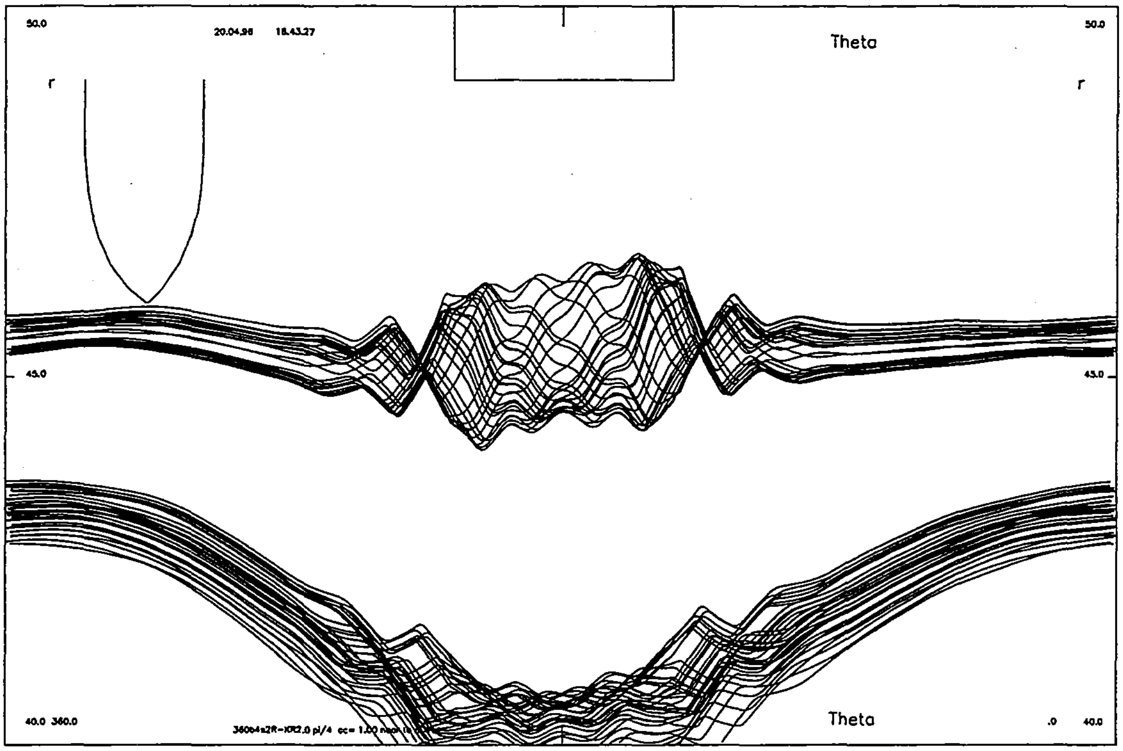

Fig. 15: Upper and lower barriers of the main stochastic region.

Trace of two field lines during 100 turns. The upper one starts in the $m = 14$ islands region, the lower one between the 23/8 and 11/4 mode.

4.4 Appendix

4.4.1 Accuracy Tests

The accuracy of the Gourdon Code was tested by tracing one field line a number of turns and checked to which extend it came back to the starting point.

Field lines on closed surfaces or intact islands can be traced several hundred times around the torus; with a step size of 1 to 2 cm, the starting point is missed by less than 10^{-4} cm. Field lines of a stochastic region can only be followed about 40 turns with an accuracy of 10^{-3} cm. A smaller step size down to 0.1 cm does not enhance the number of reliable turns significantly.

Related to this number of reliable turns is the question of stability of the field line equations (1), i. e. the property of the cross section of a bundle of field lines to remain in a restricted area. If the magnetic field structure turns the equations to be unstable, the cross section of a bundle turns to expand in one direction exponentially and two neighboring field lines separate as

$$\delta = \delta_0 \cdot e^{\frac{l}{l_c}} \tag{4}$$

where δ is the distance of two field lines, l is the distance along the field lines, and l_c is the KOLMOGOROV length (as already discussed in the last section).

For the maximum perturbation current of 15 kA and the phase $\omega t = 0$, the KOLMOGOROV length calculated in the stochastic region measuring the distortion of a bundle of field lines in a poloidal cut (see fig. 13a) amounts to about

$l_c \approx 850$ cm.

It is not surprising that in this case the number of reliable turns is limited to about 40.

For field lines on closed surfaces or intact islands, the accuracy is sufficient for more than 2,000 turns. For field lines within stochastic regions, one might make errors for an individual field line. For some considerations one wants to know the behavior of field lines for more than 40 turns. The domain wherein a stochastic field line is moving is interesting as well as their radial excursion during a larger number of toroidal turns.

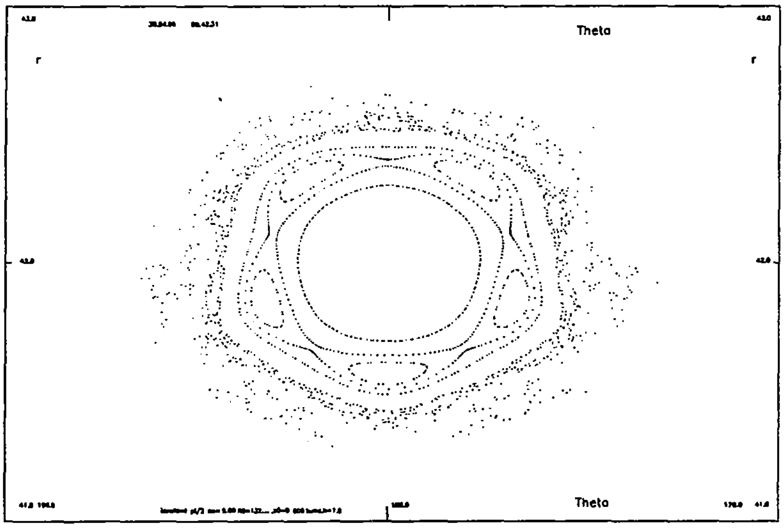

Fig. 16: Accuracy test: The accuracy is sufficient to distinct between the outer stochastic region and the inner island/subisland system. The starting point for the border of the island region differs 10^{-3} cm from the one covering the stochastic region.

As demonstrated in fig. 16 it has been found that a stochastic field line does not cross the border to the intact island region during 3,000 turns, if the integration step size was small enough (≤ 1 cm). Two field lines starting 10^{-3} cm apart from each other show a completely different behavior: one forms a closed island, the other covers a large stochastic region.

The situation is different and difficult to survey when starting field lines in a "sticky region". Field lines starting from very proximate points (distance $< 10^{-4}$ cm) whether cover a narrow band or a large region which in addition depends on the integration step size. More investigations have to be done here.

Two more accuracy tests have been made:

- The approximation of the helical windings by polygons.

  360 straight lines are necessary for one helix. The results with 720 straight lines do not differ essentially.

- A 62×48×62 R, ϕ, z mesh was used for storing and interpolating the magnetic field of the perturbation coils (the periodicity 4 in ϕ direction was used). Comparison with the direct field calculation does not show substantial differences.

4.4.2 Poincaré Plots and Net Fields without and with Compensation

Figures 17a and b show the Poincaré plots for the setup without and with compensation. The asymmetry of the uncompensated system oscillates during the dynamic operation which may lead to unwanted plasma motions. The R component of the net ($n = 0$) perturbation field is plotted in figures 18a and b. In the uncompensated case the amplitude reaches values up to 200 G. After compensation as explained in subsection 4.2.2.2 (see fig. 3) there remain two peaks of +70/–20 G at the very edge of the plasma.

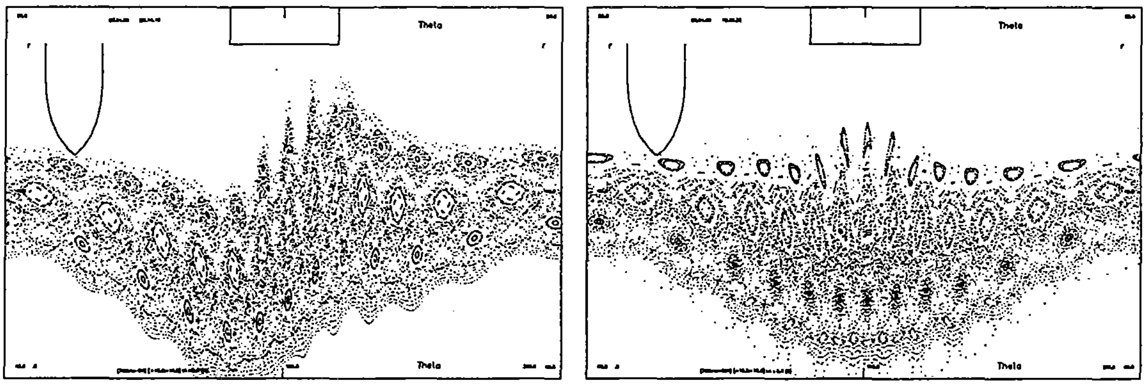

Fig. 17a – b: Poincaré plots of the uncompensated (**a**) and compensated (**b**) setup.

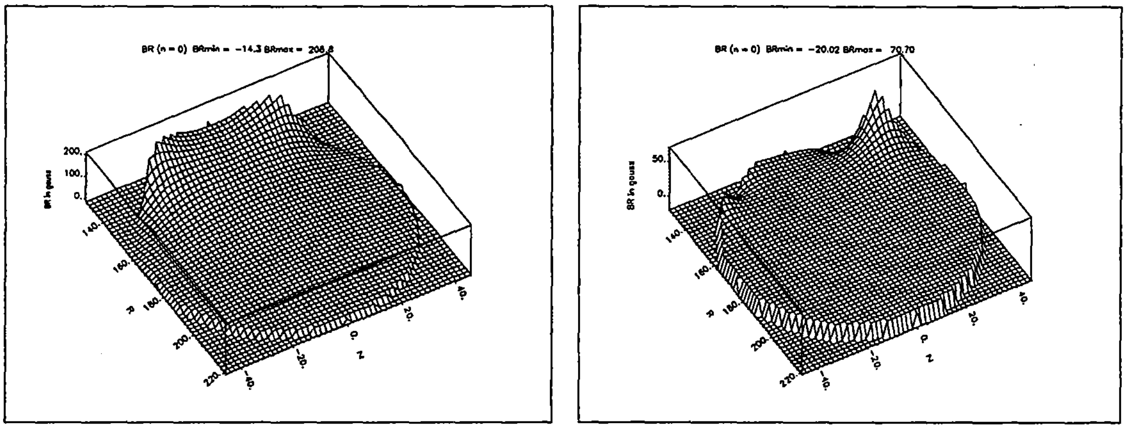

Fig. 18a – b: The net ($n = 0$) R component of the uncompensated (**a**) and the compensated (**b**) field.

4.4.3 Geometrical Effects on the Island Width

As mentioned in section 4.3.1, the island width measured from the Poincaré plots is smaller (by a factor of 0.6) than predicted by the standard formula used in section 3.2. Calculations were made with three different positions of perturbation coils: a) at the high field side, b) at the low field side and c) at the upper and lower side (see fig. 19). All coils were led one turn in toroidal direction and produced the same island system. In each case the Fourier components of the $m = 12$, $n = 4$ mode were calculated in the intrinsic coordinate system. The island width at the high field side measured from the Poincaré plots then were compared with the results from the standard formula which are shown in table 2.

One has to take into account that the island width is a function of the poloidal angle. In our case the island width at the high field side is by a factor of 1.4 larger than the mean width.

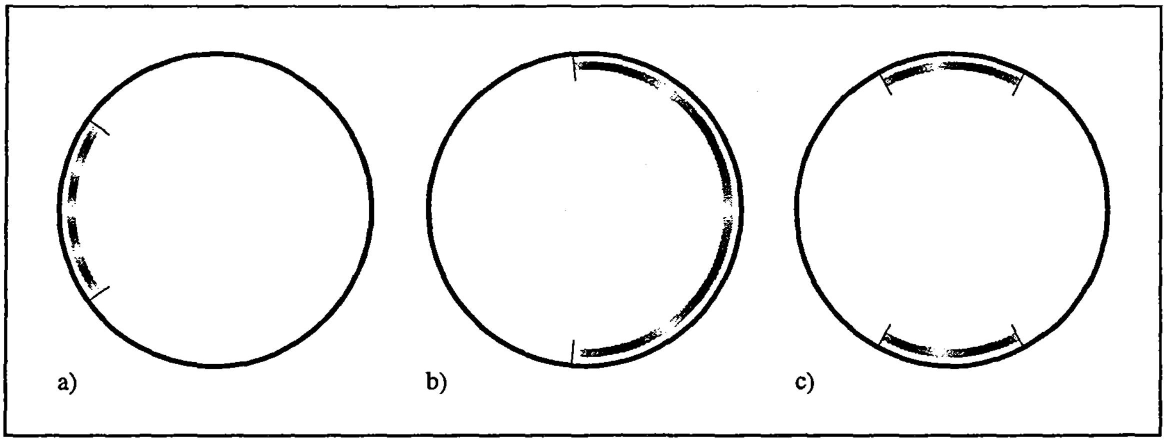

Fig. 19: Three different positions of perturbation coils: a) at the high field side, b) at the low field side and c) at the upper and lower side

	$B_{12,4}$	Δ_{standard}	Δ_{standard} at HFS	$\Delta_{\text{Poincaré}}$ at HFS	$\frac{\Delta_{\text{standard}} \text{ at HFS}}{\Delta_{\text{Poincare}} \text{ at HFS}}$
a) HFS	4 G	2.5 cm	3.4 cm	2.0 cm	0.6
b) LFS	35 G	7.4 cm	10.4 cm	12.5 cm	1.2
c) top and bottom	22 G	5.9 cm	8.3 cm	8.3 cm	1.0

Table 2: Island widths for three different positions of perturbation coils.

The island diameters measured from the Poincaré plot are different from the standard theory, depending on the position of the perturbation coils. An explanation for this difference will be published in the near future.

From table 2 it can be seen that the position of the perturbation coils at the high field side not only causes a smaller value of the Fourier component due the smaller distance between the conductors. It has also an additional effect on the island diameter when the Fourier components have the same value. Roughly there is a dependence from the coil position which is proportional to $(\overline{R}/R_0)^{3/2}$ ($\overline{R}$ is the mean major radius at the resonant surface where the perturbation field acts).

4.4.4 Applying *m*/*n* = 6/2 and *m*/*n* = 3/1 modes

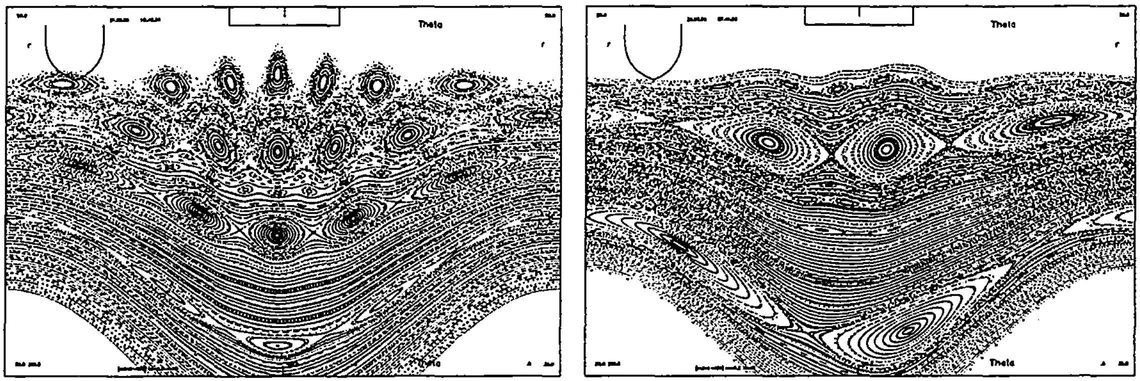

Fig. 20a – b: *m*/*n* = 6/2 and *m*/*n* = 3/1 structures at low perturbation current.

a: (*m*/*n* = 6/2, *cc* = 0.2) The major island chains 7/2, 6/2, 5/2 and 4/2 are well visible.

b: (*m*/*n* = 3/1, *cc* = 0.1) The perturbation affects mainly the $q = 3$ and $q = 2$ surfaces.

The design of the coil system allows also the use of mode structures different from $m = 12$, $n = 4$. By switching each two or four neighboring coils in parallel, $m/n = 6/2$ and $m/n = 3/1$ modes can be created respectively. Figures 20a and b show Poincaré plots of these structures at low perturbation current.

4.4.5 Literature

[1] H. P. Zehrfeld, IPP Garching, private communication

[2] M. Z. Tokar', Sov. J. Plasma Phys. 5(2) 1979 (p. 260)

[3] W. Feneberg, Eighth European Conference on Controlled Fusion and Plasma Physics, Prague 1977, Vol. I, p. 4

5. Near Field Structure of the Magnetic Field

K.H. Finken,
Institut für Plasmaphysik, Forschungszentrum Jülich, Association EURATOM-KFA

The aim of this paragraph is an attempt of better understanding the magnetic field pattern and particle flux to the limiter in front of the perturbation coils. In TORE SUPRA this layer is called the "laminar zone" and the main difference to the ergodic zone is attributed to the different connection length of the magnetic field lines which is long in the ergodic layer and of the order of one toroidal turn in the near field.

In this section a new approach is tried. The total field is taken as a superposition of the equilibrium field and the perturbation field. Instead of solving the magnetic field of a torus, the cylindrical solution is discussed first. To arrive to an analytic solution the model is further simplified: The toroidal field is substituted by a constant axial field, the current by a current filament along the axis (this is a good approximation as long as the current in the ergodic zone is zero) and in the first step of the approximation the perturbing field, created by a helical current sheath at the radius a, has the form $\underline{B}(r,\varphi,z) = \underline{b}(r)\cdot\exp[i(l\varphi+kz)$.

For the following considerations, a helical coordinate system is defined with unit vectors in radial direction ($\hat{e}_r$), 2) in the direction of the perturbation current $\hat{e}_{hel}$ i.e. in helical direction and 3) into the direction perpendicular to (1) and (2) i.e. $\hat{e}_{hel\perp} = \hat{e}_r \times \hat{e}_{hel}$. In this coordinate system the perturbation field components are in $\hat{e}_r$ and $\hat{e}_{hel\perp}$ directions only; the main component of the equilibrium field is in $\hat{e}_{hel}$ direction and a smaller component in the direction $\hat{e}_{hel\perp}$: $b_{hel\perp\text{-}eq} = (b_{pol}/r - B_z/m) = (0.16\cdot a/r - 0.177)$ T. The numbers are selected such that they correspond to the TEXTOR data: $B_z = 2.25$ T, $m=(l\cdot R)/(n\cdot a) = 12.7$ (the slope of the helix), and the value b_{pol} is such that the slope of the helical perturbation current equals the pitch of the equilibrium field at $r/a = 0.9$ (resonance condition). At this value of $r/a=0.9$ the value of $b_{hel\perp\text{-}eq}$ is zero. The helical equilibrium field component is $b_{hel\text{-}eq} \approx b_z = 2.25$ T.

The differential equation for the perturbation field can be solved in form of a recusing relation. For a steep slope of the helix, one obtains

$$b^{i}_{r\text{-}pert} = -l \cdot a_o \cdot \left(\frac{r}{a}\right)^{l-1} \cdot \sin(\phi)$$

$$b^{o}_{r\text{-}pert} = -l \cdot a_o \cdot \left(\frac{r}{a}\right)^{-l-1} \cdot \sin(\phi)$$

$$b^{i}_{hel\perp\text{-}pert} = -l \cdot a_o \cdot \left(\frac{r}{a}\right)^{l-1} \cdot \cos(\phi)$$

$$b^{o}_{hel\perp\text{-}pert} = l \cdot a_o \cdot \left(\frac{r}{a}\right)^{l-1} \cdot \cos(\phi)$$

The index "i" refers to the solution inside the current sheath and "o" to the outside one, $1*a_o$ is the perturbation amplitude at the current sheath and Φ is the angle in the helical coordinate system.

The total magnetic field components in the $\hat{e}_r$-$\hat{e}_{hel\perp}$ plane $b_{tot} = (b_{hel\perp\text{-eq}} + b_{hel\perp\text{-pert}})\hat{e}_{hel\perp} + b_{r\text{-pert}}\hat{e}_r$ has some fix points, where the $b_{tot} = 0$. Fig. 1 shows the radii of these fix points as a function of the perturbation field amplitude inside the current sheet. Depending on the amplitude, two, three and one fix point solution can be found. The phase condition of the "left" branch requires $\varphi = 2j\pi/l$, $j=0,1,\ldots$ and it is an "x-point"; this branch persists for all perturbation amplitudes. The phase of the "middle" branch ($0.9 \leq r/a \leq 0.98$) and the "right" branch are $\varphi=(2j + 1)\pi l$ where the middle one is an "O-point" and the right one an "x-point". Above a perturbation amplitude of $l \cdot a_o \approx 12 * 1.5 \cdot 10^{-3}$ T (for $l=12$) the middle and right solution disappear and additional fix points remain in the current sheet and outside.

A field line tracing within the $\hat{e}_r$-$\hat{e}_{hel\perp}$ plane provides either closed or open curves depending on the starting position and the perturbation amplitude. Examples of these contour plots - in particular for contours near the separatrix - are shown in Figs. 2 - 5. At a low perturbation amplitude of $12 \cdot 2 \cdot 10^{-4}$ T, an island like structure is found near the resonance surface $r/a = 0.9$. With increasing amplitude the closed area increases and reaches for $a_o = 7.4 \cdot 10^{-4}$ T the current layer. The solution of the three fix points is shown in Fig. 4. This case is representative for a perturbation current of about 2.4 kA/mode in TEXTOR. Finally Fig. 5 shows the case corresponding to a perturbation current of 4.8 kA. Under the assumption of complete helical symmetry, the contour plots represent ψ-functions as well.

The complete helical coil system will show no ergodicity of the magnetic field lines because only one Fourier component is present. This feature changes, if the helix is wound only over strip e.g. 1/3 of the azimuthal circumference. Now the perturbed magnetic field contains many Fourier components and both the axial and the helical symmetry are broken. Therefore ψ-functions do not exist any longer.

It is assumed, however, that nevertheless the magnetic field pattern near the perturbation coils and away from it can be composed of two parts: outside of the perturbation area the field lines are taken from the equilibrium field only and near the perturbation coils it is treated as sum of the equilibrium field and perturbation field. The analysis is performed again in the $\hat{e}_r$-$\hat{e}_{hel\perp}$ plane. The effect of the finite strip width of the perturbation coils is taken into account by following the field lines over a maximum length in helical direction of $2\pi R$ which corresponds to one toroidal path in the torus. It is of particular interest to determine the area from which the magnetic field lines intersect at least once the wall during one toroidal turn ($\Delta z = 2\pi R$). To find this, starting points of the field lines were chosen at $r/a = 1$ and field lines were traced backwards. Examples of this analysis are shown in Figs. 6 and 7. In agreement with the expectations, the field lines penetrate less deep for the lower perturbation current than for the higher current. For the 10 kA perturbation current, about 50% of the area with $0.85 \geq r/a$ 1 is covered.

The data are explained in the following way: Particles starting from outside the perturbation coil influence follow the equilibrium field and move in the given representation along horizontal lines (at the resonance layer $r/a=0.9$ they stay on the same phase while due to the shear all other field lines follow the horizontal direction). These equilibrium field lines enter the perturbation pattern at an arbitrary but predictable phase. If they end in the area marked by the finite length field lines the particles will be swept to the wall within a toroidal turn. If the enter the other area the particles will predominantly be swept towards the plasma core. The perturbation field in this representation can be regarded as a vortex. One sees also that the highest heat and particle flux would occur near the separatrix because there the field lines penetrate deepest into the plasma.

For the proposed perturbation coils an analysis following basically this idea has been started. Up to now the magnetic field has been projected into the helical coordinate system and the fix points described above have been found. As was found in Fig. 1 the three fix-point solution is found for a small range of perturbation current amplitudes. The characteristic value for this solution agrees within 20% between the cylindrical model and the proper coils. It is therefore assumed that the simplifications in the model due to the cylindrical geometry and due to neglecting the transition between equilibrium and perturbation limited fields are not critical.

The near field model may not be of importance for TEXTOR only, it may also be transferable to divertor scenarios of the stellarators like WENDELSTEIN 7X with its island divertor concept and LHD (Japan) with a near field type divertor concept. At TEXTOR, the near field will reach deep inside the island / ergodic zone and the evaluation and separation of effects due to the near field and due to the "resonant islands" will not be trivial. There will be an option to study preferentially the interaction with the islands or with the near field by leaning the plasma either on the toroidal ALT-II limiter (remote from the perturbation coils) or on the inner bumper limiter.

Figure captions:

Fig. 1: Solution for the fix points in helical symmetry. At a low perturbation field two solutions exist, in a narrow band three solution exist and for higher amplitudes only one.

Fig. 2: Contour plot in the $\hat{e}_r$-$\hat{e}_{hel\perp}$ plane for a low perturbation amplitude.

Fig. 3: Contour plot in the $\hat{e}_r$-$\hat{e}_{hel\perp}$ plane for a perturbation amplitude $a_o = 7.4 \cdot 10^{-4}$ T; for this case the separatrix just touches the boundary r/a = 1.

Fig. 4: Contour plot in the $\hat{e}_r$-$\hat{e}_{hel\perp}$ plane for a perturbation amplitude $a_o = 1.5 \cdot 10^{-3}$ T; for this case three fix point solutions are found inside the cylinder.

Fig. 5: Contour plot in the $\hat{e}_r$-$\hat{e}_{hel\perp}$ plane for a perturbation amplitude $a_o = 3.0 \cdot 10^{-3}$ T; this case corresponds to a perturbation current of 4.8 kA.

Fig. 6: Contour plot in the $\hat{e}_r$-$\hat{e}_{hel\perp}$ plane for a perturbation amplitude $a_o = 1.5 \cdot 10^{-3}$ T; this case corresponds to a perturbation current of 2.4 kA. The lines starting at r/a=1 represent magnetic field lines with a length of $2\pi R$, i.e. they would wind once toroidally in the near field of the perturbation coil. The radial scale is expanded relative to Fig. 4.

Fig. 7: Contour plot in the $\hat{e}_r$-$\hat{e}_{hel\perp}$ plane for a perturbation amplitude $a_o = 3.0 \cdot 10^{-3}$ T; this case corresponds to a perturbation current of 4.8 kA. The lines starting at r/a=1 represent magnetic field lines with a length of $2\pi R$, i.e. they would wind once toroidally in the near field of the perturbation coil. The radial scale is expanded relative to Fig. 5.

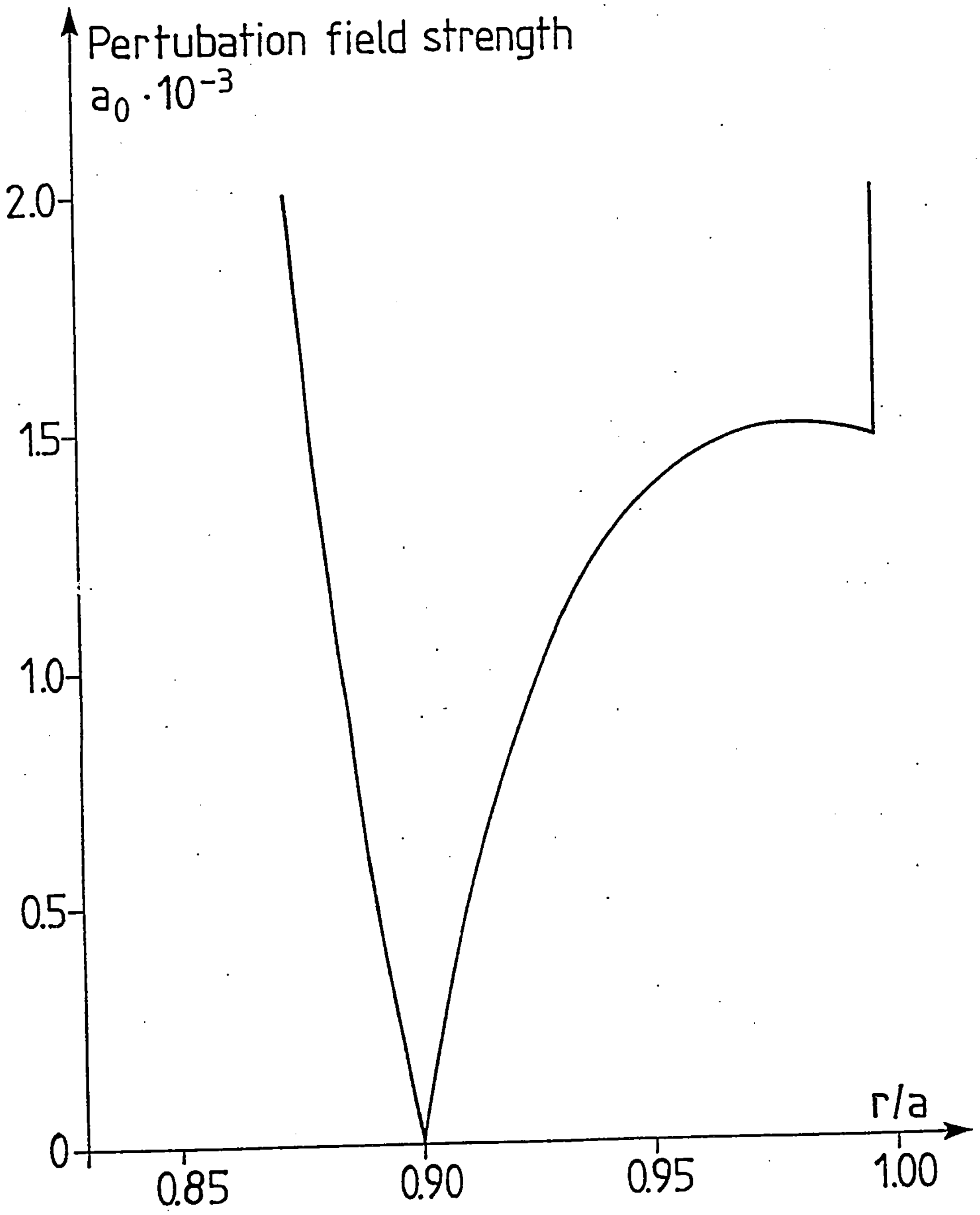
Pertubation field strength
$a_0 \cdot 10^{-3}$
2.0
1.5
1.0
0.5
0
r/a
0.85
0.90
0.95
1.00

Figure 1

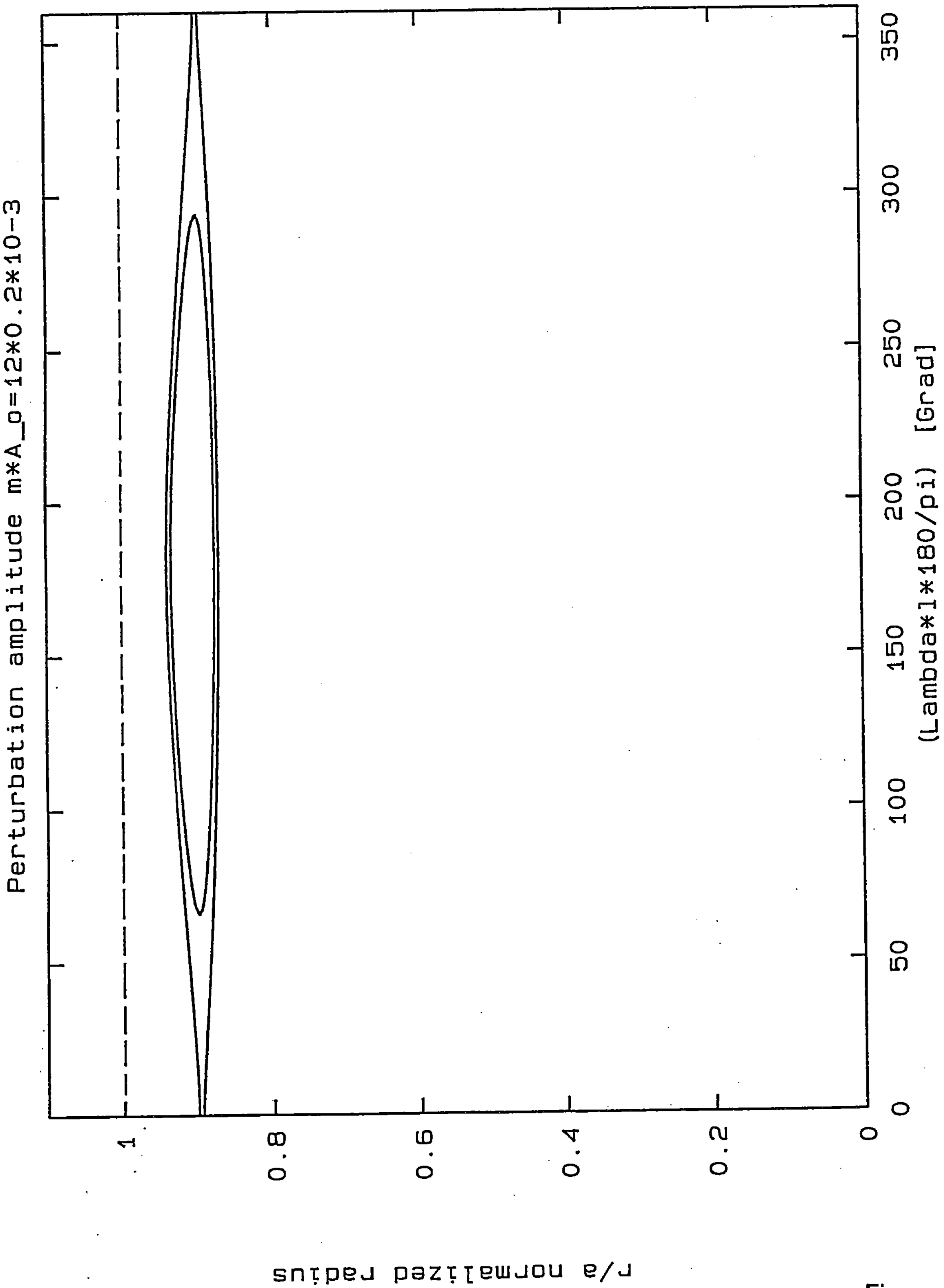
Perturbation amplitude m*A_o=12*0.2*10-3
r/a normalized radius
1
0.8
0.6
0.4
0.2
0
0
50
100
150
200
250
300
350
(Lambda*l*180/pi) [Grad]

Figure 2

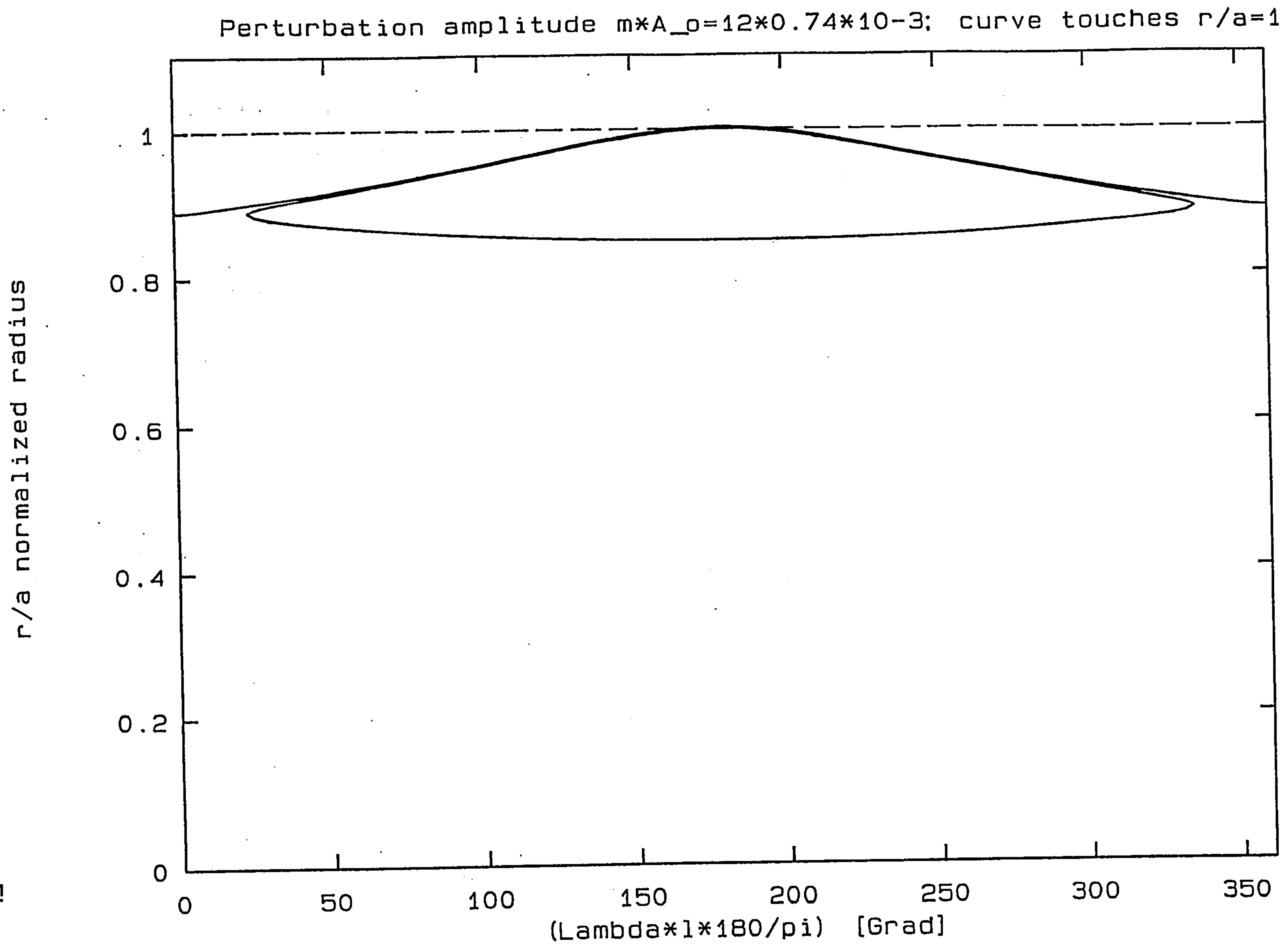
Perturbation amplitude m*A_o=12*0.74*10-3; curve touches r/a=1
r/a normalized radius
1
0.8
0.6
0.4
0.2
0
0
50
100
150
200
250
300
350
(Lambda*l*180/pi) [Grad]

Figure 3

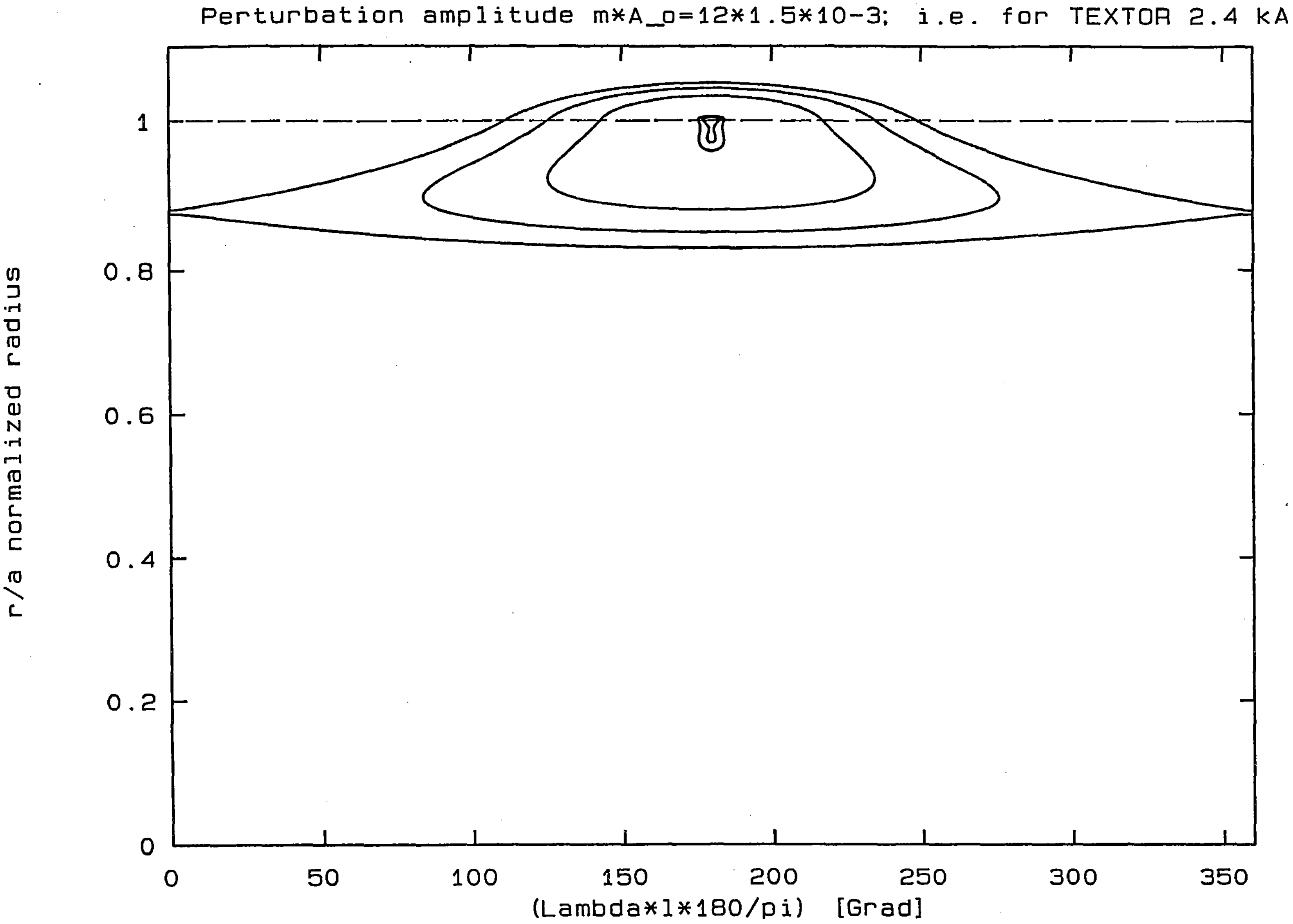
Perturbation amplitude m*A_o=12*1.5*10-3; i.e. for TEXTOR 2.4 kA
r/a normalized radius
1
0.8
0.6
0.4
0.2
0
0
50
100
150
200
250
300
350
(Lambda*l*180/pi) [Grad]

Figure 4

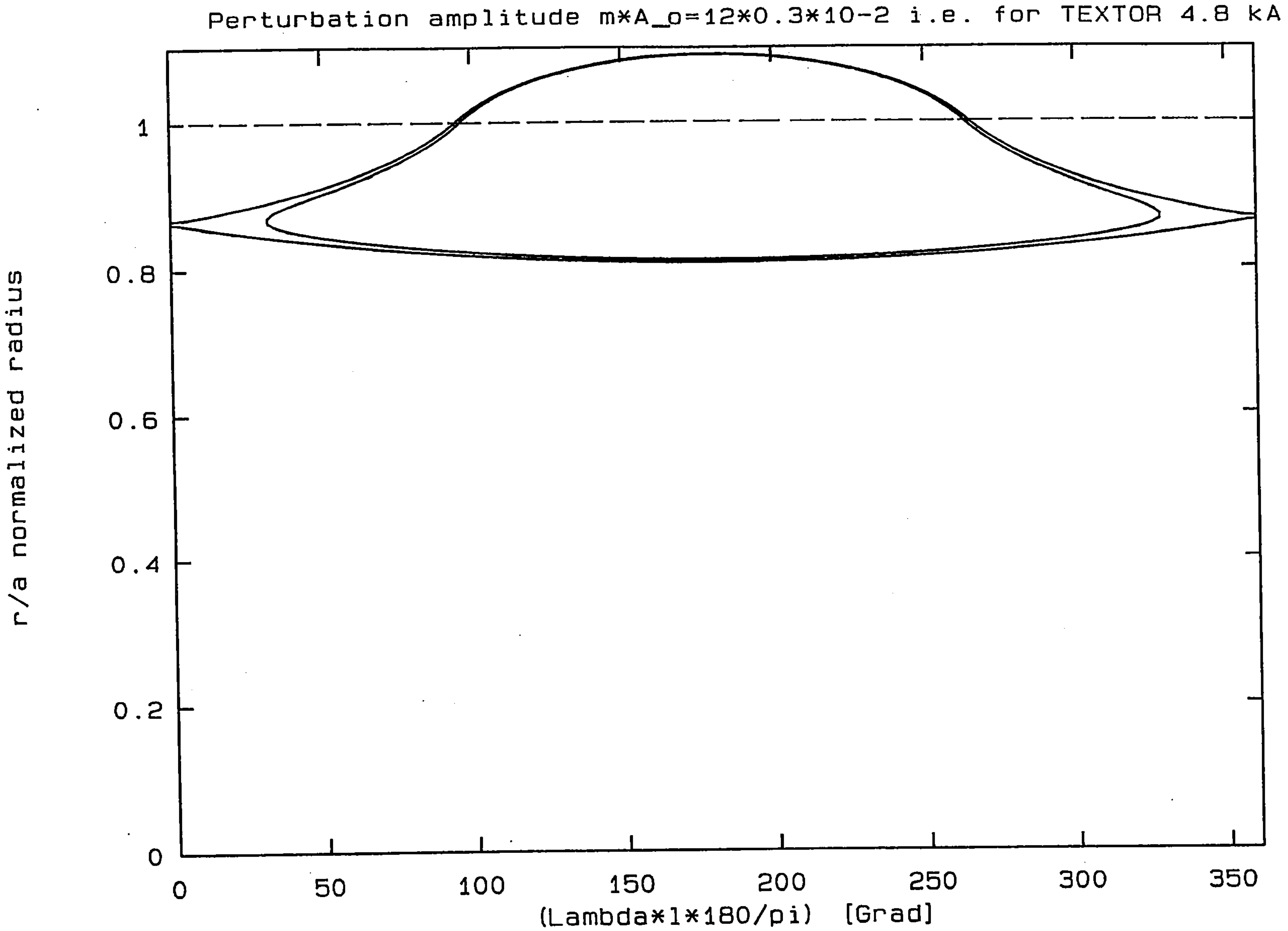
Perturbation amplitude m*A_o=12*0.3*10-2 i.e. for TEXTOR 4.8 kA
r/a normalized radius
0
0.2
0.4
0.6
0.8
1
0
50
100
150
200
250
300
350
(Lambda*l*180/pi) [Grad]

Figure 5

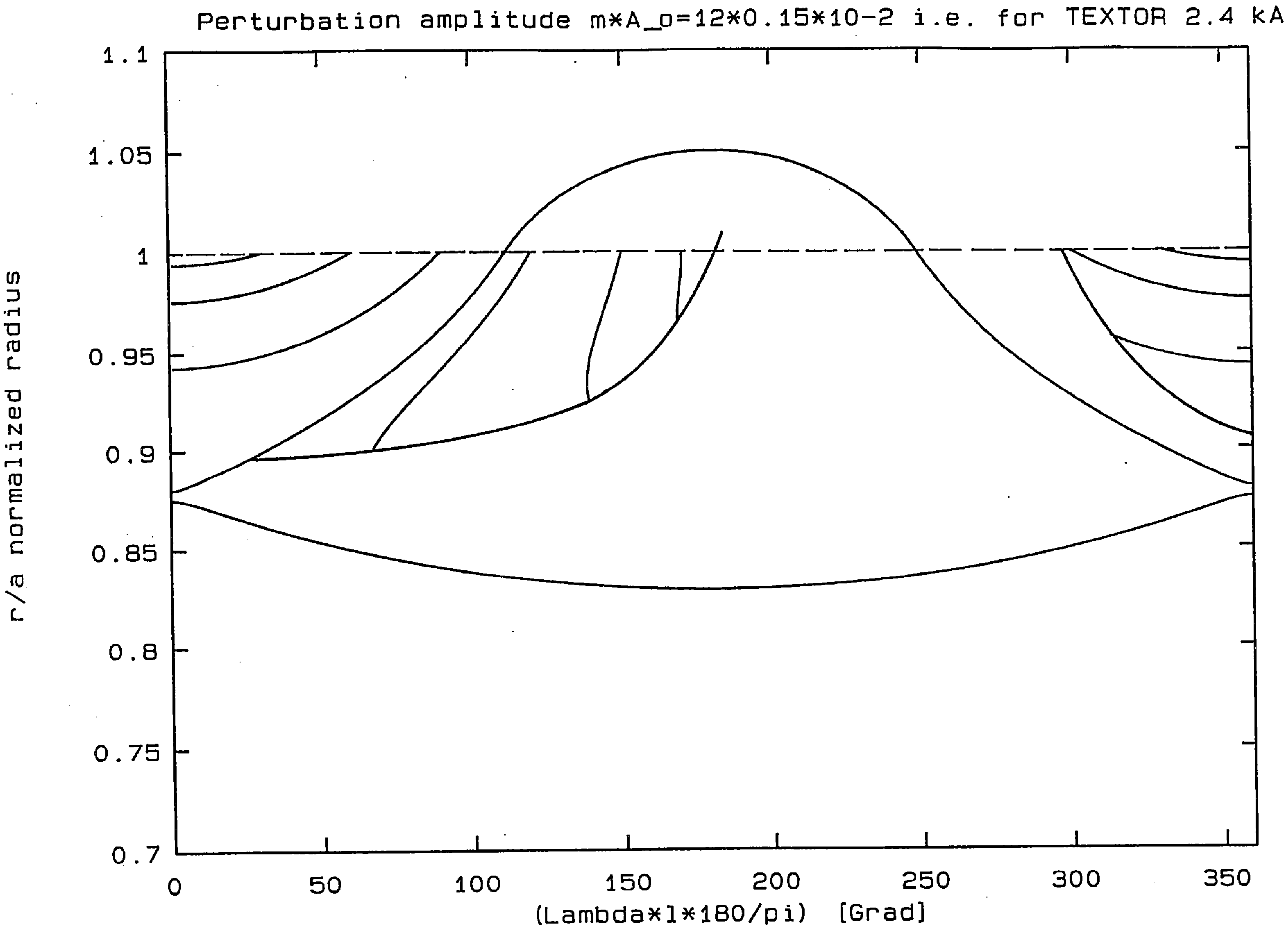
Perturbation amplitude m*A_o=12*0.15*10-2 i.e. for TEXTOR 2.4 kA
r/a normalized radius
1.1
1.05
1
0.95
0.9
0.85
0.8
0.75
0.7
0
50
100
150
200
250
300
350
(Lambda*l*180/pi) [Grad]

Figure 6

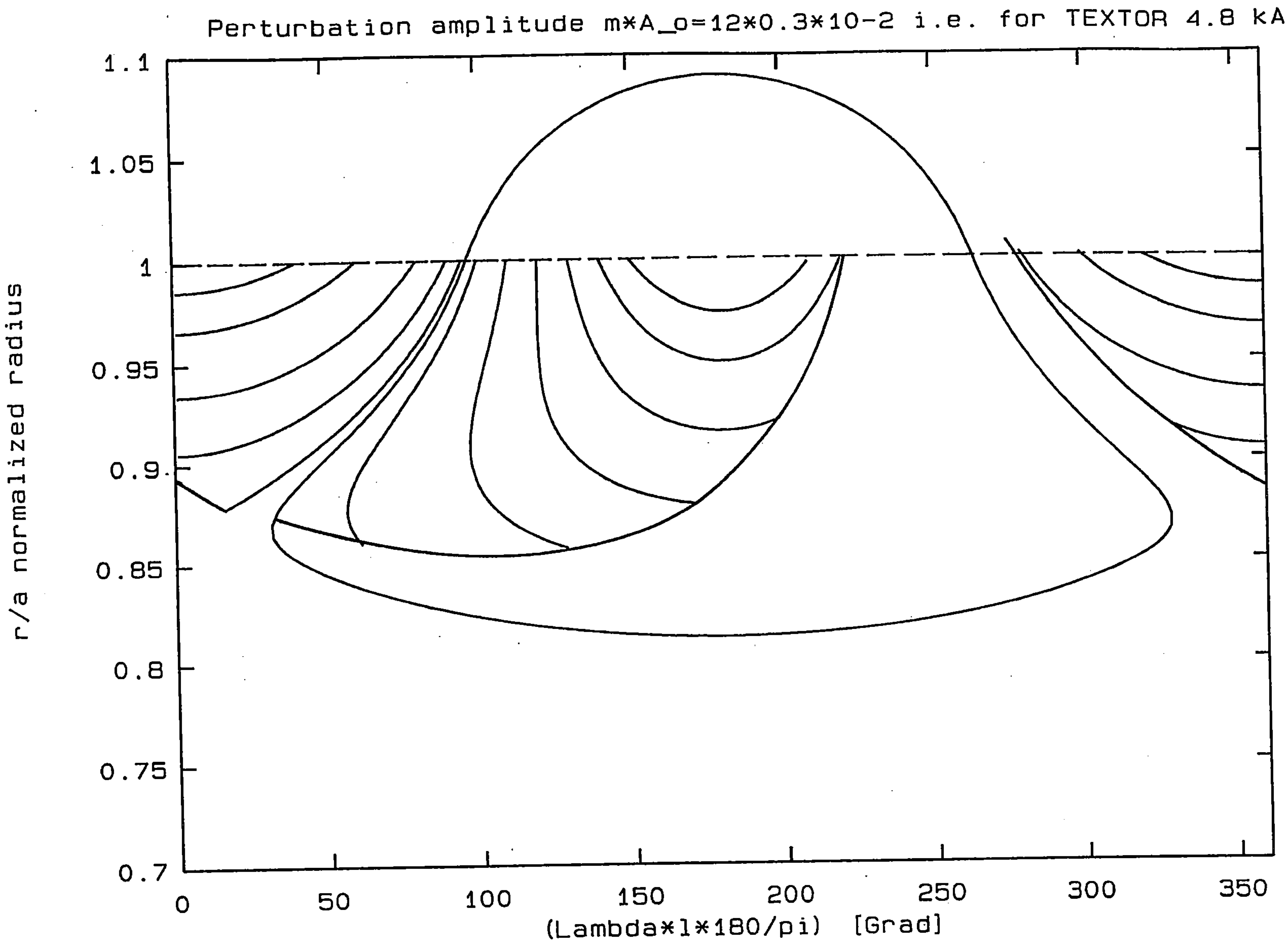
Perturbation amplitude m*A_o=12*0.3*10-2 i.e. for TEXTOR 4.8 kA
r/a normalized radius
1.1
1.05
1
0.95
0.9
0.85
0.8
0.75
0.7
0
50
100
150
200
250
300
350
(Lambda*l*180/pi) [Grad]

Figure 7

6. Physics Considerations for the TEXTOR in-Vessel High Field Side (HFS) Certurbation Coils

T. Evans,
General Atomic, San Diego, USA

6.1 General discussion of HFS versus LFS magnetic perturbation coils

The proposed system of perturbation coils to be installed inside the TEXTOR vacuum vessel is unique in several respects. These coils will be wound toroidally around the TEXTOR centerpost with a helical pitch matching the angle of the magnetic field lines on the q = 3 surface at the equatorial plane on the High Field Side (HFS) of the discharge. The only other experiment with internally mounted coils is Tore Supra[1,2,3]. Tore Supra has six modular coils located on the Low Field Side (LFS) of the plasma. The Tore Supra coils produce sizable poloidal harmonics ranging between m=16 and 24 with either an n=6 or n=3 toroidal mode number depending on the toroidal phasing of the currents in the six coil modules. Since the poloidal mode number of the TEXTOR coils is centered at m=12 the radial decay of the perturbation field will be somewhat slower than in the TORE SUPRA case. All other ergodic limiter experiments (e. g., TEXT[4,5] and JIPP T-IIU[6]) have used modular coils located outside the vacuum vessel.

Since toroidal field variations produce changes in the size and the shape of the magnetic islands driven by the perturbation coils there are interesting plasma physics effects to be considered when analyzing the topology of the islands and their relationship to the production of an ergodic layer. These are, in principle, independent of the location of the perturbation coils, from the resonant point of view, once the geometric properties of the resonant conditions are established. Nevertheless, a competing process for coils located in close proximity to the plasma is the non-resonant or so-called near field effects of the coils. These near field effects compete with the resonant effects (i. e., islands and ergodic layer effects) to influence the trajectories of the magnetic field lines when they make a close approach to the perturbation coils. Thus, the location of the coils is important because the near field effects will be competing either with radially narrow, poloidally elongated, islands for LFS located coils or radially extended, poloidally compress, islands when the coils are located on the HFS. These considerations are important to keep in mind when assessing the local field line intersection patterns on plasma facing surfaces in the two configurations and when analyzing the plasma transport effects caused by the magnetic islands and the ergodic layer.

With respect to the island/ergodic layer transport considerations one must know the width of the ergodic layer compared to the depth of penetration of the near field effects for a given coil current and coil location. Since the near field effects increase with the current in the perturbation coils, the depth of penetration of the near field effects into the edge plasma also increases with perturbation coil current. As discussed in the paragraph about the "Structure of the Near Field" there is possibly a close connection between near field effects and ergodicity; both effects may just be different pictures of the underlaying physics. Detailed investigations are required on this field.

On Tore Supra the TRIPND field line tracing code[7] was used to calculate the near field penetration distance for the Tore Supra coils. Because of the relatively fast radial decay (i. e., higher poloidal mode spectrum) of the Tore Supra coils and the modular coil design, rather larger perturbation coil currents are required to produce the ergodic layer in Tore Supra. Additionally, since the Tore Supra perturbation coils are located on the LFS the ratio of the local radial fields near the coils to the toroidal field is larger than if the same set of coils were located on the HFS. The net results is that the near field effects distort the field lines locally such that the entire ergodic region is pulled out to the coils and the walls at each of the six toroidal coil locations. Thus, while the vacuum magnetic topology appears to be ergodic the particles and heat are never feel the effect of the ergodicity because they are lost to plasma facing surfaces around the coils modules before they experience a significantly long residence time in the ergodic structure. Thus, Tore Supra is only able to produce a truly ergodic layer (i. e., for the heat and particle fluxes) when the plasma of reduced radius is positioned against the HFS wall and the current in the ergodic divertor coils is kept between 18 to 36 kA depending on the edge safety factor, the radius of the plasma, and the ergodic volume required[3].

In TEXTOR, a smaller perturbation coil current is required to produce the desired ergodic volume. The GOURDON field line tracing code predicts an ergodic layer with a DED perturbation coil current between 9 and 15 kA depending on the volume one wants to fill with ergodic flux (see the paragraph on "Structure of the Ergodized Layer" in this document for additional details on the GOURDON Code calculations for TEXTOR). A similar analysis of the TORE SUPRA coils with the TRIPND field line tracing code gives an ergodic threshold current of 24 to 36 kA in order to achieve the desired ergodic volume and edge safety factor. In TORE SUPRA the width of the vacuum field ergodic layer with an ergodic divertor current of 24 kA is approximately 12 cm (on the LFS) and the near field effects of the perturbation coils dominate the outer 15 to 20 cm of the plasma in this configuration. In TEXTOR, a 9 kA the ergodic layer is approximately 3 cm in width on the LFS and 7 cm in width on the HFS. The near field effects of the TEXTOR HFS coils only affect a small fraction of the 7 cm ergodic layer in this case. Moreover, with the resonant layer positioned in the optimal configuration to achieve good power sharing between the inner bumper limited and the ALT II limiter, results from the GOURDON code indicate that a sufficiently large ergodic volume will exist between the core plasma and the region where local effects from the perturbations coils dominated to effectively radiate a sizable fraction of the core heat flux to the vessel walls.

6.2 What is expected to be learned from the TEXTOR HFS coil configuration?

As discussed in the previous section, the TEXTOR coil geometry is particularly interesting because the ergodic layer is wider on the HFS of the discharge and the local perturbation coil effects do not destroy the entire ergodic layer. Unlike Tore Supra, the ergodic and local effects will coexist in TEXTOR and can be used to optimize the power and particle exhaust processes while maintaining good core confinement conditions. This, combined with the dynamic capabilities of the ergodic field structures and the extensive array of plasma diagnostics on TEXTOR, put the proposed DED program in a unique position to answer a number of critical questions which are needed to better understand the physics of mixed ergodic-island layers and how they can be used as an adaptive interface between hot, well confined, plasmas and plasma facing components (PFCs) which need to be protected from high heat fluxes.

It should be noted that experiments in Tore Supra resulted in very different plasma responses depending the position of the plasma. With the plasma limited on the LFS near the ergodic divertor coils the plasma density decreased dramatically and the recycling flux increased as soon as the ergodic coils were activated. In this geometry the local perturbation field from the ergodic divertor coils connected a relatively large fraction of the edge magnetic flux directly to the divertor coils and the walls behind the coils. Thus, the edge of the plasma (i. e., r/a ^{3} 0.8) is connected to these PFCs over a relatively short distance. The ergodicity of the field lines has no real effect on the heat or particles because the effective connection length is to short for ergodic effects to play a role. If on the other hand, the Tore Supra plasma is limited on the HFS wall and the ergodic divertor current is kept as low as possible, while obtaining a reasonably wide ergodic layer without introducing significant near field effect (i. e., reducing the plasma radius and moving the plasma as far away form the coils as possible), the plasma response is exactly opposite that in the LFS configuration. These effects have been carefully documented in both ohmic[8,9] and additionally heated plasmas[3]. Therefore, based on the Tore Supra results for HFS versus LFS limited discharges, we see that there are clearly some important physics issues which need to be sorted out in connection with the effects of magnetic topology in the edge of the plasma. The TEXTOR DED program will be in a extremely good position to address these unresolved ergodic layer physics issues both because of the position of the perturbation coils and because of the availability of a comprehensive set of plasma diagnostics which will be specifically tailored for these studies.

Based on our experience from previous ergodic boundary experiments we would argue that there are a range of questions concerning phenomenon such as: plasma detachment, the properties of MARFEs and their onset, disruptions and their avoidance, transport and fluctuations in ergodic layers, the detailed properties of magnetic islands, recycling control, radiation control, and impurity screening effects which can be addressed more effectively than in previous experiments with the TEXTOR HFS perturbation coil design. In addition, the TEXTOR DED data will provide a different view of the ergodic boundary and its effects on the core-PFC interface. This information is essential for developing the analytical and numerical models which are required if one expects to scale up the ergodic boundary concept for high power, reactor grade, plasma applications and for developing effective edge plasma feedback control strategies which will be needed in power reactors.

References

1. A. Grosman, T. E. Evans, Ph. Ghendrih et al, Plasma Physics and Controlled Fusion, **32** (1990) 1011.

2. A. Grosman, T. E. Evans, E. Agostini et al., J. Nucl. Mat. **176 - 177** (1990) 493

3. T. E. Evans, M. Goniche, A. Grosman et al., J. Nucl. Mat. **196 - 198** (1992) 421.

4. S. C. McCool, A. J. Wootton, M. Kotschenreuther et al., Nucl. Fusion **30** (1990) 167

5. T. E Evans, J. S. deGrassie, G. L. Jackson et al., J. Nucl. Mat., **145-146** (1986) 812

6. T. E. Evans, J. S. deGrassie, H. R. Garner et al., J. Nucl. Mat. **162-164** (1989) 636

7. T. E. Evans and the ASDEX Team, "Measurements of Poloidal and Toroidal Energy Deposition Asymmetries in ASDEX Divertors", Max-Planck-Institut für Plasmaphysik Report Number. IPP III/154, March 1991 and

   T. E. Evans, Europhysics Conference Abstracts, **Vol. 15C** (1991) II-65. Presented at the 18th European Conference on Controlled Fusion and Plasma Physics, Berlin, Germany, 3-7 June 1991

8. T. E. Evans, A. Grosman, D. Guilhem et al., "Plasma Performance Control During Ergodic Divertor Experiments in Tore Supra", in the Bull. Am. Phy. Soc., 35 (1990) 1998. Presented at the 32nd Annual Meeting of the American Physical Society, Division of Plasma Physics, Cincinnati, OH, 12-16 November 1990

9. T. E. Evans, A. Grosman, D. Guilhem et al., "Plasma Performance Control During Ergodic Divertor Experiments in Tore Supra", CEA Euratom DRFC/CAD Report Number EUR-CEA-FC-1419, March 1991

Part III: Specific Aspects

7. Parametric Variation of the Inboard Field Line Pitch Angle

A. Rogister,
Institut für Plasmaphysik, Forschungszentrum Jülich, Association EURATOM-KFA

7.1 Introduction

The rod array of the Edge Ergodic Limiter on TEXTOR has been designed to generate magnetic islands on the $q \equiv q_s = 3$ magnetic surface (q is the safety factor), assuming $B^{(0)}_{\phi,a} = 2.25$ Tesla (toroidal magnetic field at the centre of the cross-section of the last closed magnetic surface, LCMS, or separatrix), $I_p = 0.42$ MA (total plasma current), and

$$\left\langle \beta_{pol} \right\rangle_{r=a} \equiv \left(16\ \pi \int_0^a P\ rdr\right) / \left(r B_\chi^{(0)}\right)^2_{r=a} = 1;$$

a is the minor plasma radius; ϕ is the toroidal angle, $B_\chi^{(0)}$ (r) is the average of the poloidal magnetic field, $B_\chi\ (r, \chi)$, over the poloidal like-angle χ. If the major radius $R_a^{(0)}$ at the centre of the LCMS is 1.75 m, the nominal edge safety factor is $q_a = 3.24$ [$q(r) = 5r^2\ B^{(0)}_{\phi,r}\ /\ R_r^{(0)} I(r)$ with the units: meter, tesla, mega-ampere]. We obtain here, by means of a large aspect ratio expansion of the tokamak equilibrium, the equation of the pitch of the field lines on the outer magnetic surfaces as function of $\left\langle \beta_{pol} \right\rangle, \ell_i$ (internal inductance of the toroidal current), q(r) and ε (inverse aspect ratio). The relation to be satisfied between variations of these quantities away from their design values in order to maintain a resonant drive of magnetic islands then follows.

It should be noted that, up to first order in $\varepsilon \sim a / R$, the Shafranov shift Δ is of order $\varepsilon^2 R$; as a consequence, the theory does not distinguish between the major radii $R_a^{(0)}$ and $R_0^{(0)} \equiv R_0$ which refer, respectively, to the centre of the LCMS and to the magnetic axis, nor between $B^{(0)}_{\phi,a}$ and $B^{(0)}_{\phi,0} \equiv B_{\phi,0}$.

7.2 Geometrical Considerations

It is convenient to introduce orthogonal Gauss surfaces $\Psi(\vec{r}), \chi(\vec{r})$ and $\phi(\vec{r})$ such that $\Psi(\vec{r}) = \Psi_i$ are toroidal nested magnetic flux surfaces:

$$\Psi_i = \frac{1}{2\pi} \int_0^{2\pi} d\phi \int_0^{\Psi_i} d\Psi \; h_\phi h_\psi B_\chi ,$$

where $h_\phi \equiv \left|\vec{\nabla}\phi\,(\vec{r})\right|^{-1}$, $h_\psi \equiv \left|\vec{\nabla}\Psi(\vec{r})\right|^{-1}$,

$\chi(\vec{r}) = \chi_J$ is the family of toroidal surfaces orthogonal to the formers and limited by the magnetic axis [equation: $\Psi(\vec{r}) = 0$], and $\phi(\vec{r}) = \phi_k$ are the planes orthogonal to the $\Psi(\vec{r}) = \Psi_i$ and to the magnetic axis.

Within the framework of the large aspect ratio expansion, the flux surfaces $\Psi(\vec{r}) = \Psi_i$ can be identified with excentric circles. There exists therefore a transformation from $\Psi(\vec{r}) = \Psi_i$ to $\hat{\Psi}(\vec{r}) = r_i$, where the r_i's are the circles radii. It is possible to show, from the mere pressure balance and Ampere's equations, that the metric of the Gauss space is fully described by the equations(1) (note that $\chi = 0$ in the outer equatorial plane of the torus):

$$h_r = 1 - \Delta' \cos\chi \tag{1a}$$

$$h_\chi = r\left(1 - \int_a^r \frac{\Delta'}{r'}\, dr' \; \cos\chi\right) \tag{1b}$$

$$h_\phi = R_0\left(1 + \varepsilon \;\cos\chi\right), \tag{1c}$$

where $\varepsilon \;(r) \equiv r / R_0$, $\Delta'(r) = d\Delta(r) / dr$; the Schafranov shift $\Delta(r)$ is solution of the equation

$$\Delta'' = \frac{1}{R_0} - \Delta' \frac{d}{dr} \;\ell n\left(B_\chi^{(0)2} r\right) - \frac{8\pi}{R_0 B_\chi^{(0)2}}\, r\, \frac{dP}{dr}, \tag{2}$$

where P(r) is the plasma pressure. It is readily seen that the Shafranov shift is small (is of order ε) in comparison to the minor radius:

$$\frac{\Delta}{r} \sim \frac{r}{R_0} \equiv \varepsilon ,$$

provided the local poloidal bêta, or rather the local parameter

$$\alpha^*(r) \equiv -\frac{8\pi}{B_\chi^{(0)2}}\, r\, \frac{dP}{dr}$$

is small in comparison to 1/ε (is of order unity). We note that the related variable $\alpha(r) = -\left(8\pi R q^2 / B^2\right) dP/dr \equiv \varepsilon\alpha^*$ is the key parameter of high-n ballooning mode theory$^{(2)}$.

In this representation, the poloidal and toroidal magnetic fields are given, up to first order in the ε expansion, by the expressions

$$B_\phi = B_{\phi,o}\left(1 - \varepsilon\cos\chi\right), \tag{3a}$$

$$B_\chi = B_\chi^{(0)}\left(1 - \Lambda\cos\chi\right), \tag{3b}$$

$$\Lambda = \varepsilon - \Delta'. \tag{3c}$$

$B_{\phi,0}$ is the toroidal magnetic field generated by the coils; $B_\chi^{(0)}(r)$ is the solution of the equation

$$\frac{1}{r}\frac{d}{dr}\left(rB_\chi^{(0)}\right) = \frac{4\pi}{c}J_\phi, \tag{4}$$

where $J_\phi(r)$ is the toroidal current density resulting from the induced loop voltage or other drives.

The critical parameter for the spontaneous or external generation of magnetic islands is the pitch of the undisturbed magnetic field lines:

$$\nu(r,\chi) \equiv \left(\frac{d\phi}{d\chi}\right)_{\vec{B}} = \frac{B_\phi h_\chi}{B_\chi h_\phi}. \tag{5}$$

The safety factor q(r) being defined by

$$q = \oint \nu(r,\chi)\,\frac{d\chi}{2\pi} = \frac{B_{\phi,0}r}{B_\chi^{(0)}R_0}, \tag{6}$$

one also has

$$\nu(r,\chi) \equiv q(r)\left[1 - \left(\varepsilon + \Delta' + \int_a^r \frac{\Delta'}{r'}dr'\right)\cos\chi\right] \tag{5'}$$

The interpretation of the safety factor $\nu(r,\chi)$ is best given by considering first an infinite plasma cylinder, R_0 being then an axial periodicity length. It is evident that a *complete* helical current carrying rod array, covering the entire magnetic surface r = r_0, should have the same *periodicity* as the equilibrium magnetic field on the rational magnetic surface r = r_s on which magnetic islands are to be generated; thus

$$\frac{i_\phi r_0}{i_\chi R_0} = \frac{B_{\phi,0} r_s}{B_\chi^{(0)}(r_s) R_0} = q(r_s) = \frac{m}{\ell}.$$

The safety factor q(r) and, by extension, the pitch angle $\nu(r,\chi) \equiv (d\phi / d\chi)_{\vec{B}}$ are thus mere geometrical factors related to the periodicity of the helix: cylindrical geometry introduces, by comparison with slab geometry, a factor proportional to r; in toroidal geometry, the Shafranov displacement of the centre of the magnetic surfaces leads to the additional factor $h_\chi(r,\chi) / r$.

7.3 Variations of the Pitch Angle of the Field Lines

In the proposed experiment, the current carrying rod array does not cover the full range of poloidal angles but, rather, is limited to $\chi \in]-\theta_0 + \pi, \theta_0 + \pi[$ with θ_0 of the order of $\pi / 3$. As a consequence, the relation between the toroidal and poloidal current components, on the one hand, and the corresponding magnetic field components, on the rational surface r = r_s defined by $q(r_s) = m / \ell$, on the other hand, will be

$$\frac{i_\phi h_\chi(r_0, \chi = \pi)}{i_\chi R_0[1 - \varepsilon(r_0)]} = \frac{B_{\phi,0}[1 + \varepsilon(r_s)] h_\chi(r_s, \chi = \pi)}{B_\chi^{(0)}(r_s)[1 + \Lambda(r_s)] R_0[1 - \varepsilon(r_s)]} = \nu(r_s, \chi = \pi). \tag{7}$$

Noting that $r_0/r_s = 1 + (r_0 - r_s)/r_s$, where the ratio $(r_0 - r_s)/r_s$ is also small (say of order ε), the ratio $h_\chi(r_0,\pi) / h_\chi(r_s,\pi)$ can be approximated by r_0/r_s, the correction being of order ε^2; likewise, the ratio $R_0[1 - \varepsilon(r_0)] / R_0[1 - \varepsilon(r_s)]$ can be approximated by unity; thus

$$\frac{i_\phi}{i_\chi} = \frac{B_{\phi,0}}{B_\chi^{(0)}(r_s)}\left[1 + \Delta'(r_s) - \frac{r_0 - r_s}{r_s} + 0(\varepsilon^2)\right] \tag{7'}$$

where both $\Delta'(r_s)$ and $(r_0 - r_s) / r_s$ are of order ε.

The above considerations refer to the reference discharge for which the rod array is designed. If other discharges are now considered, in which Δ' is varied by modifying either the plasma pressure of the internal inductance [Eqs. (10a), (10b) and (11) hereafter], then the parameter of which the variations have to be discussed is

$$\nu(r,\pi) = q(r)\left[1 + \left(\varepsilon + \Delta' + \int_a^r \frac{\Delta'}{r'} dr'\right)\right]. \tag{8}$$

One finds

$$\frac{\delta\nu(r,\pi)}{\nu(r,\pi)} = \frac{\delta q(r)}{q(r)} + \left(\delta\varepsilon + \delta\Delta' + \delta\int_a^r \frac{\Delta'}{r'} dr'\right); \tag{9a}$$

it is noted that $\delta\varepsilon = \varepsilon\left[(\delta r / r) - (\delta R_0 / R_0)\right]$ is necessarily quite small (at least of order ε^2); it thus can usually be neglected, a significant pressure scan (i.e. one corresponding to variations of order unity of the poloidal bêta) entailing a range of variations of Δ' of order ε; $\delta\int_a^r dr'\Delta' / r'$ is likewise negligible.

Integrating Eq. (2), with the requirement that Δ' be finite (actually vanishes) on the magnetic axis, yields:

$$R_0\Delta' = \frac{1}{rB_\chi^{(0)2}} \int_0^r \left(B_\chi^{(0)2} - 8\pi r' \frac{dP}{dr'}\right) r' dr' \tag{2'}$$

$$\equiv r\left(\frac{\ell_i}{2} + \langle\beta_{pol}\rangle - \beta_{pol}\right).$$

Here $$\beta_{pol} = \frac{8\pi P}{B_\chi^{(0)2}} \tag{10a}$$

is the plasma to poloidal magnetic field *local* pressure ratio,

$$\langle\beta_{pol}\rangle = \frac{16\pi \int_0^r \mathrm{P}r' dr'}{r^2 B_\chi^{(0)2}} \tag{10b}$$

is the ratio of the average kinetic pressure, within the magnetic surface of radius r, to the local poloidal magnetic pressure at r and

$$\ell_i = \frac{2\int_0^r r' dr' B_\chi^{(0)2}}{r^2 B_\chi^{(0)2}} \tag{11}$$

is the internal inductance of the toroidal current. Hence, in leading order,

$$\delta\Delta' = \frac{r}{R_0}\left(\frac{\delta\ell_i}{2} + \delta\langle\beta_{pol}\rangle\right), \tag{12}$$

assuming the ranges of $\delta\langle\beta_{pol}\rangle$ and $\delta\ell_i$ to be of order unity; we have neglected the local poloidal β. Equation (9a) then yields:

$$\frac{\delta\nu(r_s,\pi)}{\nu(r_s,\pi)}=\frac{\delta q_s}{q_s}+\frac{r_s}{R_0}\left(\frac{\delta\ell_i}{2}+\delta\langle\beta_{pol}\rangle\right) \qquad (13a)$$

Assuming that all of the plasma current flows within the magnetic surfaces of interest, one has $I(r)=I_p$, thus $\delta I=\delta I_p$, and

$$\frac{\delta q_s}{q_s}=\frac{\delta B_{\phi,0}}{B_{\phi,0}}-\frac{\delta I_p}{I_p}+2\frac{\delta r_s}{r_s}-\frac{\delta R_0}{R_0}. \qquad (13b)$$

According to the observed "profile resiliency" [3], the temperature profile and thus (if the variation of the bootstrap current is negligible) the current density profile may, to a good approximation, be considered as having a canonical form, q_a *being fixed*. Under those conditions, $\delta\ell_i=0$ if

$$q_s=q_a r_s^2/a^2 \qquad (14)$$

and hence the radius r_s of the rational surface are held fixed. The pitch $\nu(r,\pi)$ of the field lines therefore cannot be held constant on the initial surface r_s when varying the pressure. The pitch $\nu(r_s+\delta r_s,\pi)$ on the surface $q_s+\delta q_s$ can however be identical to the initial pitch $\nu(r_s,\pi)$ if

$$\frac{\delta q_s}{q_s}=2\frac{\delta r_s}{r_s}=-\frac{r_s}{R_0}\delta\langle\beta_{pol}\rangle \qquad (15)$$

If q_a is increased (decreased) in ohmic discharges, the current density profile has been observed[4] to shrink (to expand), J(r/a) being a canonical function of $q_a^{1/2}r/2^{1/2}a$. The width of the current channel is thus proportional to $q_a^{-1/2}$. Since, outside the current channel, the radius $r=r_s$ of the surface $q=q_s$ is also proportional to $q_a^{-1/2}$, it follows[5] that $\delta\ell_i(r_s)=0$. Once again, the pitch of the magnetic field line $\nu(r_s,\pi)$ cannot be preserved on the initial rational surface, i.e. with $\delta q_s=0$ and $\delta r_s=-r_s\delta q_a/2q_a$, when varying the pressure. One can however obtain $\delta\nu(r_s,\pi)=0$ on the surface $q_s+\delta q_s$ where

$$\frac{\delta q_s}{q_s}=\frac{\delta q_a}{q_a}+\frac{2\delta r_s}{r_s}=-\frac{r_s}{R_0}\delta\langle\beta_{pol}\rangle \qquad (16)$$

Owing to the experimental design, the rational surfaces $q_s=3$, $q_s=(12\pm 1)/4$, etc, have a special significance. Thus $\delta q_s=\pm 1/4$, etc, in Eqs. (15) and (16). If $\delta q_a=0$, then

$\delta r_s = r_s \delta q_s / 2q_s \equiv \pm r_s / m\hat{s}$, etc., $\hat{s}$ being the shear parameter which, in the currentless outer layer of cylindrical cross section tokamaks, is equal to 2; m = 12 is the reference poloidal mode number.

It might thus be expected that the effect of magnetic islands will be felt for discrete sets of values of $\langle \beta_{pol} \rangle$, *separated by "quantum" jumps* $\delta \langle \beta_{pol} \rangle$ *of order* $R_0 / 12 r_s \sim 1/3$.

In Appendix, analytical forms of $\langle \beta_{pol} \rangle$ and ℓ_i are given for certain families of pressure and current density profiles.

7.4 Appendix

In accordance with approximations mentioned in the text, we consider pressure and current density profiles of the form

$$P(r) = P_0\left[1 - \left(r / a^*\right)^2\right]^{\lambda} \qquad r \le a^* < r_s \qquad \text{(A-1a)}$$

$$P(r) = 0 \qquad a^* \le r, \qquad \text{(A-1b)}$$

and

$$J(r) = J_0\left[1 - \left(r / a^*\right)^2\right]^{\mu} \qquad r \le a^* < r_s \qquad \text{(A-2a)}$$

$$J(r) = 0 \qquad a^* \le r \qquad \text{(A-2b)}$$

Defining $\rho \equiv r / a^*$, it follows immediately that

$$I_p = \frac{\pi a^{*2} J_0}{\mu + 1}, \qquad \text{(A-3)}$$

$$B_\chi^{(0)} = \frac{2 I_p}{c a^*} \frac{\left[1 - \left(1 - \rho^2\right)^{\mu+1}\right]}{\rho}, \qquad \rho \le 1 \qquad \text{(A-4a)}$$

$$B_\chi^{(0)} = \frac{2 I_p}{c a^*} \frac{1}{\rho}, \qquad \text{(A-4b)}$$

$$\ell_i = \frac{\int_0^{\rho^2} \left[1 - (1 - x)^{\mu+1}\right]^2 dx / x}{\left[1 - \left(1 - \rho^2\right)^{\mu+1}\right]^2}, \qquad \rho \le 1 \qquad \text{(A-5a)}$$

$$\ell_i = \ell_i(\rho = 1) + 2\,\ell n\,\rho, \qquad \rho \geq 1 \qquad \text{(A-5b)}$$

$$\left\langle \beta_{pol} \right\rangle = \frac{2\pi a^2 \langle P \rangle}{\left(I_p / c\right)^2} \frac{1 - \left(1 - \rho^2\right)^{\lambda + 1}}{\left[1 - \left(1 - \rho^2\right)^{\mu + 1}\right]^2}, \qquad \rho \leq 1 \qquad \text{(A-6a)}$$

$$\left\langle \beta_{pol} \right\rangle = \left\langle \beta_{pol} \right\rangle (\rho = 1), \qquad \rho \geq 1 \qquad \text{(A-6b)}$$

where $\langle P \rangle = 2\int_0^a \Pr dr / a^2 = \left(a^* / a\right)^2 P_0 / (\lambda + 1)$ is the volume average pressure.

The internal inductance of the toroidal current (A-2a) can be cast in the form

$$\ell_i = \left[1 - \left(1 - \rho^2\right)^{\mu + 1}\right]^{-2} \left(\sum_{n'=0}^{\mu} - \sum_{n'=\mu+1}^{2\mu+1} \right) \frac{1 - \left(1 - \rho^2\right)^{n' + 1}}{n' + 1}, \qquad r \leq a^* \qquad \text{(A-7)}$$

for μ entire [this result follows immediately from the identity $1 - y^n = (1 - y)\sum_{n'=0}^{n-1} y^{n'}$]. Assuming μ=3, which is typical of tokamak ohmic discharges, yields $\ell_i(\rho = 1) = 1.45$. If the plasma current is 420 kA, the toroidal magnetic field B_ϕ = 2.25 Tesla and the major radius R_0 = 1.75 m, the q=3 surface has a minor radius r = r_s = 0.44 m; if the current channel is limited by the surface q = 2.5, then a^* = 0.40 m. Hence $\ell_i(r = r_s) = \ell_i(r = a^*) + 2\ell n(r_s / a^*) = 1.64$.

Assuming further $N_0 = 5 \times 10^{19}$ m^{-3}, $T_{e,0} = T_{i,0}$ = 1keV, λ = 3 ($N \propto T^{1/2} \propto J^{1/3}$) yields $\left\langle \beta_{pol} \right\rangle (\rho \geq 1) = 0.23$. $\left\langle \beta_{pol} \right\rangle$ values of order unity require larger densities and larger temperatures; in view of the high density limit, auxiliary heating is then required.

With the above data, Δ' ($r = r_s^*$) = 0.264 and Λ($r = r_s$) = -0.012, the latter result implying that the dependence of the poloidal magnetic field on the rational surface q=3 is very weak. However, if $\left\langle \beta_{pol} \right\rangle = 1$ and, as above, $\ell_i(r = r_s) = 1.64$, then $\Delta'(r = r_s) = 0.458$ and $\Lambda(r = r_s) = -0.207$.

References

[1] A. Rogister, Orthogonal Curvilinear Coordinates for a Large Aspect Ratio Tokamak with Circular Flux Surfaces, Jül-2233 (Forschungszentrum Jülich GmbH, 1988); as the centre of the LCMS is kept fixed in the experiment (when varying e.g. $\langle \beta_{pol} \rangle$), rather than the position of the magnetic axis, we have identified the arbitrary function $f^{(0)}(\chi)$ appearing in the definition of h_χ with $-\cos\chi \int_0^a dr' \Delta' / r'$.

[2] J.W. Connor, R.J. Hastie and J.B. Taylor, Phys. Rev. L,ett. 40, 396 (1978).

[3] B. Coppi, Comments Plasma Phys. Contr. Fusion 5, 261 (1980).

[4] H. Soltwisch, W. Stodiek, J. Manickam, J. Schlüter in *Plasma Physics and Controlled Nuclear Fusion Research 1986*, (IAEA, Vienna, 1987) Vol. 1, p. 263.

[5] H.P. Furth, Plasma Phys. Control. Fusion 28, 1305 (1986) and C.Z. Cheng, H.P. Furth, A.H. Boozer, Plasma Phys. Control. Fusion 29, 351 (1987) have argued that as q_a is raised above 2, the tearing Δ'-stable solution with the highest inductance remains identical to the stable J(r) profile obtained for $q_a = 2$, but scaled down in radial extent in proportion to $(2/q_a)^{1/2}$.

8. Penetration of the Rotating Magnetic Field into the Plasma

D. Faulconer, R. Koch,

Laboratoire de Physique des Plasmas-Laboratorium voor Plasmafysica, Ecole Royale Militaire-Koninklijke Militaire School, Bruxelles-Brussel, Belgium, Association EURATOM-Belgian State

8.1. Introduction

For present purposes the TEXTOR dynamic ergodic coil array can be viewed as a toroidally extended multipole antenna on the inboard side of the tokamak, the conductors of which lie on a given magnetic surface and run almost parallel to the magnetic field thereon (coil and field helicities match exactly in the outer plasma on the q=3 surface (q is safety factor)). Standard phasing of the currents in the individual conductors presents a predominantly m=12, n=4 current excitation to the plasma (~exp(-iωt); m,n are poloidal, toroidal mode numbers, respectively).

Under normal TEXTOR running conditions Ohmic current $\mathbf{I_0}$ is antiparallel to $\mathbf{B_0}$; viewing the poloidal section with inboard side to the left, both $\mathbf{I_0}$ and the j (toroidal) direction are taken to point out of the page giving for the component of the wave vector parallel to $\mathbf{B_0}$.

$$k_{//} = \frac{m - nq}{Rq\left(1 + \left(\frac{r}{Rq}\right)^2\right)^{\frac{1}{2}}} \qquad (1.1)$$

The wave **k**'s are calculated on the inboard equatorial plane in slab approximation. We shall adopt the following conventions: the minor radius direction is *r*, the toroidal direction *z* and the poloidal one *y*, forming the reference frame (*r*,*y*,*z*). We shall consider a second reference frame (x, y_T, $z_{//}$) with $z_{//}$ the direction of $\mathbf{B_0}$, $x=-r$ and y_T the direction transverse to $\mathbf{B_0}$ lying in the magnetic surface; for $q=\infty$, (x, y_T, $z_{//}$) = ($-r$,$-y$,z). In these coordinates an arbitrary vector **w** is written (w_x, w_T, $w_{//}$). We shall first work in the system (x, y_T, $z_{//}$) linked to the magnetic field. The transverse component of the wavevector is:

$$k_T = \frac{m - \frac{n}{q}\left(\frac{r}{R}\right)^2}{r\left(1+\left(\frac{r}{Rq}\right)^2\right)^{\frac{1}{2}}} \qquad (1.2)$$

and k_X is to be determined from the dispersion relation. Here

$$q = \frac{q(0)(r/r_0)^2(\alpha_j+1)}{1-\left(1-(r/r_0)^2\right)^{(\alpha_j+1)}} \qquad (1.3)$$

Imposing $q(0)=1$, $q(.42)=3$, and plasma radius $r_0=.46$ (mks units), one has $a_j=2.6$; the wave properties are evaluated at the plasma edge ($r=.46$) giving from the above formulae ($R_o=1.75$, $R=1.29$) $q(.46)=3.6$, $k_T=26$, $k_{//}=-.51$. For the calculations a value $B_o=3.4$T was taken, corresponding to $B_o=2.5$T on-axis, with $n_e=5.\ 10^{18}\mathrm{m}^{-3}$ as edge density for a deuterium plasma and $T_e=T_i=100$ eV.

8.2 Wave propagation at low frequency

In order to investigate the penetration of the field created by the coils, we shall first determine which are the waves that can propagate inside the plasma. To do so, we adopt a WKB point of view where the field is assumed to vary as exp [i(**kx**-ωt)] and examine the plasma dispersion relation in two limits: an augmented version of a cold collisional plasma and a warm collisional plasma.

The waves in the plasma are described by Maxwell's equations (in the WKB limit ∇=i**k**) :

$$\nabla\times\mathbf{H} = \mathbf{j}_p - i\omega\varepsilon_0\mathbf{E} \qquad (2.1)$$

$$\nabla\times\mathbf{E} = i\omega\mathbf{B} \quad , \quad \mathbf{B} = \mu_0\mathbf{H} \qquad (2.2)$$

where $\mathbf{j}_p$ is the particle current described by a conductivity tensor $\overline{\overline{\sigma}}$

$$\mathbf{j}_p = \overline{\overline{\sigma}}\,\mathbf{E} \qquad (2.3)$$

and Eqs.(2.1-2.3) can be recast in terms of the dielectric tensor $\overline{\overline{\varepsilon}}$:

$$\bar{\bar{\varepsilon}} = \mathbf{I} + i\bar{\bar{\sigma}} / \omega\varepsilon_0 \qquad (2.4)$$

$$\nabla \times \nabla \times \mathbf{E} = \frac{\omega^2}{c^2} \bar{\bar{\varepsilon}}\, \mathbf{E} \qquad (2.5)$$

Plasma wave descriptions differ by the choice of approximations leading to different expressions of the dielectric tensor. In the cold plasma limit,

$$\frac{\partial \bar{\bar{\varepsilon}}}{\partial \mathbf{k}} = 0$$

and the system allows two propagation modes : (1) the compressional Alfvén wave or fast wave or magnetosonic wave, that we shall refer to as the fast wave (FW) and (2) the shear Alfvén wave that we shall refer to as the shear wave (SW).

In the warm plasma approximation, finite ion gyroradius corrections are kept up to first order in temperature $[0(k_\perp^2 r_{Li}^2)]$ while a full kinetic description is kept in the parallel direction, involving the Fried & Conte dispersion function. In this warm plasma description there exists an additional (kinetic wave) solution.

8.2.1 Augmented cold, collisional dispersion relation

Our point of departure is the cold, collisional, linearized momentum equation for the α-th particle species in absence of zero order particle drifts

$$m_\alpha \frac{\partial \mathbf{v}_\alpha}{\partial t} = q\left(\mathbf{E} + \mathbf{v}_\alpha \times \mathbf{B}_0\right) - m_\alpha \nu_\alpha \mathbf{v}_\alpha \qquad (2.6)$$

$\nu_i=(m_e/m_i)\nu_e$ is used for ion collision frequency with ν_e put equal to 10^5 Hz for the edge conditions above. With dependence ~exp[i(**k**·**r**-ωt)],

$$\mathbf{v}_\alpha = \begin{bmatrix} \frac{i(\omega+i\nu_\alpha)}{(\omega+i\nu_\alpha)^2-\omega_{c\alpha}^2} & \frac{-\omega_{c\alpha}}{(\omega+i\nu_\alpha)^2-\omega_{c\alpha}^2} & 0 \\ \frac{\omega_{c\alpha}}{(\omega+i\nu_\alpha)^2-\omega_{c\alpha}^2} & \frac{i(\omega+i\nu_\alpha)}{(\omega+i\nu_\alpha)^2-\omega_{c\alpha}^2} & 0 \\ 0 & 0 & \frac{i}{\omega+i\nu_\alpha} \end{bmatrix} \frac{q_\alpha \mathbf{E}_\alpha}{m_\alpha} \qquad (2.7)$$

whence the vector of complex oscillation amplitudes, $\Delta \mathbf{r}_a = \mathbf{v}_a/(-iw)$ and the conductivity tensor $\mathbf{j} = \sum_\alpha n_\alpha q_\alpha \mathbf{v}_\alpha = \overline{\overline{\sigma}} \cdot \mathbf{E}$. The case of a rotating plasma can be dealt with via replacement of ω by its Doppler-shifted value $\omega - k_z v_{0z}$.

For $\alpha = e$ the denominator of the 3,3 element of the above tensor is modified to $\omega + i\nu_e - k_{//}^2 k_B T_e / m_e w \omega$ in order to account for the effect of parallel electron pressure. Solubility of the wave equation $\mathbf{k} \times (\mathbf{k} \times \mathbf{E}) + k_o^2 \overline{\overline{\varepsilon}} . \mathbf{E} = 0$ requires the following dispersion relation be satisfied ($k_\perp^2 = k_x^2 + k_T^2$)

$$a_T k_\perp^4 - \left[\left(\frac{\varepsilon_1^2 - \varepsilon_2^2}{\varepsilon_1} + \varepsilon_3\right)k_o^2 - k_{//}^2\left(\frac{\varepsilon_3}{\varepsilon_1} + 1\right)\right]k_\perp^2 + \varepsilon_3\left(k_o^4 \frac{\varepsilon_1^2 - \varepsilon_2^2}{\varepsilon_1} + \frac{k_{//}^4}{\varepsilon_1} - 2k_o^2 k_{//}^2\right) = 0 \qquad (2.8.1)$$

where a second (finite ion Larmor radius) thermal correction,

$$a_T = 1 + (k_o^2 \varepsilon_3 k_B T_i / \varepsilon_1 m_i \omega_{ci}^2)\omega_{pi}^2 [1/(\omega_{ci}^2 - \omega^2) - 1/(4\omega_{ci}^2 - \omega^2)] \qquad (2.8.2)$$

has been included to render the shear Alfvén wave "kinetic"; $\varepsilon_{11} = \varepsilon_{22} \equiv \varepsilon_1$, $\varepsilon_{12} = -\varepsilon_{21} \equiv i\,\varepsilon_2$, $\varepsilon_{33} \equiv \varepsilon_3$ have been used.

In order to determine accessibility of the coil fields to the q=3 surface, scans of $k_x = \sqrt{(k_\perp^2 - k_T^2)}$ were made for frequencies extending to 10^7 Hz, the expanded upper limit allowing contact to be made with the familiar ICRH range. For the plasma parameters noted in Section 1, values for both waves are plotted simultaneously on Fig.1, a given plot showing either the real or the imaginary parts of the two k_x's (only the roots with positive $\mathrm{Im}\{k_x\}$ are retained); note that the plotted function is shown as zero when its absolute value becomes less than 1, with use of logarithmic (base 10) scales outside this region. The compressional wave shows vacuum dispersion, $k_x = \sqrt{(k_A^2 - k_T^2 - k_{//}^2)} \approx i k_T$ ($k_A = \omega / v_A$, v_A=Alfvén velocity), giving reasonably good penetration across the 4 cm between the plasma edge and the q=3 surface (recall k_x in mks units). To the contrary, the shear wave wavenumber has prohibitively large imaginary part over all but the upper end of the region relevant to the dynamic limiter, around 10^4 Hz. In fact k_x becomes large enough to invalidate our neglect of finite Larmor radius effects.

It is striking that the exclusion of the shear field becomes more complete as the frequency drops, in contrast to the classical skin depth behavior. In view of the large $k_\perp$ values in question, one can derive an approximate dispersion relation for this wave by balancing the quartic and quadratic terms in the full dispersion and using $|\varepsilon_3| >> |\varepsilon_2|, |\varepsilon_1|$

$$k^2_{\perp shear} \approx \frac{\varepsilon_3}{a_T\varepsilon_1}\left(k_o^2\varepsilon_1 - k_{//}^2\right) \qquad (2.9)$$

Let us see in what sense this formula contains the classical behavior. Taking T_i low enough to have $a_T \approx 1$ and assuming $k_o^2|\varepsilon_1| >> k_{//}^2$ (i.e. $\omega^2 >> k_{//}^2 v_A$ if $\omega^2 << \omega_{ci}^2$), one has $k_\perp^2 \approx k_o^2\varepsilon_3 \approx k_o^2(\varepsilon_3 - 1) = k_o^2 i\sigma_{33}/\omega\varepsilon_o = i\mu_o\omega\sigma_{33}$; further assuming k_T small such that $k_x \approx k_\perp$ gives for the skin depth of the shear Alfvén wave

$$\delta_{shear} = \frac{1}{\mathrm{Im}\{k_{xshear}\}} = \frac{1}{\mathrm{Im}\{\sqrt{i\mu_o\omega\sigma_{33}}\}} = \sqrt{\frac{2}{\mu_o\omega\sigma_{33}}} \qquad (2.10)$$

where we have neglected $k_{//}^2 k_B T_e/m_e\omega$ in $\sigma_{33} = \omega_{pe}^2\varepsilon_o/(-i\omega + \nu_e + ik_{//}^2 k_B T_e/m_e\omega)$ and taken $\nu_e >> \omega$ to find σ_{33} real. Thus for small enough $k_{//}$ the classical behavior of increasing penetration with decreasing ω is recovered. However, over the relevant range, $f \leq 10^4$, $k_{//}$ is far greater than such values and $\omega^2 << k_{//}^2 v_A^2$.

8.2.2 Warm collisional plasma

The warm collisional plasma dispersion relation is obtained by truncating the general dielectric tensor expression of Stix [1992] to first order in $(k_\perp^2 r_{Li}^2)$. The explicit developments are given in [Bhatnagar et al. (1983)]. In addition, electron-ion collisions are introduced via the simple collision term $(\frac{\partial f}{\partial t}) = -\upsilon f$ in Vlasov's equation, using the expressions for slow ions and fast electrons given in the NRL plasma formulary. The essential modification is that ω is replaced by $\omega + i\upsilon$ in the Z dispersion function, as defined in [Descamps et al. 1991] (plus in certain other places in the dielectric tensor). These elements are implemented in the dispersion code HOTRUF.

Cases were run for the same parameters as in Section 2.1. The results are given in Fig.2. There are problems of numerical stability at frequencies below 10 Hz. The two non-FW roots are of the same order of magnitude, namely that of $k_\perp \approx r_{Li}^{-1}$. This means that both of these roots are strongly affected by temperature corrections and have values that lie outside the validity range of warm plasma theory. By exclusion this implies that there exists no root with low $|k_\perp| << r_{Li}^{-1}$ other than the FW.

Including the results of Section 2.1 in the picture, the conclusion is that only the FW will transmit long wavelength ($\lambda >> r_{Li}$) magnetic structure and that the additional wave(s) that may exist in the plasma : (1) are most probably strongly damped or evanescent with e-folding length $\approx r_{Li}$ and (2) have a dispersion that is strongly dependent on the details of the plasma model. In conclusion, the magnetic perturbation will be transmitted by the FW that has the vacuum dispersion and the other polarisations will be blocked at the plasma surface ($E_{//} = 0$).

8.3 Polarisation : the low frequency limit of the FW

It is well known that the FW equations can be obtained by taking the zero electron mass limit in the dielectric tensor. This amounts to taking $\varepsilon_3 \to \infty$ which in turn implies $E_z \to 0$. The FW equations are then usually written in terms of E_y and B_z (see e.g.[Koch, 1986]). However, in the dynamic ergodic divertor (DED) problem, considering electric fields is not very illuminating because at low frequency the current excitation of the DED coils generates nearly no electric field. In this respect, one can anticipate that in the low frequency limit, the E_z=0 condition won't affect anything other than the electrostatic component of the field, not present here as there is no excitation charge. We thus shall express the FW equation in terms of the magnetic field using Eq.(2.1):

$$\mathbf{E} = -\frac{c^2}{\omega} \bar{\bar{\varepsilon}}^{-1} (\mathbf{k} \times \mathbf{B}) \tag{3.1}$$

Using this in Eq. (2.2) gives

$$k_0^2 \mathbf{B} = -\mathbf{k} \times [\bar{\bar{\varepsilon}}^{-1} (\mathbf{k} \times \mathbf{B})] \tag{3.2}$$

The FW equations are obtained by taking the limit $\varepsilon_3 \to \infty$. We also take the low frequency limit

$\varepsilon_2=0,\ \varepsilon_1=i\sigma_1/\omega\varepsilon_0 \approx \frac{\omega_{Pi}^2}{\omega_{ci}^2}$

$$k_0^2\varepsilon_1\mathbf{B} = k_z^2\begin{pmatrix}B_x\\B_y\\0\end{pmatrix} - k_zB_z\begin{pmatrix}k_x\\k_y\\0\end{pmatrix} + \begin{pmatrix}0\\0\\k^2B_z\end{pmatrix} \tag{3.3}$$

or, separating components

$$\left(k_z^2 - \frac{\omega^2}{V_A^2}\right)\begin{pmatrix}B_x\\B_y\end{pmatrix} = \begin{pmatrix}k_x\\k_y\end{pmatrix}k_zB_z \tag{3.4}$$

$$(k^2 - \frac{\omega^2}{V_A^2})B_z = 0 \tag{3.5}$$

At low frequency (i.e. for $\omega/k_z << V_A$), these yield respectively

$$\mathbf{B} = \mathbf{k}\frac{B_z}{k_z} \tag{3.6}$$

$$k^2\, B_z=0 \Rightarrow k^2=0. \tag{3.7}$$

These equations are equivalent to the magnetostatic field equations :

$$\mathbf{k}\times\mathbf{B}=\mathbf{0}$$

$$\mathbf{k}.\mathbf{B}=0$$

The first relation implies Eq.(3.6) and subsequently the second one implies Eq.(3.7)

Conclusion: At low frequency the FW equations are identical to the magnetostatic field equations.

Corollary: The E_z=0 condition on the FW should not affect the magnetic field penetration.

The condition for the FW equations to reduce to the vacuum magnetostatic field equations is

$\frac{\omega}{|k_z|} << V_A$, i.e. (for $\omega_{pi} \gg \omega_{ci}$)

$$|k_z| >> k_0\frac{\omega_{pi}}{\omega_{ci}} \tag{3.8}$$

Under the edge conditions defined in Section 1, this amounts to

$$|k_z| >> 13k_0 \approx 2.7\,10^{-3}m^{-1} \quad \text{(at 10 kHz)} \tag{3.9}$$

Note : Eq.(3.6) shows that the limit where the current is purely parallel (=>B_z=0, k_z=0) is singular. Examination of the coupling problem will shed more light on this.

8.4 Field coupled by a wire current to an infinite plasma slab.

In this section, we compute explicitly the magnetic field induced by the current flowing on an infinitely thin wire placed in front of the plasma at an arbitary angle α to the *z*-direction see Fig. 4.1. The geometry is that of Fig.4.2 and the space is assumed infinite in the *y* and *z* directions. Note that we place the origin of the *r* coordinate at the conductor location. In this infinite space case, the angle between $\mathbf{B}_0$ and the toroidal direction is irrelevant, so we take $\mathbf{B}_0 = B_0 1_z$. Note that the direction of $\mathbf{B}_0$ is independent of *r* so that the theory investigates coupling to a plasma with a constant *q*. The effects of the variation of *q* will be discussed in Sections 5 and 6.

8.4.1 Wire current spectrum

We consider a current I = 1 A on a filamentary wire at an angle α to the $\mathbf{B}_0$ direction :

$$\mathbf{J} = \begin{pmatrix} 0 \\ \operatorname{tg}\alpha \\ 1 \end{pmatrix} \delta(y - z\operatorname{tg}\alpha)\delta(r) \equiv \begin{pmatrix} 0 \\ \operatorname{tg}\alpha \\ 1 \end{pmatrix} J(y,z)\delta(r) \tag{4.1}$$

The current spectrum follows from

$$J(k_y,k_z) = \int_{-\infty}^{\infty} e^{-ik_y y - ik_z z}\delta(y - z\operatorname{tg}\alpha)\,dydz = \delta(k_z + k_y\operatorname{tg}\alpha) \tag{4.2}$$

We define the components of **k** along (subscript *l*) and perpendicular to (subscript *p*) the direction of the current:

$$k_l = k_z\cos\alpha + k_y\sin\alpha,\quad k_p = k_y\cos\alpha - k_z\sin\alpha \tag{4.4}$$

The current spectrum can be rewritten

$$J(k_y, k_z) = \delta(k_l/\cos\alpha) \tag{4.5}$$

8.4.2 Coupling theory

We compute the coupling in the slab geometry shown in fig.4.2. We use the formalism of [Koch et al, 1986] where all field components can be derived from B_z (TE part of the field) and E_z (TM part). It is assumed that only the FW exists inside the plasma and that E_z=0 everywhere in the homogeneous plasma, and in particular at its surface.

$$B_z = \mu_0 \dot{D}(r,0) j_y, \quad j_y = \delta(k_l / \cos\alpha)\,\mathrm{tg}\,\alpha \tag{4.6}$$

with $$\dot{D}(r,0) = \frac{p\,\mathrm{ch}[p(r+a)] + i\xi_1 H^2\,\mathrm{sh}[p(r+a)]}{p\,\mathrm{sh}[p(a+d)] + i\xi_1 H^2\,\mathrm{ch}[p(a+d)]}\mathrm{sh}(pd) \quad \text{for } -a<r<0 \tag{4.7.1}$$

$$H^2 = k_0^2 - k_z^2,\ p^2 = k_y^2 + k_z^2 - k_0^2,\ k_0 = \omega / c \tag{4.7.2}$$

and ξ_1 is proportional to the surface impedance of the plasma :

$$\xi_1 = \left[\frac{E_y}{\omega B_z}\right]_{x=-a} \tag{4.7.3}$$

This TE part of the field couples to the FW inside the plasma. The TM part follows from

$$E_z = \frac{1}{\omega\varepsilon_0} S(r,0)\,(ik_z k_y j_y - iH^2 j_z) \tag{4.8}$$

with $$S(r,0) = -\frac{\mathrm{sh}[p(r+a)]\,\mathrm{sh}(pd)}{p\,\mathrm{sh}[p(a+d)]} \quad \text{for } -a<r<0 \tag{4.9}$$

and $$k_z k_y j_y - H^2 j_z = (\frac{k_z}{\cos\alpha} k_l - k_0^2)\,\delta(k_l / \cos\alpha) = -k_0^2 \delta(k_l / \cos\alpha) \tag{4.10}$$

This implies that $E_z \propto \omega$. The TM part of the field is blocked by the infinite parallel conductivity of the plasma $E_z(r=-a) = 0$.

The other magnetic field components are given by

$$B_r = \frac{1}{H^2}[\frac{\omega k_y}{c^2} E_z + ik_z \frac{dB_z}{dr}] \tag{4.11}$$

$$B_y = \frac{1}{H^2}[-k_z k_y B_z + \frac{i\omega}{c^2}\frac{dE_z}{dr}] \tag{4.12}$$

8.4.3 Surface impedance of the FW at low frequency

As we have seen, at low frequency the FW becomes the vacuum wave. Taking $\omega \to 0$, $\varepsilon_2 \to 0$, we obtain for the $k_\perp$ of the FW

$$k_\perp^2 = k_0^2 \varepsilon_1 - k_z^2 \rightarrow -k_z^2$$

Recalling that the FW equations have constant coefficients, we thus obtain an analytic expression for ξ_1 :

$$\xi_1 = -\frac{\sqrt{k_\perp^2 - k_y^2}}{k_\perp^2} \rightarrow \frac{ip}{k_z^2} \tag{4.13}$$

which is the same value as for vacuum, and hence there is no reflection at the plasma surface.

Because ξ_1 takes the same value as for vacuum, the expression of B_z is the same as for coupling to vacuum :

$$B_z = \mu_0 \; e^{p(r-d)} \, \mathrm{sh}(pd) \, \delta(k_l / \cos\alpha) \, \mathrm{tg}\alpha \qquad \text{for } -a<r<0 \tag{4.14}$$

We now compute the other **B**-field components from Eqs.(4.11) and (4.12). We first note that the TM contributions ($\propto E_z$) to these fields all decay like ω^2 at low frequency and can thus be neglected in this limit. Accordingly, in the region $-a<r<0$

$$B_r = \frac{ik_z^2}{H^2} \frac{B_z}{\sin\alpha} \tag{4.15}$$

$$B_y = \frac{k_z^2}{H^2} \frac{B_z}{\mathrm{tg}\alpha} \tag{4.16}$$

$$B_l = B_y \sin\alpha + B_z \cos\alpha = \frac{k_0^2 B_z}{H^2} \cos\alpha \tag{4.17}$$

where we have used $k_z=-k_y$ tg a which follows from Eq.(4.2). The magnetostatic components of the field created by the wire in vacuum are obtained by taking $k_0 \rightarrow 0$ i.e. $H^2 \rightarrow -k_z^2$ and are

$$B_r = -iB_z / \sin\alpha \tag{4.18}$$

$$B_y = -B_z / \mathrm{tg}\alpha \tag{4.19}$$

$$B_l = 0 \tag{4.20}$$

Thus, we conclude that the magnetic field generated by the wire in the region $-a<r<0$ is identical to the magnetostatic field generated by the wire in vacuum as long as: (1)

$k_0^2 << k_z^2$ such that Eqs.(4.15)-(4.17) become identical to the vacuum equations (4.18)-(4.20) and (2) the FW equations reduce to the magnetostatic equations for vacuum. Note that this latter condition ($|k_z| > 13\ k_0$) enforces the former ($|k_z|>k_0$). Under these conditions, the facts that (1) the field in $-a<r<0$ is identical to that for vacuum and (2) the FW equations reduce to the vacuum field equations, imply that the field in presence of plasma is everywhere identical to that in vacuum. The stronger of the conditions for being in the vacuum limit is Eq.(3.9) which is equivalent to saying that the region $|k_z|<13k_0$ should contain only a small part of the current spectrum. The corrections to the vacuum field components due to finite frequency are small in proportion to ω^2.

When the angle $\alpha \to 0$, Eqs.(4.14)-(4.16) show that $B_z \to 0$ but that B_r and B_y remain finite. However, at the same time the current spectrum Eq. (4.2) tends to $\delta(k_z)$ which selects only $k_z=0$ in violation of the condition $|k_z|>>13k_0$. This implies that there is a limit to the smallness of the angles α for which the field is as in vacuum. Again employing Eq. (4.2) one has that $k_z=-k_y \operatorname{tg}\alpha$ should be much larger in magnitude than $13k_0$. Considering now the array of DED conductors, we have noted that $k_y \approx 26\text{m}^{-1}$. Thus we get the condition

$$\operatorname{tg}\alpha > \frac{13k_0}{26} \approx 10^{-4} \text{ for } f=10\text{kHz} \tag{4.21}$$

The angle given by Eq.(4.21) is extremely small so that, in the framework of this theory, we conclude that the magnetic field induced by the DED conductors will be identical to that induced in vacuum.

8.5. Field coupled by a ribbon current to a periodic slab

Although it will not alter significantly the conclusions reached in the previous section, the quantization of k-space resulting from the doubly periodic nature of a torus adds a number of subtleties to the computation of the coupling. We shall now assume that space is periodic in z (period $2\pi R$=8.1m) and y (period $2\pi r_0$=2.89m), so that $k_z=n/R$ and $k_y=m/r_0$. Due to the periodic nature of space, it is no longer possible to consider a single current of infinite length like Eq.(4.1), because it is not periodic. We thus have to consider a current of finite length and the associated feeders. Although the latter can be ignored in a purely magnetostatic computation, they cannot be ignored in electromagnetic computations [Koch 1986]. We shall consider a conductor that also has a finite width w=2.8cm, located at a distance of d=1.5cm from the conducting back wall and of a=2cm from the plasma (see Fig.4.2.). Its thickness is zero.

As the coupling code BRACC [Descamps et al., 1991] is available we have used it to check the correctness of the theory of Sect.4. BRACC was originally designed to compute the coupling of ICRH antennas to the FW. It assumes $q=\infty$ and the parallel plasma conductivity to be infinite (E_z=0 everywhere in the plasma). It was modified to allow considering antennas making an arbitrary angle α with the z direction (instead of purely poloidal). We consider an antenna centered at $y=z=0$. In order to allow it to be rotated by 90° without hitting the boundaries of the periodic space we have taken a length l=2.88m. Unfortunately, the code being designed to compute the field *radiated* by the FW inside the plasma, the number of poloidal and toroidal modes is rather limited ($|n|<400$, $|m|<50$). We examine the behaviour of the B_y, B_z field components on a magnetic surface inside the plasma (r=cst) in a region near the antenna center (so that the finite antenna length plays no role). It was first checked that, as follows from Section 3, the plasma density plays a negligible role in the problem, i.e., taking $n_e=5\ 10^{18}\ \mathrm{m}^{-3}$ at the edge gives the same result as taking n_e=0. Second it was checked that the magnetic field in the plasma has the same structure as that of the vacuum field surrounding a conductor and rotates with the conductor. Figure 4.3 shows the distribution of the magnetic field components for the case where the conductor is rotated by α=5°. This field distribution is as expected. Fig 4.4 shows the variation of the y and z components of $\mathbf{B}$ at $y=z=0$ at the plasma surface (r = -2.01 cm) and inside the plasma (r = -2.5 cm). The relation between the two reflects the $1/|r|$ dependence of the field. As the angle α is decreased from 90° to 0° the B_z component behaves approximately as $\sin\alpha$ and the B_y component as $\cos\alpha$ as should be for the vacuum magnetostatic field. The progressive drop of the modulus $(B_y^2+B_z^2)^{1/2}$ as α is decreased from 90° to 0° is due to the fact that the poloidal representation is poorer than the toroidal one (the maximum k_y is 109m^{-1} for which $k_y\, w/2=1.52<\pi$). On the contrary, the strong drop in the B_y magnitude near α=0 is a genuine effect reflecting the fact that only the FW field is coupled and not the total vacuum field. In particular, if for α=0 one takes an antenna that is exactly $2\pi R$ long, one will obtain B_y=0 because in such a case the k_z spectrum is reduced to the k_z=0 contribution, a part of the spectrum that one anticipates to be strongly reflected. One should further note in Fig.4.4 that the strong drop in magnitude near α=0 sets in at angles $\alpha\approx2°$ much larger than the limit angle given by Eq.(4.21).

This behaviour is explained by a more detailed analysis of the coupling model in the periodic case (to be published). The drop in field magnitude near α=0 results from the partial or complete reflection of the Fourier components with $|k_{//}|<13k_0$. In BRACC, the effect is strongly magnified by the hypothesis $q=\infty$. For a realistic value q=3.6, the field reduction when the current is aligned with the magnetic field is by less than 2% and the width of the reduction zone is ±1°. The "more irrational" q is the less the reduction. For q=3, the reduction is by 18%. The width of the reduction zone is larger for smaller r_0, R.

The strongest reflections discussed above are a result of assuming q to be *constant and rational* over the plasma edge region. This is a highly contrived idealization unsuited to studying wave access to a *localized internal* rational surface, since it leads to the $k_{//}$=0 rational surface condition, when satisfied, existing simultaneously in r throughout the whole plasma edge region of interest (as with $q=\infty$). We thus relax the assumption of a flat q profile and examine the variation of $k_{//}$ about the rational surface of a dominant mode of excitation. Imposing the condition for reflection after expansion of $k_{//}$ about the rational surface at r_1.

$$|k_{//}| = \left| -\frac{n}{R} + \frac{m}{qR} \right| = \frac{1}{R} \left| -n + \frac{m}{q(r_1)} - \frac{m}{q^2(r_1)} q'(r_1)\Delta r \right| < 13k_0 \tag{5.1}$$

or using $q(r_1)=m/n$:

$$|\Delta r| < \left| \frac{m}{n^2} \frac{13k_0R}{q'(r_1)} \right| \tag{5.2}$$

or equivalently :

$$|\Delta q| < \left| \frac{m}{n^2} 13k_0R \right| \tag{5.3}$$

Thus one has absence of reflection to within Δr (Δq) of the rational surface (q value). For TEXTOR, using m=12, n=4, $|\Delta r|$ is seen to be orders of magnitude below the distance between the edge and the q=3 rational surface, showing good penetration.

8.6. Coupling to the singular layer

In the preceding sections, we have adopted the point of view of " high frequency-short wavelength waves ", where all relevant propagation modes are examined but where the corrections due to gradients of the equilibrium quantities are neglected. This analysis has led to the conclusion that the coupling is essentially that of the magnetostatic vacuum field. However, nonuniformity of equilibrium quantities introduces an important modification (cf Eq.(6.3) below).

The standard theory of tearing modes gives in the ideal MHD limit the equation [Goldston & Rutherford Eq (20.14)] which we rewrite

$$\frac{\partial}{\partial r}\left[\rho_0\mu_0(\omega^2-k_{//}^2V_A^2)\frac{\partial u_r}{\partial r}\right]-k^2\rho_0\mu_0(\omega^2-k_{//}^2V_A^2)u_r=0 \tag{6.1}$$

with ρ_0 the mass density and $\bar{k}=k\overline{e_y}$. To make the connection with previous theory let us first consider the uniform plasma limit. In this case, we can factorise Eq.(6.1) as follows:

$$(\omega^2-k_{//}^2V_A^2)\left[\frac{\partial^2}{\partial r^2}-k^2\right]u_r=0 \tag{6.2}$$

The first factor is the degenerate form of the shear wave equation [obtained by taking the limit of $\varepsilon_3\to\infty$ in Eq.(2.9), which implies $k_0^2\varepsilon_1-k_{//}^2\approx\omega^2/V_A^2-k_{//}^2=0$] while the second factor is the FW equation. This identification reflects the fact that the zero electron mass limit was taken in deriving the MHD equation (6.1).

Taking the low frequency limit, replacing $u_r=-\omega B_r/(kB_{y0})$ and using $k_{//}=k_yB_{y0}/B_{z0}$, Eq.(6.1) can be rewritten in a form given by [Wesson, 1981]:

$$\frac{d^2B_r}{dr^2}-k^2B_r=\frac{\mathbf{k}.\mathbf{B}_0''}{\mathbf{k}.\mathbf{B}_0}B_r \tag{6.3}$$

(The prime denotes d/dr)

We thus recover the well-known result that there exists a singular layer in the plasma where $k_{//}=0$. In passing, note that this condition is none other than the Alfvén resonance condition $\omega=k_{//}V_A$ for low frequency. However, in the present case, the singular layer only exists if

$B_0'' \propto j_{0z}' \neq 0$. Otherwise there is no singularity. In the near vicinity of the layer where $k_{//}=0$, the validity of ideal MHD breaks down and Eq.(6.3) must be replaced by other equations taking finite resistivity into account. The region where finite resistivity plays a role is known as the " resistive layer " and its thickness is

$$\delta = \frac{(\gamma\eta\rho_0)^{1/4}}{(k_0 B_0')^{1/2}}$$

where γ is the growth rate of the tearing mode and η the resistivity. A clear exposé of the theory can be found in [Goldston & Rutherford 1995].

8.7. Experimental verification and acknowledgements

Experiments have been performed on PISCES to investigate field penetration. A filamentary excitation was inserted inside the plasma. Measurements of the external field with and without plasma gave identical results up to 1kHz. Technical problems prevented meaningful measurements at higher frequency. We wish to thank Dr. R. Doerner and Prof. R.W. Conn from UCSD for their help in making these measurements.

8.8. Conclusion

In conclusion this analysis has shown that the field of the DED coils is expected to penetrate the plasma in the same manner as the vacuum magnetostatic field generated by the coils, up to the resistive layer defined by $k_{//}=\mathbf{k}.\mathbf{B}_0=0$. This conclusion is valid for all frequencies considered ($f \leq 10$kHz). We have investigated only what is known as the " outer " problem in tearing mode theory. The computation of the interaction with the singular layer has been done in previous work [Lazzaro & Nave, 1988 and others] where the outer solution and the coupling to the exciting current use the equivalent of Eq.(6.3).

References

Bhatnagar V.P., Koch R., P. Geilfus, Kirkpatrick R., Weynants R.R., *A ray-tracing modeling of the JET ICRF heating*, LPP-ERM/KMS Brussels Report n^o 81, (1983).

Descamps P., et al., *Global Modes Excitation in TEXTOR and Comparison with Theory*, Plasma Physics and Controlled Fusion **33**(1991)1109.

Goldston R.J., Rutherford P.H., *Introduction to Plasma Physics*, IOP, Bristol (1995).

Koch R., Bhatnagar V.P., Messiaen A.M., Van Eester D., *A global solution of the ICRH problem based on the combined use of a planar coupling model and hot-plasma ray-tracing in tokamak geometry*, Computer Physics Communications, **40**(1986)1.

Lazzaro E., Nave F.F., *Feedback Control of Rotating Resistive Modes*, Physics of Fluids **31**(1988)1623-1629.

Stix T.H., *Waves in Plasmas*, AIP, New York, (1992).

Wesson J.A., Plasma Physics & Nucl. Fus Research, Ed. R.D. Gill, Academic Press N.Y.(1981) 216-229.

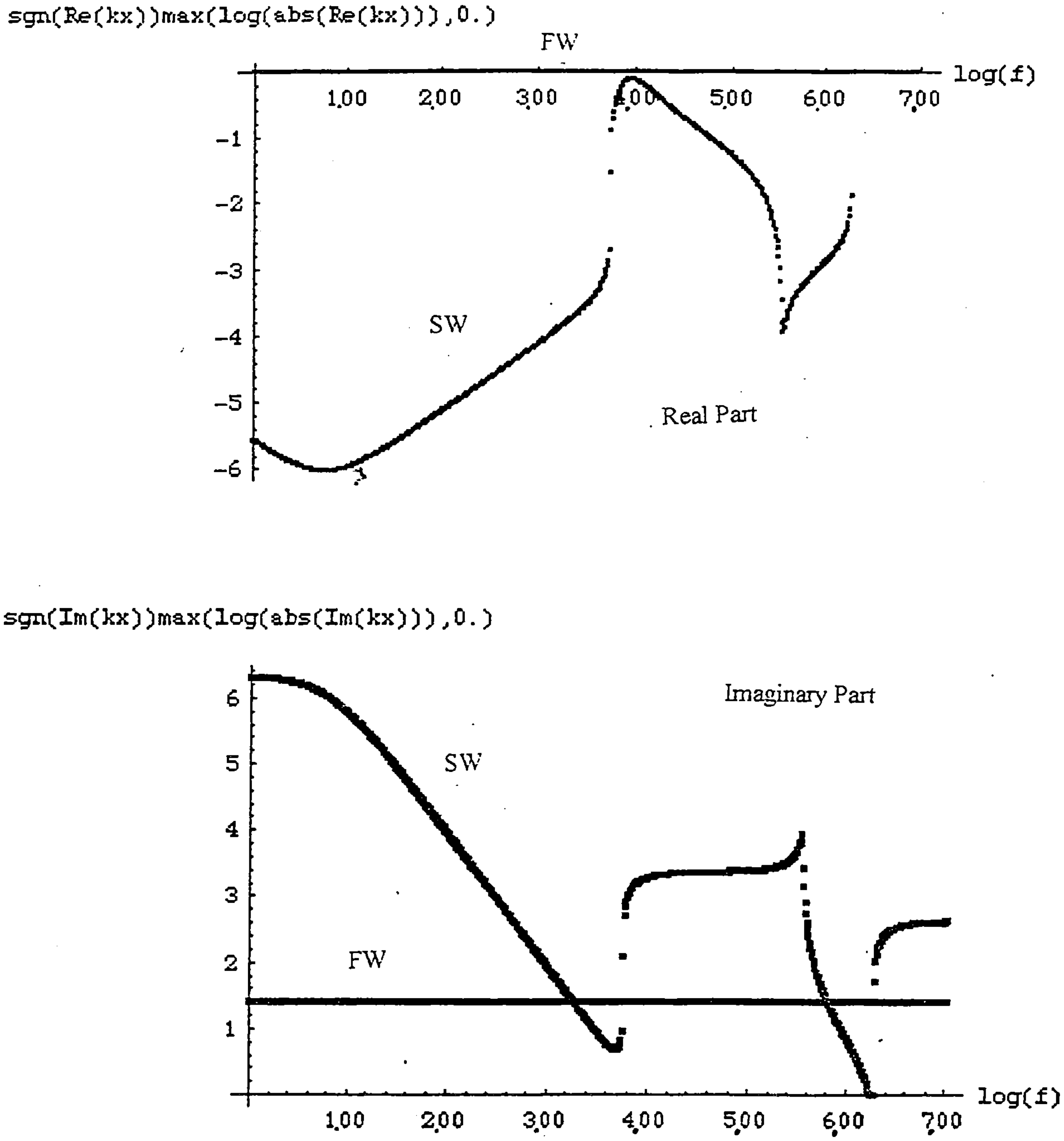

Fig.1. Plots of the real and imaginary parts of the radial component of the wavevector k_x for the two waves of the augmented cold plasma dispersion relation.

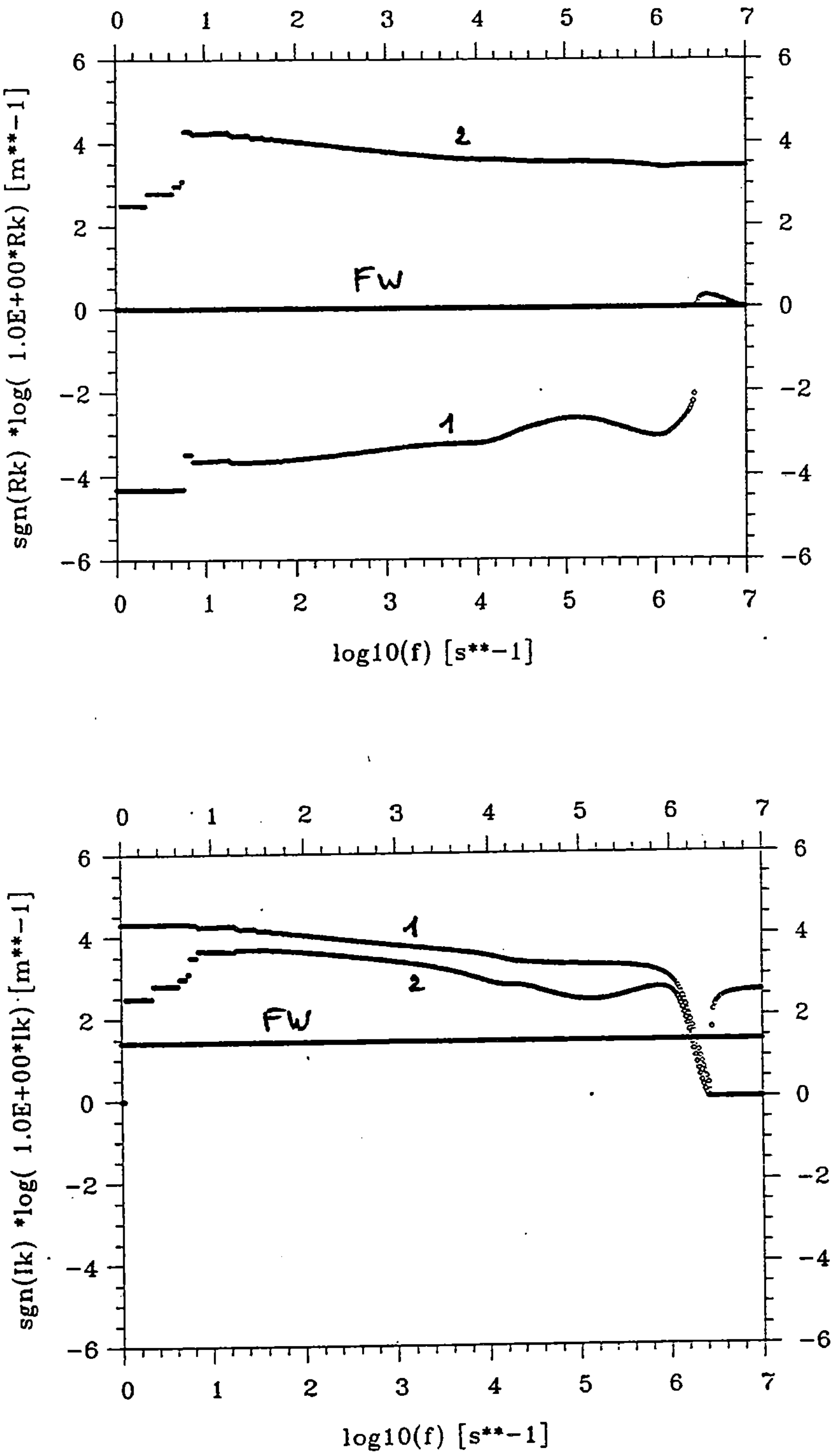

Fig.2. Plots of the real and imaginary parts of the radial component of the wavevector k_x for the FW and the two other small wavelength roots (labelled 1 and 2) of the warm plasma dispersion relation.

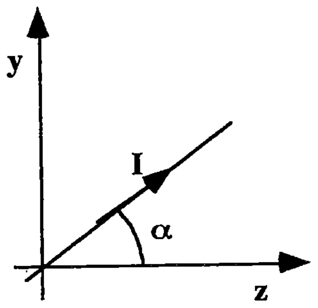

Fig.4.1. Filamentary current

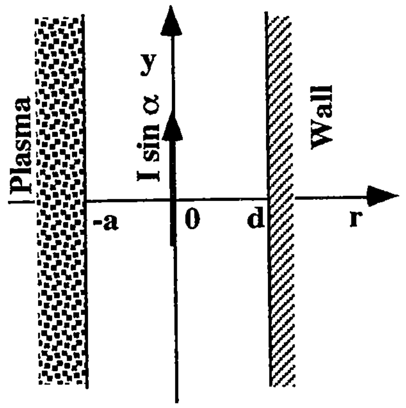

Fig. 4.2. Slab coupling geometry

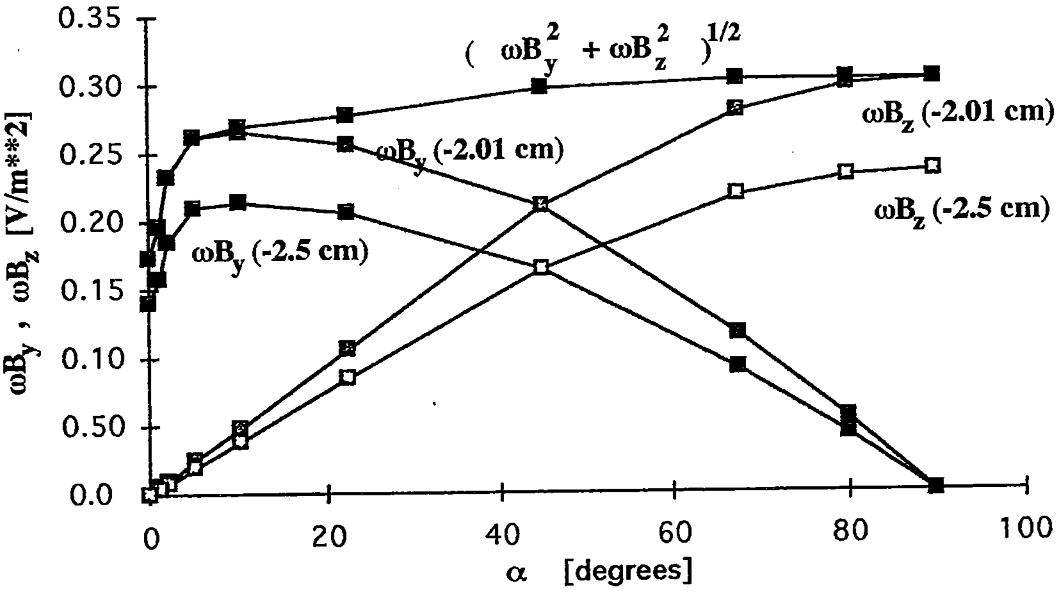

Fig. 4.4. Variation of the magnetic induction components inside the uniform plasma versus angle α between ribbon current and static magnetic field.

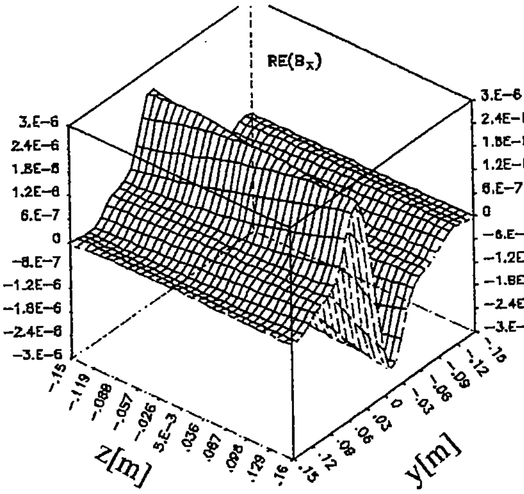

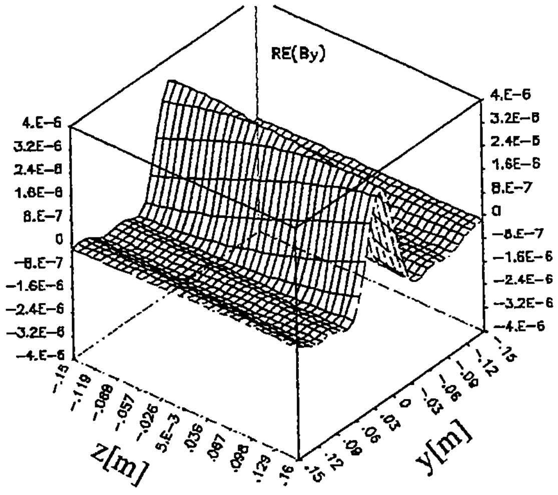

Fig.4.3. Field generated in the plasma on the plane located at x=-2.5cm by a ribbon current flowing at an angle of 5° to the z direction.

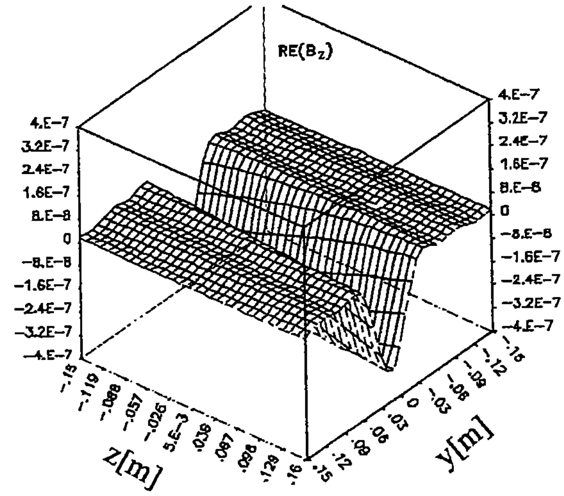

9. Considerations on Diagnostics during Operation with the Dynamic Ergodic Divertor on TEXTOR-94

K.H. Finken[1], *G. Van Oost*[2]

[1]*Institut für Pasmaphysik, Forschungszentrum Jülich, Association EURATOM-KFA*
[2]*Laboratoire de Physique des Plasmas - Laboratorium voor Plasmafysica,*
Association "EURATOM-Belgian State", Ecole Royale Militaire - Koninklijke Militaire School,
Brussels

Operation with the Dynamic Ergodic Divertor operation will open a new or modified access to a series of physics questions. To address these different questions the use of some specific diagnostics is required. In the following, the goals, put in order according to the applied perturbation frequency are outlined, the requirements on diagnostics are discussed and some details of the relevant diagnostic equipment are given.

During static or quasistatic operation (DC and 50 Hz) the most important goals are (1) improved particle (in particular He) removal, (2) high performance operation with optimized radiative mantle together with sufficient density and impurity control and (3) investigation of the potential of the helical near field divertor. In addition, the specific structure of the plasma boundary imposed by the perturbation will be investigated. The latter questions relate to (4) an island dominated structure (at a low perturbation current) and (5) an ergodized boundary structure. At a perturbation frequency of about 1 kHz the recycling of particles on the pump limiter or on the divertor target plates may start to become modified; topic (6) are the physics questions related to this point. The basic idea behind the high frequency operation of the DED (in the range from 1 kHz to 10 kHz) is the assumption that either the (toroidal) plasma flow or wave structures such as tearing modes or MHD-modes will be accelerated by or locked to the imposed moving perturbation pattern. The resulting questions will therefore be (7) the determination of the plasma flow and (8) the influence on mode locking, disruption avoidance and confinement improvement.

(1), (2): The topics (1) and (2) have already been treated carefully for several years. The diagnostics on particle and helium removal (probes in the pump limiter ALT-II and the plasma boundary, gas flow measurements in the exhaust systems, CXRS for helium and impurities, modified Penning gauge for He) and for high confinement radiative mantle experiments (feed-back controlled gas injection, emission spectroscopy, tomography, plasma energy diagnostics) are installed and need adaption only on those locations where flanges will be required for DED feed-throughs. Specific questions for particle removal and optimized seed impurity radiation resulting from the DED operation relate to the width of the particle, temperature and power decay lengths. These questions can be treated by the different atomic beam diagnostics (thermal and energetic Li beams, He beams, diagnostic beam), scanning probes, Thomson scattering, (in phase gated) CCD cameras and IR scanners. Most of these diagnostics are in operation and have sufficient spatial and temporal resolution; a specific diagnostic hydrogen beam is in preparation and a spatially highly resolving Thomson scattering system will be provided by the FOM partners which also allows to detect details of the electron velocity distribution.

(3): The analysis of the helical near field divertor requires e.g the knowledge of particle and power fluxes and their spatial distribution on the divertor target plates. For these measurements, IR scanners, (in phase-gated) CCD cameras and spectroscopic systems are available. In addition it is foreseen to measure the electrical current and voltage on selected graphite tiles of the divertor target plates which are mounted on insulated structural material.

(4),(5): The Poincaré plots show detailed structures such as islands, dissolved islands and barrier zones poloidally and toroidally distributed all around the torus. Poincaré plots mean just a mapping technique and they do not imply that the local values of the magnetic field in the island or ergodic zone away from the perturbation coils differ from the unperturbed equilibrium field. This may change - and is then important for the understanding of the confinement and events such as "snakes" -if the plasma reacts in such a way that the islands are filled with particles (and that they therefore require confinement currents). To resolve the fine island structures or the structure due to the ergodized magnetic field, the diagnostics must be sensitive to density, temperature or magnetic variations in the plasma edge and must have a good radial (range of several millimeters) and - for rotating perturbation fields - a good temporal (1/100 of the inverse DED frequency) resolution. On TEXTOR-94 these requirements are fulfilled by several atomic beams, scanning probes, Mirnov coils, Thomson scattering and microwave reflectometry. For low frequency magnetic field measurements Hall probes will be tested. The coarse 3/1 and 2/1 islands can be resolved by bolometry and by ultrasoft X-ray tomography from FOM (photon energy 50 - 500 eV).

(6): At frequencies above 1 kHz we possibly expect a decoupling of the recycling flux from the primary flux to the target surface. This decoupling may result in a phase delay between these fluxes, a smearing out of the recycling flux or even a reduction. The recycling process may be important for the confinement. The recycling flux can be measured spectroscopically (H_α; standard technique for τ_p). A gated intensified CCD camera is available allowing iterative exposures as short as 1 ms duration. For power flux measurements at one spot, IR diodes with a microsecond time resolution are in preparation.

(7): It is estimated that the fast rotating DED pattern results in a force of a few Newton, sufficient for imposing a plasma rotation or a plasma flux locking in the wave field. (In addition, a toroidal momentum of similar magnitude can be imposed to the plasma core by neutral beam injection.) The toroidal and poloidal rotation velocities will be measured by CXRS and by emission spectroscopy. In case such a differential rotation changes the energy confinement, this effect would be measured by standard diagnostics.

(8): Tearing modes and MHD activities are measured on TEXTOR-94 by Mirnov coils and by densely positioned ECE-channels. This technique can be applied for the questions of mode locking and unlocking. A related question is the development of disruptions. Also this question has been studied on TEXTOR-94 and will remain of continuous interest.

Ergodization of the magnetic field in the core may deteriorate the plasma confinement. A sensitive method for detecting magnetic field perturbations in the core plasma is the analysis of synchrotron radiation from runaway electrons and microwave mode conversion. The synchrotron technique has been developed on TEXTOR-94 and can most likely be applied for interesting ergodzation studies. Cross-polarization microwave scattering has been studied on TORE SUPRA and its installation on TEXTOR-94 is planned by the FOM group. The modification of transport due to the DED, in particular at high frequencies, may lead to distortions of the electron velocity distribution which can be detected by the high resolution Thomson scattering.

Details to diagnostics

I) Emission spectroscopy (edge and core)

a) Various *line resolving spectroscopy systems* in the visible, UV, VUV and X-ray spectral ranges (standard for plasma physics) for determination of fluxes and densities, penetration depths, velocity distributions, toroidal and poloidal rotation of hydrogen isotopes and impurity ions.

b) 26 *bolometric* channels for tomographic reconstruction of the radiation profiles. The system is used for feedback control of the radiative mantle (important for DED). Time resolution: 20 ms; poloidal resolution: $m \leq 3$.

c) 72 *soft X-ray* channels for radial and time resolved MHD mode analysis in core plasma (tomography). Time resolution: 50 ms; spatial resolution: 2 cm.

d) The FOM institute plans the installation of a *multilayer-based soft X-ray camera* system for the investigation of multi-charged ion transport. The system images in particular the plasma boundary in the ultrasoft x-ray region with photon energies between 50 eV and 500 eV (radiative mantle, important for DED). Time resolution: about 0.1 ms, spatial resolution: 1 cm.

II) Atomic beams

a) *Thermal Li beam* for n_e measurement in SOL (10^{17} m$^{-3} \leq n_e \leq 10^{19}$ m^{-3}).
Time resolution: 0.5 ms, (for profile: 10 ms); spatial resolution: 1 mm.

b) *Double Li beam* for radial and poloidal density fluctuations and phase velocities in the SOL.

c) *35 keV Li beam* for the measurement of n_e- and T_i-impurity-profiles (by CXRS)as well as poloidal rotation velocity. Range: outer 30 cm of plasma cross section. Time resolution: 4 ms; spatial resolution: 5 mm.

d) *Laser ablation* (e.g. 6 eV Li) for n_e- and T_e-profile measurements in plasma edge. Single shot; spatial resolution: 1.1 mm.

e) *He beams* (superthermal and supersonic) for n_e-, T_e-profile measurements as well as for fluctuations. Range: 2×10^{18} m^{-3} $\leq n_e \leq$ 2×10^{19} m^{-3}; 10 eV $\leq T_e \leq$ 200 eV. The supersonic beam has larger penetration depth and allows electron temperature fluctuation measurements. One beam will be located at the high field side just in between the DED coils. Time resolution ≥ 0.3 ms; radial resolution: 1 mm.

f) The *CXRS* by means of the neutral heating beam provides the core and edge profiles of impurity densities, ion temperatures of hydrogen isotopes and impurities and of their toroidal velocities. Time resolution: 40 ms; spatial resolution: 15 radially distributed channels where each channel can feed three independent spectrometers.

g) The *CXRS hydrogen (deuterium) diagnostic beam* provides similar information as in (f) but without heating the plasma. The beam is modulated (thus increasing the sensitivity) and also provides the poloidal plasma rotation velocity.

III) Probes

a) Two *fast scanning probes* located at different poloidal and toroidal locations provide boundary profiles of n_e, T_e, floating potential, poloidal electric field and their fluctuations (100 kHz). Single or multiple exposures; 80 ms in, 80 ms dwell and 100 ms out.

b) *Rotating electric double probes* for measuring Mach number and flow direction. A novel "sandwich" probe for determining the perpendicular flow component is under development. In addition a rotating and radially fast scanning manipulator is being built.

c) A *rake probe* with 9 radially distributed pins can measure the electrical field in the boundary plasma during the whole discharge.

d) For *magnetic field* measurements both a *Hall probe* and a *pick-up probe* will be developed. The Hall probe has operated successfully in the PISCES (UCSD) plasma source up to frequencies of 1 kHz; at higher frequencies pick-up probes seem more attractive (very important for the DED).

e) The pump limiter ALT-II is equipped with several diagnostics for measuring the particle exhaust flux, including *Langmuir- and flux probes* located in the collecting scoop area.

IV) Imaging systems

a) For DC operation of the DED, normal *calibrated CCD cameras* provide information on the spatial distribution of the fluxes of hydrogen isotopes and of different charge states of ions both on the pump limiter ALT-II and on the divertor target plates. To observe the flux distribution during the AC operation, the cameras have to be gated in phase with the DED. The gating time should not exceed 1/100 of the inverse frequency; however, multiple exposure during the time of a frame (20 ms) is allowed. This technique of gating an intensified CCD camera has been applied on TEXTOR-94 during pellet injection experiments.

b) Two *IR-scanners* (sensitive in the range 3 mm $\leq l \leq$ 8 mm) have been used extensively for determining the temperature distribution on limiters, the power flux density, the power decay length and - in combination with other diagnostics - the power balance. Studies of disruptive discharges have demonstrated that a time resolution as short as 0.1 ms can be utilized. The systems are well suited for observations of the divertor target plates.

c) The same IR scanners are used for the detection of the *synchrotron radiation* distribution by runaway electrons. This measurement is sensitive to magnetic field perturbations in the plasma core.

V) Microwave diagnostics

a) 20 *ECE channels* provide a spatially well resolved electron temperature profile. Several of these channels are grouped very densely for detailed measurements on MHD islands around rational q-surfaces. The time resolution (sampling rate 10 - 25 kHz) is sufficient to resolve details of the rotating island patterns. (important for the DED resonant mode investigations). The FOM investigates possibilities to extend this system to allow correlation ECE.

b) *Broadband reflectometry* (26 - 37 GHz) allows the measurements of density low frequency fluctuations and island structures in the range of $0.8 - 1.7\times10^{19}$ m^{-3}.

c) A 10 channel *pulse-radar reflectometer* (18 - 57 GHz) can measure density profiles in the range of 0.4 - 4×10^{19} m^{-3}. The absolute radial resolution is about 1 cm, the relative resolution will be better depending on details of the density profile.Repetition rate 2 ms for four points on the density profile.

d) A *three wave correlation spectrometer* with variable amplitude modulation frequency and poloidally separated antennae will allow density fluctuation measurements in the density gradient zone as well as poloidal structures and motions (in preparation).

e) A *collective millimeter wave scattering* diagnostic system measures density fluctuations between 150 kHz and 2 MHz. The k-vector varies between 9 cm^{-1} in to core to 36 cm^{-1} at the edge of the plasma.

f) A *cross-polarization microwave scattering* system has been developed on TORE SUPRA to detect magnetic field fluctuations. The FOM institute plans to install two independent antennae emitting in O-mode (with tiltable mirrors) at the LFS and an array of receiver antennae in X-mode at the HFS.

VI) Laser diagnostics

a) The FOM institute plans the installation of a spatially *highly resolving Thomson scattering* arrangement for measuring n_e and T_e over the whole plasma diameter (up to the boundary). It has a spatial resulution of 2.5 mm and a wavelength resolution of 5 nm (150 channels both for spatial and for spectral resolution); it has been developed in particular for the detection of plasma filamentation.

b) The *laser induced fluorescence diagnostic* (in the UV and VUV spectral region) allows the determination of density and velocity distributions of atomic hydrogen isotopes and light impurities in the boundary layer. The spatial resolution ranges from 1 mm - 1 cm. The typical detection limit lies around 5×10^{14} m^{-3}.

VII) Magnetic diagnostics

As standard magnetic diagnostics TEXTOR has an m=2 coil to detect precursors of disruptions, an m=3 coil to detect higher order MHD modes, a compensated magnetic loop to measure the diamagnetic energy and an array of 12 poloidal and 8 toroidal Mirnov coils with a sampling rate of 20 kHz.

Part IV: Modelling - Results and Developments

10 Modelling of Plasma and Impurity Behaviour in a Tokamak with a Stochastic Layer

M.Z.Tokar'

Institut für Plasmaphysik, Forschungszentrum Jülich, Association EURATOM-KFA

In this section the used model for the transport of energy and charged particles in a stochastic layer is considered and validated by comparison of computations by the code RITM with measurements in TORE SUPRA discharges without and with static Ergodic Divertor.

10.1 Transport in Stochastic Magnetic Field

10.1.1 Behaviour of Magnetic Field Lines

The correlation length L_c, related to Chirikov's parameter σ_{Chir} [1], and the diffusivity D_{Fl} of field lines in the radial direction (see II.3) are of great importance for the transport of particles and energy in a stochastic layer. The radial gap δ between two neighboring lines increases with the distance l from a reference position. For l smaller than L_c $\delta \approx \delta(0) \cdot \exp(l/L_c)$ and in the opposite case of $l \gg L_c$ the behaviour of lines is chaotic e.i. δ increases according to the diffusion law [2,3]: $\delta(l) \approx (D_{Fl} \cdot l)^{1/2}$. For the modelling of Tore-Supra discharges with Ergodic Divertor σ_{Chir} and D_{Fl} found by the field line tracing code MASTOC [4] have been used. The radial profiles of these characteristics are presented in Fig.1.

10.1.2 Transport Coefficients

Different approaches are proposed in the literature for evaluation of the effective

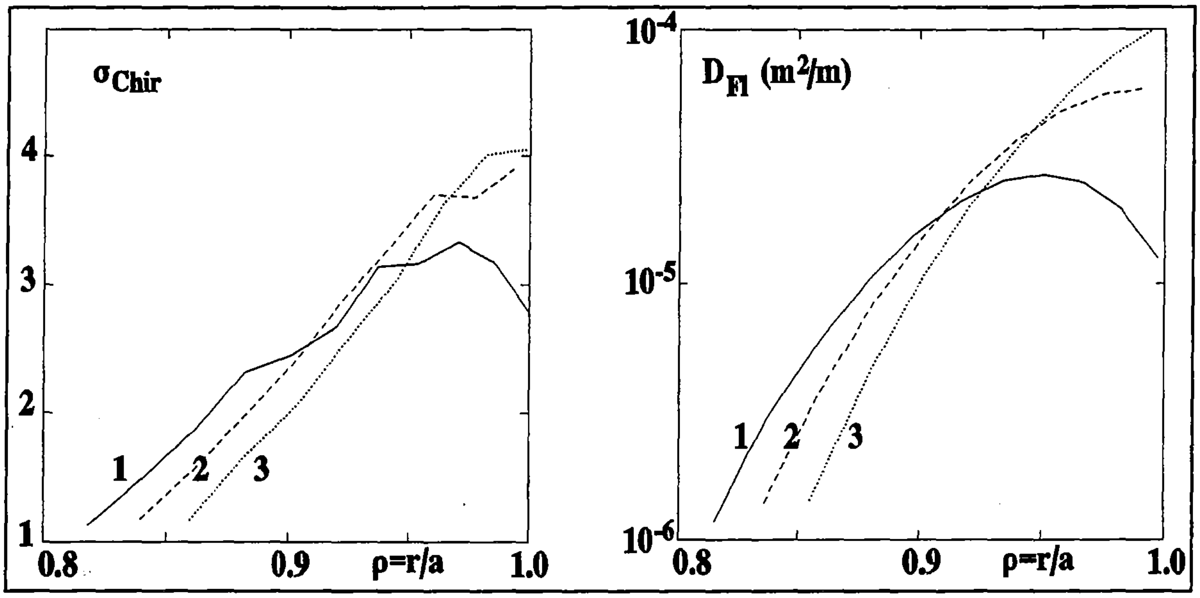

Figure 1 Radial profile of the Chirikov parameter and field line diffusivity in Tore-Supra calculated by the code MASTOC (Grosman *et al* 1994): 1 - I_p = 1.3 MA, 2 - 1.4 MA, 3 - 1.5 MA.

transport coefficients in a stochastic layer. In the present modelling we base the one proposed first in Ref.^{2} for the heat transfer and extended in Ref.^{5} for the transport of charged particles. As distinct from these publications the formulas obtained in the present paper describe smoothly the variation of transport coefficients between the cases without and with stochastization. Moreover this approach is applied here to consider the transport of impurity ions.

The equations governing the magnetic field lines have Hamiltonian properties. Thus the area of the cross-section of a narrow beam of lines does not change with displacement in the toroidal direction. This has important consequences for the transport of charged particles and energy under conditions of stochastization. Without losses e.g. due to perpendicular transport, the total number of particles and their thermal energy are the same in each cross-section of the beam. Therefore the parallel gradients of the plasma temperature and pressure reduce to zero. The same holds for the flows of heat and particles. Thus the divergence of the field lines itself does not lead to a transport in the radial direction and one should take into account the perpendicular transfer.

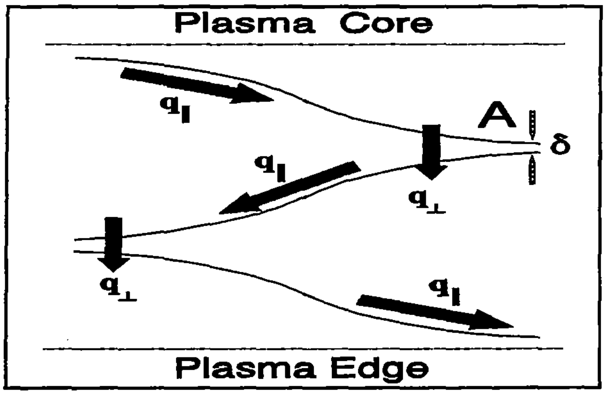

Figure 2 Scheme of heat flows in stochastic magnetic field

Schematically the flows of heat or charged particles in a stochastic field, where the flux from the plasma core maintains a certain radial temperature or density gradient, is shown in Fig.2. Let us consider two field lines which are "close" to each other in the region A. The closeness means that the radial gap δ between the lines is small enough so that the perpendicular transport keeps the temperature or density difference at a low level. With displacement from A the lines diverge and penetrate into the regions where the plasma quantities differ significantly. Thus arising parallel gradients generate flows of energy and particles between regions of different radial position which are connected by the perpendicular transport inside these regions.

One of the relations connecting the characteristic distance L between regions of sufficiently different plasma parameters and δ has been found from the variation principal applied to the continuity equation ^{3}. It states:

$$\delta \cdot \exp(\frac{L}{L_c}) \approx \sqrt{D_{Fl} \cdot L}\,, \tag{1}$$

e.i. such L is of most importance for the transport for which the exponential divergence of the lines of force evolves into stochastic behaviour. The radial gap $\Delta = \delta \cdot \exp(l/L_c)$ between the lines at this distance gives the characteristic dimension of the parameter change across the stochastic layer. To find further relations between L and δ one should take into account specific mechanisms of the energy and particle transport parallel and across magnetic field lines.

Heat transfer. Neglecting sources and sinks of energy the heat balance equation can be written as follows:

$$\frac{\partial q_r}{\partial r} + \frac{\partial q_\|}{\partial l} = 0. \tag{2}$$

(It is taken into account here and henceforth that the stochastic layer is significantly thinner than the plasma minor radius r and a plane geometry is applicable). Using the characteristic dimensions L and δ one obtains estimates for the components of the heat flux density, $q_r \approx \kappa_r T/\delta$ and $q_\| \approx \kappa_\| T/L$, and Eq.(2) results in:

$$\delta \approx L \cdot \sqrt{\kappa_r / \kappa_\|}\,. \tag{3}$$

It is assumed that the transport perpendicular to the field lines, i.e. the heat conductivity component κ_r, does not change with stochastization. For $\kappa_\|$ we assume the classical Spitzer's coefficient, $\kappa_\parallel^{Sp}$, corrected by a factor which takes the finite path length λ_h between coulomb collisions of particles which predominantly carry heat into account [6]:

$$\kappa_\parallel = \frac{\kappa_\parallel^{Sp}}{1+\lambda_h/L}. \tag{4}$$

Here λ_h exceeds the path length of thermal particles by a factor of 15-50. Combining Eqs.(1), (3) and (4) one obtains the following transcendent equation to L:

$$\exp\left(\frac{2L}{L_c}\right) = \frac{D_{Fl}}{L+\lambda_h}\cdot\frac{\kappa_\parallel^{Sp}}{\kappa_r}. \tag{5}$$

This has a physically meaningful positive solution if stochastization is sufficiently strong i.e. for $\lambda_h < D_{Fl}\kappa_\parallel^{Sp}/\kappa_r$.

The effective heat conductivity in the stochastic layer is estimated from the definition of the averaged radial heat flux:

$$\langle q_r\rangle \equiv \kappa_r^{eff}\cdot\frac{T}{\Delta} \approx \kappa_r\cdot\frac{T}{\Delta}+\kappa_\parallel\cdot\frac{T}{L_T}\cdot\langle\frac{B_r}{B}\rangle\,, \tag{6}$$

where the first term gives the contribution due to perpendicular heat conduction and the second term due to transport along perturbed lines of force. According to the definition of the diffusivity of magnetic field lines it follows $<B_r/B> \approx (D_{Fl}/L_c)^{1/2}$ for $L<L_c$; in the case of $L>L_c$ $<B_r/B> \approx \Delta/L \approx (D_{Fl}/L)^{1/2}$. Taking this into account we obtain from Eq.(6):

$$\kappa_r^{eff} \approx \kappa_r\cdot\left[1+\sqrt{\min\left(1,\frac{L}{L_c}\right)}\cdot\exp\left(\frac{2L}{L_c}\right)\right]. \tag{7}$$

As it can be seen $\kappa_r^{eff} \rightarrow \kappa_r$ if $L/L_c \rightarrow 0$. Physically this means that an increase of the correlation length (e.g. due to a weaker overlapping of the magnetic islands) results in a weakening of the stochastization effect on the transport. In the opposite case of large L Eqs.(6) and (7) reduce to the formula in Ref.[2] for $\lambda_h=0$. However, the latter assumption is usually not fulfilled for typical plasma parameters in an ergodic layer. E.g. for $T_e=50$ eV and $n_e=10^{13}$ cm^{-3} one has $\lambda_h \approx 10^4$ cm which is significantly larger that a typical magnitude of L. Thus the correction taking into account the finiteness of λ_h is of importance and leads to a reduction of κ_r^{eff} by an order of magnitude.

Transfer of main particles. As by heat transfer the flow along lines of force contributes to the effective radial diffusion of particles in the stochastic layer. In the continuity equation

$$\frac{\partial}{\partial r}\left(-D_r\frac{\partial n}{\partial r}\right)+\frac{\partial nV_\parallel}{\partial l} = 0, \tag{8}$$

where D_r is the particle diffusivity perpendicular to the field lines, this flow is described by the second term. The flow velocity $V_\parallel$ is assumed subsonic and governed by the sum of the motion equations of electrons and main ions[5]:

$$\frac{\partial}{\partial l}[n(T_e+T_i)] = \frac{\partial}{\partial r}\left(D_r\frac{\partial nV_\parallel}{\partial r}\right). \tag{9}$$

Here the right hand side takes into account the dissipation of the parallel momentum with perpendicular diffusion and viscosity; following Ref.[5] we have neglected in Eq.(9) terms containing the temperature gradient because they are small in comparison with those dependent on the gradient of density.

Replacing again the derivatives in Eqs.(8) and (9) by the division by the characteristic dimensions and combining the result with Eq.(1) one finds the following expression for L:

$$L = \frac{L_c}{2}\cdot\ln\frac{D_{Fl}c_s}{D_r}, \tag{10}$$

with $c_s=[(T_e+T_i)/m_i]^{1/2}$ being the ion sound velocity.
A consideration, analogous to the performed one to find κ_r^{eff}, leads us to the following formula for the effective particle diffusivity:

$$D_r^{eff} \approx D_r\cdot\left[1+\sqrt{\min\left(1,\frac{L}{L_c}\right)}\cdot\exp\left(\frac{2L}{L_c}\right)\right]. \tag{11}$$

If $L_c \ll L$ Eq.(11) results in the formula of Ref.[5]: $D_r^{eff} \approx D_{Fl}\cdot c_s$.

The effect of stochastization on the convection velocity of the main ions is neglected. It is proportional to the parallel temperature gradient and is small in comparison with the effect on the diffusivity governed by the gradient of the density[3,5].

Transfer of impurities. Chaotic thermal motion of impurity ions along stochastic field lines contribute to their diffusive displacement in the radial direction and the induced flux is proportional to the density gradient. An analogous treatment as for the background particles results in a diffusivity $D_r^{z,eff}$ for impurities of the charge z governed by Eq.(11), but the corresponding L should be calculated with replacement of the ion sound velocity c_s in Eq.(10) by the thermal velocity $c_{th}=(T_i/m_z)^{1/2}$.

Besides there are forces inducing motion of impurities in a preferential direction: electric field and friction with the main ions. This results in a convective flux proportional to the particle density n_z. Since these forces can accelerate impurity ions to a velocity exceeding the thermal one the inertial term should be taken into account in the motion equation along the field lines[7]:

$$\frac{\partial}{\partial l}[n_z m_z (V_\parallel^z)^2] = \frac{\partial}{\partial r}\left(m_z D_r \frac{\partial n_z V_\parallel^z}{\partial r}\right) + ezn_z E_\parallel - n_z m_z \frac{V_\parallel^z - V_\parallel}{\tau_z}. \tag{12}$$

Here τ_z is the time between coulomb collisions with the main ions and the parallel electric field $E_\parallel$ is governed by the force balance of electrons:

$$0 = -\frac{\partial n_e T_e}{\partial l} - eE_\parallel n_e. \tag{13}$$

(As for the treatment of main ions we neglect in Eqs.(12) and (13) terms which depend on the temperature gradient, e.g. thermal force, because $|dT/dl|/T \ll |dn/dl|/n$).

Combining these equations and replacing again the derivatives by division by the characteristic dimensions found for the main particles in the last section we obtain the following expression for the parallel convective velocity of impurity ions:

$$V_\parallel^z = \sqrt{V_1^2 + V_2} - V_1, \tag{14}$$

where $V_1=(c_s/2^{1/2}+L/\tau_z)/2$ and $V_2=c_s\cdot L/\tau_z+z\cdot T_e/m_z$.

In the approximation assumed $V_\parallel^z$ is always positive because the electric field and friction with the main ions are directed towards the regions of lower plasma pressure - toward the plasma edge. This motion along field lines results in displacement of particles with the radial velocity $V_r^{z,st}$:

$$V_r^{z,st} \approx V_\parallel^z \cdot \sqrt{\frac{D_{Fl}}{\max(L_c,L_n)}} \quad . \tag{15}$$

It should be superimposed with the velocity of the impurity convection across unperturbed magnetic surfaces. It is assumed in the present modelling that this is governed by the neoclassical effects[8]:

$$V_r^{z,neo} = \frac{q^2 \varrho_i^2}{\tau_{ii}} z \left(\frac{K}{n_i} \frac{\partial n_i}{\partial r} + \frac{H}{T_i} \frac{\partial T_i}{\partial r} \right), \tag{16}$$

where ρ_i and τ_{ii} are the gyro-radius and time between coulomb collisions of the main ions, the coefficients K and H depend on the collisionalities of the main and impurity particles.

Thus the radial flux density of impurity ions in the stochastic layer is given by the expression:

$$\Gamma_r^z = -D_r^{z,eff} \frac{\partial n_z}{\partial r} + \left(V_r^{z,st} + V_r^{z,neo} \right) \cdot n_z . \tag{17}$$

As we will see later conversely to the main ions the diffusivity of impurities does practically not change with stochastization due to the larger mass. Simultaneously, their convection velocity is influenced significantly and this is mainly responsible for the so called "impurity screening" by stochastization[9].

In our previous consideration[10] the effect of stochastization on convection of impurity ions has been ignored. The influence of the parallel electric field and friction with the main ions was taking into account under assumption that these forces enhance *diffusive* motion of impurities. Formally this has been done combining $V_\parallel^z$ from Eq.(14) with c_{th} to find L and $D_r^{z,eff}$ according to Eqs.(10) and (11). Assumption of a purely diffusive character of $V_r^{z,st}$ is not satisfied for all charge states: due to further ionization the density of not fully stripped ions decreases towards the plasma core while the flux associated with parallel motion is directed towards the edge. Nevertheless, this approach has allowed to reproduce the main effect of the ED e.i. reduction of the concentration of intrinsic impurities, and can be used for qualitative estimates. At the same time the present consideration distinguishing the effect of stochastization on the diffusive and convective motion of impurities is more straightforward and gives a better agreement with the data of measurements (see section 3.1).

10.1.3 Code RITM

The code RITM (Radiation from Impurities in Transport Model)[11] describes self-consistently the interaction of the main and impurity particles through radiation and dilution in the plasma domain inside the last closed magnetic surface (LCMS). RITM has been applied successfully to reproduce the evolution of plasma parameters during detachment in limiter tokamaks, under conditions of strong radiative edge cooling by puffing of neon into TEXTOR.

RITM solves time-dependent one-dimensional transport equations describing the variation of the densities and temperatures of neutral and charged particles of the main and impurity plasma components in the direction perpendicular to the magnetic surfaces. Neutral particles are described in the hydro-dynamic approximation, anomalous pinch velocity and diffusion are assumed for charged components. The distributions of impurities over different charge states is defined in non-corona approximation taking into account their ionization, recombination, charge-exchange with hydrogen neutrals, anomalous diffusion and neo-classical convection due to collisions with the main ions.

Both convective and conductive components are included into the heat transport of electrons and ions. Energy sources and sinks take into account the ohmic heating with self-consistently calculated profiles of the current density and electric-conductivity; additional heating from neutral beams and RF with profiles found in TRANSP modelling; interaction of the main ions with neutrals in reactions of ionization, recombination, charge-exchange; energy losses from electrons on line radiation and bremsstrahlung from main and impurity neutrals and ions.

In ohmic plasmas in Tore-Supra without ED particle and electron heat diffusivities are described by an Alcator-like scaling: $D_r = A_D/n_e$ and $\chi_r^e \equiv \kappa_r^e/n_e = \alpha_\chi D_r$, respectively. The parameters A_D and α_χ are determined from coincidence of the measured and calculated particle and energy confinement times. The pinch velocity V_r of the main ions is defined by the relation $V_r = \alpha_V D_r r/a^2$ with the coefficient α_V chosen to reproduce the experimental peaking factor of the electron density profile. The diffusivity of impurity ions is the same as that of the main ones, the pinch velocity is calculated according to the neo-classical theory[8] as well as the heat diffusivity of the main ions[12]. For additionally heated plasmas a good agreement of calculated and measured profiles were found for the Rebut-Lallia model[13]. In discharges with the Ergodic Divertor D_r^{eff} and χ_r^{eff} are calculated according to the formulas of the previous section, where D_r and χ_r are the same as in the configuration without ED.

For plasmas without ED the LCLS is determined by the surface touching the limiter with a major radius R_0 of 240 cm and a minor radius a of 77cm. In the configuration with the ergodic layer the LCMS is located 2 cm deeper into the plasma and roughly coincides with the inner border of the so called "laminar" layer which is the plasma domain where the lines of force hit the wall elements. The boundary conditions imposed at LCMS prescribe the percentages of molecules and atoms in the fluxes of hydrogen neutral particles recycling from the wall, their velocities, e-folding lengths of densities and temperatures of charged particles, δ_n and $\delta_T{}^{i,e}$, respectively. These conditions are determined from experimental data or found self-consistently in calculations coupled with the edge two-dimensional code package EB2-EIRENE[14]. In the present consideration we confine ourselves to the experimental approach only. The influxes of impurity neutrals are chosen to reproduce in the calculations the measured radiation level.

10.2 Results of Modelling and Comparison with Experimental Data

10.2.1 Ohmic Discharges with Intrinsic Impurities

Two discharges in Tore-Supra, shot 19807 without ED and shot 19808 with ED, of the same plasma current (1.6MA) and mean electron density $<n_e>$ ($2.85 \cdot 10^{13}$cm^{-3} at $t \approx 9$s) have been modelled by RITM to analyze the effect of stochastization on the intrinsic carbon and oxygen impurities. Fig.3, where the measured time evolution of the plasma effective charge Z_{eff} and radiated power P_{rad} is presented for these discharges, manifests plasma purification and simultaneous increase of the radiation losses (at the chosen time t=9s) caused by activation of the ED.

Comparison of the results of computations and measurements shows that a reasonable agreement is achieved for $A_D=7 \cdot 10^{16}$cm^{-3}, $\alpha_\chi=3$ and $\alpha_V=1.5$. The following e-folding lengths of the density and temperatures at the LCMS were assumed: $\delta_n=1$, $\delta_T{}^e=2$ and $\delta_T{}^i=3$ cm in the limiter configuration and $\delta_n=3$, $\delta_T{}^e=3$ and $\delta_T{}^i=8$ cm in the ED case, respectively.

Plasma parameters. The calculated profiles of the electron heat diffusivity and diffusivity of

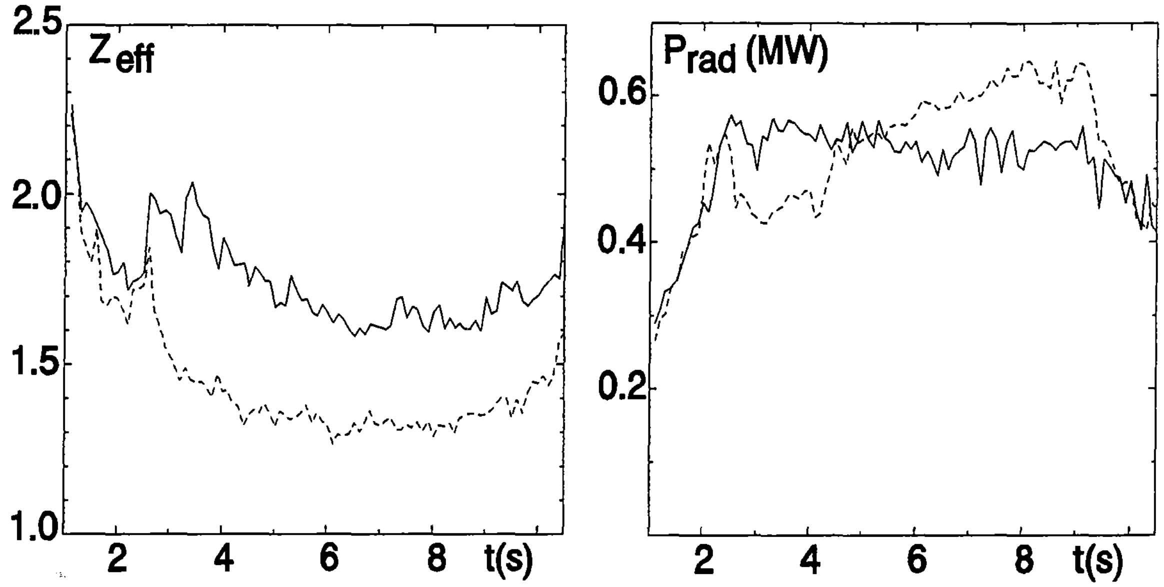

Figure 3 Measured evolution of the plasma effective charge and radiated power during shots 19807 without ED (------) and 19808 with ED (- - -). The ED resonance condition is fulfilled from 2.5 to 9.2s.

deuterons without and with ED are presented in Fig.4. It can be seen that in the stochastic layer (r > 0.8a) χ_r^{eff} exceeds χ_r by a factor of 4. This is significantly less than what would be expected under the assumption of $\kappa_{\|} = \kappa_{\|}^{Sp}$ (Ref.[15]). Thus the restriction of the parallel heat flow by a high path length of the electrons which carry heat, as described by the denominator in Eq.(4), is of importance for a reasonable estimate of χ_r^{eff}.

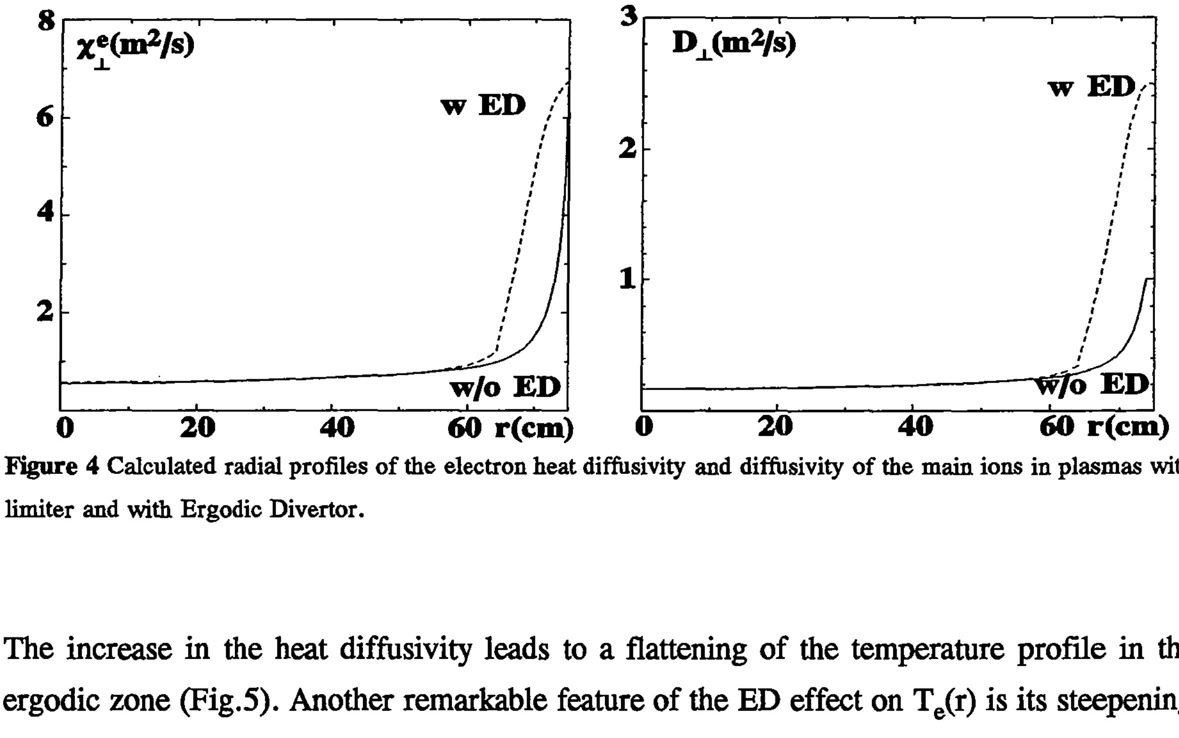

Figure 4 Calculated radial profiles of the electron heat diffusivity and diffusivity of the main ions in plasmas with limiter and with Ergodic Divertor.

The increase in the heat diffusivity leads to a flattening of the temperature profile in the ergodic zone (Fig.5). Another remarkable feature of the ED effect on $T_e(r)$ is its steepening outside the stochastic layer, $45 < r < 65$cm, which will be analyzed in the next section. The calculated profiles of the electron temperature agree with the experimental data also shown in Fig.5.

Ions are heavier than electrons and therefore stochastization changes the particle transport less than the transport of heat. Due to this reason D_r^{eff} exceeds D_r only by a factor of 3. Nevertheless, since stochastization practically does not affect the pinch velocity of the main ions[3] this leads to flattening of the density profile at the plasma edge and $n_e(a)$ increases from $3\cdot10^{12}$ to $6\cdot10^{12}$ cm^{-3} with activation of ED. These values are in agreement with measured magnitudes of the plasma density at the LCMS which are of $3\cdot10^{12}$ and $7\text{-}9\cdot10^{12}$ cm^{-3}, respectively.

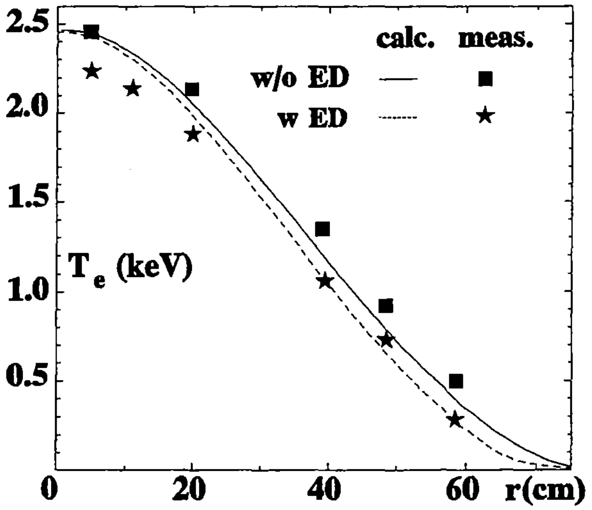

Figure 5 Calculated and measured radial profiles of the electron temperature.

Impurity density and radiation. In the present computations the influxes of carbon and oxygen neutrals were chosen to reproduce the measured radiation level γ_{rad}, being the ratio of the radiated and lunched power, and the ratio of Ly-α line emission from H-like ions of C and O. In the limiter case $\gamma_{rad} \approx 0.34$ and Ly-α(C)/Ly-α(O) $\approx$ 10.4 and for the ED configuration these values are 0.4 and 4.8, respectively. To reproduce the values in the limiter configuration, the ratio of impurity influx to outflow of deuterons, the impurity yield, should be 0.033 for C and by an order of magnitude smaller for O. This is in an agreement with measurements on TEXTOR[16] (Unterberg *et al 1993*). In the case of the ED plasma the carbon yield is reduced to 0.01 due to diminution of the physical sputtering with decreasing temperature at the LCMS from 18 to 10 eV. The oxygen yield does not change significantly with ED.

Fig.6 shows the calculated radial profiles of Z_{eff} and of the density of the radiated power Q_{rad}. The found magnitudes of the plasma effective charge manifest that the model used reproduces well plasma purification by activation of the ED. Note that the agreement with the measurements is significantly better than it was obtained without taking the effect of stochastization on the convection of impurities into account[10]: $Z_{eff}(r=0) \approx 1.26$ (Fig.6, present paper), $Z_{eff}(r=0) \approx 1.11$ (see Fig.3 in [10]) and the measured $Z_{eff} \approx 1.35$. Comparison of the calculated profiles of the radiated power density predict an increment of the radiated power by stochastization results from broadening of the radiation zone.

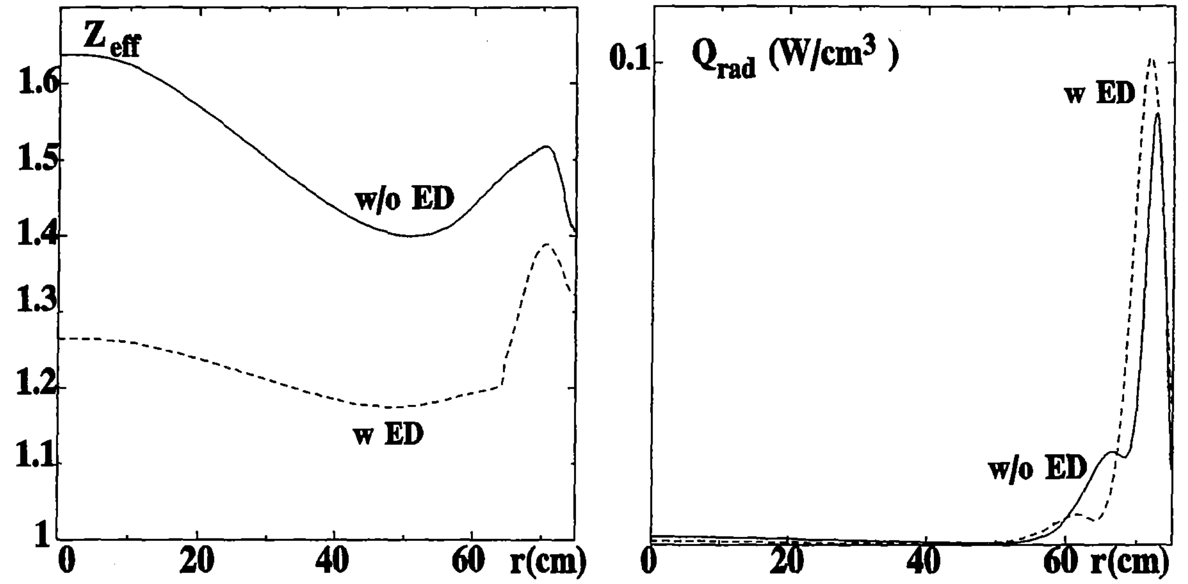

Figure 6 Calculated radial profiles of the effective plasma charge and density of radiated power.

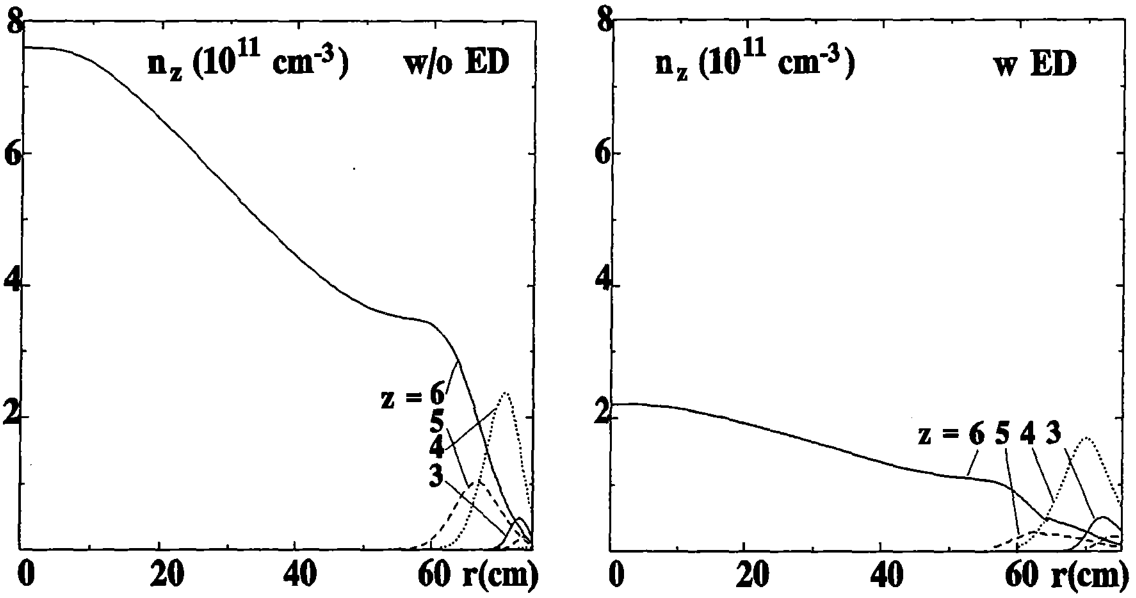

Figure 7 Calculated radial profiles of the densities of different charge states of carbon impurity.

To understand the causes of the above changes it is instructive to analyze the alterations in the radial profiles of the densities of impurity ions of different charge states (Fig.7). It can be seen that stochastization influences differently the bare carbon nuclei which make the main contribution to the total impurity density in the plasma core, the He-like particles which determine the impurity density at the edge and the Li-like and lower ionized ions which contribute dominantly to the radiation. In spite of a significant decrease of the impurity yield the peak densities of He-like and lower ionized ions remain practically unchanged but the profiles becomes broader. Conversely, the densities of nuclei and H-like particles decrease significantly.

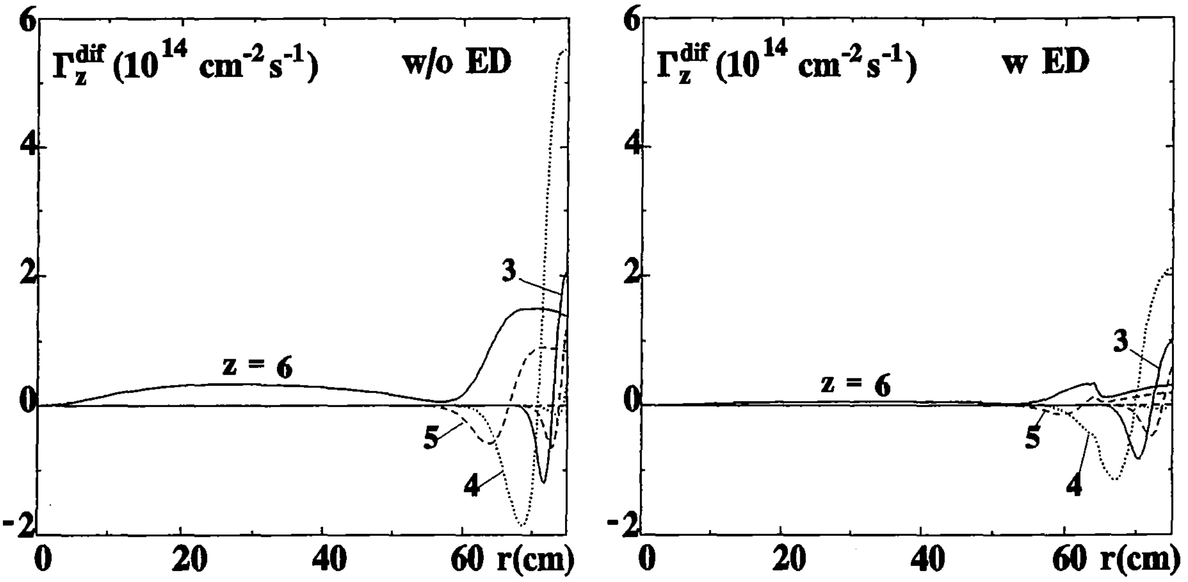

Figure 8 Calculated diffusive component of the flux density of different charge states of carbon impurity.

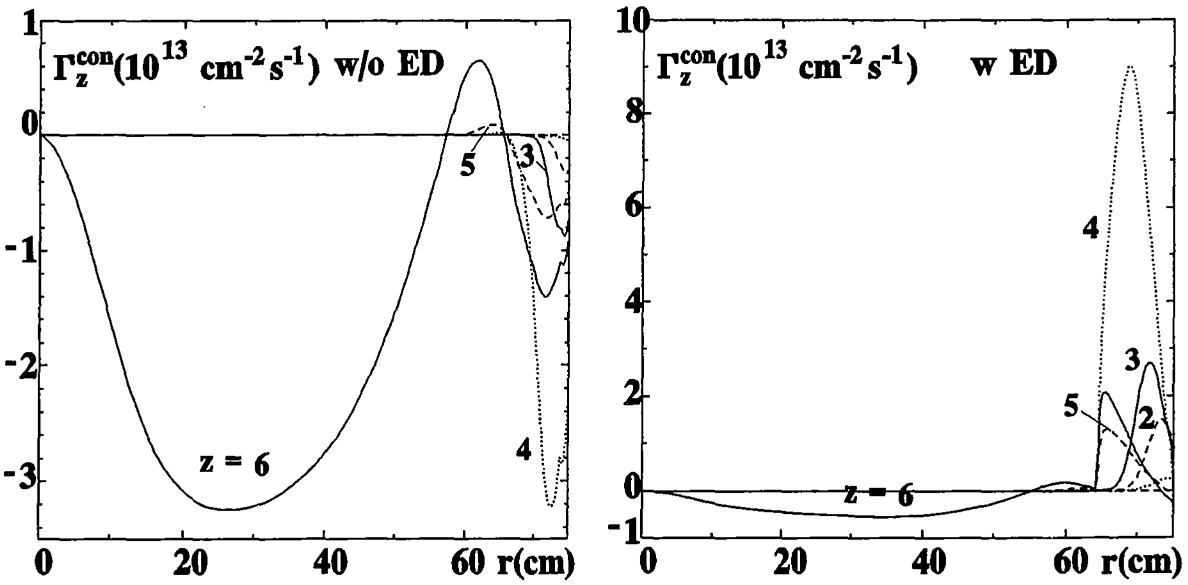

Figure 9 Calculated convective component of the flux density of different charge states of carbon impurity.

Such alterations in the particle densities are caused by changes in the diffusive and convective components of the particle fluxes whose radial profiles are presented in Fig.8 and Fig.9. It can be seen that stochastization alters both diffusion and convection but in the latter case the changes are of an especially dramatic character. In the case without ED this part of the flux is purely neo-classical; at the edge it is governed predominantly by the radial gradient of the density of the main ions and, being negative, directed toward the plasma centre. The situation changes dramatically with stochastization: electric field and friction with deuterons drag impurities to the LCMS and their convection velocity becomes positive in the stochastic layer. Nevertheless for the ions of $Z \leq 4$ this component of the flux remains unimportant in comparison with the diffusive one even with ED. As it will be shown in the next Section changes in the profiles of these states are governed mainly by the reduction of the electron temperature with stochastization and decrease of their ionization rate. For H-like particles and nuclei convection competes effectively with diffusion; as a result a transport barrier is produced which leads to the reduction of the density of these particles in the plasma core (see Section 4.3).

10.2.3 Additionally Heated Discharges with Neon Puffing

In this section the applicability of the approach for description of the transport of energy and particles in the stochastic layer (section 2) is demonstrated for conditions of additionally heated discharges. This is of importance because without ED the transport characteristics of these discharges differ significantly from ohmic plasmas discussed above. We confine ourselves by consideration of neon impurity which was puffed in to create a peripheral radiating layer[17].

Fig. 10 shows the radial profiles of the total density of neon ions and their radiation calculated by RITM for the conditions of shots 14514 (without ED, power of additional heating $P_{add}=3.6$ MW, volume averaged electron density $<n_e> \approx 5.3\cdot10^{13}cm^{-3}$ at $t\approx 6s$) and 13927 (with ED, $P_{add}=4.5$ MW, $<n_e> \approx 3.53\cdot10^{13}cm^{-3}$). In agreement with observations the ratio between the total power radiated by Ne and the product of the central Ne density and $<n_e>$ is increased by a factor of 3-4 in the case with ED. Moreover the absolute magnitude of this ratio agrees also with the measurements: it rises from 4.7 to $12\cdot10^{-38}MW\cdot cm^6$ in experiment and from 5.8 to $14\cdot10^{-38}MW\cdot cm^6$ in the modelling.

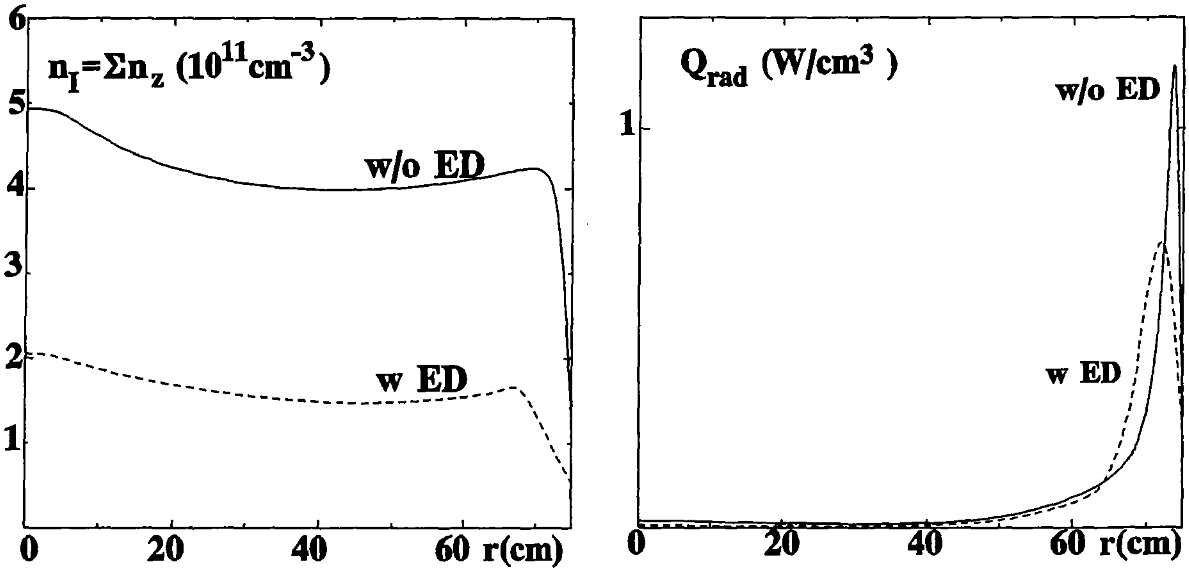

Figure 10 Calculated radial of the total density of neon ions and density of power radiated from them.

10.3 Conclusion.

Stochastization of the magnetic field at the plasma periphery is an experimentally proven approach to control the behaviour of plasma and impurities in tokamaks. Theoretical modelling of this behaviour is of importance to understand better the physical processes in thermonuclear devices.

To perform such a modelling the information on the Chirikov parameter and on the diffusivity of the lines of force in the stochastic layer given by the mapping code MASTOC has been used. The effective radial transport coefficients for heat and main particles have been estimated on the basis of well-known approaches[2,3,5]. Effective diffusivities and convection velocities of impurity ions are found from an analytical treatment of impurity motion along stochastic field lines. The one-dimensional code RITM, taking self-consistently into account the interaction of plasma and impurities in the domain inside the last closed magnetic surface, has been used to solve the transport equations.

The results of calculation are in good agreement with the data of measurements on the tokamak Tore-Supra which is equipped with ergodic divertor producing a peripheral stochastic layer with a width of 20% of the plasma minor radius. The computation reproduces well changes in the profiles of the plasma and impurity parameters by activation of the ED: decrease of the temperature and its gradient in the stochastic zone, steepening of $T_e(r)$ in the plasma core, increase of the plasma density at the edge, reduction of the concentration of intrinsic impurities by a factor of 3 with simultaneous increment of the edge radiation, increase of the power radiated per one ion of seeded impurities.

Interpretation of the results on the basis of simple qualitative models allows to identify the causes of the effects cited above:

steepening of the temperature profile outside the stochastization zone follows from the contraction of the current channel and from the increase of the ohmic heating in the plasma core;

increase of the edge density results from the change in the balance between convection and diffusion of the main ions in the stochastic zone;

reduction of the total impurity density is caused by the diminution of the impurity yield with decreasing edge temperature and by changes in the convective transport in the stochastic layer: friction with the main ions flowing along field lines and action of the parallel electric field leads to convection of impurity ions toward the plasma boundary and "impurity screening" arises;

reduction of the plasma temperature in the stochastic zone leads to a longer life-time of Li-like impurity ions which are the main radiator and therefore it leads to larger radiation losses.

In spite of a remarkable agreement of the results of one-dimensional modelling with experimental data it is important to proceed to two- and three-dimensional models which are already used for modelling of configurations with poloidal divertors and mechanical limiters. In the case of the ED this is dictated by the segmentation of the coils which generate the perturbations of the magnetic field. Moreover a coherent approach to describe the behaviour of magnetic field lines and motion of charged particles e.g. by means of Monte-Carlo methods would make the determination of transport coefficients in a stochastic layer more reliable.

References

1. C.DeMichelis et al, Nucl. Fusion **35** (1995) 1133
2. A.B.Rechester, M.N.Rosenbluth Phys. Rev. Letters **40** (1878) 38
3. A.Samain et al, Phys. Fluids B **5** (1993) 471
4. A.Grosman et al Proc. 2d European Fusion Programme Workshop (Bruxelles: Royal Military Academy) (1994) 236
5. H.Capes et al, Contrib. Plasma Phys. **32** (1992) 192
6. J.F.Luciani et al Phys. Rev. Lett **51** (1983) 1664
7. S.I.Braginskii in Reviews of Plasma Physics, Consultants Bureau (Leontovich M A Ed.) vol 1 (1995) 205
8. K.W.Wenzel, D.J.Sigmar Nucl. Fusion **30** (1990) 1117
9. Breton C et al. Nucl. Fusion **31** (1991) 1774
10. Tokar' M Z et al, to be published in J. Nucl. Mater.
11. Tokar' M Z Plasma Phys. Controlled Fusion **36** (1994) 1819; Physica Scripta **51** (1995) 665
12. Hinton, Hazeltine, Rev. Mod. Phys. **48** (1976) 239

13. P.H.Rebut et al Phys. Fluids B3 (1991) 2209

14. M.Baelmans et al, Proc. 22th European Conf. on Controlled Fusion and Plasma Physics (Innsbruck: European Physical Society) vol 19C (1995) p IV-321

15. Ph. Ghendrih et al. Contrib. Plasma Physics **32** (1992) 179

16. B.Unterberg et al 1993, Proc. 20th European Conf. on Controlled Fusion and Plasma Physics (Lisboa: European Physical Society) vol 17C (1995) p 663

17. A.Grosman et al, J. Nucl. Mater. **220-222** (1995) 188

11. 2D plasma edge transport modeling of DED operation

M. Baelmans, P. Börner, B. Küppers, D. Reiter
Forschungszentrum Jülich GmbH

11.1. Introduction

In order to assess the effects of enhanced cross field transport, as expected during DED operation, on the edge plasma characteristics in TEXTOR, a series of simulation runs was carried out with the EB2-EIRENE code. The EB2 code [3] computes the two dimensional plasma flow (one cross field co-ordinate and one co-ordinate for the flow along the field in an axi-symmetric configuration. This latter co-ordinate is projected into the poloidal plane). This flow is, in general, driven by the boundary conditions (e.g., particle and energy flow from the core into the edge region), the plasma sink action of the limiters and wall surfaces, and the MHD-fluid dynamical forces. For all cases studied here the flux-surface separating the core and the plasma edge region was chosen at a=40 cm. The wall was taken at a=55 cm, hence the computational domain was a poloidal ring bounded by these two (non- concentric, due to the Shafranov shift) circles.

For the parallel flow direction classical transport laws in the high B-field approximation are adopted, whereas in the cross field direction purely diffusive transport, with ad hoc anomalous transport coefficients (as free model parameters) are assumed. For the computations presented here the flow is assumed to be strictly ambipolar (no electrical currents) and all generically diamagnetic flows (in the $\nabla\Psi \times \vec{B}$ direction) are neglected. This reduces the EB2 model to the original B2 model [10]. Hence only first order effects are studied here, excluding from discussion, e.g., asymmetries caused by other than purely configurational effects.

Dominant terms in the balance equations near the limiters are non-local sources and sinks due to elastic and in-elastic interaction of the plasma with the cloud of neutral particles formed there. The recycling neutrals and their influence on the plasma flow is treated on a linear but fully kinetic level by the EIRENE Monte Carlo Code [11].

A consistent description of neutral and charged particle transport is obtained by a specially designed linkage between these two codes, which operate on the same numerical grid and run in an iterative mode until overall convergence [12].

Only steady states are considered here. These are identified by the estimated global "residuals" for the particle, momentum and energy balance equations. The iterations are stopped if these residuals indicate a characteristic time constant of the system of one second or slower.

Two series of runs have been performed: firstly a density and power scan using a validated cross field transport model obtained from previous studies for typical discharges in TEXTOR, with the toroidal belt pumped limiter ALT-II acting as main limiter. The appropriate boundary conditions and transport coefficients in these "standard operating conditions" (see below) are adopted from those identified with RITM-EB2-EIRENE [1]. The second series was run on the identical configuration, using identical boundary conditions and model parameters except for the anomalous cross field transport coefficients. These latter coefficients have been modified to account for the perturbed field configuration in such a way that the parallel transport along the inherently three-dimensionally (inclined) perturbed field is translated into an effective cross field transport in the unperturbed configuration. By doing this enhanced cross field transport laws are obtained from the magnetic field calculations in [2].

11.2. Specifications for the EB2-EIRENE Model

11.2.1. Geometrical Aspects

The computational domain is the poloidal segment between the a=40 cm and the a=55 cm magnetic surfaces (see figure 1).

The flux surface with a minor radius of 46 cm is taken to be centered at a major radius of 1.75 m and a Shafranov shift of 6 cm is assumed. Into the resulting orthogonal mesh both the ALT II limiter, positioned at 46 cm minor radius and 45 degrees underneath the outer equatorial plane, and the bumper limiter on the high field side are introduced. This is done by a local distortion of the mesh in the very neighborhood of the plasma facing components to match the non-orthogonal surfaces, such that each mesh cell either lies completely inside or completely outside the solid structure. The mesh cells inside the solid objects are then isolated from the remaining computational domain.

The toroidal field is taken to be inversely proportional to the major radius R with a reference value of 2.25 T at R = 1.75 m. The poloidal magnetic field B_θ is determined by the assumption of constant magnetic flux between flux surfaces and from a prescribed plasma current enclosed by a magnetic flux surface. This leads to

$$\int_{\psi_1}^{\psi_2} B_\theta R dr = C \ , \tag{1}$$

where ψ_1 and ψ_2 label magnetic flux surfaces, R the major radius and r the minor radius. Further,

$$\oint B_\theta(\theta, r) d\theta = I(r) = \int_0^r j(r) dr \ . \tag{2}$$

In the present study a total plasma current of 350 kA[1] and a radial dependence of the current density inside the separatrix:

$$j(r) = j_o(1 - (\frac{r}{a_0})^2)^{q_a} \tag{3}$$

was assumed, with

$$q_a = \frac{2\pi}{\mu_0} \frac{a_0^2}{R_0} \frac{B_0}{I_p} = 5.0 \frac{a_0^2}{R_0} \frac{B_0\,(\mathrm{T})}{I_p\,(\mathrm{MA})} \tag{4}$$

and j_o is determined by the total plasma current I_p [3].

Outside the separatrix the toroidal current density is assumed to be zero.

11.2.2. Equations and Transport Coefficients

In the ideal case of a pure hydrogenic plasma ($Z_i = 1$; $n \equiv n_i = n_e$) the five standard B2 equations [10] for the evolution of ion density n, the parallel and radial flow velocity components $V_{\|}$ and V_r, and electron and ion temperatures T_e and T_i written in an orthogonal co-ordinate system with one co-ordinate along the magnetic flux surface in the poloidal cross-section (u^θ) and one co-ordinate normal to the flux surface (u^r) are solved. For multi-fluid computations

---

[1] In the magnetic calculations in [2] utilized below the plasma current was 420 kA. For defining the "reference model" without DED operation we resort to parameters from 350 kA discharge simulations, because those have been most extensively validated against experiments.

an additional continuity equation and momentum equation is solved for each ion species. The ion temperatures are assumed to be the same for all ion species. The resulting equations are listed in appendix A.

Since the computations presented here have been performed without explicit consideration of intrinsic impurities such as Carbon or Oxygen, a radial radiation profile is introduced, with profile parameters matched from experimental information. The profile shape is assumed to be given by the fitting expression :

$$P(r) = \left(1 - \left(\frac{r - r_{max}}{a - r_{max}}\right)^2\right) \cdot P_{max}$$

within the radial segment determined by the condition $((r - r_{max})/(a - r_{max}))^2 < 1$, where :

$P(r)$	:	radiated power in W/m^3
P_{max}	:	maximum radiated power density W/m^3
r	:	radial co-ordinate
r_{max}	:	minor radius at which the profile peaks
a	:	minor radius where the profile is cut off

In all calculations described here the following values have been used :

P_{tot}[kW]	122.7	total radiated power
a[m]	0.462	minor radius where the profile is cut off
r_{max}[m]	0.6*0.462	minor radius where the profile peaks

Table 1: Parameters for radiation profile

With this assumption only a minor fraction of the P_{SOL} is radiated within the edge region considered here, namely 14 kW. The radiation profile is taken to be the the same for all cases in order to reduce the number is parmeters. In more self-consistent calculations still to be done the widening of the radiation profil and the increase in P_{tot} during ergodized field operation, even at reduced impurity levels (as observed in TORE SUPRA and modelled with the RITM code) must be taken into account.

For the transport parallel to the magnetic field classical transport coefficients are employed. Kinetic corrections to account for velocity space effects are introduced via flux limiting factors as defined in [3]. These guillotine factors for the classical parallel transport fluxes are set to 0.2 and 0.4 for electron heat flux and parallel ion viscosity respectively. These values have been matched from more detailed kinetic computations [4], but, should be rather insensitive parameters for the low recycling conditions (hence: small parallel gradients only) studied here.

11.2.2.1. Cross Field Transport for "Standard Conditions"

It has been found from previous code validation for TEXTOR conditions that radial transport coefficients depend on heating scenarios [5].

Therefore flux surface averaged radial transport coefficients used here have been deduced from earlier modeling results with RITM-EB2-EIRENE [1] for I-mode conditions. However, the inward pinches used there have now been condensed with the radial diffusivities to effective cross field transport coefficients resulting in the same radial fluxes. This was done for cases with varying degree of radiation cooling (ranging from 30 to 90 %), and resulting power fluxes into the edge plasma between 0.3 and 1.3 MW.

This led to the following choice of radial transport coefficients, for the different power fluxes into the edge plasma region :

D_r[m^2/s]	0.6	radial particle diffusion coefficient
$k_{r,e}$[m^2/s]	1.5	radial thermal diffusion coefficient for electrons
$k_{r,i}$[m^2/s]	2.5	radial thermal diffusion coefficient for ions
v_r[m^2/s]	1.0	radial viscous diffusion coefficient

Table 2: Radial diffusivities for $P_{SOL} = 0.3$ MW (90 %= radiation)

D_r[m^2/s]	1.2	radial particle diffusion coefficient
$k_{r,e}$[m^2/s]	5.0	radial thermal diffusion coefficient for electrons
$k_{r,i}$[m^2/s]	5.0	radial thermal diffusion coefficient for ions
v_r[m^2/s]	1.0	radial viscous diffusion coefficient

Table 3: Radial diffusivities for $P_{SOL} = 0.9$ MW (60 %= radiation)

The radial transport coefficients are then determined as $\kappa_r^e = nk_{r,e}$, $\kappa_r^i = nk_{r,i}$ and $\eta_r^i = mnv_r$.

$D_r[\mathrm{m}^2/\mathrm{s}]$	1.8	radial particle diffusion coefficient
$k_{r,e}[\mathrm{m}^2/\mathrm{s}]$	9.0	radial thermal diffusion coefficient for electrons
$k_{r,i}[\mathrm{m}^2/\mathrm{s}]$	7.5	radial thermal diffusion coefficient for ions
$v_r[\mathrm{m}^2/\mathrm{s}]$	1.0	radial viscous diffusion coefficient

Table 4: Radial diffusivities for $P_{SOL} = 1.3$ MW (30 %= radiation)

11.2.2.2. Transport Model Simulating DED Operation

Strictly, ergodization is a three-dimensional phenomenon. To describe its effects within the two-dimensional model considered here a set of enhanced flux surface averaged cross field transport coefficients is derived.

This effective cross field transport model is applied to the region inside the separatrix only, where stochastization is expected to be important. Outside the separatrix in the scrape-off layer the transport coefficients are set constant and equal to the value at the separatrix.

The model for the transport of particles and heat in a stochastic magnetic field [6] combines features of both radial and parallel transport and the magnetic topology. (The divergence of field lines alone does not lead to additional transport in the radial direction [6].) Various approaches to combine the stochastic field structure with transport laws in unperturbed fields are discussed in the literature. Our simulations described here are based on the approach proposed by Rechester and Rosenbluth [7] for the heat transfer and by Samain et al. [6] for the particle transport.

This results in a modified radial electron thermal diffusivity :

$$\kappa_r^{erg} = \kappa_r^{std} \cdot [1 + \frac{\exp(2x_T) - 1}{2\sqrt{x_T}}] \ . \tag{5}$$

where κ_r^{erg} and κ_r^{std} are the electron thermal diffusivities in case of ergodization and in standard (unperturbed) conditions, respectively. $x_T = L_T/L_c$ is the ratio of a characteristic temperature gradient length L_T to the Kolmogorov correlation length L_c. The latter depends on the degree of island overlapping : $L_c \approx qR\sigma_{Chir}^{-4/3}$ [8] , with q the safety factor and σ_{Chir} the Chirikov parameter [9]. It can be seen that for $x_T \longrightarrow 0$, i.e., for large correlation lengths in case of weaker overlapping of magnetic islands the stochastization effect becomes weaker $\kappa_r^{erg} \longrightarrow \kappa_r^{std}$.

L_c is determined from magnetic field structure calculations, and the ratio x_T (and hence L_T) can then be determined from the transcendent equation:

$$(e^{2x_T}-1)\cdot(1+\frac{\alpha\lambda_c}{L_c x_T}) = 2\frac{D_{FL}}{L_c}\frac{\kappa_{\|}}{\kappa_r^{std}} , \tag{6}$$

with λ_c the electron mean free path, $\alpha \approx 15$ and $D_{FL} = L_c \sum B_{r,k}^2$, the magnetic diffusivity. This latter diffusivity is again obtained from magnetic field calculations from the amplitudes of the magnetic perturbations $B_{r,k}$.

Similarly, an expression for the particle diffusivity can be found :

$$D_r^{erg} = D_r^{std} \cdot [1 + \frac{\exp(2x_n)-1}{2\sqrt{x_n}}] . \tag{7}$$

where D_r^{erg} and D_r^{std} are, respectively, the particle diffusivities in case of ergodization and in standard conditions. $x_n = L_n/L_c$ is the ratio of a characteristic density gradient length L_n to the Kolmogorov correlation length L_c. x_n is again given implicitly by a transcendent equation :

$$e^{2x_n} - 1 = \sqrt{2}x_n \frac{D_{FL}c_s}{D_r^{norm}} , \tag{8}$$

with $c_s = \sqrt{(T_e + T_i)/m_i}$ the ion sound velocity.

The data on stochastization of the magnetic field structure for TEXTOR with DED operation is taken from [2]. From the data in this paper the following Kolmogorov length L_c, safety factor q and magnetic diffusivity D_{FL} are deduced at various radial positions (see table 5). L_c and q are then linearly interpolated, for D_{FL} a logarithmic interpolation is employed.[2]

The resulting enhanced radial transport diffusivities are shown in figure 2 and 3 for particle and electron energy transport, respectively. The diffusivities are most strongly affected around 42 cm minor radius. The enhancement of radial particle diffusivity is up to a factor 5.2 for high edge densities and up to a factor 11 for low edge densities, whereas for the enhancement of radial thermal diffusivity this factor is even 18 in case of low edge density and low power flux (strong radiation cooling). Inside this region, at smaller radii, transport is practically not affected. By contrast, transport coefficients are still enhanced in the scrape-off layer.

---

[2] By the time of writing this there is still a substantial uncertainty in these parameters, as there is, certainly, also in transport models based on such parameters. However, as the modelling results below indicate, the TEXTOR boundary plasma will remain in low recycling mode also during DED operation. Hence these differential effects on cross field transport should well be accessible experimentally, because interpretation of radial plasma edge density and temperature profiles is not contaminated by large unknown recycling sources in the SOL.

r[cm]	D_{FL}[cm]	L_C[cm]	q	σ_{Chir}
38	3.44×10^{-5}		2.5	
39		267	2.625	1.66
40	6.51×10^{-4}		2.75	
41		115	2.875	3.12
42	5.86×10^{-3}		3	
43		106	3.125	3.32
44	3.75×10^{-3}		3.25	
45		87	3.375	3.85
46	1.56×10^{-2}		3.5	

Table 5: Magnetic data for DED radial transport model

11.2.3. Boundary Conditions

On the **magnetic flux surface at 40 cm**, the ion density n_i and total edge power P_{SOL} are prescribed and varied as model parameters. The ion density there was varied from $n_i = 1 \times 10^{19}\text{m}^{-3}$ to $n_i = 4 \times 10^{19}\text{m}^{-3}$ with increments of $1 \times 10^{19}\text{m}^{-3}$.

The power fluxes into the plasma edge region through this surface, varied from 0.3 to 0.9 and 1.3 MW, is made up of two parts : the fraction by the electrons and the fraction carried by the ions. Again, based on the results of RITM-EB2-EIRENE applications mentioned earlier [1], this lead to the following choice of boundary conditions for the energy equations :

$\underline{P_{SOL} = 0.3 \text{ MW :}}$

$Q_{r,e} = 120$ kW

$Q_{r,i} = 180$ kW

$\underline{P_{SOL} = 0.9 \text{ MW :}}$

$Q_{r,e} = 450$ kW

$Q_{r,i} = 450$ kW

$\underline{P_{SOL} = 1.3 \text{ MW :}}$

$Q_{r,e} = 780$ kW

$Q_{r,i} = 520$ kW

Finally,

$V_\theta = 0$ m/s, i.e., zero poloidal velocity, is chosen as boundary condition for the parallel momentum equation.

At the **limiters**, were magnetic field lines intersect material boundaries, plasma sheath edge conditions are imposed :

$$V_\theta = \frac{B_\theta}{B} c_s$$

$$Q_\theta^e = 4.8 T_e n V_\theta$$

$$Q_\theta^i = (3.0 T_i + 0.5 T_e) n V_\theta$$

Boundary conditions at the **vessel structure**, parallel to magnetic flux surfaces, are fixed by prescribing radial profile decay lengths there. The SOL decay lengths at a minor radius of 55 cm are set to rather high values :

$$\lambda_n = \lambda_{T_e} = \lambda_{T_i} = 21.2 \ = \mathrm{cm}$$

The radial fluxes to the other **material boundaries aligned with the magnetic surfaces** are set to zero. It should be noted that this parameter is largely unknown and will need further investigation. This important parameter, however, is very sensitive to H_α diagnostics [5] and can hence be determined from further model validation.

11.2.4. Neutral Particle Transport Modeling

The neutral particles originate at material structures from recombining plasma flux. The emission of neutral D-atoms and D_2-molecules from an incident flux of energetic D^+-ions or D-atoms is computed by the TRIM code [11], and used as source and boundary conditions for neutral particle transport in the EIRENE code. In all results presented here Carbon limiters and a Stainless Steel vessel was assumed. The atomic and molecular data are taken from [13], and the selection of relevant processes from that database was the EIRENE-default selection for hydrogenic plasmas (loc.cit). The linear Boltzmann equation for neutral particle transport in the plasma background provided by the EB2 modeling is then solved by Monte Carlo techniques. The source terms in the MHD-fluid equations for the next EB2 iteration are then obtained as appropriately weighted functionals of the neutral particle distribution function.

Pumping at the ALT-II limiter is simulated by an albedo coefficient for the plasma flux onto surfaces underneath the ALT-II blade. The same effective pumping speed (as inferred from independent 3D Monte Carlo simulations of the detailed ALT-II vacuum system and plasma scoop region) was assumed for incident Deuteron and Helium ions.

11.2.5. Impurity Modeling and Radiation

In order to study the influence on the Helium removal efficiency of ALT-II under DED conditions a few runs have been performed including Helium ions (He^{+} and He^{++} as additional ion species and He atoms as additional neutral particle species. In this case the same transport coefficients and boundary conditions were used for He^{+} and for He^{++} as for D^{+}. Only the
the edge density prescribed at the innermost flux surface of the computational domain with minor radius of 40 cm was modified to:

$$n_{\mathrm{He}^{+}} \approx 0.0 \ ,$$

$$n_{\mathrm{He}^{++}} = 0.05 n_{\mathrm{D}} \ .$$

resulting in a somewhat higher electron density in each case as compared to the corresponding case without Helium.

11.3. Results

In this section the numerical results for the various edge densities and edge power levels obtained from the DED transport model are compared with those for operation under standard conditions. General features of DED operation can be inferred from inspecting the results of the most extreme cases considered here, i.e., edge densities of $1 \times 10^{19}\mathrm{m}^{-3}$ and $4 \times 10^{19}\mathrm{m}^{-3}$ and power fluxes into the edge of 0.3 MW and 1.3 MW (next subsection). Subsequently, particle and energy fluxes as well as heat power loads to the various material components are discussed, as well as inferred quantities such as the impact of ergodization on physical sputtering yields.

11.3.1. Global Features

In figures 4 to 11 contour plots for the edge plasma profiles: density, electron and ion temperature and ion particle sources are shown for the 4 extreme cases mentioned above. The results are given for "standard" conditions and for the DED-cross field transport model described above. Figures 4 to 7 show the cases with low edge densities ($1 \times 10^{19}\mathrm{m}^{-3}$) for low and high edge power values (0.3 MW and 1.3 MW respectively). Generally the impact of recycling is very low, as can be inferred from the poloidal uniformity of the plasma profiles. Figures 8 to 11 summarize the cases with high edge densities ($4 \times 10^{19}\mathrm{m}^{-3}$). Due to enhanced local recycling relatively high ion densities are build up underneath the ALT-II blade (see also table 6). This is particularly pronounced in the high power case with DED operation and indicates improved particle removal with DED operation (see below).

$n_{SOL,max}$	Q = 0.3 MW		Q = = 1.3 MW	
n	without DED	with DED	without DED	with DED
$1 \times 10^{19}\mathrm{m}^{-3}$	$6.56 \times 10^{18}\mathrm{m}^{-3}$	$4.84 \times 10^{18}\mathrm{m}^{-3}$	$7.30 \times 10^{18}\mathrm{m}^{-3}$	$4.95 \times 10^{18}\mathrm{m}^{-3}$
$4 \times 10^{19}\mathrm{m}^{-3}$	$3.57 \times 10^{19}\mathrm{m}^{-3}$	$2.32 \times 10^{19}\mathrm{m}^{-3}$	$3.69 \times 10^{19}\mathrm{m}^{-3}$	$8.97 \times 10^{19}\mathrm{m}^{-3}$

Table 6: Maximum SOL density

The most pronounced feature in the DED cases is the strong flattening of profiles (as expected from enhanced radial transport). and temperature profiles. For a fixed edge density at 40 cm minor radius this leads to higher SOL densities. On the other hand, for the same edge input power, temperatures are lowered at 40 cm minor radius and slightly enhanced in the SOL, as compared to standard operation conditions.

This leads to a spatially wider distribution of particle sources, but not to a transition into a significantly higher recycling regime. (This is, because, still, a significant fraction of re-ionization takes place in the confined plasma region, in all cases considered here.)

Hence: DED divertor operations seems to act just oppositely as poloidal divertor operation, which, generally, upon transition into high recycling mode, leads to a peaking of recycling profiles.

This is shown in table 7, where the peaking factor $\frac{S_n}{\int S_n dV/V}$ is listed, with S_n the local particle source and V the volume. For the high power cases the recycling at the vessel becomes much more important during ergodization (quantified below), see figures 7 and 11.

Inspecting in somewhat more detail the plasma profiles, here exemplarily in the outer mid-plane, the effect of ergodization on the plasma edge becomes more evident:

The overall enhancement of the particle diffusivity leads to flatter density profiles (see figure 12). Therefore, with prescribed edge density at 40 cm minor radius, the SOL densities are also increased. The local maximum of the radial particle transport coefficient (see figure 2) leads to a locally more flattened ion density profile near 42 cm minor radius. The higher SOL densities

	Q = 0.3 MW		Q = 1.3 MW	
	without DED	with DED	without DED	with DED
$1 \times 10^{19} m^{-3}$	148	37	126	92
$4 \times 10^{19} m^{-3}$	131	20	211	147

Table 7: Peaking factor for particle sources

mostly result in larger fluxes to the scoops under DED operation (and, consequently, more particles are pumped at the fixed pumping speed of the vacuum system (see table 8). Since this leads to larger particle fluxes from the core under otherwise identical conditions (see table 9), this then results in somewhat steeper particle density profiles near r = 40 cm, where the particle diffusivity is not effected by the ergodization.

However, for the extremest case of high density and high edge power, there seems to be a saturation, probably caused by stagnation of flow under the ALT-II blades, due to enhanced local recycling in the scoop region (see also section).

Furthermore the enhanced particle fluxes crossing at r = 40 cm (reduced particle confinement time) at given input power level lead to significantly lower plasma temperatures in the edge. This can clearly be seen for the radial ion temperature profile in figure 13, where the standard radial transport model was used, as compared to fig. 14.

	Q = 0.3 MW		Q = 1.3 MW	
	without DED	with DED	without DED	with DED
$1 \times 10^{19} m^{-3}$	$1.50 \times 10^{21} s^{-1}$	$5.19 \times 10^{21} s^{-1}$	$6.66 \times 10^{21} s^{-1}$	$1.23 \times 10^{22} s^{-1}$
$4 \times 10^{19} m^{-3}$	$6.86 \times 10^{21} s^{-1}$	$1.02 \times 10^{22} s^{-1}$	$3.04 \times 10^{22} s^{-1}$	$2.66 \times 10^{22} s^{-1}$

Table 8: Particle fluxes to the scoops

	Q = 0.3 MW		Q = 1.3 MW	
	without DED	with DED	without DED	with DED
$1 \times 10^{19} m^{-3}$	$1.37 \times 10^{21} s^{-1}$	$4.90 \times 10^{21} s^{-1}$	$3.98 \times 10^{21} s^{-1}$	$7.63 \times 10^{21} s^{-1}$
$4 \times 10^{19} m^{-3}$	$3.20 \times 10^{21} s^{-1}$	$7.92 \times 10^{21} s^{-1}$	$1.16 \times 10^{22} s^{-1}$	$1.09 \times 10^{22} s^{-1}$

Table 9: Particle fluxes to the edge

From these tables also the existance of a moderate flux amplification both in the STANDARD and the DED model. If one compares the fluxes into the edge with not only the fluxes to the scoop region, but instead with the total partcile fluxes to ALT-II, one finds flux amplification factors between 3 and 7 (the larger values at large density, high power conditions). Again, these amplification factors seem to be rather uneffected by the cross field transport law.

11.3.2. Particle Fluxes and Heat Loads

Next we will discuss the effects of ergodization on particle fluxes and heat load onto the various plasma facing components of the Tokamak. We distinguish between the plasma facing section of the ALT-II limiter blade, referred to as "ALT" in the figures, and the surfaces underneath the ALT-blade connecting the blade with the vessel, to represent in a 2D fashion the 16 scoops and 8 plenum boxes. These surfaces will be referred to as "SCOOPS". Furthermore there is the bumper limiter "BUMPER" and the vessel structure referred to as "WALL". We will first describe the influence of DED operation on particle and heat loads to the ALT-limiter. Next, the effects on particle and heat load on the SCOOPS are described. Finally, we will discuss the change in particle and energy fluxes to BUMPER limiter and to the WALL.

11.3.2.1. Fluxes to ALT-Limiter

Figure 15 shows that the particle fluxes Γ_{ALT} are only slightly influenced by ergodization. By contrast, as shown in figures 16 and 17 the electron and ion energy fluxes $P_{el.,ALT}$ and $P_{ion,ALT}$ strongly decrease with the DED radial transport model. This leads to a decrease in total power to ALT (see figure 18, $P_{tot} = P_{el.,ALT} + P_{ion,ALT} + 13.6\text{eV} \cdot \Gamma_{ALT}$, by a factor 1.4 to 2.2. This effect increases with the power level in the edge plasma region.
The effect of ergodization on the local peak power load is even more pronounced (see figure 19) : the peak power load is decreased by a factor 1.8 to 4.3. However, the peak power load does not longer show a dependency on edge densities. This results in a strongest effect for low plasma edge densities. Note that distinct from usual divertor operation this reduced power load is not a consequence of enhanced local recycling, but instead of a direct redistribution of plasma flow onto a larger area (without complicated neutral particle flow patterns to be established and maintained as required, e.g., in the dynamic gas target regime currently envisaged for the poloidal divertor in ITER).

11.3.2.2. Fluxes to the Scoops

The particle fluxes to the scoops increase with ergodization. From figure 20 it can be seen that this flux enhancement is less pronounced for higher edge densities and even reversed for high density and high edge power. When the local recycling (plasma plugging) builds up a plasma density maximum under the blades, i.e. for high density and high edge power, then also the total power load is significantly decreased (see figure 21). Due to a flatter profile the maximum local power load is decreased by a factor 2 only in DED operation (see figure 22). However, these power fluxes are an order of magnitude lower than those to the ALT-limiter.

11.3.2.3. Fluxes to the Bumper Limiter

The particle fluxes to the bumper limiter are increased by a factor 1.8 to 7.2 (see figure 23) during DED operation. The total power (figure 24) is also increased by a factor ranging between 1.1 and 4. The maximum power load to the bumper limiter (figure 25) is hardly changed with ergodization at all. It should, however, be noted here that these fluxes only include fluxes to the side walls of the limiter, since material surfaces parallel to the magnetic field lines do not receive any fluxes at all due to the boundary conditions prescribed there (see section).

11.3.2.4. Fluxes to the Wall

As expected DED operation leads to significantly higher densities and temperatures near the vessel structures. Both particle fluxes and total power are strongly increased (see figures 26 and 27). However, due to the large area available the enhanced maximum power load of a several ten kW/m^2 (see figure 28) still remains far below any critical value.

11.3.2.5. Pumping

Pumping is facilitated during DED operation due to larger particle fluxes in the scoop region (see above). All cases show a somewhat larger ratio of Deuteron flux to the albedo surfaces (scoops) to the Deuteron flux into the SOL (i.e., the radial particle flux at r=46cm) as compared to Helium. This de-enrichment is not altered significantly during DED operation, all fluxes are increased by roughly the same factor in the corresponding cases. Hence neither beneficial nor negative effects (other than the larger fluxes to the pumps at fixed pumping speed) can currently be concluded for Helium removal.

A key difference to poloidal divertor operation is the fact that regardless of the cross field transport model (standard or DED) the edge plasma is rather little affected by altering the modeled pumping speed for fixed plasma conditions at the core-edge interface (r=40cm here). Due to the configurational difference of the ALT-II limiter to poloidal divertors in all cases the re-ionization in the core plasma of neutral atoms recycled at the ALT-blade remains the dominant particle sink (hence the low recycling regime encountered throughout), whereas in poloidal divertors reduced particle removal usually results in fundamental different operation conditions (high recycling regime with strong plasma temperature gradients along the field, due to transition from convected to conducted heat transport).

11.3.3. Sputtering Yields

Favorable effects of ergodization can most directly be seen from the reduced surface sputtering rates. Figures 29 and 30 show the impact of DED operation on global sputtering rates due to impact of energetic charge exchange deuterium atoms and due to impact of plasma ions accelerated in the near surface electrostatic sheath potentials. Except for the low density high edge power case, ergodization lowers the global sputtering rates by up to a factor 3.5 for sputtering by atoms and even by a factor of 6.7 for sputtering by plasma ions. Self sputtering, e.g., of C-ions, chemical sputtering, as well as sputtering by Oxygen atoms (due to the accidental resonance of charge exchange between hydrogenic atoms and singly charged oxygen ions) still need to be assessed in further simulations.

11.4. Conclusions

The EB2-EIRENE code system or parts thereof (EIRENE, B2) are currently extensively used worldwide to interpret various plasma experiments, to validate plasma transport models and to predict conditions in the edge plasma regions in future experiments, e.g., in ITER. This code system has been applied also to TEXTOR discharges for many years (in fact: the code development itself and first applications ever had been carried out for TEXTOR in the late eighties).

From a computational plasma edge transport model validated against typical TEXTOR experimental conditions in the last year a so called "DED transport model" has been derived. This model combines anomalous cross field transport, classical transport along the field and independent magnetic topology calculations for perturbed field lines.

This results, at least locally, in strongly enhanced cross field transport as compared to the anomalous coefficients inferred from previous simulations of TEXTOR discharges.

A series of simulation runs has been carried out, varying the plasma density and power level in the edge plasma region (hence the degree of radiation cooling). From a comparison of the results from this study of cases with and without the DED enhanced cross field transport we find largely relaxed heat load conditions on the exposed surfaces, significantly reduced sputter rates and more favorable conditions for particle removal (reduced particle confinement at fixed installed pumping speed). Physically this is caused by a direct redistribution of the plasma flow in the SOL, which is probably the most significant distinction to poloidal divertor operation in other Tokamaks:

in the latter this redistribution of power loads is via the neutral particle channel and associated charge exchange and other power spreading mechanisms (with the resulting technologically conflicting requirements of both trapping the neutrals in the divertor (favoring a closed configuration) and removing the plasma facing components from the divertor plasma flow as far as possible (requiring a more open configuration).

The model investigations on DED operation on TEXTOR indicate that many of the favorable features of a high recycling divertor can possibly also be accessed in low recycling conditions, e.g., also with limiters, if the particle and heat flow in the edge plasma region is directly influenced.

Furthermore, due to the low recycling conditions retained under DED operation interpretation of experimental results, e.g., inferring transport coefficients from measured radial edge profiles, is greatly facilitated, as compared to high recycling poloidal divertor operation.

Many important questions in this DED transport model (as compared to the "standard transport model") have still to be addressed, such as e.g., impurity transport, and the consistency of core and edge plasma transport simulations. The work at least with respect to these two aspects is currently underway.

References

[1] M. Baelmans, D. Reiter, M. Tokar et al., Proc. of 22nd EPS Conf. on Contr. Fus. and Plasma Phys., Bournemouth, U.K., part IV(1995), 341.

[2] A. Nicolai, K.H. Finken, B. Giesen et al., Proc. of 22nd EPS Conf. on Contr. Fus. and Plasma Phys., Bournemouth, U.K., part IV(1995), 321.

[3] M. Baelmans, "Code Improvements and Applications of a Two-Dimensional Edge Plasma Model for Toroidal Fusion Devices",Dissertation at Katholieke Universiteit Leuven, Afd. Toeg. Mechanica, Celestijnenlaan 300A, 3001 Leuven, Belgium (1993).

[4] Y. Igithkanov, IPP-Garching, private communication.

[5] D. Gray, PhD Thesis, Jül-Report, to be printed.

[6] A. Samain, T. Blenski, Ph. Gendrih et al., Phys. Fluids B 5 (1993) 471.

[7] A.B. Rechester, M.N. Rosenbluth, Phys. Rev. Lett. 10 (1978) 38.

[8] De Michelis et al., Nucl. Fus. 35 (1995) 1133.

[9] B.V. Chirikov, Phys. Reports 52 (1979) 265.

[10] B.J. Braams, "Numerical Studies of the Two-Dimensional Scrape-off Layer", Proc. of 11th Eur. Conf. on Contr. Fus. and Plasma Phys., Aachen, 7D-II, pp. 431-434, (1983).

[11] D. Reiter, "The EIRENE code, Version Jan. 92, Usermanual", KFA Jülich report, JÜL-2599 Mar. 1992.

[12] D. Reiter, "Progress in 2-Dimensional Plasma Edge Modelling", J. Nucl. Mat., Vol.196-198, p.241 (1992).

[13] R.K. Janev, et al., (1987). Springer Series on Atoms and Plasmas, Vol. 4.

Appendix : Model Equations

The multi-fluid code EB2 can compute a background plasma in combination with one or more impurity species. For each ion charge state a continuity and a parallel momentum equation is solved. For the ion energy equation thermal equilibrium between all ion species is assumed. The diamagnetic contribution to the poloidal flow velocity is ignored and electron density and velocity follow from the assumption of charge neutrality and absence of an electric current. Classical multi-species theory, Refs. [1] and [2] give rise to a rather complicated system of force-friction relations, both for the parallel and the radial transport. In the B2-model the classical theory is used as a guide to obtain a simplified set of equations for the parallel transport. These equations are consistent with the standard classical theory in the limit when one fluid is dominant and all others are trace impurities. Specifically, the following system of equations is solved for N species :

Continuity of species a :

$$\frac{\partial}{\partial t}(n_a) + \frac{1}{\sqrt{g}}\frac{\partial}{\partial u^\theta}\left(\frac{\sqrt{g}}{h_\theta}n_a V_{\theta,a}\right) + \frac{1}{\sqrt{g}}\frac{\partial}{\partial u^r}\left(\frac{\sqrt{g}}{h_r}n_a V_{r,a}\right) = S_n^a \tag{9}$$

Momentum balance of species a

$$\begin{aligned}
&\frac{\partial}{\partial t}\left(m_a n_a V_{\|,a}\right) + \frac{1}{\sqrt{g}}\frac{\partial}{\partial u^\theta}\left(\frac{\sqrt{g}}{h_\theta}m_a n_a V_{\theta,a}V_{\|,a} - \frac{\sqrt{g}}{h_\theta^2}\eta_\theta^a\frac{\partial V_{\|,a}}{\partial u^\theta}\right)\\
&+\frac{1}{\sqrt{g}}\frac{\partial}{\partial u^r}\left(\frac{\sqrt{g}}{h_r}m_a n_a V_{r,a}V_{\|,a} - \frac{\sqrt{g}}{h_r^2}\eta_r^a\frac{\partial V_{\|,a}}{\partial u^r}\right) =\\
&\quad\frac{B_\theta}{B}\frac{1}{h_\theta}\left[-\frac{\partial p_a}{\partial u^\theta} - \frac{Z_a n_a}{n_e}\frac{\partial p_e}{\partial u^\theta} + c_e\left(\frac{Z_a}{Z_{eff}} - 1\right)Z_a n_a\frac{\partial T_e}{\partial u^\theta} + c_i\left(\frac{Z_a^2}{Z_{eff}^2} - 1\right)n_a\frac{\partial T_i}{\partial u^\theta}\right]\\
&\quad+\sum_{b=1}^{N}F_{ab} + S_{mV_\|}^a
\end{aligned} \tag{10}$$

Diffusion of species a :

$$V_{r,a} = -\frac{D_n^a}{h_r}\frac{\partial}{\partial u^r}(\ln n_a) - \frac{D_p^a}{h_r}\frac{\partial}{\partial u^r}(\ln p_a) \tag{11}$$

Electron energy balance :

$$\begin{aligned}
&\frac{\partial}{\partial t}\left(\frac{3}{2}nT_e\right) + \frac{1}{\sqrt{g}}\frac{\partial}{\partial u^\theta}\left(\frac{\sqrt{g}}{h_\theta}\frac{5}{2}nV_\theta T_e - \frac{\sqrt{g}}{h_\theta^2}\kappa_\theta^e\frac{\partial T_e}{\partial u^\theta}\right)\\
&+\frac{1}{\sqrt{g}}\frac{\partial}{\partial u^r}\left(\frac{\sqrt{g}}{h_r}\frac{5}{2}nV_r T_e - \frac{\sqrt{g}}{h_r^2}\kappa_r^e\frac{\partial T_e}{\partial u^r}\right) =
\end{aligned}$$

$$S_E^e - k\left(T_e - T_i\right) + \frac{V_\theta}{h_\theta}\frac{\partial p_e}{\partial u^\theta} + \frac{V_r}{h_r}\frac{\partial p_e}{\partial u^r} \tag{12}$$

Ion energy balance :

$$\begin{aligned}
&\frac{\partial}{\partial t}\left(\frac{3}{2}nT_i + \sum_a \frac{1}{2}\rho_a V_{\|,a}^2\right) + \\
&\frac{1}{\sqrt{g}}\frac{\partial}{\partial u^\theta}\left[\frac{\sqrt{g}}{h_\theta}\left(\sum_a \frac{5}{2}n_a V_{\theta,a}T_i + \sum_a \frac{1}{2}\rho_a V_{\theta,a}V_{\|,a}^2\right) - \frac{\sqrt{g}}{h_\theta^2}\left(\kappa_\theta^i\frac{\partial T_i}{\partial u^\theta} + \sum_a \frac{1}{2}\eta_\theta^a\frac{\partial V_{\|,a}^2}{\partial u^\theta}\right)\right] + \\
&\frac{1}{\sqrt{g}}\frac{\partial}{\partial u^r}\left[\frac{\sqrt{g}}{h_r}\left(\sum_a \frac{5}{2}n_a V_{r,a}T_i + \sum_a \frac{1}{2}\rho_a V_{r,a}V_{\|,a}^2\right) - \frac{\sqrt{g}}{h_r^2}\left(\kappa_r^i\frac{\partial T_i}{\partial u^r} + \sum_a \frac{1}{2}\eta_r^a\frac{\partial V_{\|,a}^2}{\partial u^r}\right)\right] = \\
&\qquad S_E^i + k\left(T_e - T_i\right) - \frac{V_\theta}{h_\theta}\frac{\partial p_e}{\partial u^\theta} - \frac{V_r}{h_r}\frac{\partial p_e}{\partial u^r}
\end{aligned} \tag{13}$$

where,

$$\begin{aligned}
\sqrt{g}, h_\theta, h_r &= metric\, coefficients, \\
Z_a, m_a &= charge\, number\, and\, mass\, of\, an\, ion\, of\, species\, a, \\
S_n^a, S_{mu_\|}^a &= volume\, sources\, of\, ions\, and\, parallel\, momentum\, for\, species\, a, \\
S_E^e, S_E^i &= volume\, sources\, of\, electron\, and\, ion\, energy, \\
\eta_\theta^a, \eta_r^a &= poloidal\, and\, radial\, viscosity\, coefficients\, for\, species\, a, \\
F_{ab} &= friction\, force\, on\, ion\, species\, a\, due\, to\, species\, b, \\
c_e, c_i &= coefficients\, in\, the\, thermal\, force\, for\, electrons\, and\, ions, \\
D_n^a, D_p^a &= diffusion\, coefficients\, for\, species\, a, \\
\kappa_\theta^{e,i}, \kappa_r^{e,i} &= heat\, conduction\, coefficients, \\
k &= energy\, equipartition\, coefficient.
\end{aligned}$$

Auxiliary physical quantities are the mass density, $\rho_a = m_a n_a$; the electron and ion pressures for species a, $p_e = n_e T_e, p_a = n_a T_i$; the total pressure, $p = p_e + \sum_a p_a$. Further, $k(T_e - T_i)$ is the rate of energy transfer from electrons to ions.

The poloidal coefficients are related to classical parallel coefficients according to $\eta_\theta^a = \left(B_\theta^2/B^2\right)\eta_\|^a$, and similarly for $\kappa_\theta^{e,i}$. For κ_θ^e, there exists a possibility to incorporate a flux limitation. The radial coefficients η_r^a, D_n^a, D_p^a, κ_r^e and κ_r^i are anomalous.

The friction force F_{ab} (which is proportional to $V_{\|,b} - V_{\|,a}$) is taken from [3]. The equipartition coefficient k, parallel heat conduction coefficients $\kappa_\|^e$ and $\kappa_\|^i$ and the parallel viscosity coefficients

$\eta^a_{\parallel}$ are computed using the formulae given in Ref. [3] for the case of a simple plasma (one ionic species), with the following replacements :

Equipartition coefficient :

$$\begin{aligned} Simple\,plasma &: \; k \propto Z_i^2 m_i^{-1} n_i n_e \\ Multiple\,ion\;species &: \; k \propto \sum_a Z_a^2 m_a^{-1} n_a n_e \end{aligned} \tag{14}$$

Parallel electron heat conduction coefficient :

$$\begin{aligned} Simple\,plasma &: \; \kappa^e_{\parallel} \propto Z_i^{-1} \\ Multiple\,ion\;species &: \; \kappa^e_{\parallel} \propto \sum_a Z_a n_a / \sum_b Z_b^2 n_b \end{aligned} \tag{15}$$

Parallel ion heat conduction coefficient :

$$\begin{aligned} Simple\,plasma &: \; \kappa^i_{\parallel} \propto Z_i^{-4} m_i^{-1/2} \\ Multiple\,ion\;species &: \; \kappa^i_{\parallel} \propto \sum_a Z_a^{-2} n_a / \sum_b Z_b^2 n_b \sqrt{2 m_a m_b / (m_a + m_b)} \end{aligned} \tag{16}$$

Parallel ion viscosity coefficient :

$$\begin{aligned} Simple\,plasma &: \; \eta^i_{\parallel} \propto Z_i^{-4} m_i^{1/2} \\ Multiple\,ion\;species &: \; \eta^i_{\parallel} \propto Z_a^{-2} n_a / \sum_b^2 n_b \sqrt{2/(m_a + m_b)} \end{aligned} \tag{17}$$

These expressions are a simplification of the complete multi-species transport theory, but they have a correct limit in the case when one species dominates.

Ionization and recombination rates in combination with atomic data [4] provide information for particle, momentum and energy sources. In addition sinks for the energy equation due to Bremsstrahlung and line-radiation are computed.

References

[1] S.I. Braginskii, “Transport Processes in a Plasma”, in Reviews of Plasma Physics, Vol.1, M. Leontovich, Ed., Consultants Bureau, New York, p.205 (1965).

[2] F.L. Hinton, "Collisional Transport in Plasmas", in "Handbook of Plasma Physics", M.N. Rosenbluth and R.Z. Sagdeev, Eds., North-Holland Publ. Company, New York, Vol.1, p.147 (1983).

[3] NRL Plasma Formulary, NRL Publication 0084-4040, Naval Research.

[4] K. Behringer, "Description of the Impurity Transport Code STRAHL", JET-Report, JET-R(87)08, JET Joint Undertaking, Abingdon, U.K. (1987).

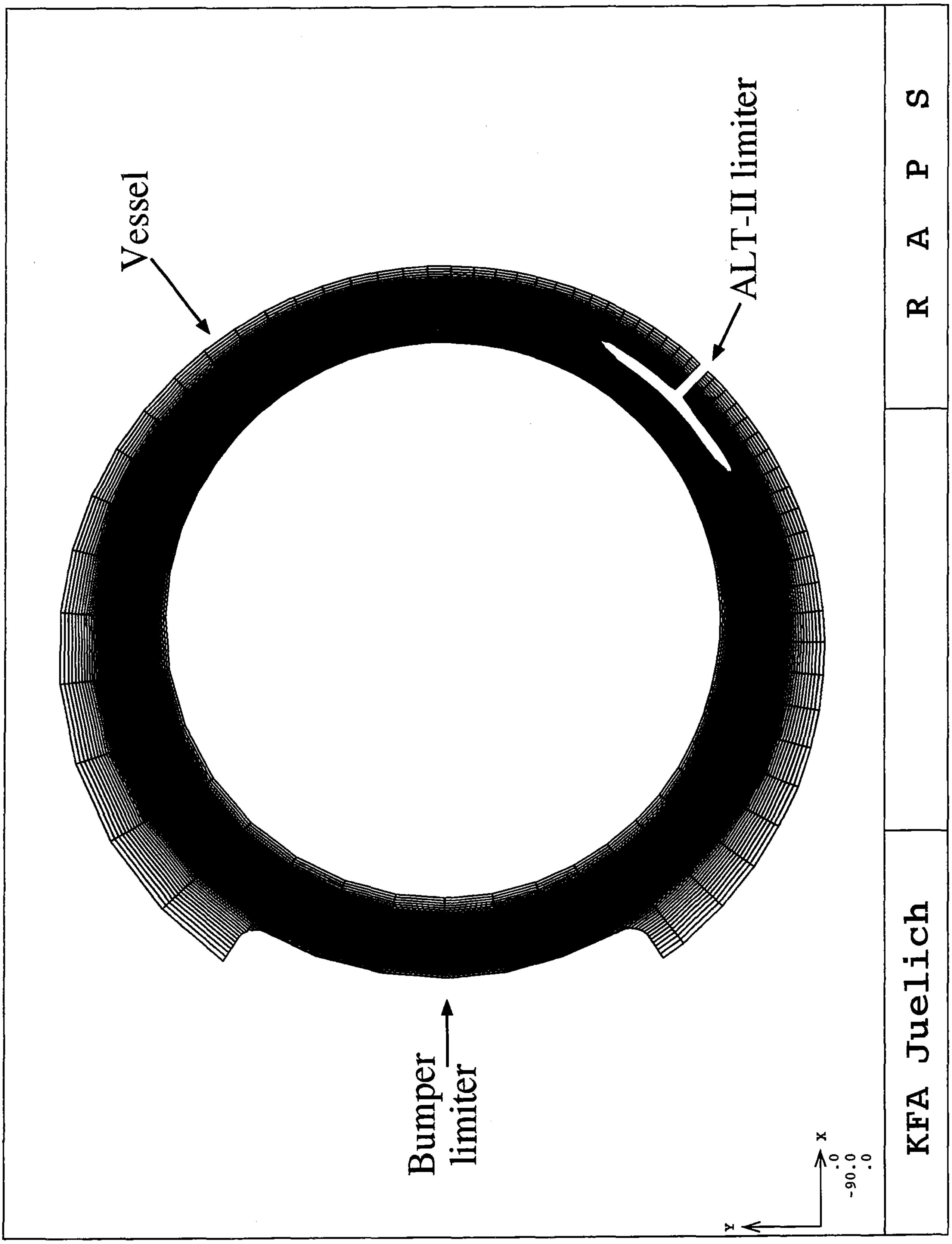

Figure 1: Numerical grid for simulation of the TEXTOR edge with EB2-EIRENE

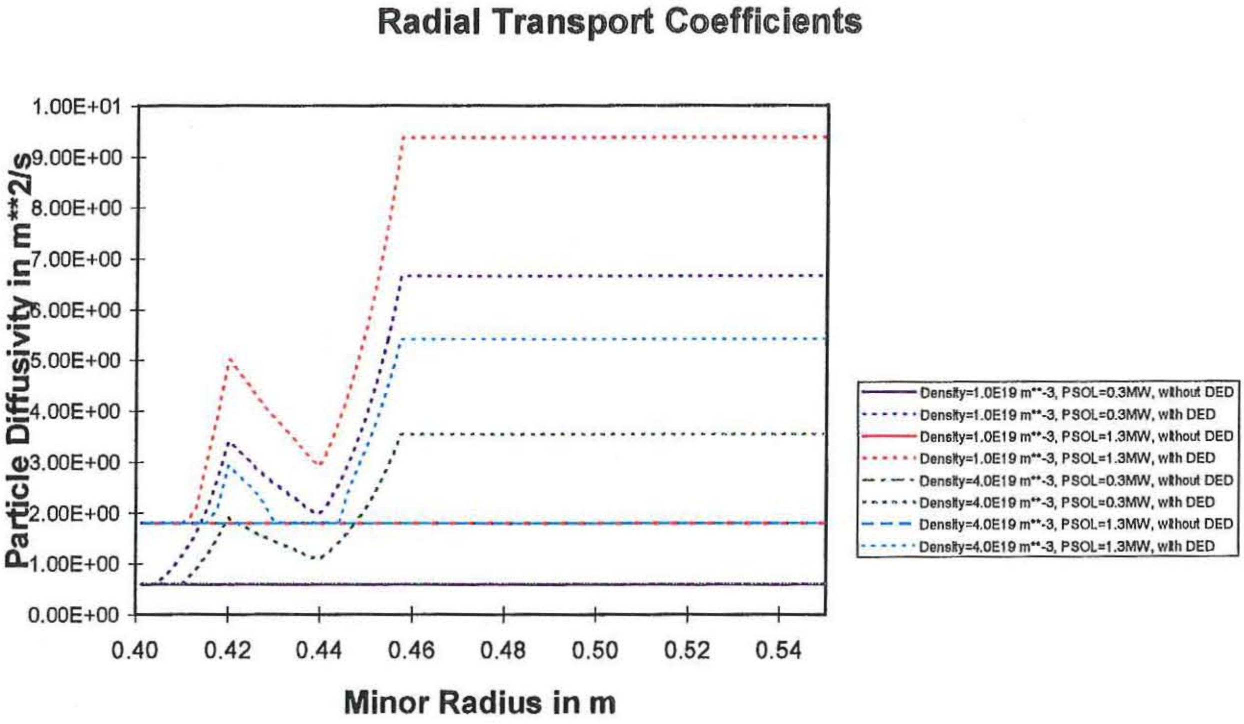

Figure 2: Particle diffusion coefficients

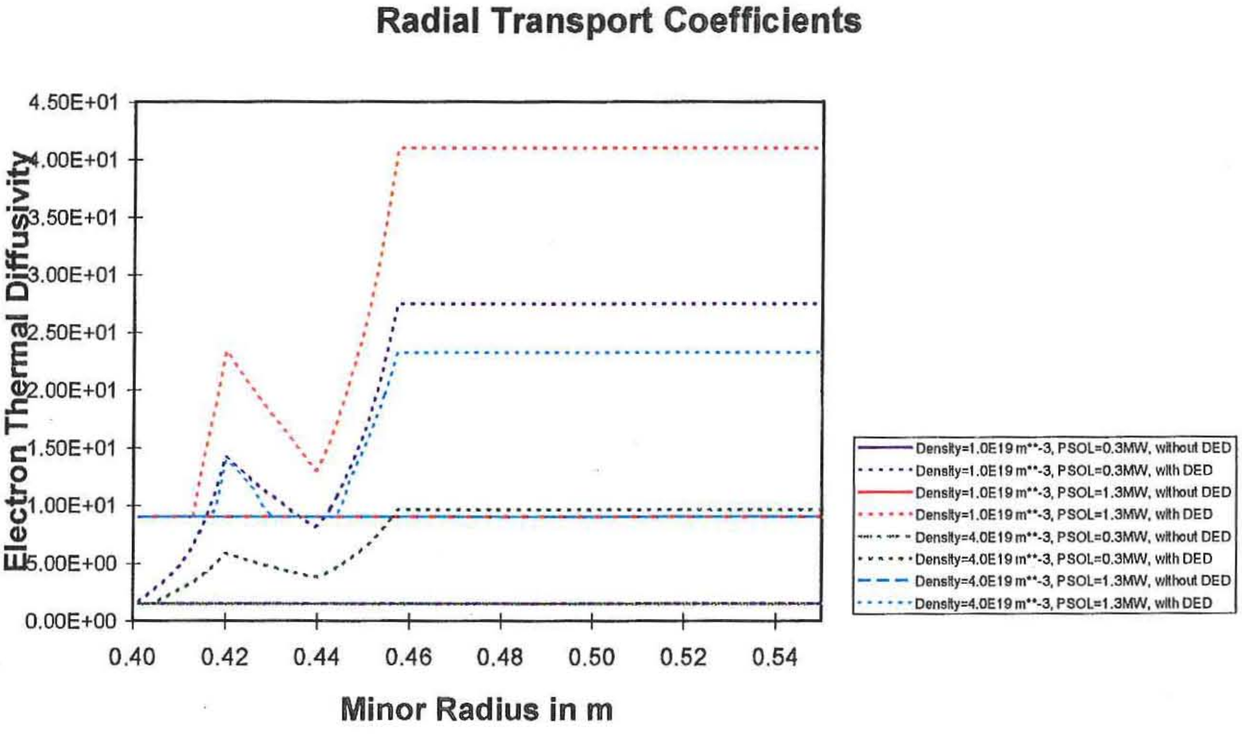

Figure 3: Electron thermal diffusivities

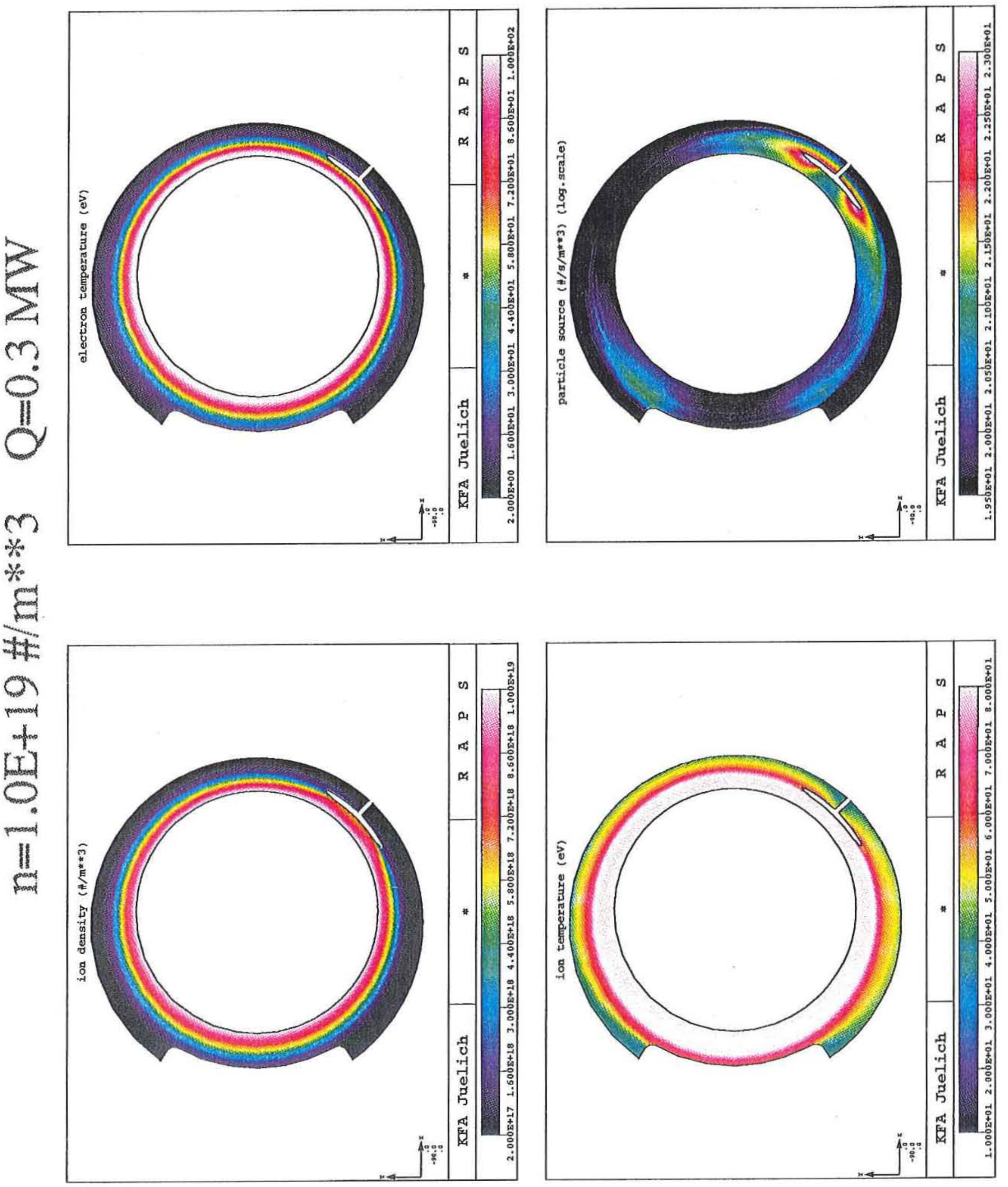

Figure 4: Computational results for $n = 1 \times 10^{19} \mathrm{m}^{-3}$ and Q = 0.3 MW without DED

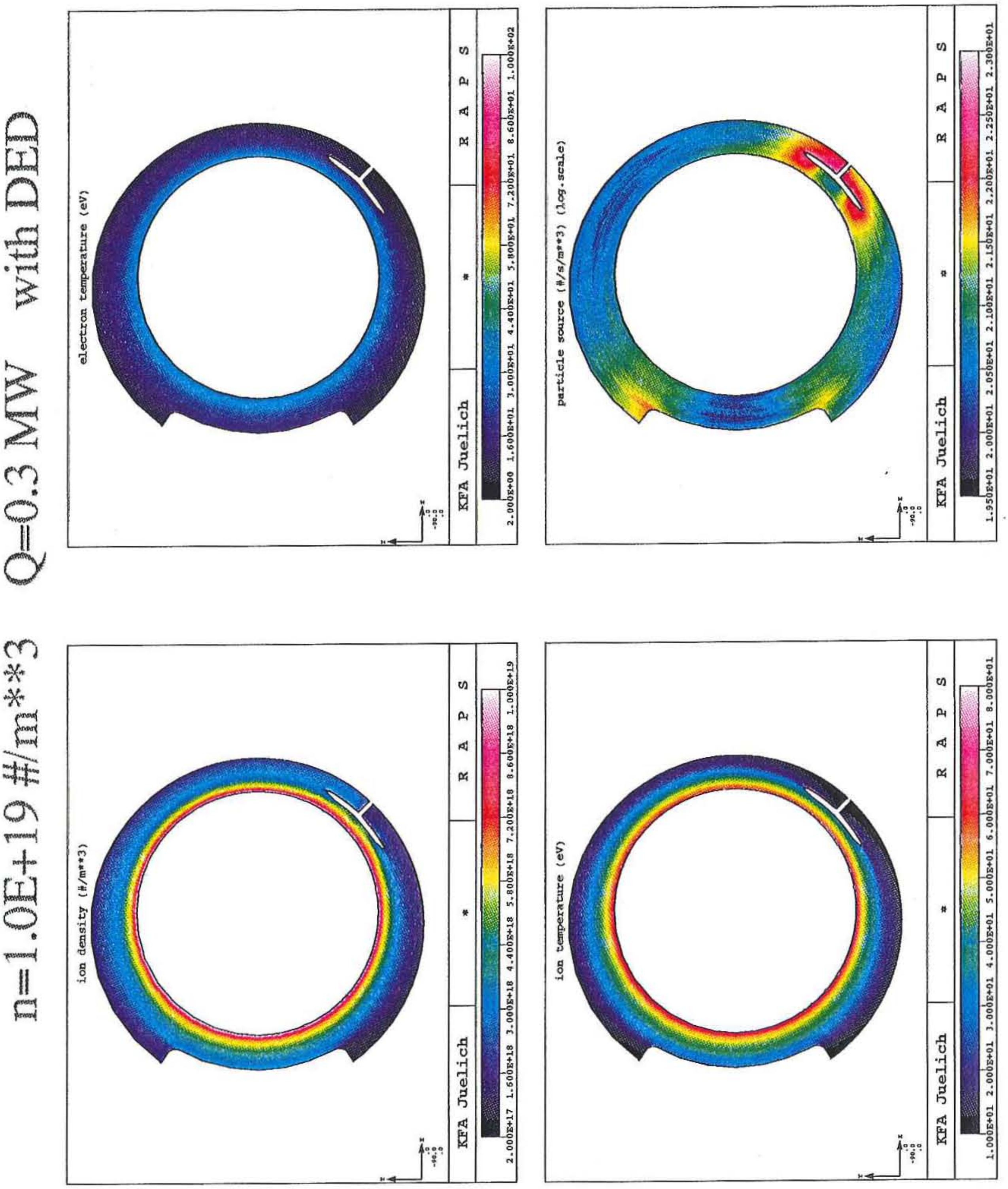

Figure 5: Computational results for $n = 1 \times 10^{19}\text{m}^{-3}$ and Q = 0.3 MW with DED

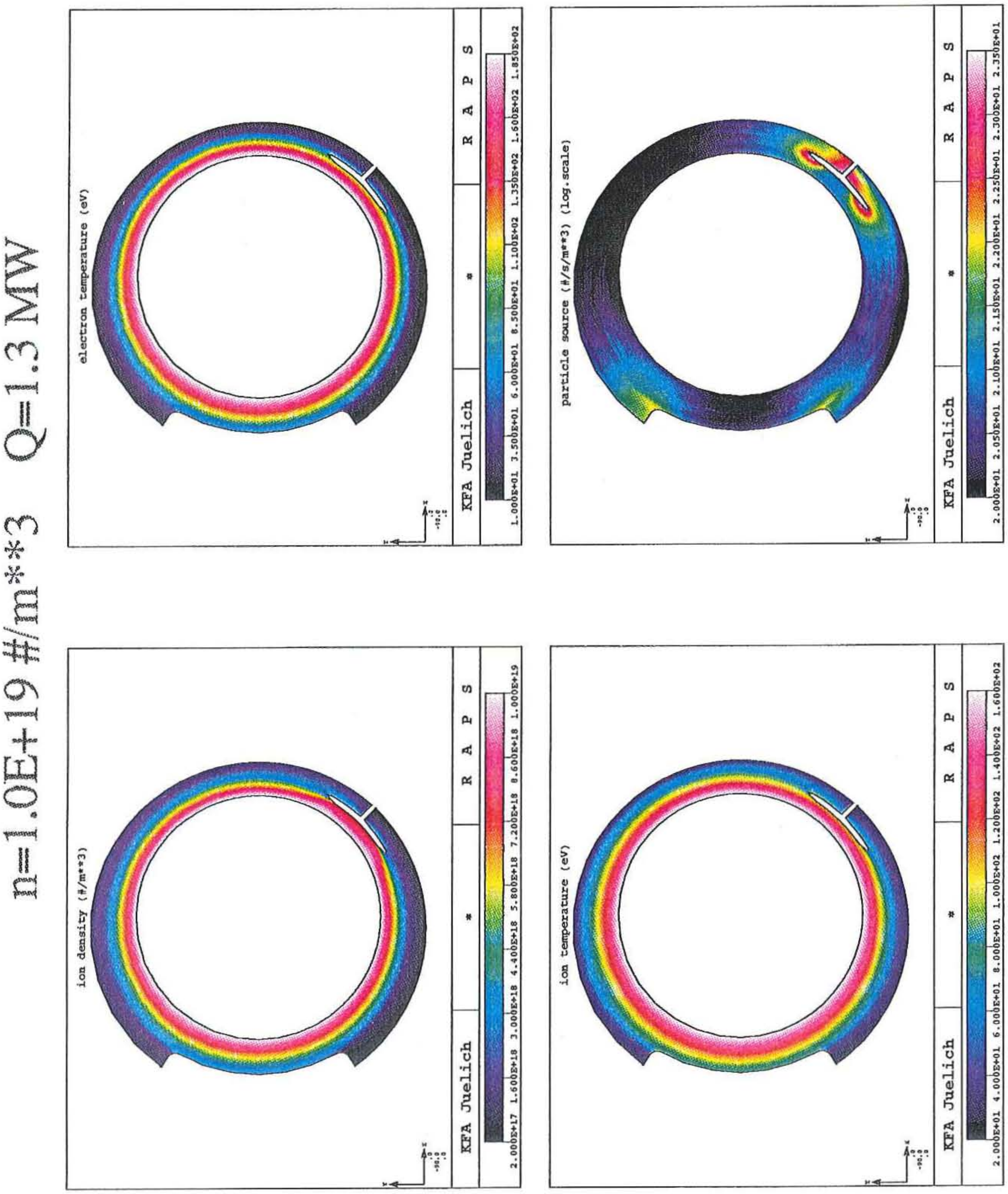

Figure 6: Computational results for $n = 1 \times 10^{19}\mathrm{m}^{-3}$ and Q = 1.3 MW without DED

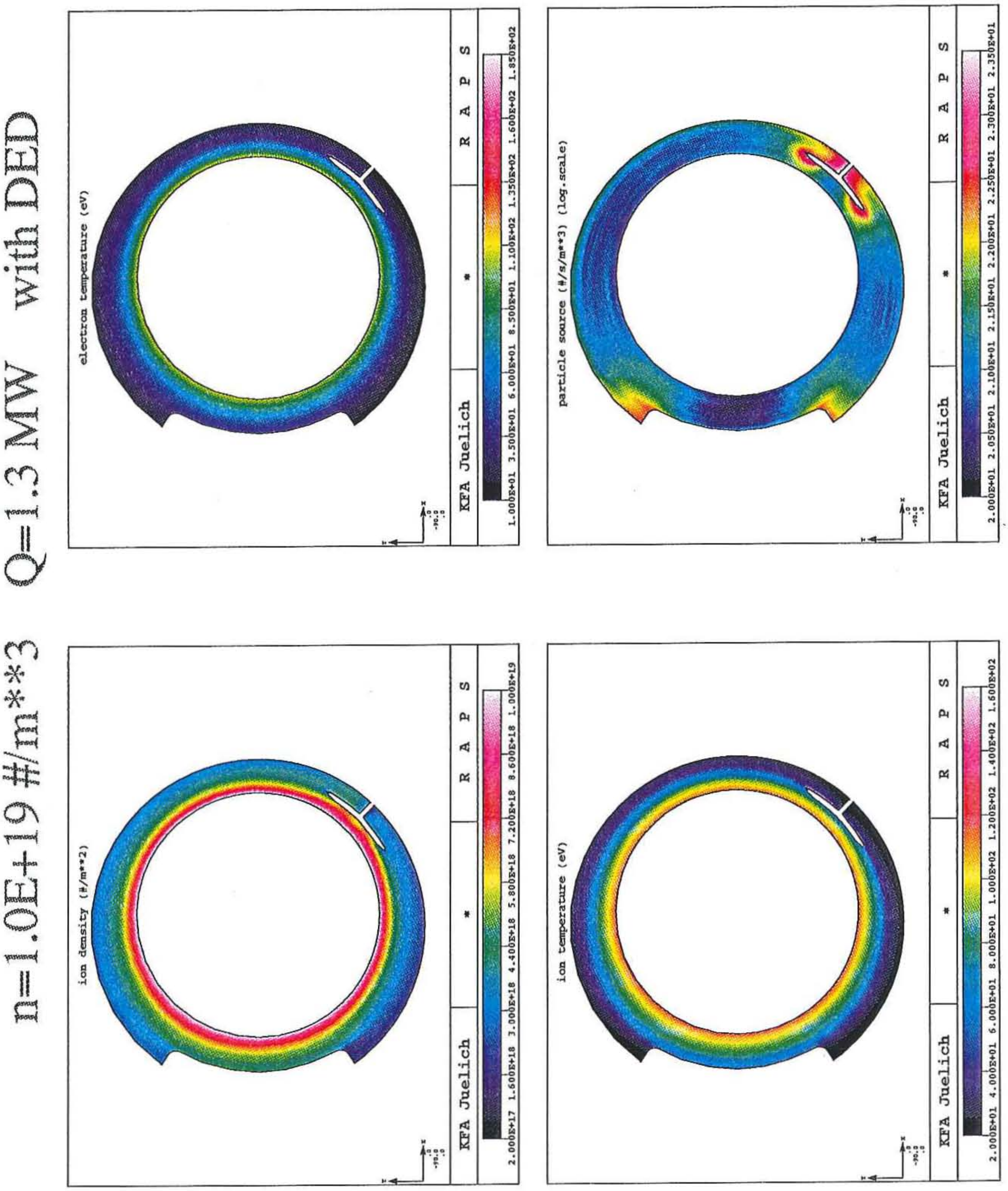

Figure 7: Computational results for $n = 1 \times 10^{19}\mathrm{m}^{-3}$ and Q = 1.3 MW with DED

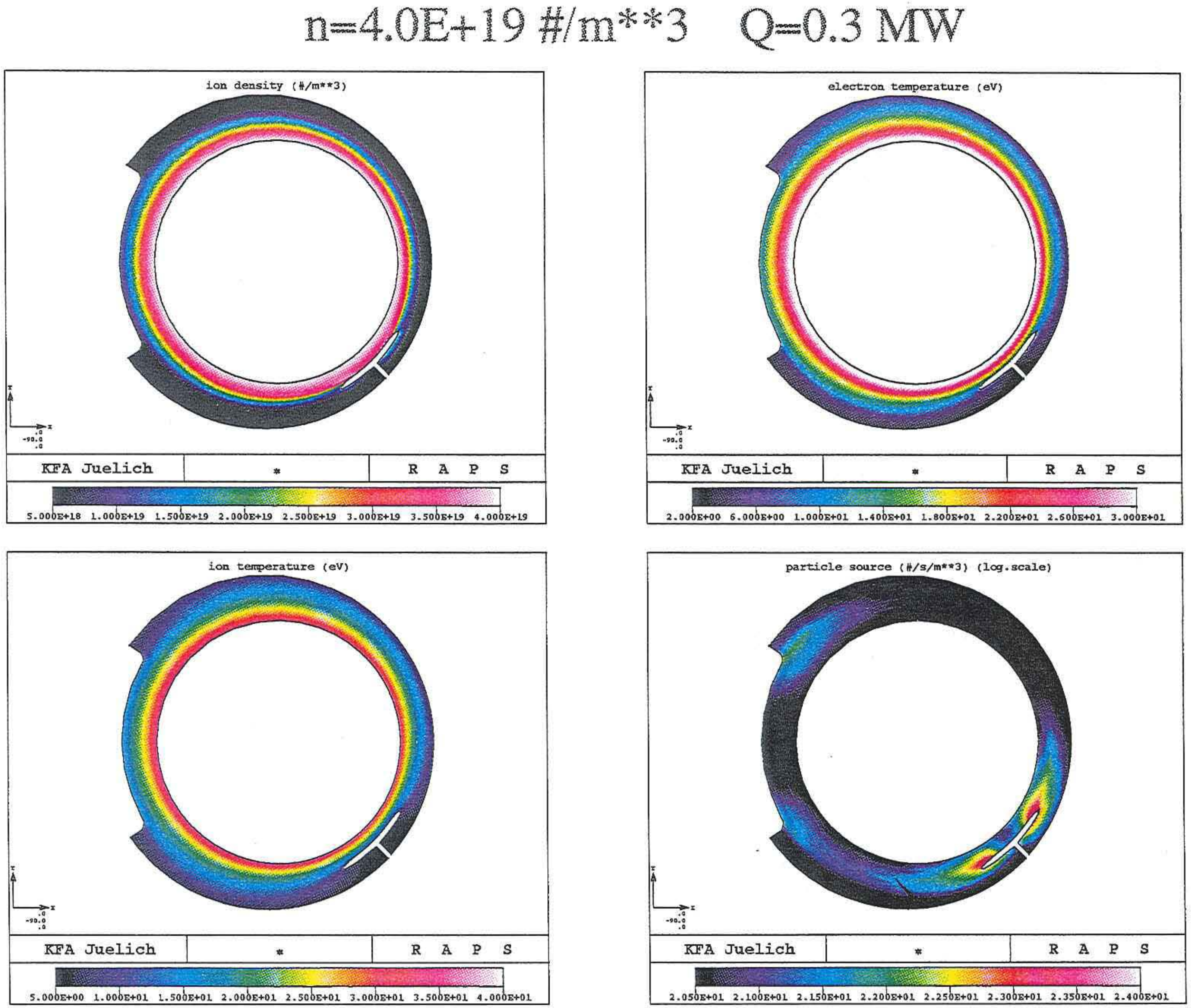

Figure 8: Computational results for $n = 4 \times 10^{19}\mathrm{m}^{-3}$ and Q = 0.3 MW without DED

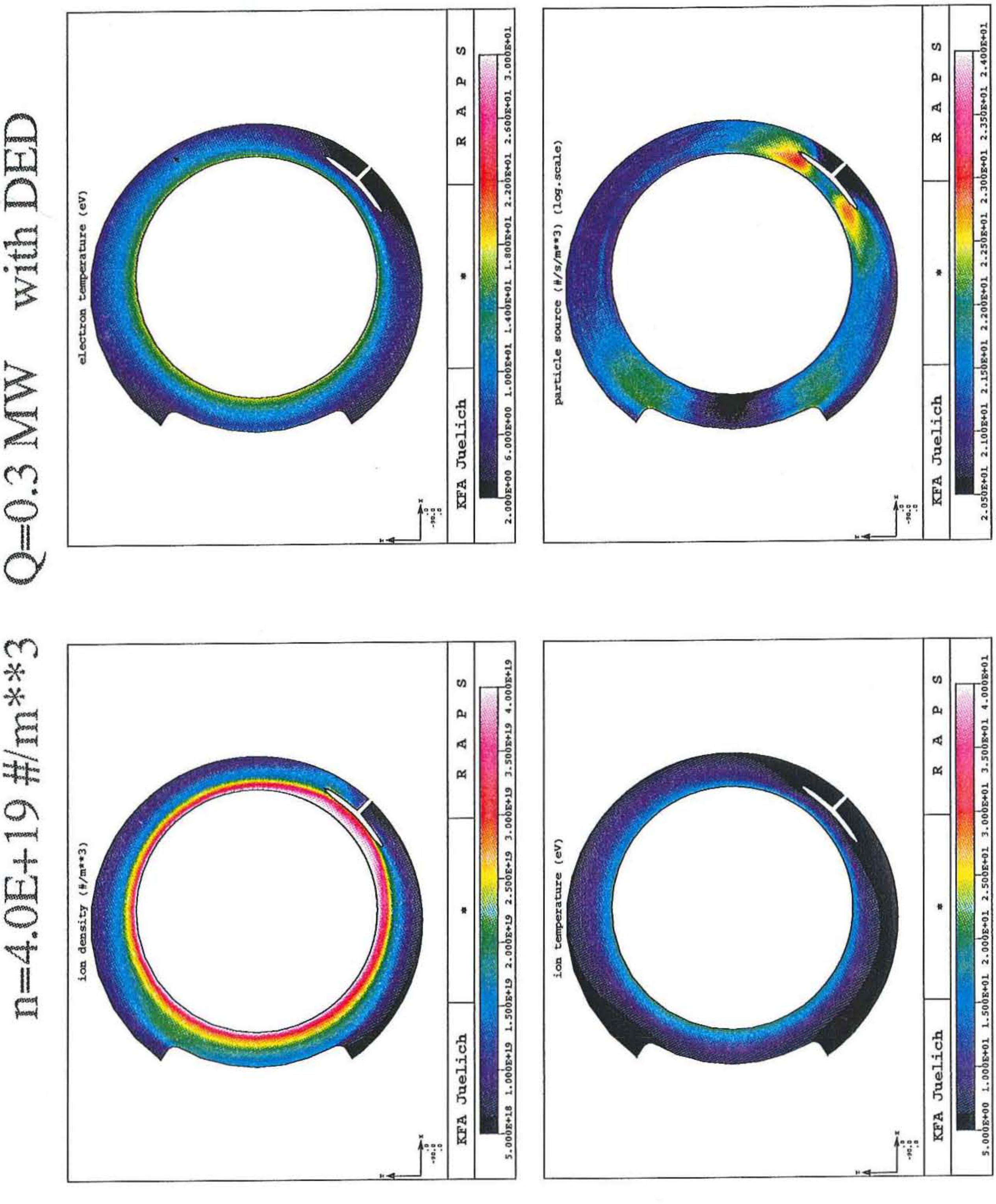

Figure 9: Computational results for $n = 4 \times 10^{19}\mathrm{m}^{-3}$ and Q = 0.3 MW with DED

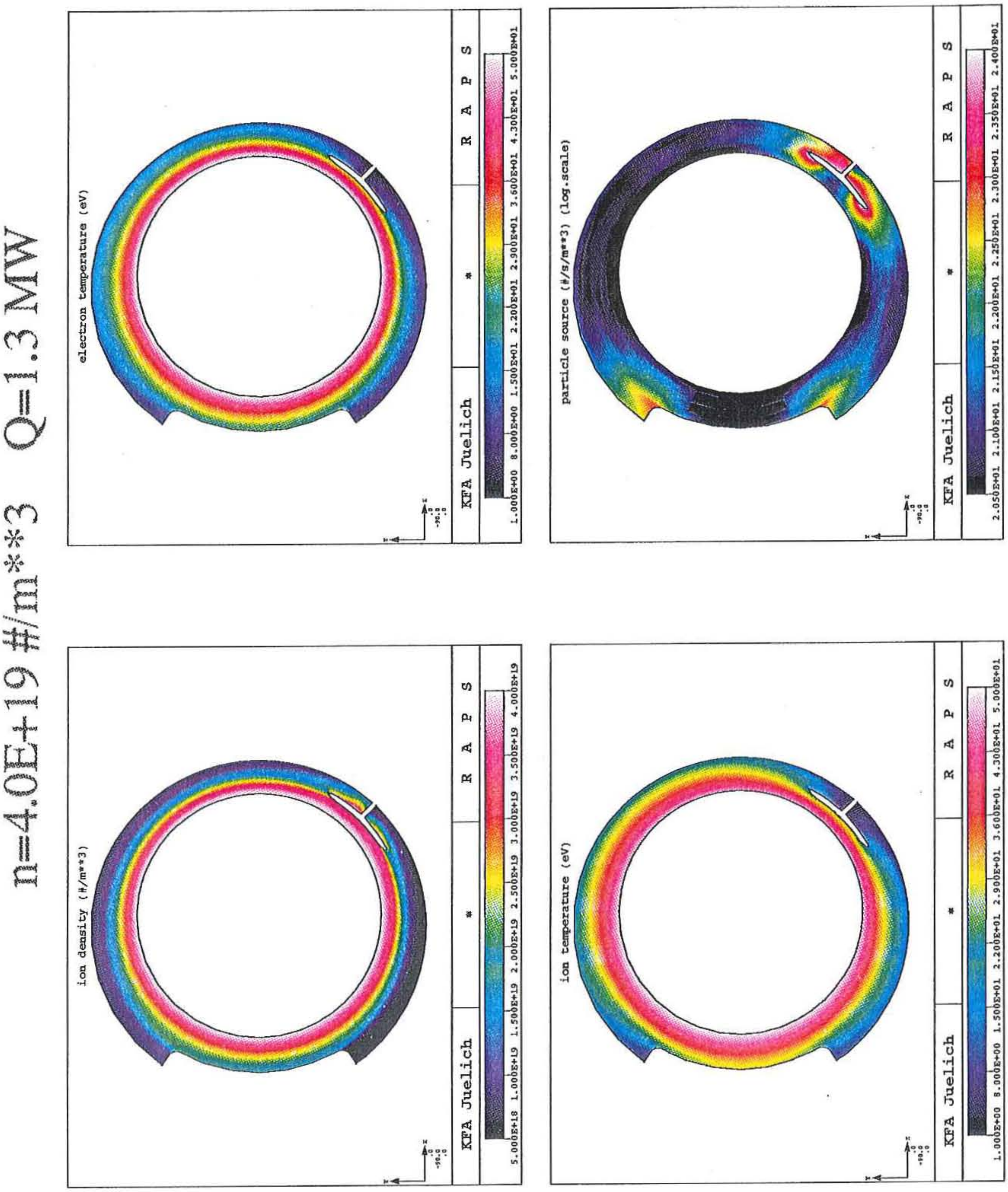

Figure 10: Computational results for $n = 4 \times 10^{19}\mathrm{m}^{-3}$ and Q = 1.3 MW without DED

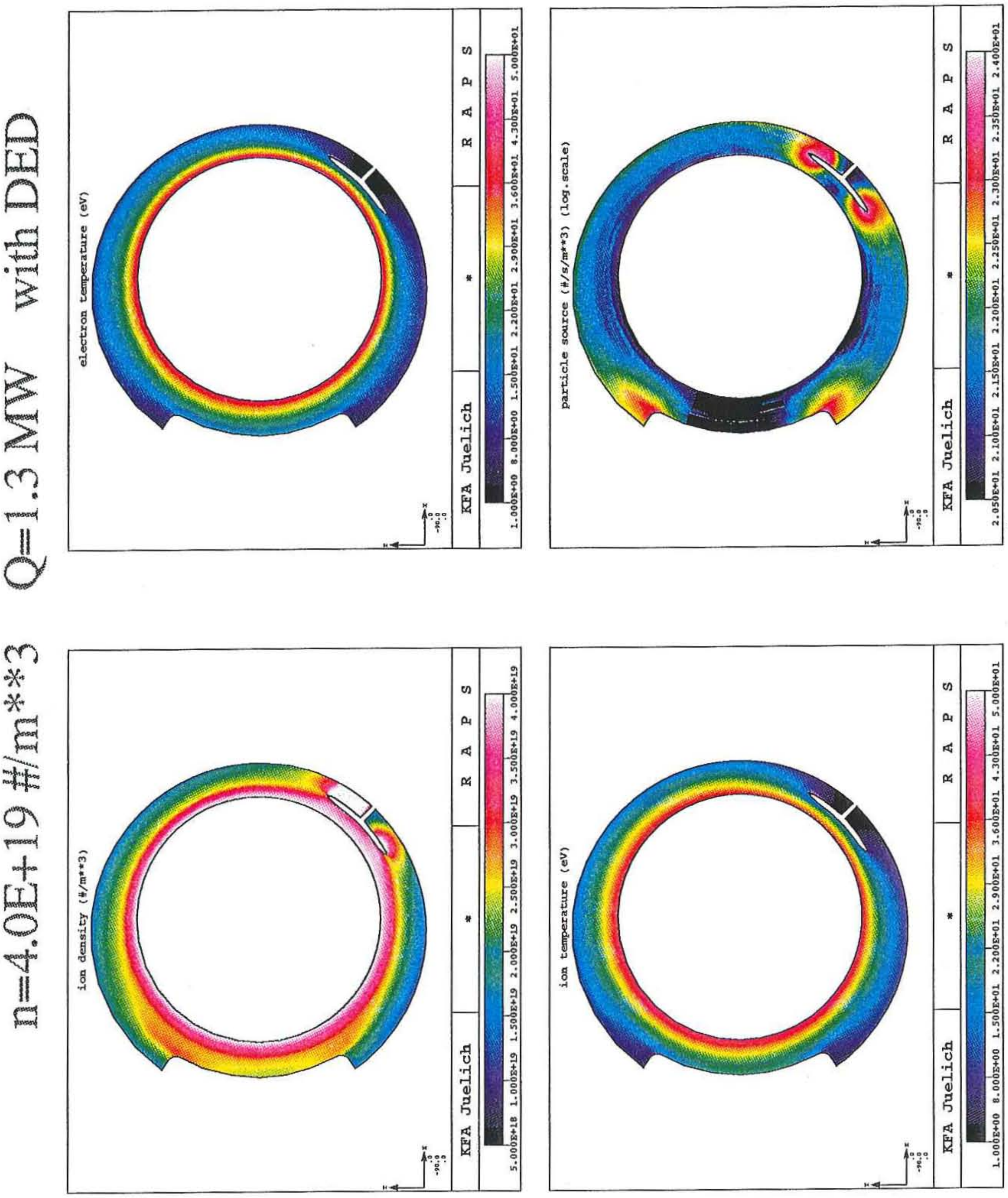

Figure 11: Computational results for $n = 4 \times 10^{19}\mathrm{m}^{-3}$ and Q = 1.3 MW with DED

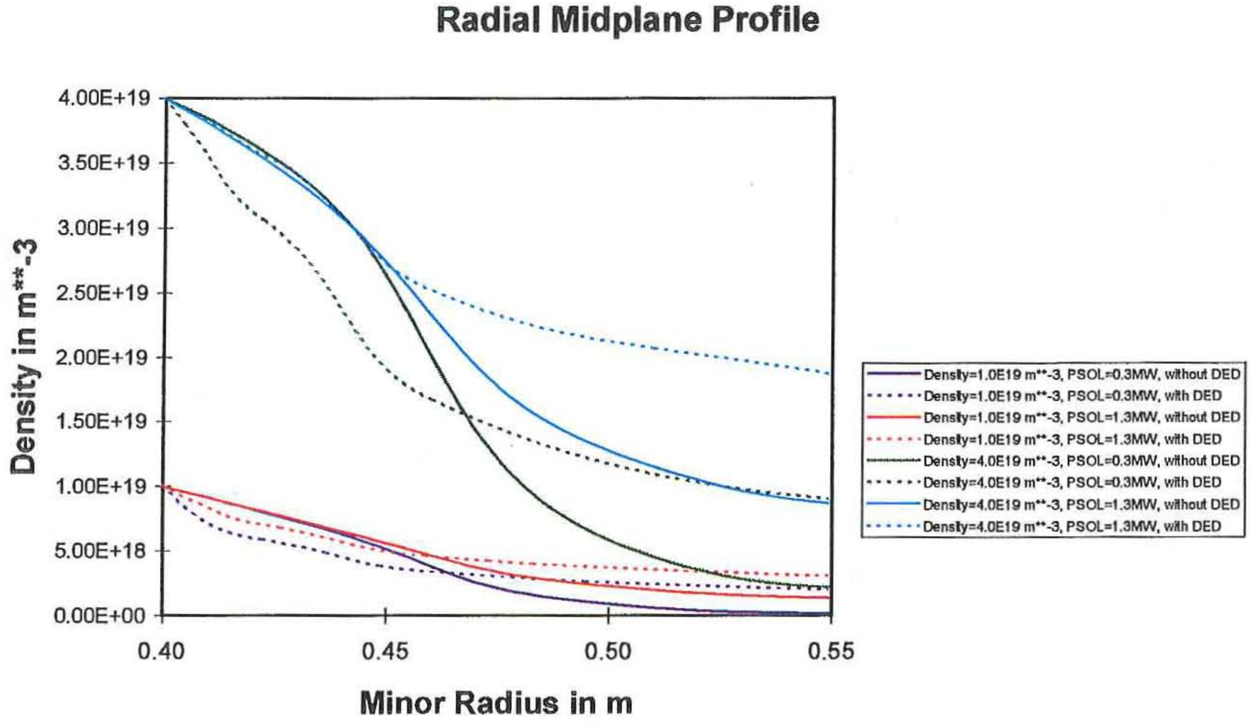

Figure 12: Radial density profiles

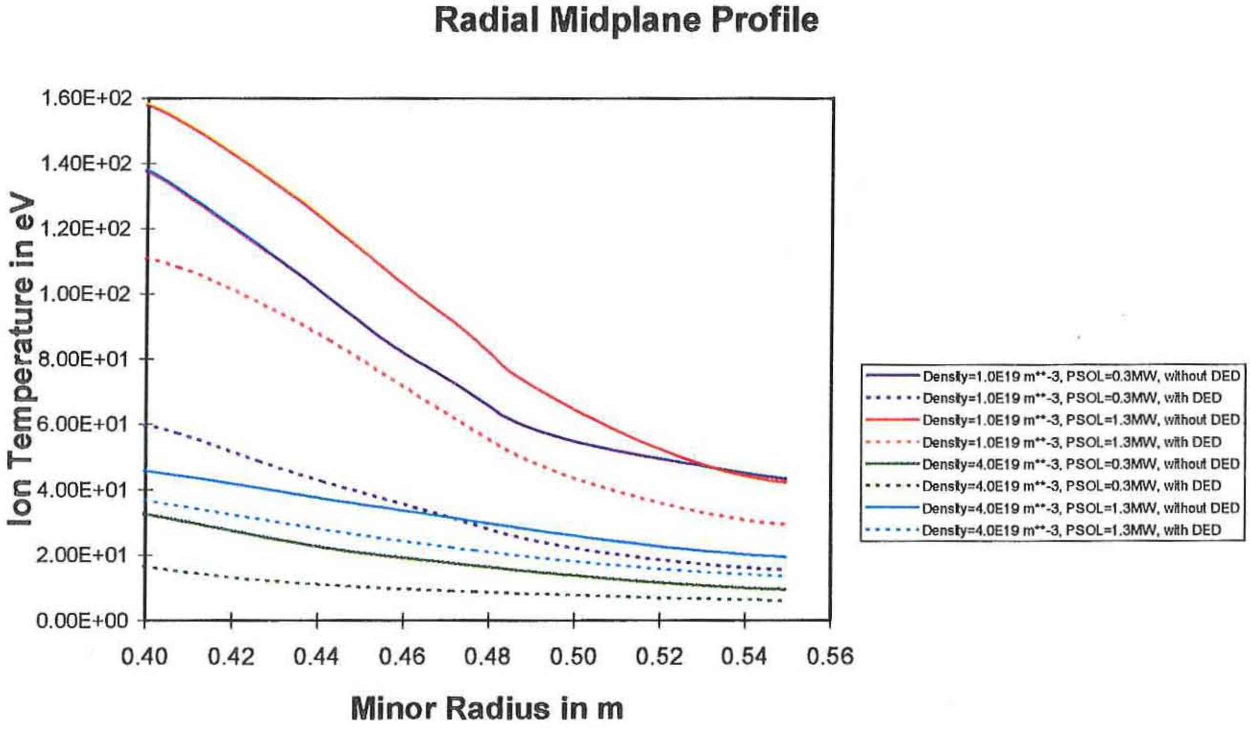

Figure 13: Radial ion temperature profiles

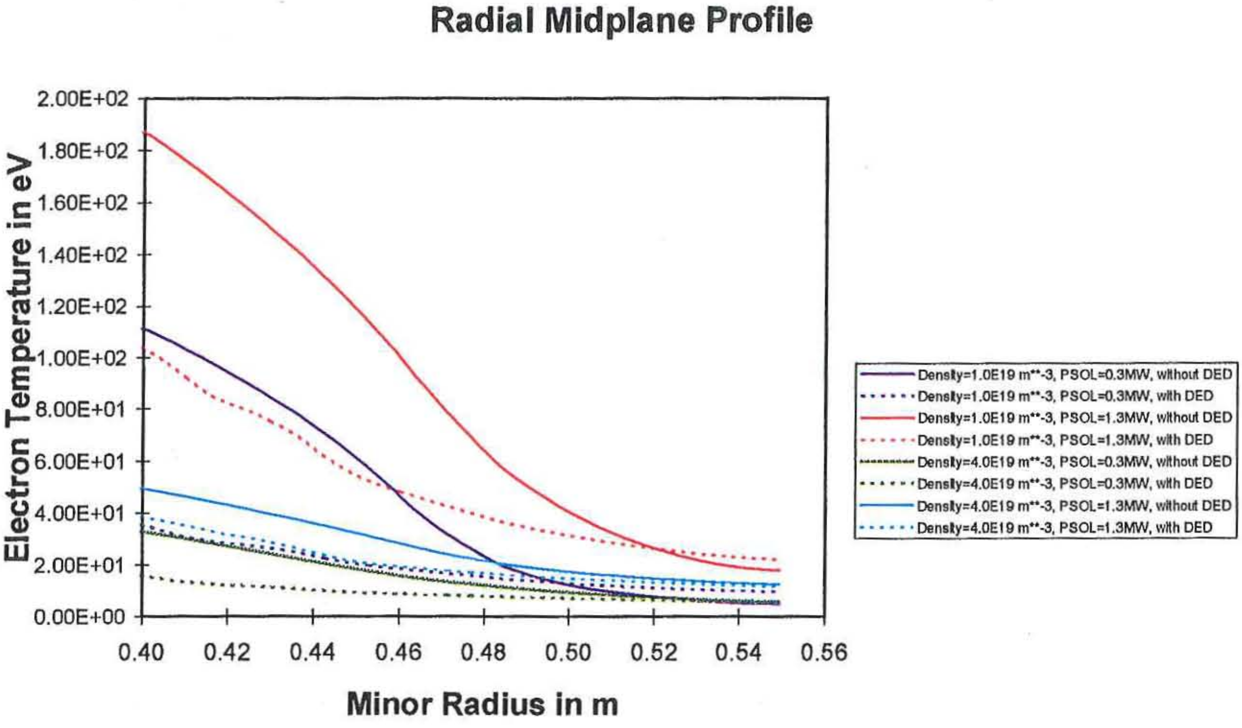

Figure 14: Radial electron temperature profiles

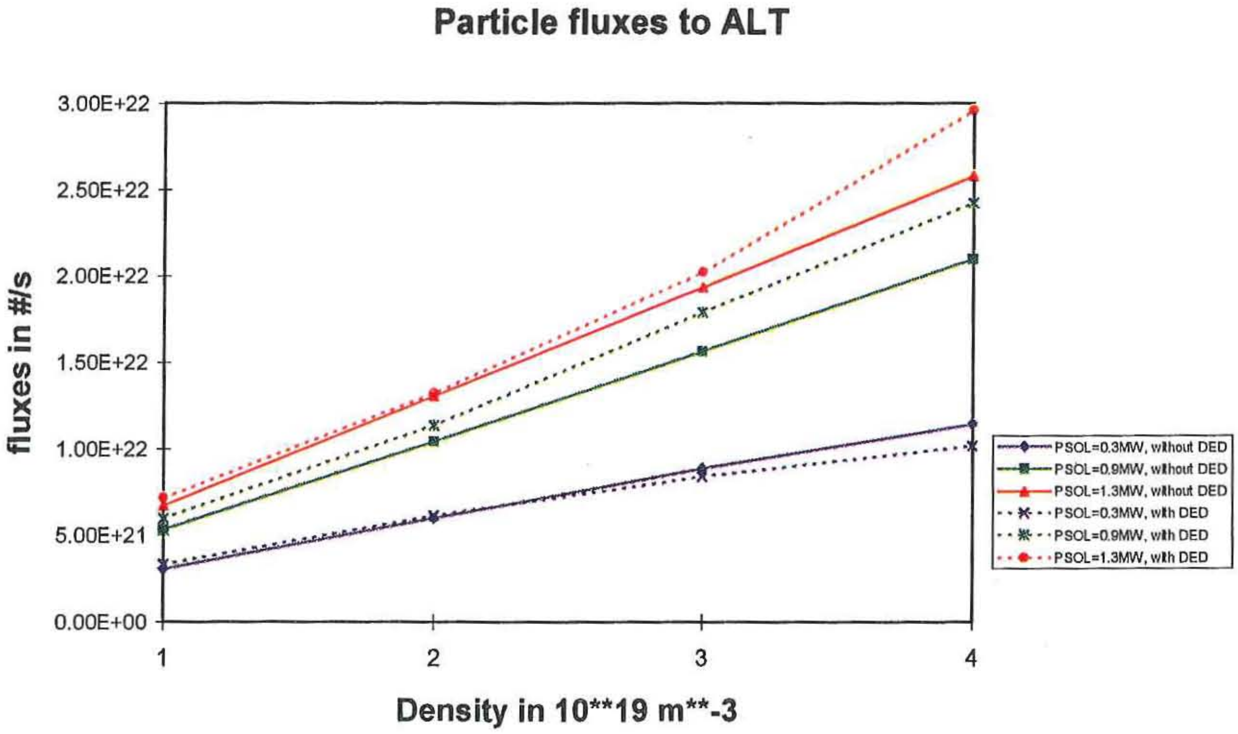

Figure 15: Particle flux to ALT

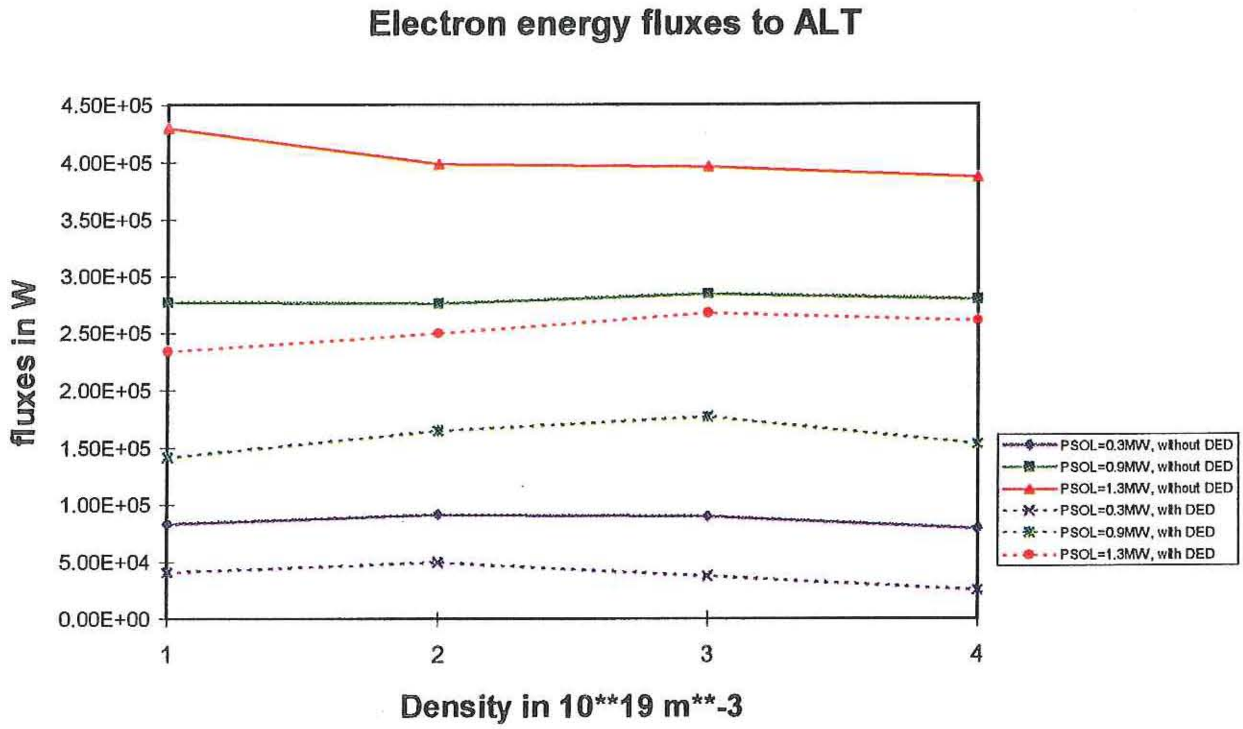

Figure 16: Electron energy flux to ALT

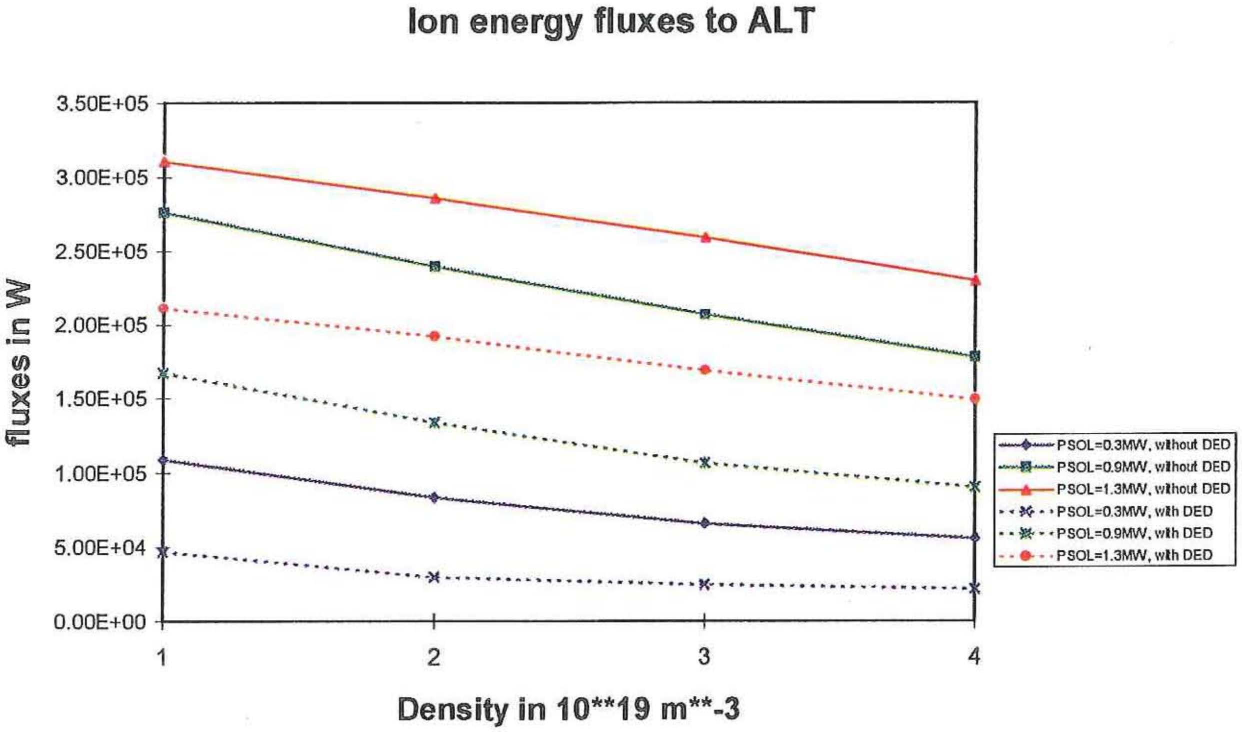

Figure 17: Ion energy flux to ALT

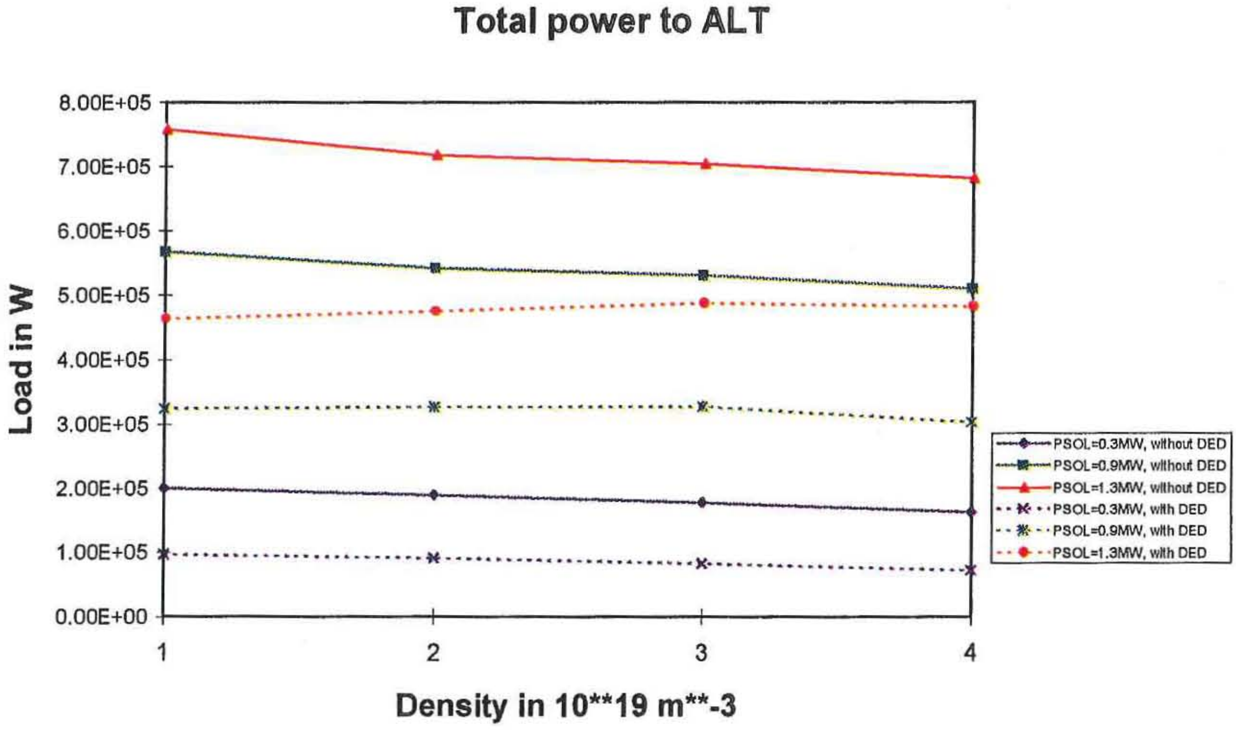

Figure 18: Total power to ALT

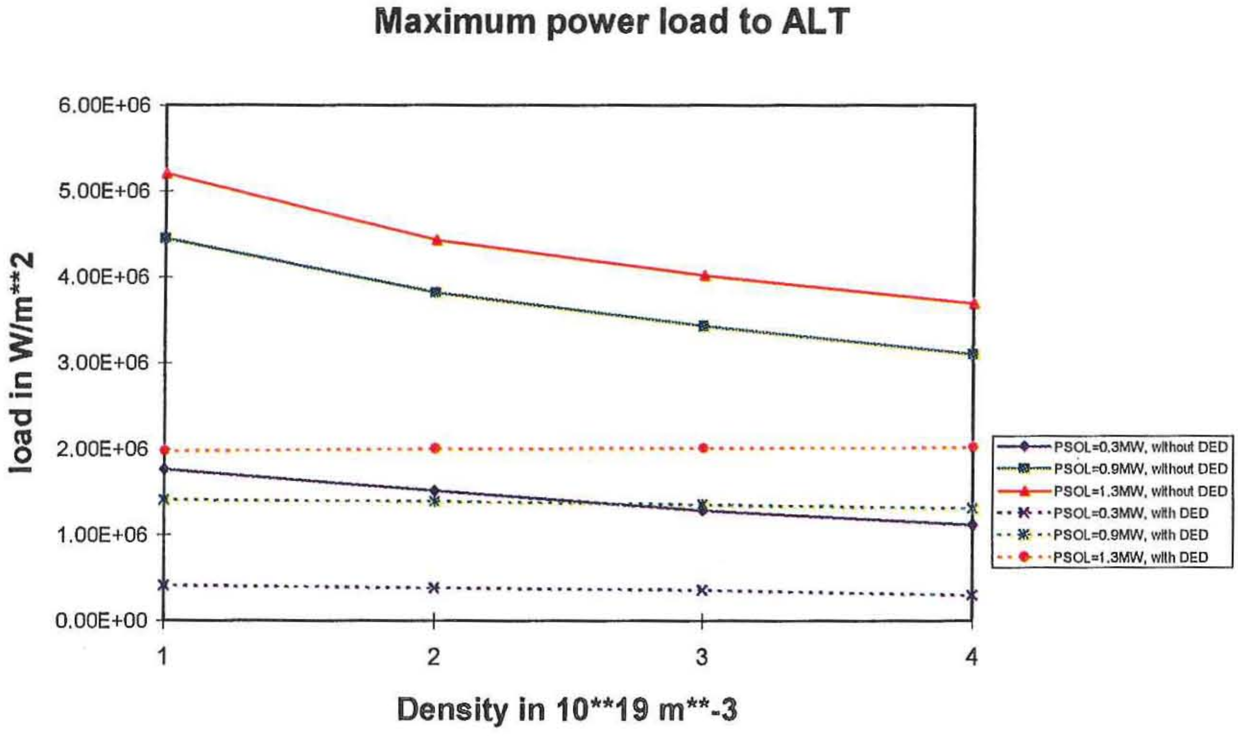

Figure 19: Maximum power load to ALT

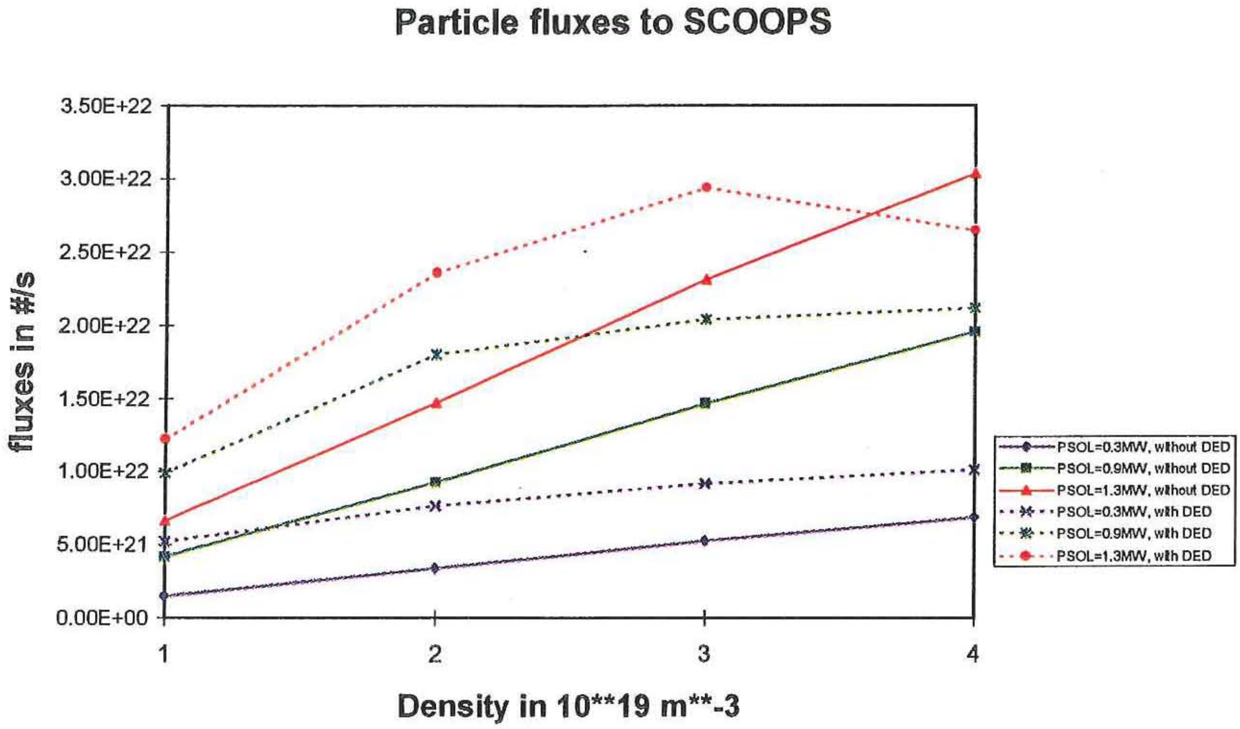

Figure 20: Particle flux to the scoops

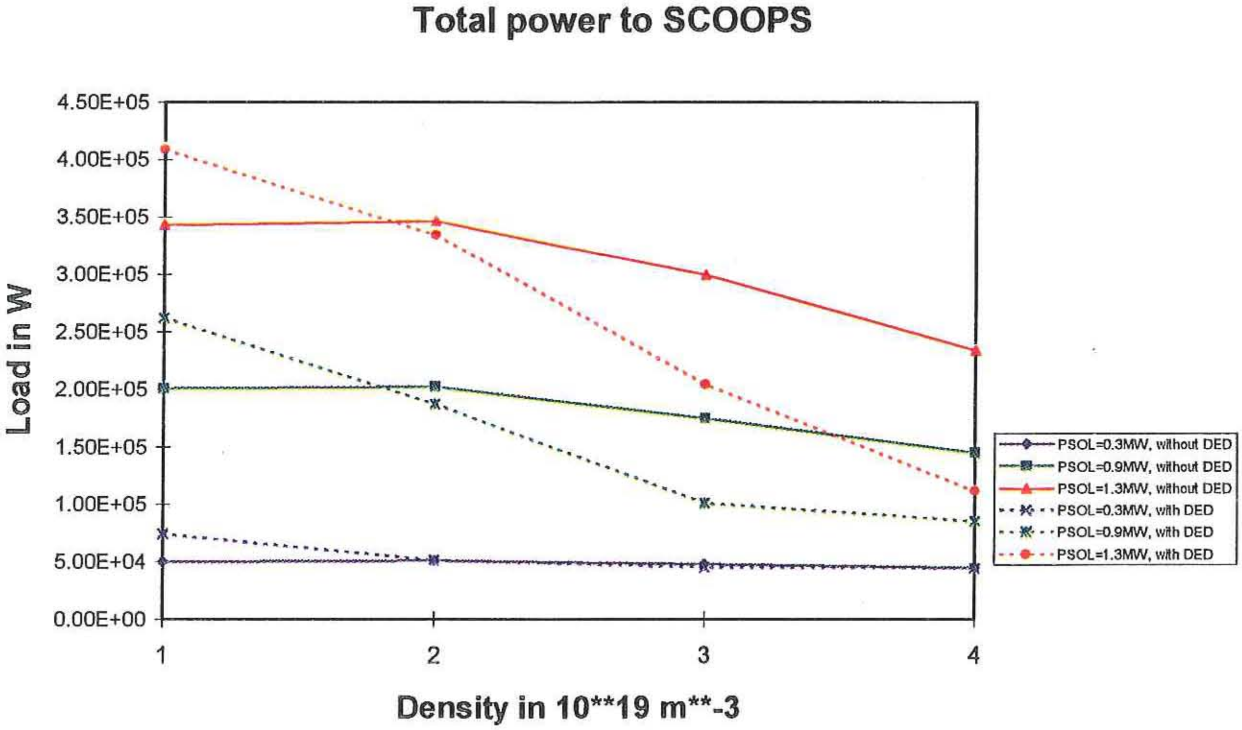

Figure 21: Total power to scoops

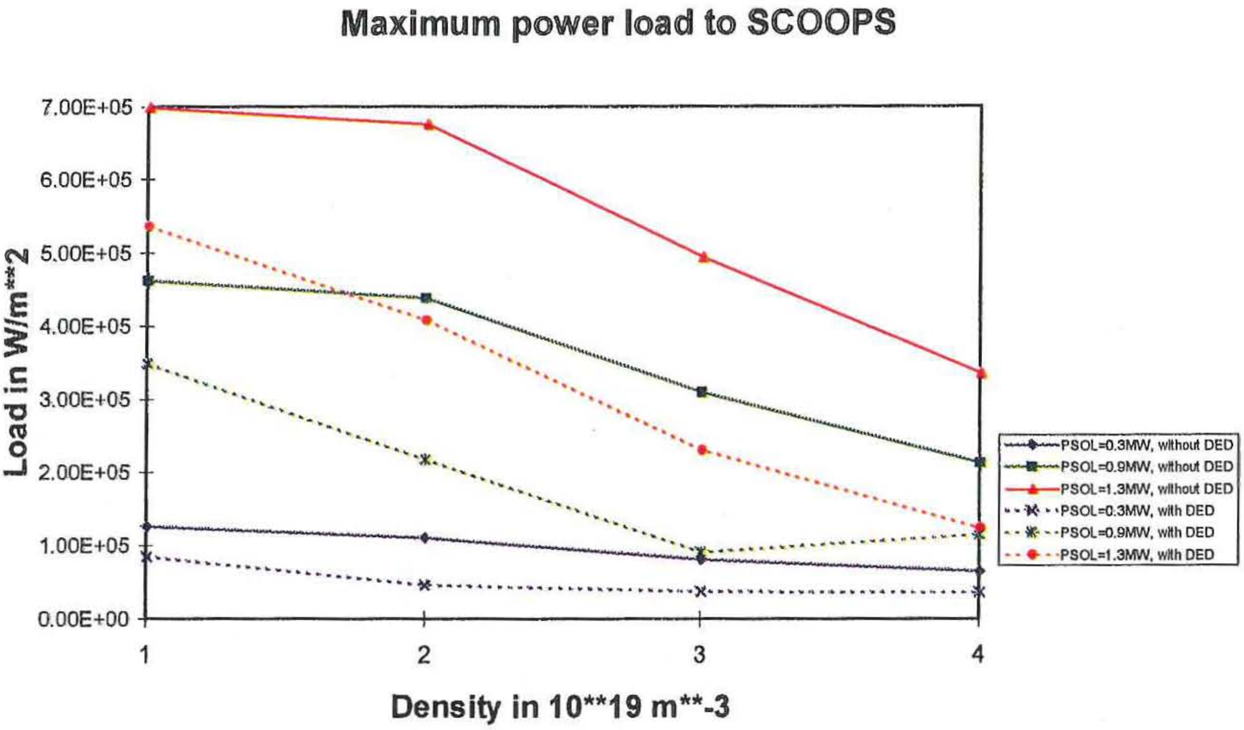

Figure 22: Maximum power load to scoops

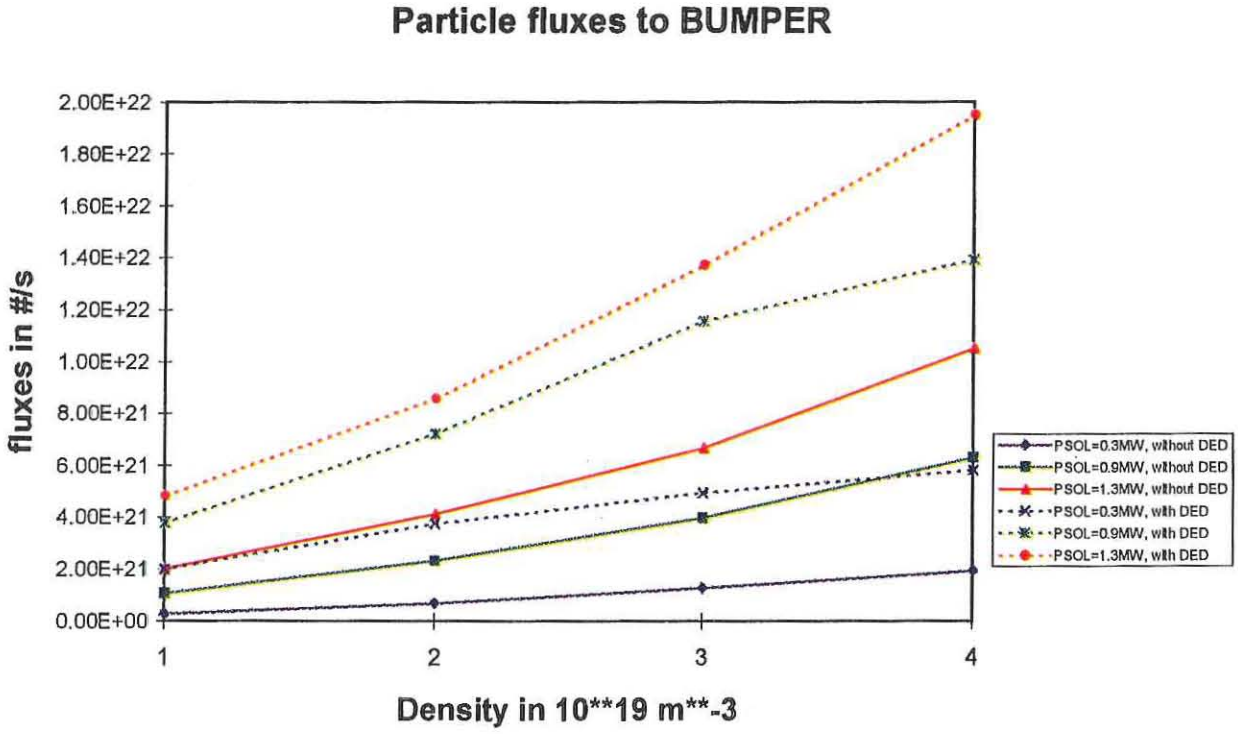

Figure 23: Particle flux to the bumper limiter

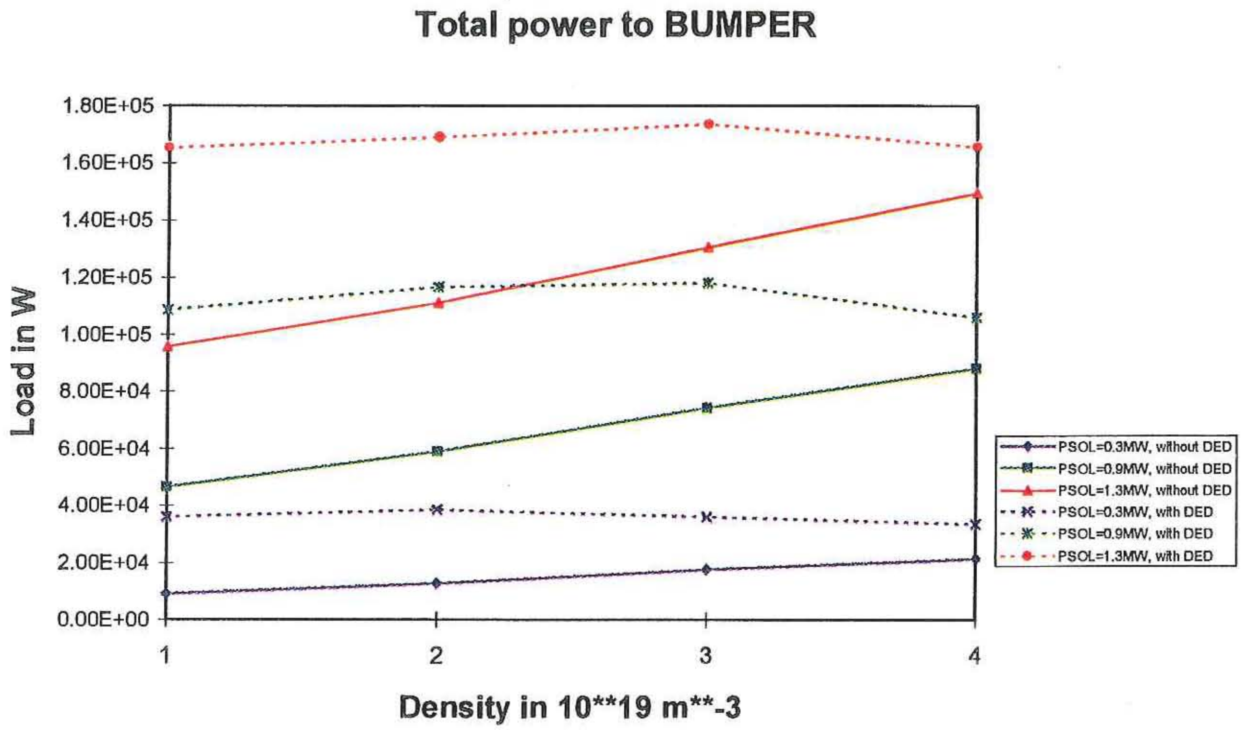

Figure 24: Total power to the bumper limiter

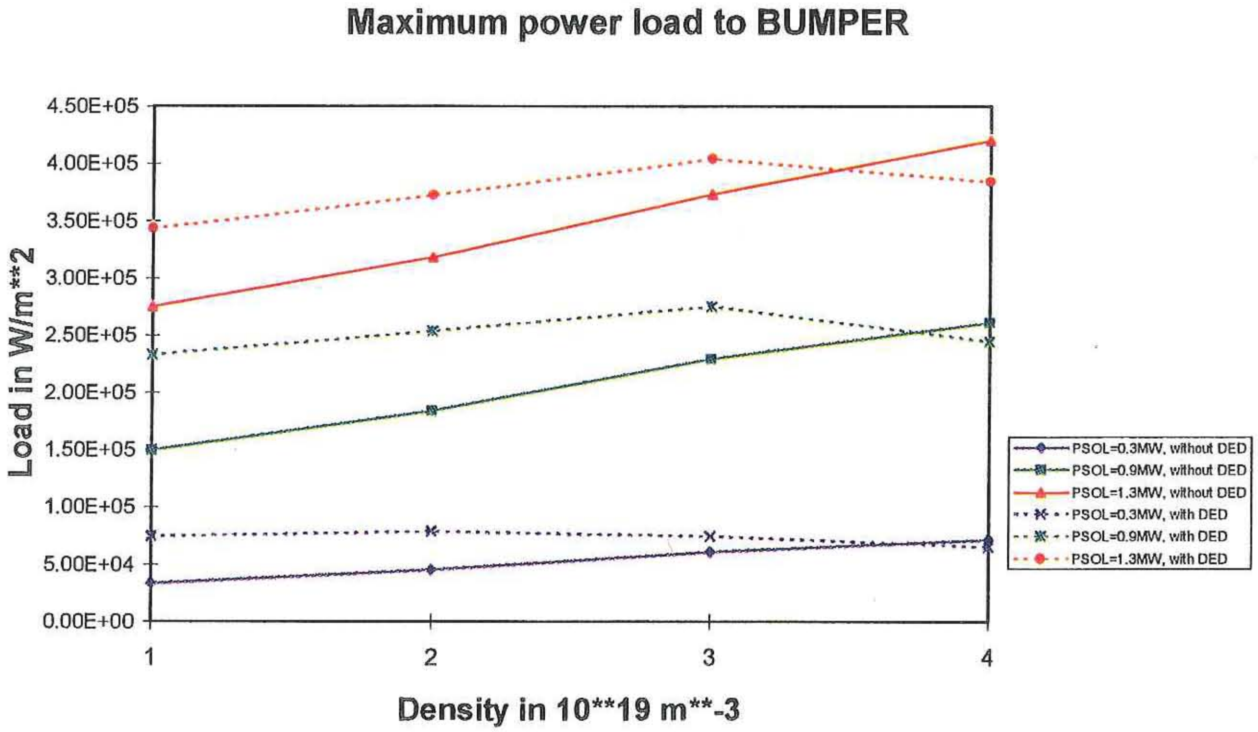

Figure 25: Maximum power load to the bumper limiter

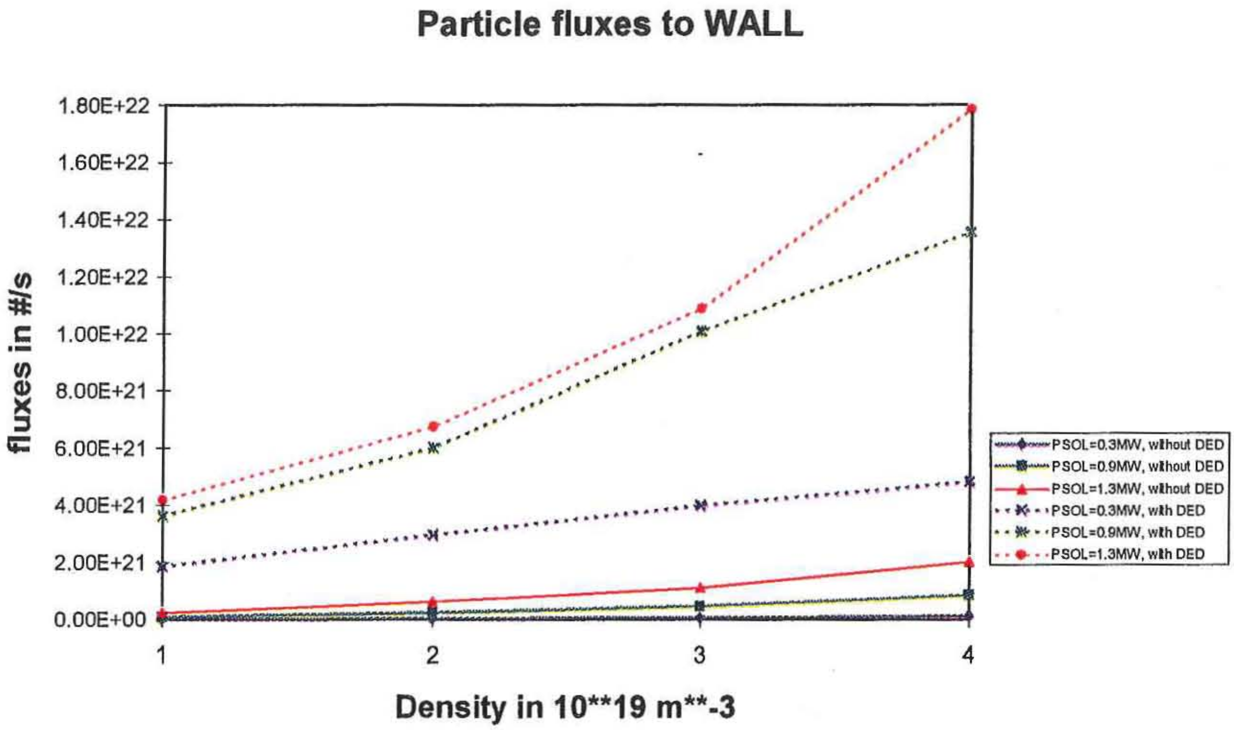

Figure 26: Particle flux to the vessel

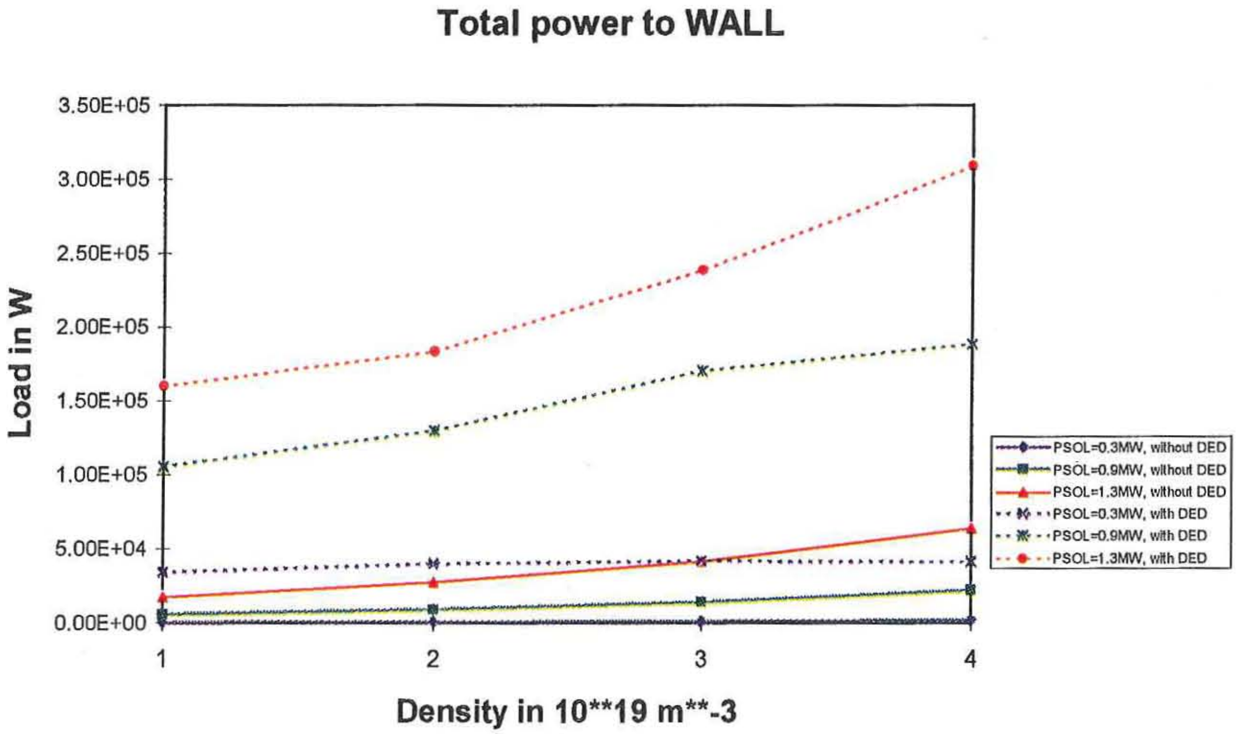

Figure 27: Total power to the vessel

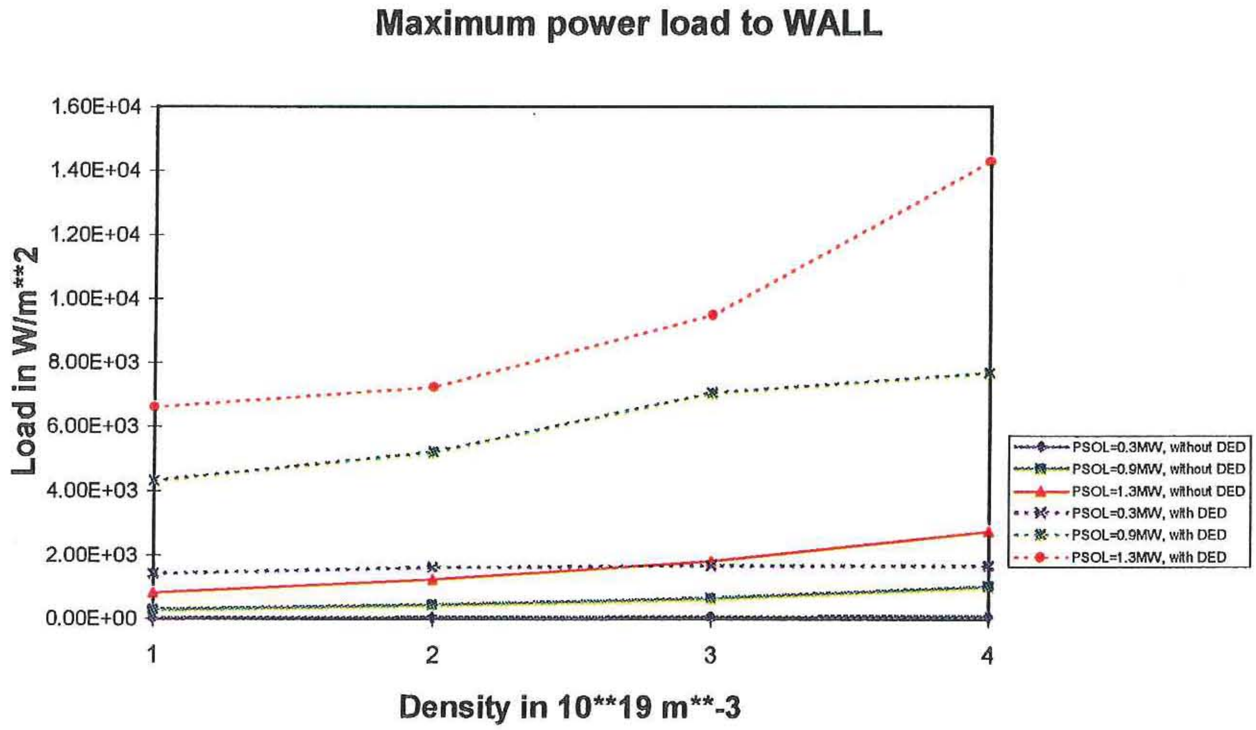

Figure 28: Maximum power load to the vessel

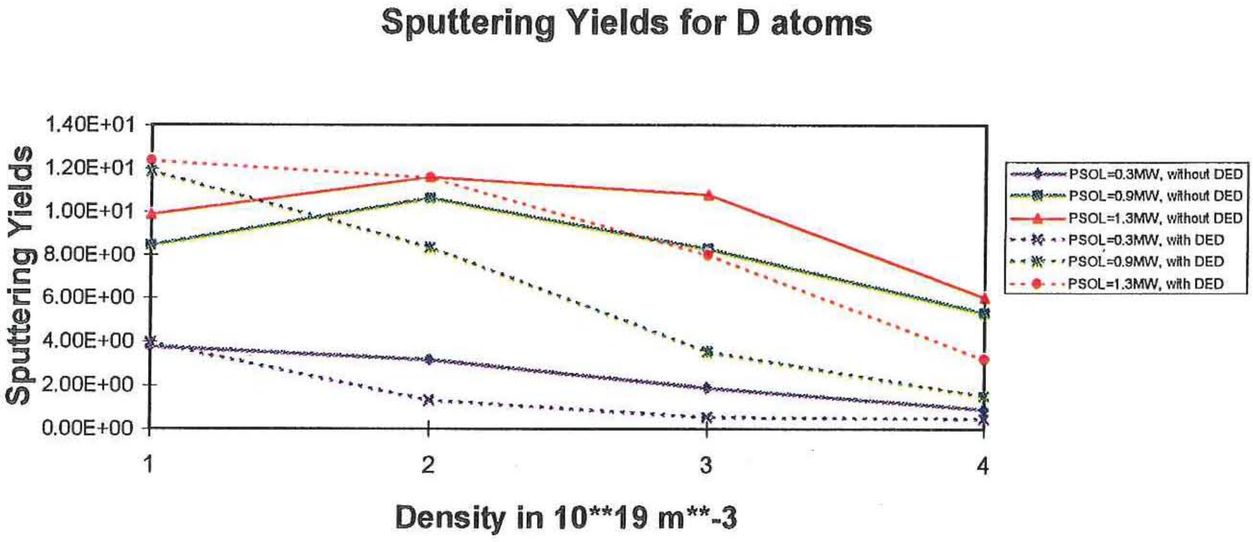

Figure 29: Sputtering yields for atoms

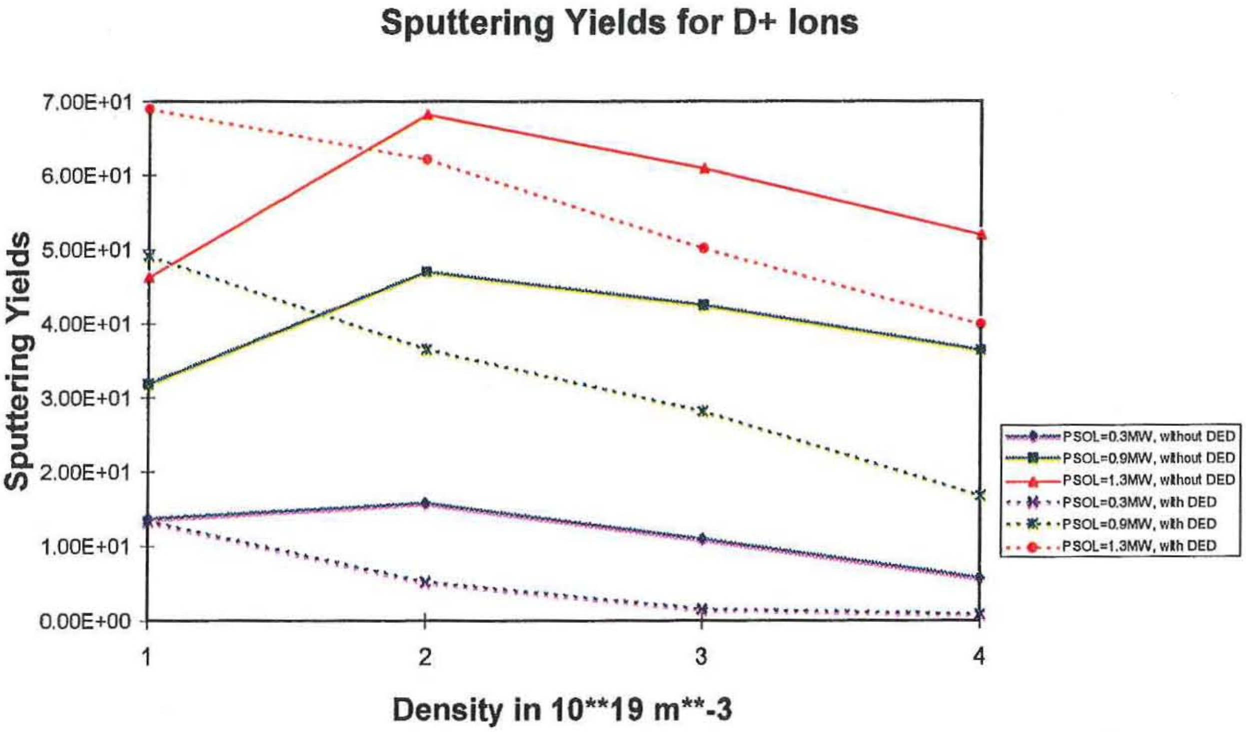

Figure 30: Sputtering yields for ions

12. Particle drift trajectories in the rotating field of the Dynamic Ergodic Divertor in the TEXTOR tokamak - a Monte-Carlo study

A. Montvai

FOM-Instituut voor Plasmafysica 'Rijnhuizen"
Associate EURATOM-FOM, The Netherlands

1 Introduction

The planned edge ergodization experiment in the TEXTOR tokamak introduces a qualitatively new element in the series of edge-transport studies with chaotic magnetic field (a review is given for instance in [1]). In this case the magnetic field of the supplementary system of coils can be applied not only as a static perturbation, but in the form of a traveling wave too, which is running in the toroidal direction. At the upper frequency limit in the parameter space of the DED (10^4 Hz) the phase velocity of the perturbing wave-pattern is in the region of the thermal velocity of an ion population of about 30 - 50 eV temperature. The coincidence of these characteristic velocities creates the possibility of introducing significant changes in the resulting drift trajectories as compared to the static case.

An assessment of the induced alterations of the particle- and energy transport in the boundary layer are of interest to a number of parallel studies. Results of this kind of analysis can serve as input for edge-modeling systems of codes like the EB2-EIRENE code (described elsewhere in this series of reports). The spatial variations in the locally averaged drift velocities can deliver information of engineering interest: spatial fluctuations of wall loads, etc. Later during the actual functioning of the DED these results can help in interpreting the measurements.

In order to arrive at a qualitative picture of the alterations in the radial transport of particle due to the influences of the DED field a numerical study is underway using algorithms based on Monte-Carlo techniques. At this stage only test particle trajectories are computed and analyzed statistically. This means, that the transport model implemented lacks of a number of important features. No attempt has been taken to arrive at a self-consistent picture. The effects of toroidal electrostatic field, collective plasma effects and particle collisions are entirely neglected. However the numerical possibilities of taking into account these mechanisms are provided for. In fact their effects will be analyzed in a later stage of the study. In this report the basic features of the numerical approach and the first results of the statistical analysis of the derived database is reported only.

2 The numerical background of the study

A system of programs has been developed consisting of the following main modules:

- Programs modeling the magnetic field
- Modules deriving characteristic vectors for the gradient- and curvature drifts in the actual magnetic field distribution. These vectors can be used to determine the local drift velocity of a given particle based on the actual parameters thereof.
- Modules setting up the initial conditions for the particle population.
- The program following the particles in time and creating the trajectory database.
- Statistical postprocessing and visualization.

2.1 The magnetic field model

In the first phase of this study a comparative analysis has been conducted of the two limiting operational regimes of the DED system. The static case (DC power supply) and the upper frequency limit of the AC operation ($10^4 Hz$) were the subjects of the numerical modeling. The complexities of the task to be solved made inevitable, that a number, occasionally strongly restrictive assumptions had to be made to simplify the dynamics involved. The necessity of doing so arose from the limitations defined by the nature of a Monte-Carlo study.

The main and most important simplification was, that the underlying magnetic field was supposed to be 'static'. The term 'static' here refers to the fact, that no effort was taken to implement any variations of the input magnetic field due to the emerging inhomogeneous drift- and current field. A second simplifying assumption was, that the DED field perturbed an idealized, toroidally symmetric equilibrium field, and no other dynamics has been taken into account in the system than the eventual rotation of the perturbation. The actual parameters of the equilibrium were as follows. Toroidal magnetic field on the geometrical axis of the torus: $B_{tor} = 2.2$ T, the value of the safety factor at the ALT-II limiter radius of 0.48 m: $q_{limiter} = 4.2$) Under these conditions the temperature- and density distribution in the outer plasma regions was supposed to be of the form shown on Fig. 1.

The distribution of the magnetic perturbation was computed by using a numerical model of the current distribution in the coils. The geometry reflected the state of the construction as per 1st of April 1996. Great care has been taken to devise a realistic current density distribution in the coils including the inevitable asymmetries of the configuration, such as feed-troughs, uncompensated currents, e.t.c. As a consequence each of the coils of the DED was represented numerically by six, helically wound primary filaments. The geometry of the helices corresponded corresponding to the actual constructional details of the current carrying cables. The resulting magnetic perturbation was then computed using the Bio-Savart law. The field was stored on a 3D grid consisting of a total of 300 000 vertices. In order to implement an approximately constant gridpoint density these vertices have been distributed along toroidal surfaces between the two limiting values of: $r_{min} = 0.3 \leq r \leq r_{max} = 0.6m$. The distance among the gridpoints was 0.05 m in the radial direction, about 0.02 m in the poloidal direction and 0.1 m along the toroidal direction. The collected experience shows, that this method of discretization delivered the precision, and the uncertainties of the results were defined by other parameters in the numerical procedure.

2.2 Derivation of the drift field

In deriving the particle drifts in the combined equilibrium + perturbing magnetic field system a method was chosen, which consisted of two steps. In the first step a pair of characteristic vectors were computed and stored all over the 3D grid defined in the starting phase. These vectors did not contain actual particle characteristics. Namely it can be shown, that the local drift velocity of a given particle is completely determined by the two vectors:

$$\begin{aligned} \vec{d}_{||} &= \frac{1}{\mathbf{B}}[\vec{b} \times (\vec{b}\nabla)\vec{b}] \qquad (1) \\ \vec{d}_{\perp} &= \frac{1}{\mathbf{B}^2}[\vec{b} \times \nabla\mathbf{B}] \end{aligned}$$

Here $\mathbf{B}$ is the local magnitude of the magnetic field, $\vec{b}$ is a unit vector in the tangent to the magnetic field line and the $||$, $\perp$ indices denote the curvature- and the gradient drift respectively.

This vector has to be multiplied by a factor containing the actual particle mass, charge and velocity parameters in order to determine the local drift velocity. However one has to note, that the local velocity of a particle with a given initial condition depends merely on the local magnitude of the induction vector:

$$\mathrm{v}_{||}^2 = \frac{2}{m}E - \lambda_0^2 \mathrm{v}_{||0}^2 \frac{\mathbf{B}}{\mathbf{B}_0} \qquad (2)$$

$$\mathrm{v}_{\perp}^2 = \frac{\lambda_0^2 \mathrm{v}_{||0}^2 \mathbf{B}}{\mathbf{B}_0} \qquad (3)$$

In this formula λ_0 is the initial pitch angle of the particle, E is the energy and $\mathbf{v}_{||0}$, $\mathbf{v}_{\perp 0}$ is the initial parallel- and perpendicular velocity respectively. Finally $\mathbf{B}_0$ represents the magnetic field strength at the starting point of the trajectory. It is to be seen, that evaluating the local velocity contains only one variable: the local magnitude of the induction vector.

This means, that storing the components of the magnetic field and the characteristic vectors of Eq. (1) one can derive the local drift vector in the given perturbed magnetic field economically.

2.3 Initialization of the particle database

The particle database was set up by generating initial conditions randomly in a toroidal shell. The volume was limited by the two radius values of $r_1 = 0.40$ m and $r_2 = 0.46$ m (the nominal boundary of the plasma) The initial conditions were generated on a toroidal shell at a distance of 0.01 m each (radially). In the toroidal direction the density of the starting points was homogeneous. The density of the starting point in the poloidal direction could be set up with homogeneous and inhomogeneous distributions too. The total number of points on a toroidal shell was chosen according the density distribution of Fig. 1.

The energy distribution of the initiated particle population followed the Maxwell distribution with a mean energy corresponding to the local temperature. (Fig. 1.) The next step in setting up the database for the initial conditions was the determination of the initial pitch angle values. In doing so equipartition of the energy between the two degrees of freedom (the parallel- and the perpendicular velocity) was assumed. Finally the direction of the initial parallel velocity was randomly chosen in the possible two directions around the torus with equal probability. The procedure described here was carried out twice creating two independent sets of initial conditions for the ions and for the electrons. They contained about 3000 particles each. The actual number depended on the aims and statistical requirements of a particular run.

2.4 Modeling the particle dynamics

The modules advancing the particle trajectories were based upon the so called 'Mapping technique' [2]. This method replaces the integration of trajectories by a set of transformations of a sufficiently dense set of poloidal sections of the torus [3]. In praxis it meant, that 100 equidistant poloidal sections were defined along the toroidal direction of the torus. The coordinates of a given drift trajectory were computed and stored for each of this poloidal sections. The determination of the coordinates of the drift trajectory on the next poloidal plane knowing the initial point on a given one was carried out as follows:

- Based on the stored component of the perturbed magnetic field the local direction and magnitude of the magnetic field is computed at the initial point.
- In the second phase the local drift velocity at this point was determined by using the stored characteristic drift vectors (Eq.'s (2) and (3)) and multiplying them with the factor corresponding to the actual magnetic field and particle parameters.
- An estimate of the endpoint of the drift trajectory on the next poloidal section was constructed based on the data delivered by the previous two operations.
- In the next step a hypothetical, 'inverse' drift was used to project back the estimate of the endpoint onto the previous poloidal section. This

'inverse' drift acted in the opposite direction as the physical drift, and its magnitude and direction were constructed by using the actual local values at the temporary endpoint. If the initial point and the reconstructed start-point were sufficiently close to each other, the estimated coordinates of the endpoint were accepted. Large discrepancies indicate the presence of large fluctuations in the magnetic- and drift fields in the given region. In this case a second iteration was made by halving the distance between the poloidal sections and doing a third order Lagrange interpolation over the the neighbouring four poloidal sections. In all practical cases this was enough for deriving a endpoint of the drift trajectory on the subsequent poloidal section with a sufficient accuracy.

- In the case of trapped particles, having turning points between two adjacent poloidal sections (this was signalized by a negative longitudinal velocity on the next poloidal section) a fifth order Runge - Kutta solver [4] was activated to integrate the trajectory through the running point back to the initial poloidal sections. After this the much faster mapping was used once again.

Finally: the local particle data (actual time value, pitch angle, parallel velocity, the characteristics of the local drift shifts between the adjacent poloidal sections) were stored to create the database for the subsequent statistical study.

3 Results

3.1 Magnetic field structure and properties of the drift fields

Properties of the perturbed magnetic field have been dealt with in detail elsewhere in this series of reports. Therefore a lengthy description of these properties is omitted here. From the point of view of the particle drifts, only one feature and its consequences have to be mentioned. Namely the perturbation is very strongly localized and is being felt by the particles only on the high field side of the torus. This fact has several important consequences.

The first one is, that the majority of trapped particles experience a nearly perfect, toroidally symmetric drift motion. This part of the particle population (especially those ones with high perpendicular energies) does not feel the presence of the localized perturbations. In contrast to that the barely trapped particles and the circulating particles just above the trapping limit are very strongly affected by the perturbations, because the majority of time of flight is spent in the deeply perturbed regions. Scattering in- and out of the trapped regions of the velocity space is expected to be enhanced by the strong perturbations of the high field side of the torus.

A second significant effect is to be expected to alter the trajectories of circulating particles well above the trapping limit. The drift of this kind of particles is a composition of two parts. In about 2/3 of the toroidal transition the drift corresponds to that of the toroidally symmetric magnetic field. In the remaining part the drift is strongly chaotic, dominated by the curvature drift. As a consequence the statistical properties of the trajectories are very hard to predict. Because of the fact, that the statistical properties of the distributions involved are not known, great care has to be taken in choosing an appropriate method of interpretation. One can not assume a priori the presence of Gaussian distributions and therefore methods of the nonparametric statistics are to be used [5].

A third property to be considered is, that the curvature- and the gradient drift caused by the perturbing field decay at a different pace towards the center of the plasma column (see Fig.'s 2.a. and 2.b.). In particular the gradient drift of particles essentially coincides with that of the axially symmetric case at a minor radius value of about 0.41 m, whereas the curvature drift decays into the axially symmetric background only at a greater distance form the DED coils (0.35 m). This point further emphasizes the importance of a careful approach towards the statistical interpretation of the data.

3.2 Particle excursions in the static and rotating regimes of the DED system

A series of runs has been completed to identify the differences between the two, qualitatively different regimes of operation: the static- and the rotating perturbations. For the sake of a reliable comparison identical sets of initial conditions were applied in both cases. On Fig.'s 3.a. and 3.b. two typical plots are to be seen. A significant difference can be identified on them, because the ions moving in the rotating field show a narrower spread around the initial conditions a as compared to the static case. This property can be explained by considering, that the rotating perturbation propagates with a velocity comparable to the ion thermal velocity. This means, that a significant fraction of the particle population sees a slowly varying field as compared to the stationary case. The result just mentioned correlates with models of particle transport in chaotic magnetic fields, treated in detail in Ref. [6]. In the paper referred to it is shown, that the diffusivity of collisional particles exhibits a frequency dependence of the form:

$$D \sim f(\frac{1}{\nu}) \tag{4}$$

Here ν is the characteristic frequency of fluctuations. The calculated spread in the radial position of ions agrees with this claim. It has to be added, that the electrons are much less significantly effected by the rotation. This is a direct consequence of the much greater difference between the phase velocity of the traveling wave and the thermal velocity of electrons.

3.3 Statistical properties of the drift-displacements

¿From the point of view of the cross-field transport the actual statistical distribution of the local drift displacements play a significant role. On Fig. 4. the distribution of the radial shifts of 10 000 magnetic field line section is to be seen. The radial shifts have been computed locally between two adjacent, poloidal planes. This localized characterization of the magnetic field line excursion was used because of the following reason. Regarding the strongly inhomogeneous structure of the perturbed magnetic field one can not expect the stochastic process describing the field line excursions to be stationary in the strict sense of the word [7]. In the case of nonstationary stochastic processes the statistical properties of the increment process are of importance [7]. The increment process, defined as the probability distribution of changes occurring in a very short time interval, contains directly accessible information on the statistical behaviour. Therefore as a practical estimate for the increment process the radial coordinate shift of a field line segment between two subsequent poloidal sections was used.

On Fig. 6. the distribution of 10 000 drift trajectory shift is to be seen for ions. The drift trajectory shift was computed between two adjacent poloidal planes. However this shift does not contain the displacement of the field line, that is it is the drift relative to the field line the particle started on the initial poloidal plane. A remarkably large difference to the fitted (and shown in solid lines) Gaussian distribution is to be observed.

¿From the point of view of the applicable transport models this deviation is of importance. It shows,, that the statistical properties of the stochastic process describing the particle excursion in the magnetic field of the DED have to be chosen properly. The non-Gaussian nature of the distributions excludes the applicability of diffusive models in general. If one nevertheless uses such a diffusive model for the interpretation of the calculated data one has to justify the procedure chosen in a case by case manner.

Finally it has to be mentioned, that the correlation between the local drift shifts and the magnetic field line displacement is very low. In connection to with that two remarks have to be made. At first this low level of correlation reflects the strongly inhomogeneous nature of the magnetic field structure and the two-component pattern of the local drifts, mentioned earlier. At second this result implies, that the application of the magnetic diffusion coefficient as an estimate for the particle diffusivity - as it has been done in [8] for instance - has to be critically reconsidered under the present conditions.

3.4 Test particle diffusion coefficient

The preceding section disclosed the non-Gaussian nature of the total drift shifts. However for a preliminary, order of magnitude estimate of the particle diffusivity it is possible to use the local data for estimating the diffusivity by using the classical formula:

$$D_{drift} = \frac{< \Delta s^2 >}{\Delta t} \tag{5}$$

In this the Δs values are local drift displacements in a toroidal distance of 0.2 m, and the Δt values are the time intervals to follow the given section of the trajectory one can get an estimate for the particle diffusivity. The produced database of particle trajectories was sufficiently large ($\sim 10^6$ local values - as defined and computed in the preceding sections), and therefore one could randomly chose a statistics containing 10^3 independent local shifts to estimate the transport coefficient.

The procedure delivered the results presented in Table I. The obvious large difference in the ion- and electron diffusivity reflects the fact, that in the present model only independent, test particle transport has been considered. The lack of inclusion of electric fields such as for instance the ambipolar fields is the cause of this deviations. It is clear, that in a more detailed analysis these effects can not be left out.

Estimated particle diffusion coefficients in the DED field (m^2s^{-1}).

radius >	0.45..0.46 m	0.46..0.47 m	0.47..0.48 m	0.48..0.50 m
electrons	4.9	11.0	43.0	$\sim$ 90
ions	0.5	2.0	n.a.	n.a.

Table 1: Table. I. Estimated test-particle diffusivities in the plasma boundary region of the TEXTOR tokamak. The perturbation is computed in the rotating phase (10^4 Hz), and with a current amplitude of 10 kA per coils. (IN certain cases the amount data was not sufficient to give a reliable estimate.)

4 Conclusions and plans for the future

The observed main features of the particle drift in the DED field can be summarized as follows:

- The perturbed drift field in the TEXTOR tokamak shows a strong poloidal asymmetry. The drift field in general follows a very inhomogeneous statistics. Furthermore there are differences in the curvature- and the gradient drifts as far as the spatial distributions are concerned. Consequently the different, characteristic regions of the velocity distributions: the trapped- and circulating particles, particles with very low and very high values of the pitch angle are affected differently in different regions of the volume close to the plasma boundary. In particular the presence of the curvature drift can be felt at a greater distance from the coil system as compared to the gradient drifts.

- There is statistically significant effect to be identified in the data generated by the rotating regime of the DED. The rotation affects the electron- and ion components differently. In accordance with theoretical estimates, the spread of the ion component in the rotating phase was narrower than that of in the static case.

- Strongly inhomogeneous statistical properties can be observed in the local drift distributions over the plasma boundary region. There are significant deviations from a purely Gaussian statistics.

- In the given field structure a very low level of correlation ($r \sim 0.1$) could be observed between the local drift shifts and the local magnetic field line shifts. This calls for a new statistical and probabilistic approach in an effort of describing the particle transport in the DED field.

As far as the future plans are concerned, several tasks and possibilities have to be mentioned.

The main task is to enhance the numerical efficiency of the system of codes. At the moment this is the limiting factor in determining the number of initial conditions during a specific run. In praxis it means, that not in all cases can be the requirements of a sufficiently selective statistics can be satisfied.

However one clear advantage of the numerical procedure constructed is that it allows for a significant widening of the particle dynamics, which can be modeled. Such effects as:

- radial electric field effects;
- the pitch angle scattering;
- particle close collisions;

are fairly easy to implement. This has to be done in the near future to be able to account for the effects of these important mechanisms of the particle transport.

5 References

[1] Ghendrih, Ph., Grossman, A., Capes, H.: EUR_CEA-FC-1571 (1996)
[2] Montvai, A.: Proc. of Phys. Comp. '92, World Scientific, Singapore, 417.
[3] Montvai, et al.: JET-R(92)05
[4] Lambert, J.D.: Computational Methods in Ordinary Differential Equations, John Wiley and Sons. (1973)
[5] Mood, M.A., Graybill, F.A., Boes, D.C.: Introduction to the Theory of Statistics, McGraw-Hill, (1974)
[6] Misguich, J.H., et al.: Diffusion Regimes for Collisional Particles in a Stochastic Magnetic field. - submitted for publication. (The existence of Ref. [6] was pointed out by K.H. Spatschek.)
[7] Grimmet, G.R., Stirzaker, D.R.: Probability and random processes, Clarendon Press, Oxford, (1989)
[8] Rechester, A.B., Rosenbluth, M.N.: (1978) Phys. Rev. Lett. **42**, 1247.

6 Figure captions

Fig. 1. Electron temperature- and density distribution in a typical TEXTOR discharge. These data were used to set up the database for initial conditions in the Monte-Carlo routine.

Fig. 2. The magnitude of the characteristics vectors derived in the perturbed magnetic field of the TEXTOR tokamak. These characteristic vectors define the local drift velocities of a particle in the given field after being multiplied by a corresponding factor containing the actual particle parameters, local velocity components, etc. (see main text). The ($\vec{d}_\perp$) (Fig. 2.a.) and the ($\vec{d}_{||}$)) (Fig. 2.b.) vectors deliver the local drift velocities for the gradient- and the curvature drifts respectively. The distributions shown have been computed on a toroidal surface at r = 0.4 m distance from the magnetic axis and are plotted in function of the poloidal- and toroidal angle.

Fig. 3. Probability density plot of the total, radial displacement (including the displacement induced by the magnetic field line excursion, and the displacement coming from the drifts) delivered by a sample of 10^4 ions. The particles were started at the plasma boundary (r=0.46 m) and were followed for five toroidal transition. The (not normalized) probability density function reflect the distribution of the particles at the endpoints of the trajectories. a - static perturbation, b - rotating field. (The solid curves represent the fitted Gaussian probability density functions.) There is a 20 percent difference to be seen in the halfwidth of the fitted Gaussians, with the rotating perturbation being narrower.

Fig. 4. Probability density plot of the field line displacement based on 10000 field line segments. 1000 initial conditions for magnetic field lines were defined over a toroidal surface with 0.46 m minor radius. The field lines were followed during 10 revolutions along the torus. This resulted 10^6 magnetic field line segments between the adjacent poloidal planes. The radial shift along the field line segment was computed between two neighbouring planes. This method of local characterization of the drift process was necessary because of the possible inhomogneities of the stochastic process describing the drift displacements (see main text). The statistical sample consisted of 10 000, randomly chosen poloidal sections.

Fig. 5. Probability density function derived from 10 000 randomly chosen ion shifts. The method of derivation of the sample is described in Sec. 3.3. It is to note, that large differences can be found between the observed distribution and the fitted (solid line) Gaussian distribution.

Fig. 6. Quantile - quantile plot [5] of the magnetic shift (as shown on Fig. 4.) and the total drift displacement (as shown on Fig. 5.). **a** - for the electrons, and **b** - for the ions. It has to be added, that a deterministic relation between the magnetic field line shift and the resulting drift shift requires a linear quantile-quantile plot. The deviations at the large (positive and negative) drift displacement regions shows, that a probabilistic approach is needed to describe the particle drifts in the DED field properly.

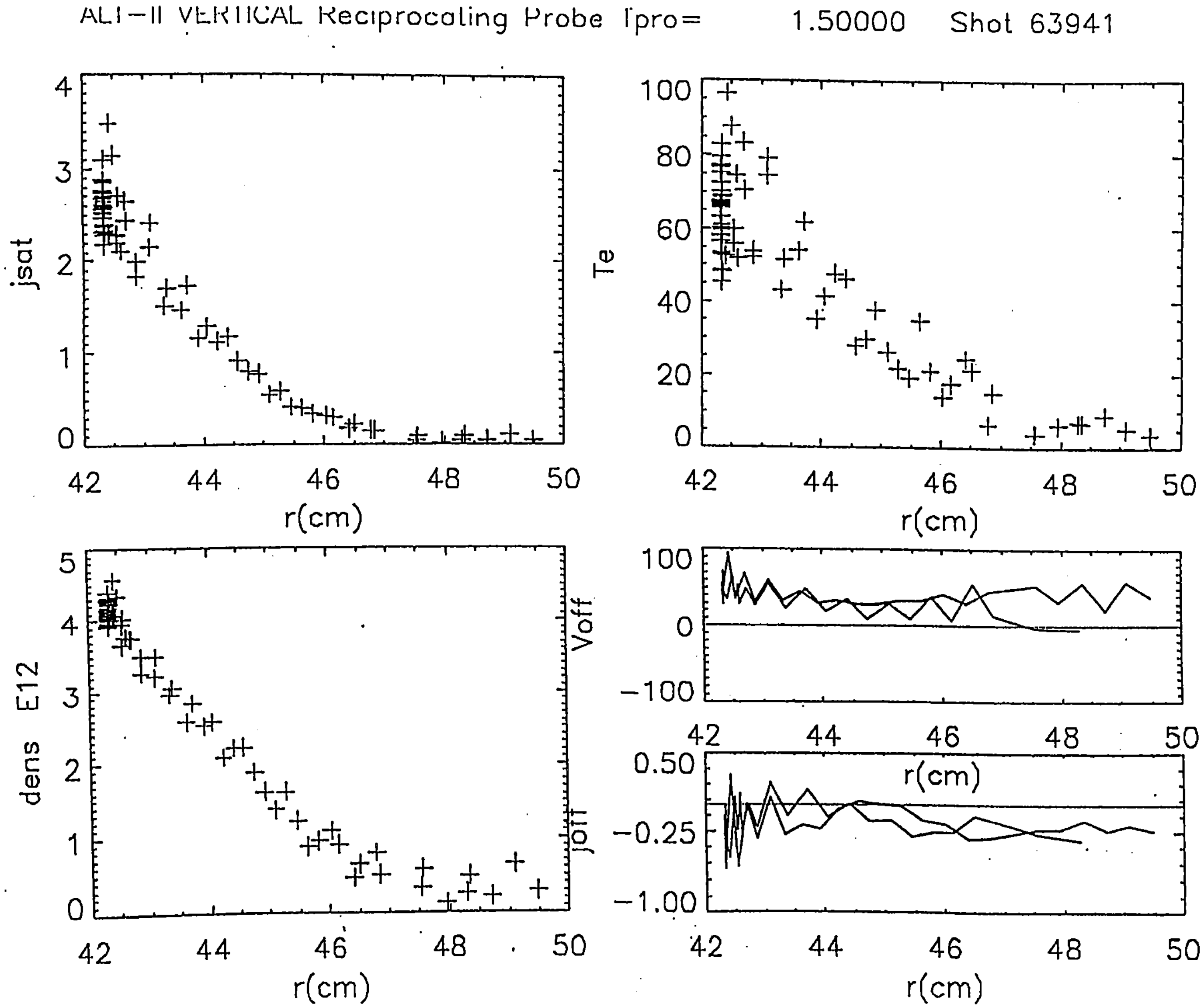
ALT-II VERTICAL Reciprocating Probe Tpro= 1.50000 Shot 63941
jsat
0
1
2
3
4
42
44
46
48
50
r(cm)
Te
0
20
40
60
80
100
42
44
46
48
50
r(cm)
dens E12
0
1
2
3
4
5
42
44
46
48
50
r(cm)
Voff
−100
0
100
42
44
46
48
50
r(cm)
joff
−1.00
−0.25
0.50
42
44
46
48
50
r(cm)

Fig. 1.

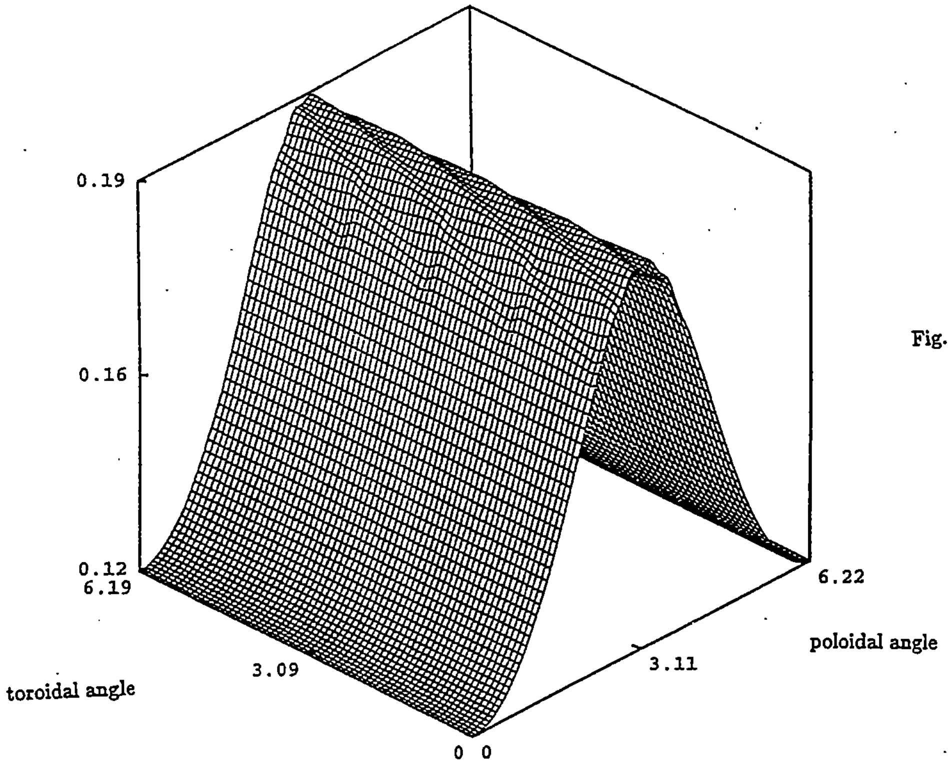
0.19
0.16
0.12
6.19
toroidal angle
3.09
0 0
3.11
6.22
poloidal angle

Fig. 2.a.

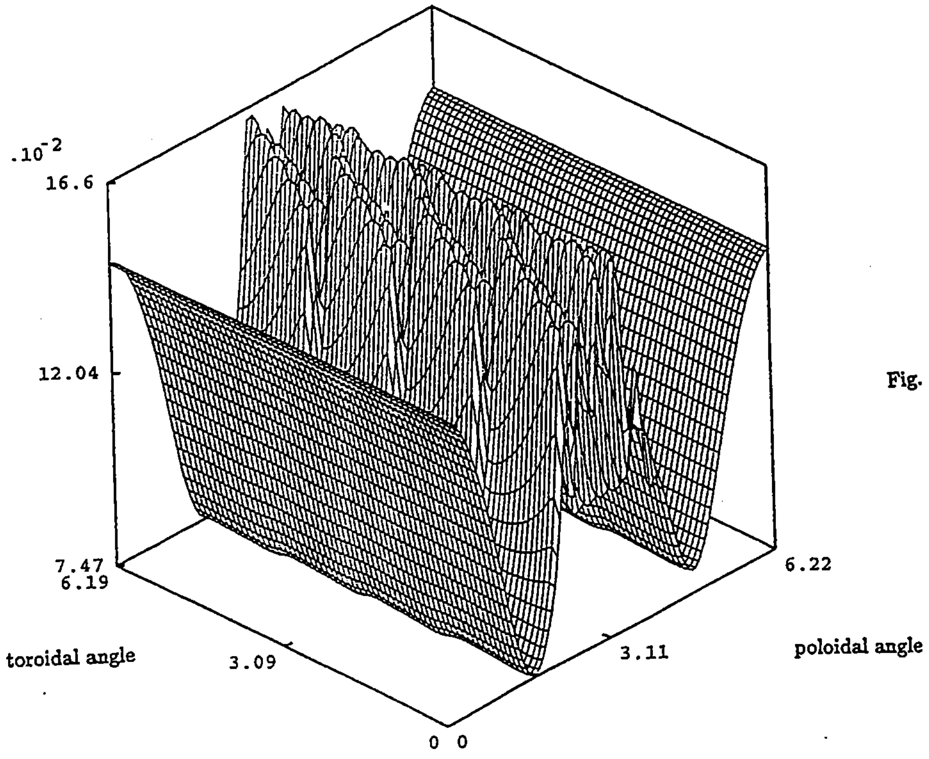
.10^-2
16.6
12.04
7.47
6.19
toroidal angle
3.09
0 0
3.11
6.22
poloidal angle

Fig. 2.b.

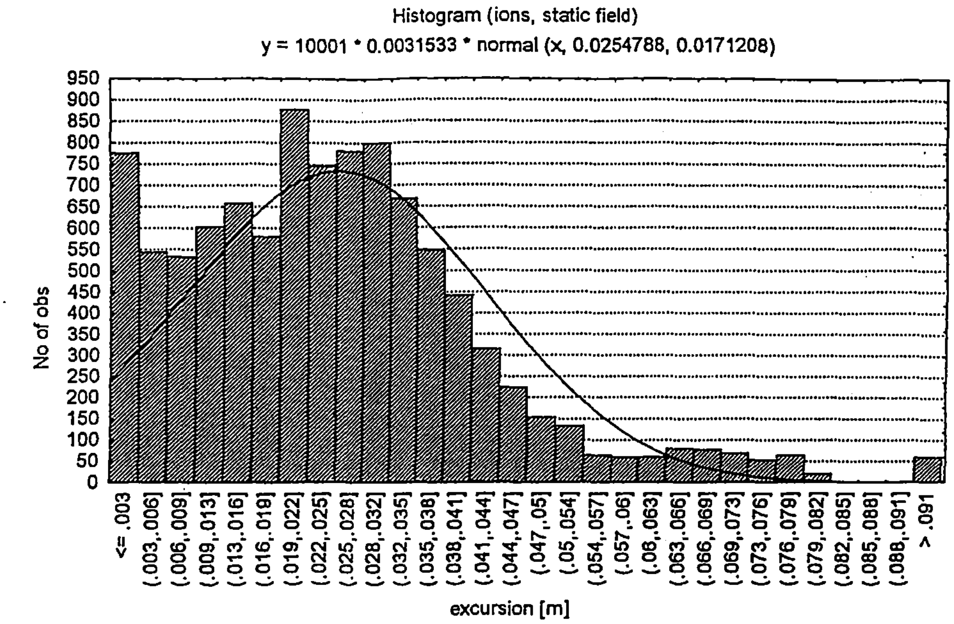
Histogram (ions, static field)
y = 10001 * 0.0031533 * normal (x, 0.0254788, 0.0171208)
No of obs
950
900
850
800
750
700
650
600
550
500
450
400
350
300
250
200
150
100
50
0
<= .003
(.003,.006]
(.006,.009]
(.009,.013]
(.013,.016]
(.016,.019]
(.019,.022]
(.022,.025]
(.025,.028]
(.028,.032]
(.032,.035]
(.035,.038]
(.038,.041]
(.041,.044]
(.044,.047]
(.047,.05]
(.05,.054]
(.054,.057]
(.057,.06]
(.06,.063]
(.063,.066]
(.066,.069]
(.069,.073]
(.073,.076]
(.076,.079]
(.079,.082]
(.082,.085]
(.085,.088]
(.088,.091]
> .091
excursion [m]

Fig. 3.a.

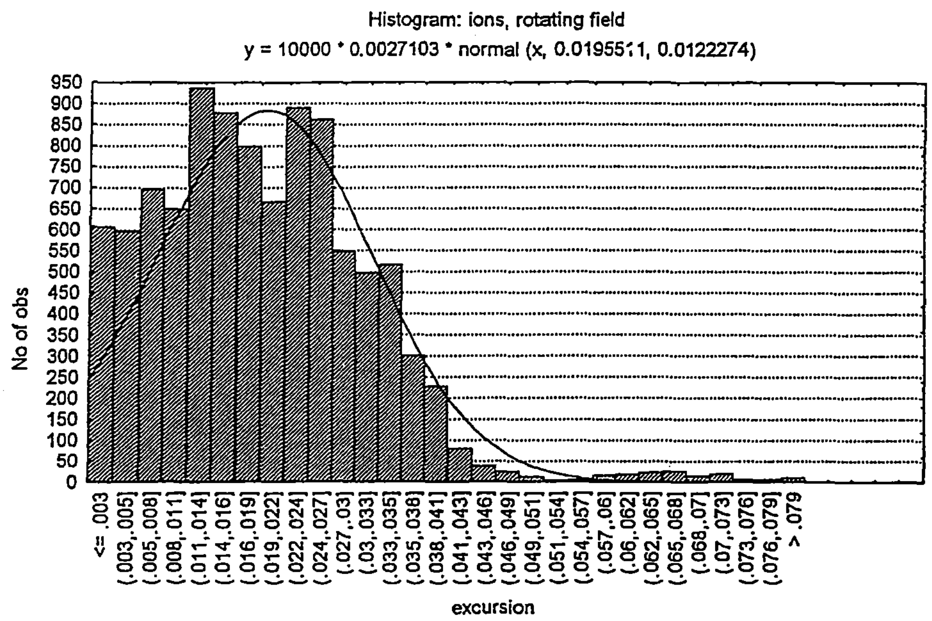
Histogram: ions, rotating field
y = 10000 * 0.0027103 * normal (x, 0.0195511, 0.0122274)
No of obs
950
900
850
800
750
700
650
600
550
500
450
400
350
300
250
200
150
100
50
0
<= .003
(.003,.005]
(.005,.008]
(.008,.011]
(.011,.014]
(.014,.016]
(.016,.019]
(.019,.022]
(.022,.024]
(.024,.027]
(.027,.03]
(.03,.033]
(.033,.035]
(.035,.038]
(.038,.041]
(.041,.043]
(.043,.046]
(.046,.049]
(.049,.051]
(.051,.054]
(.054,.057]
(.057,.06]
(.06,.062]
(.062,.065]
(.065,.068]
(.068,.07]
(.07,.073]
(.073,.076]
(.076,.079]
> .079
excursion

Fig. 3.b.

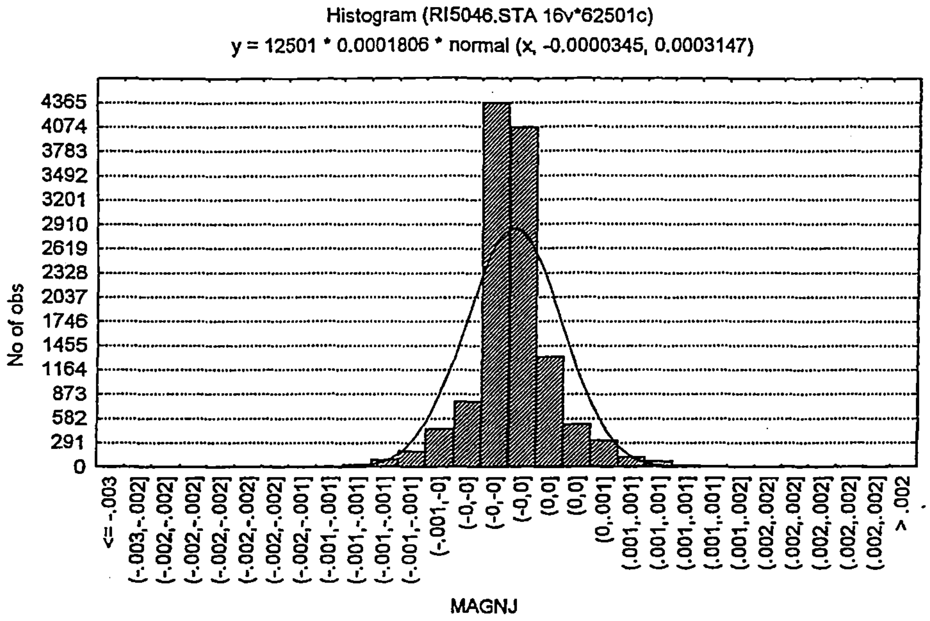
Histogram (RI5046.STA 16v*62501c)
y = 12501 * 0.0001806 * normal (x, -0.0000345, 0.0003147)
No of obs
4365
4074
3783
3492
3201
2910
2619
2328
2037
1746
1455
1164
873
582
291
0
<= -.003
(-.003,-.002]
(-.002,-.002]
(-.002,-.002]
(-.002,-.002]
(-.002,-.002]
(-.002,-.002]
(-.002,-.001]
(-.001,-.001]
(-.001,-.001]
(-.001,-.001]
(-.001,-.001]
(-.001,-.001]
(-.001,-0]
(-0,-0]
(-0,-0]
(-0,0]
(0,0]
(0,0]
(0,.001]
(.001,.001]
(.001,.001]
(.001,.001]
(.001,.001]
(.001,.002]
(.002,.002]
(.002,.002]
(.002,.002]
(.002,.002]
(.002,.002]
> .002
MAGNJ

Fig. 4.

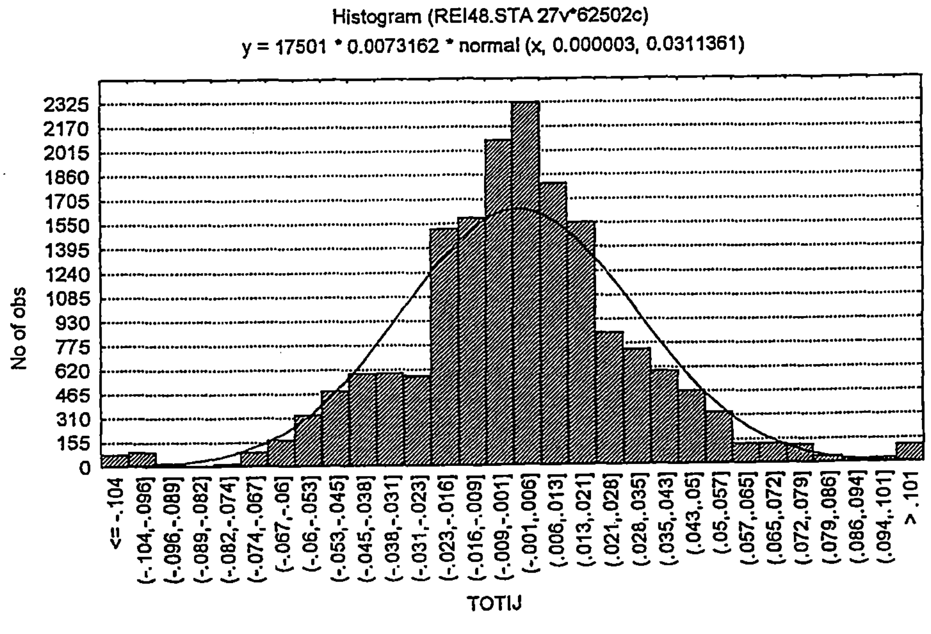
Histogram (REI48.STA 27v*62502c)
y = 17501 * 0.0073162 * normal (x, 0.000003, 0.0311361)
No of obs
2325
2170
2015
1860
1705
1550
1395
1240
1085
930
775
620
465
310
155
0
<= -.104
(-.104,-.096]
(-.096,-.089]
(-.089,-.082]
(-.082,-.074]
(-.074,-.067]
(-.067,-.06]
(-.06,-.053]
(-.053,-.045]
(-.045,-.038]
(-.038,-.031]
(-.031,-.023]
(-.023,-.016]
(-.016,-.009]
(-.009,-.001]
(-.001,.006]
(.006,.013]
(.013,.021]
(.021,.028]
(.028,.035]
(.035,.043]
(.043,.05]
(.05,.057]
(.057,.065]
(.065,.072]
(.072,.079]
(.079,.086]
(.086,.094]
(.094,.101]
> .101
TOTIJ

Fig. 5.

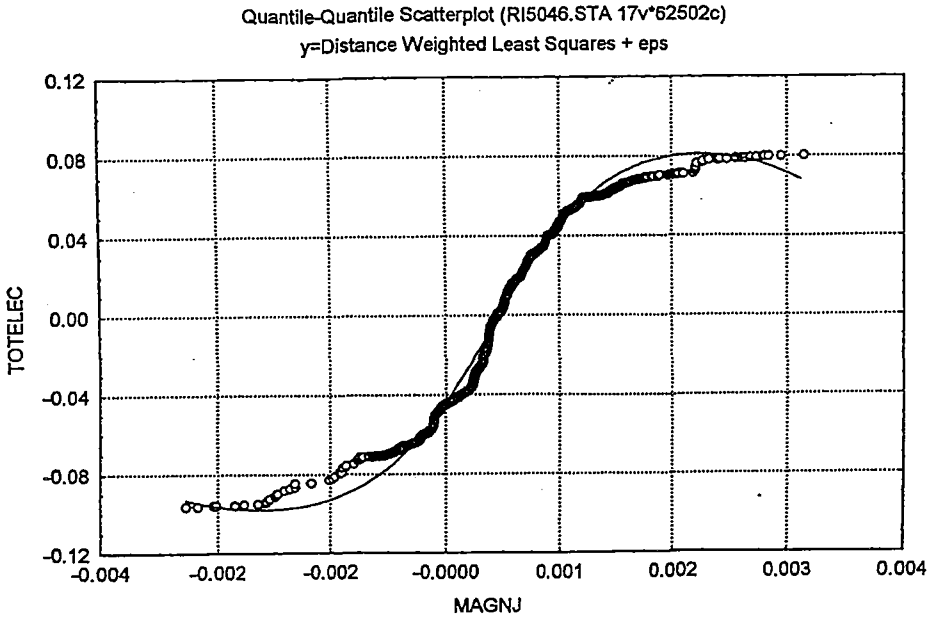
Quantile-Quantile Scatterplot (RI5046.STA 17v*62502c)
y=Distance Weighted Least Squares + eps
TOTELEC
0.12
0.08
0.04
0.00
-0.04
-0.08
-0.12
-0.004
-0.002
-0.002
-0.0000
0.001
0.002
0.003
0.004
MAGNJ

Fig. 6.a.

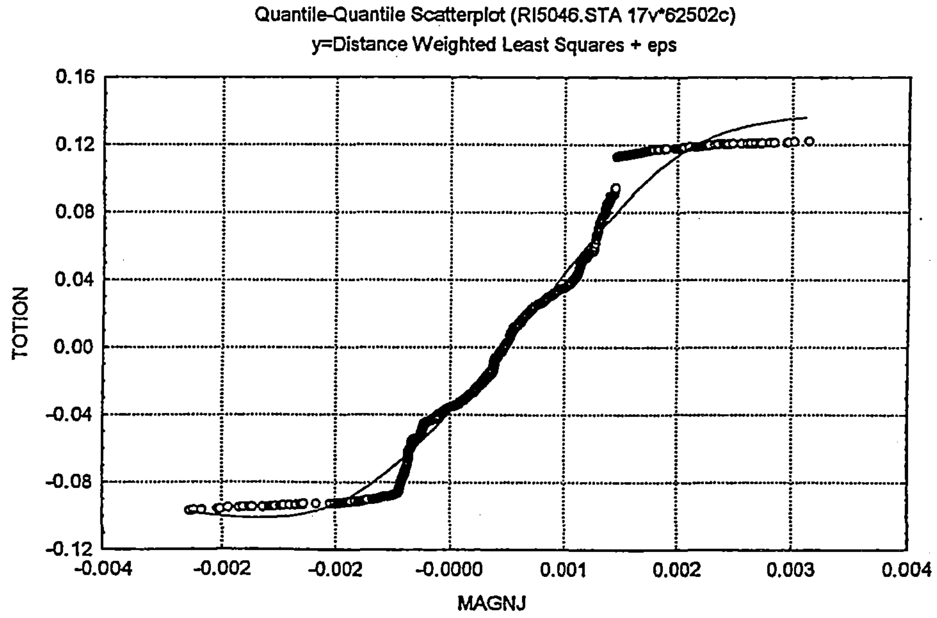
Quantile-Quantile Scatterplot (RI5046.STA 17v*62502c)
y=Distance Weighted Least Squares + eps
TOTION
0.16
0.12
0.08
0.04
0.00
-0.04
-0.08
-0.12
-0.004
-0.002
-0.002
-0.0000
0.001
0.002
0.003
0.004
MAGNJ

Fig. 6.b.

13. Model for Plasma Response for a Finite Relative Velocity between Plasma and the Magnetic Perturbation

T.H. Jensen

General Atomics, San Diego, USA

13.1 Introduction

The dynamic ergodic divertor in TEXTOR provides a unique possibility to perform experiments on plasma rotation driven by low frequency electromagnetic waves. Plasma rotation caused by low frequency waves has previously been demonstrated experimentally by Morris[1] and more recently by Oasa[2]. The key physics question of the plasma response at the singular surface to an electromagnetic perturbation with a phase velocity different from the plasma flow velocity is however not resolved. The "linear layer model" for the response, which is brought to a convenient form by Fitzpatrick[3], as well as a "nonlinear island model"[4] were found incapable of accounting quantitatively for magnetic braking experiments[5]. Therefore another heuristic model[6] was formulated which may describe the magnetic braking results. It is this heuristic model which is put forward as a guide for experiments proposed for TEXTOR. Such experiments could help determine how the singular surface response may be described. A simplified version of the heuristic model is outlined in Section 13.2.

When the singular surface response is known one can, with some confidence, determine the potential advantages of providing a plasma with rotation and rotational shear using low frequency waves. There is a wide-spread belief that such rotations may have profound beneficial effects on both ideal and resistive MHD stability, on effects of error fields, and that they may suppress turbulence which gives rise to anomalous transport.

An essential part of the heuristic model is an assumption that plasma turbulence is generated locally in the region around the singular surface. This turbulence may contribute significantly to the transport of plasma and may therefore help in reaching the goals of the dynamic ergodic divertor experiments.

In the following Subsection 13.2, a simplified form of the heuristic model of Ref. 6 is described which addresses the situation of the proposed TEXTOR experiments. In Subsection 13.3 is given a numerical example for the proposed experiments. The results suggest that the planned coils and associated power supplies will be able to produce perturbations which are large enough to drive a significant plasma rotation and turbulence which may make significant contributions to the transport.

13.2 Heuristic Model

In the following it is implied that neoclassical effects will prevail and prevent poloidal rotation of the plasma. This may well be inconsistent with the key assumption made, namely that the resistivity becomes anomalously large around the singular surface because of turbulence. Therefore the arguments from neoclassical theories may not apply. At this point we do not have a model which takes this into account.

The TEXTOR plasma is treated as a cylindrical plasma with a circular cross section. We describe the magnetic field of the unperturbed plasma using the functions F and Ψ and the helical vector, $\underline{\mu} \equiv \hat{z} + kr\hat{\theta}$ through

$$\underline{B} = F\underline{\mu} + \nabla\Psi \times \underline{\mu} \tag{1}$$

Here $\underline{r}, \underline{\Theta}$ and $\underline{z}$ are the unit vectors of an ordinary cylindrical coordinate system. We assume that $(kr)^2 \ll 1$ and $(\nabla\Psi/F)^2 \ll 1$, namely that tokamak ordering is valid. The unperturbed configuration is assumed to have two ignorable coordinates, Θ and z. The choice of description of the initial configuration is convenient for the relevant perturbations of the form $\exp\{i[nz/R + m\Theta]\}$. Here, R plays the role of the major radius of the plasma; n and m are the toroidal and poloidal mode numbers, respectively. When k is chosen so that $k = n/(mR)$, the perturbed plasma still has one ignorable coordinate in that $\underline{\mu} \cdot \underline{\nabla}$ vanishes.

We consider the simplest case, ignoring the plasma pressure, so that the condition for equilibrium of the unperturbed plasma, $(\nabla \times \underline{B}) \times \underline{B} = 0$ results in

$$\nabla F = F' \nabla\Psi; \quad \nabla^2\Psi + FF' - 2kF = 0 \tag{2}$$

Since both Θ and z are ignorable, Ψ depends only on r.

The perturbation of the magnetic field, $\underline{b}$, is represented by the functions f and φ through

$$\underline{b} = f\underline{\mu} + \nabla\varphi \times \underline{\mu} \tag{3}$$

We assume that f and φ are helically symmetric, i.e. $\underline{\mu}\cdot\nabla\varphi = \underline{\mu}\cdot\nabla f = 0$ as well as that $\partial/\partial\Theta = im$ and $\partial/\partial t = i\omega$. Again, for the sake of simplicity, here we ignore the pressure and further assume that the perturbations are so slow that inertial forces may be ignored. The perturbation is assumed caused by an externally driven current $\underline{j}_{ex} = \underline{\mu}\cdot j_{ex}$ which satisfies $\underline{\mu}\cdot\nabla j_{ex} = 0$ and $\partial j_{ex}/\partial\Theta = imj_{ex}$. The condition that the perturbed configuration is force free, namely that $[\nabla x(\underline{B} + \underline{b}) - \mu_0\underline{\mu}j_{ex}]x(\underline{B} + \underline{b}) = 0$ becomes (to first order)

$$\nabla^2\varphi + (FF')'\varphi - i\,\Gamma\,\varphi\,\delta(r - r_s) + \mu_o\,j_{ex} = 0 \tag{4}$$

Here r_s is the radius of the singular surface where $d\Psi/dr = 0$. The quantity Γ is in this context arbitrary and is a measure of the singular current, thus describing the response of the plasma at the singular surface. For a linear model, Γ is independent of φ. Since the electric field satisfies $\underline{E}\cdot\underline{\mu} = -i\omega\varphi$, one sees from (4) that Γ is real for a resistive response and complex for inductive or capacitive responses. Since inductive or capacitive responses involve the presence of a store for energy, which physically is not present (we ignore beams), we conclude that Γ is real.

In second order of the perturbation, there is an average exchange of forces between the field and the plasma at the singular surface. It is assumed that the poloidal component of the force is balanced by the neoclassical force which inhibits poloidal rotation. For the "toroidal" part of the force one finds readily

$$F_z = \frac{1}{4\mu_o}[-i\Gamma\varphi\underline{\mu}\times(f^*\underline{\mu} + \nabla\varphi^*\times\underline{\mu}) + c.c.]\cdot\hat{z} = -\frac{m\Gamma k}{2\mu_o}\varphi(r_s)\varphi^*(r_s) \tag{5}$$

For a given perturbation, $\varphi(r_s)$ depends on Γ and on the properties of the unperturbed equilibrium. In order to overcome this inconvenience we further assume for the sake of simplicity that $(FF')' \equiv \beta^2$ is a constant (inside the plasma) as well as that the singular surface at $r=r_s$ is located inside the plasma surface at $r=a$ and that $(a-r_s)^2 \ll r_s^2$. In addition we assume that the external currents are located entirely outside the plasma, $r > a$.

It is further found convenient to use, as a measure of the perturbation, the singular surface value of the perturbed flux function for the case of no induced plasma current (the "vacuum" response) $\varphi_V(r_s)$. The relationship between the external current and $\varphi_V(r_s)$ does not depend on Γ or the equilibrium properties except through the location of the singular surface. With these simplifications (more details are given in Ref. 4) one finds

$$\varphi(r_s)\varphi^*(r_s) = \frac{4m^2\varphi_V(r_s)\varphi_V^*(r_s)}{(\Delta' r_s)^2 + (\Gamma r_s)^2} \tag{6}$$

where

$$-\Delta' r_s = 2m - (\beta r_s)^2 \frac{a - r_s}{r_s} - \frac{\beta r_s J_{m+1}(\beta r_s)}{J_m(\beta r_s)} \tag{7}$$

Here, the J's stand for the Bessel functions of first kind and $\beta r_s = 3.83$ (the first root of J_1).

The basic assumption for the simplified heuristic model for the plasma response, in the singular surface region, is that turbulence, created by the perturbation field, gives rise to an anomaly of the plasma resistivity so large that the plasma can flow resistively through the (average) magnetic islands.

The frequency experienced by the plasma, flowing in z-direction (simulating the toroidal direction) is $nv/R + \omega$. Here, v is the plasma velocity and ω is the applied frequency. The resistivity needed to allow the plasma to flow resistively though the (average) islands is estimated to be

$$\eta^* = \mu_o w \left(v + R\frac{\omega}{n}\right)\frac{\varepsilon n}{\alpha m} \tag{8}$$

Here, w is an effective island width. We have also used $\varepsilon \equiv r_s/R$ and α is an adjustable multiplier describing the strength of the turbulence at the singular surface. The DIII-D experimental results[5] may be accounted for with $\alpha \sim 0.1$. It is also implied here that $v + R\omega/n$ is positive so that $\eta^* > 0$. The resistive current inside the (average) islands constitutes the singular current,

$$J_s = -i\Gamma\frac{\varphi(r_s)}{\mu_o} \tag{9}$$

Since the electric field (essentially along the field lines) experienced by the plasma is $-i(\omega + nv/R)\phi(r_s)$, one obtains for the island current

$$J_s = -i(\omega + \frac{nv}{R})\,\varphi(r_s)\,\frac{w}{\eta^*} \tag{10}$$

From (8) - (10) one obtains the desired expression for the quantity Γ,

$$\Gamma = \frac{\alpha m}{\epsilon}\frac{1}{R} \tag{11}$$

This is a limiting result of the more elaborate heuristic model[6].

The anomalous resistivity given by (8) may be associated with an anomalous diffusion coefficient for the plasma

$$D = \frac{\eta^*}{\mu_o}\frac{\beta_{pe}\sqrt{\epsilon}}{2} = w\,(v + R\frac{\omega}{n})\frac{\beta_{pe}\,\epsilon^{3/2}\,n}{2\alpha m} \tag{12}$$

Here β_{pe} is the "poloidal beta" for the electrons.

These arguments about the existence of turbulence are of course valid only if $\eta^* > \eta_{sp}$, Spitzer resistivity. This means that for small amplitudes of the perturbation, the linear layer theory[3] may be valid. For the amplitudes contemplated for TEXTOR one is well into the nonlinear regime where the assumptions on the existence of turbulence may be applicable.

Even tokamaks without any direct injection of angular momentum have Mirnov oscillations with a phase velocity which suggests a toroidal plasma rotation. The source of this rotation may be a loss rate of ions which depends on the ion angular momentum. Besides the momentum source, which is assumed independent of the toroidal flow velocity, there may be a viscous drag, proportional to the plasma viscosity, acting on the plasma. Finally, the plasma is exposed to the force acting on the singular surface (we ignore here the force from neutral beams). In a zero-dimensional description, the toroidal velocity of the plasma, v, may thus be determined by

$$2\pi r_s \, 2\pi R F_z = \mathcal{F} \left(1 - \frac{v}{v_0}\right) \tag{13}$$

Here, $\mathcal{F}$ and v_0 are constants. The latter is the velocity of the plasma in the absence of perturbations which give rise to singular surface forces. From (5), (6), (11) and (13) one can obtain an expression for the relationship between the plasma velocity and the amplitude of the perturbation applied

$$1 - \frac{v}{v_0} = \frac{\varphi_v(r_s)\varphi_v^*(r_s)}{\mu_o \mathcal{F}} \frac{8\pi^2 \alpha n m^3}{[(\Delta' r_s)^2 + (\alpha m)^2]} \tag{14}$$

13.3 Numerical TEXTOR Example

The object of this section is to relate the current in the helical coils of TEXTOR to $\varphi_v(r_s)$, used as a measure of the perturbation amplitude in Subsection 13.2, in order to determine if the amplitude of the perturbations of the planned experiments is sufficient to affect the plasma rotation and the transport. Again we approximate the TEXTOR geometry by that of a circular cross section cylinder. As a first step we approximate the coil currents, J_c, located at r=b, by

$$\underline{j_{ex}} = \mu J_c \, \delta(r-b) \tag{15}$$

and we assume the vacuum chamber wall (assumed conducting) is located at $r = r_w$. The vacuum response is determined by

$$\nabla^2 \varphi_v + \mu_o J_c \, \delta(r - b) = 0; \quad \varphi_v(r_w) = 0 \tag{16}$$

It is easy to find $\varphi_v(r)$ from (16) for

$0 < r < b$:

$$\varphi_V(r) = \varphi_V(b)\,\left(\frac{r}{b}\right)^m \tag{17}$$

and for b < r < r_w

$$\varphi_V(r) = \varphi_V(b)\,\frac{\left(\frac{r}{b}\right)^m - \left(\frac{r_w}{b}\right)^{2m}\left(\frac{r}{b}\right)^{-m}}{1 - \left(\frac{r_w}{b}\right)^{2m}} \tag{18}$$

and that

$$\mu_o\,J_c = -\varphi_V(b)\,\frac{2m}{b}\,\frac{\left(\frac{r_w}{b}\right)^{2m}}{1 - \left(\frac{r_w}{b}\right)^{2m}} \tag{19}$$

so that

$$\varphi_V(r_s)\varphi_V{}^*(r_s) = \mu_o^2\,J_c\,J_c^*\,\left(\frac{r_s}{b}\right)^{2m}\left(\frac{b}{2m}\right)^2\left[1 - \left(\frac{r_w}{b}\right)^{2m}\right]^2\left(\frac{r_w}{b}\right)^{-4m} \tag{20}$$

There are many possibilities for driving the currents through the planned helical coils. Here we only contemplate one of them.

We assume that the four turns exiting the vacuum chamber at one toroidal location each carries the current I_o cos ωt. The four turns exiting at a neighbouring toroidal location are assumed each to carry the current $I_o \cos(\omega t - \pi/2)$ and so on. One may estimate from this that the predominant excitation then is an n=1, m=3 mode with $J \approx I_o/b$. From equation (20) one finds $|\phi_V(r_s)| \approx 5 \cdot 10^{-4}$ Vs/m using $I_o = 10^4$ A, $r_s = 0.42$ m, b = 0.53 m and $r_w = 0.6$ m. This corresponds to a radial magnetic field, $b_{vr} = m|\phi_V(r_s)|/r_s$ of about $3 \cdot 10^{-3}$ Vs/m^2. This allows calculation of a toroidal force (using R = 1.75 m and $(\Delta' r_s)^2 = 1$ and $\alpha=0.1$) from (5), (6) and (11) of 40 N. This is a large force compared to that of the neutral beams available; 1.5 MW of a 50 keV hydrogen beam provides about 1 N.

The associated diffusion coefficient is also large. Using as an example $w = 2 \cdot 10^{-2}$ m and $v + R\omega/n = 10^4$ m/s, a diffusion coefficient of 30 m^2/s in the island region follows from equation (8) and (12) using $\beta_{pe} = 1/2$, $\varepsilon = 1/3$ and $\alpha = 1/10$. This diffusion may contribute significantly to spreading the heat load on the walls.

Therefore, the design of the coil system for TEXTOR appears well suited for experimental investigations of the effects og magnetic perturbations with a finite phase velocity relative to the plasma.

References

1. Morris et al., Phys. Rev. Lett., **64** (1990) 1254
2. Oasa el al.: "Experimental Results of Plasma Response on Rotating Magnetic Field on JFT-2M", Presented at US-Japan Workshop on "Island Formation in Toroidal Plasmas...", March 1994, NIFS, Nagoya, Japan
3. Fitzpatrick, Physics of Plasmas, 1 (1994) 3308
4. Jensen et al., Phys. Fluids B, **5** (1993) 1239
5. LaHaye et al., Phys. Plasmas, 1 (1994) 373
6. T. Jensen et al., GA-A 21996 (Aug. 1995), to appear in Phys. of Plasmas.

Part V: Special Application to the TEXTOR Programme

14. The Optimization of a Radiative Plasma Mantle

U. Samm
Institut für Plasmaphysik, Forschungszentrum Jülich, Association EURATOM-KFA

It is well known that the peak heat loads in a fusion reactor (e.g. ITER) would be unacceptable without distributing a significant fraction of the total power on larger areas than the wetted area of the divertor plates. A uniform distribution of the power can be achieved by line radiation. Impurities can provide a radiation level sufficiently high - e.g. 90% of the total a-particle power. By choosing the appropriate type of impurity (with an atomic mass not too high) the line radiation will be concentrated mainly at the plasma boundary outside the fusion volume, thus generating a "*cold radiative plasma mantle*".

Such plasmas have been generated successfully on limiter (TEXTOR) and divertor machines (ASDEX-U). An essential element in these experiments is the feed-back control of the impurity level (neon) to assure a safe operation at extreme values of the radiation level (approaching 100%) and at high electron densities close to the density limit. On TEXTOR recently also a feed-back system has been installed to keep the energy content of the plasma constant. A variable ICR heating power is used to react on excursions in energy confinement. This is important to avoid instabilities and to stay below the b-limit.

The performance of such plasmas turns out to be favorable in many respects. The discharges are thermally stable and quasi-stationary. The energy confinement times are kept on a high level. This has been shown under H-mode conditions (ASDEX-U), but also "L-mode" discharges show improved confinement. On TEXTOR the improved confinement regime (I-mode) can be extended to the highest electron densities and shows energy confinement times comparable with the ITER ELM-free H-mode scaling.

Edge radiation cooling seems to be attractive to solve the power exhaust problems of a fusion reactor. However, the feasibility of this scheme is limited due to impurity transport to the plasma centre. Even if impurity radiation losses from the centre can be minimized by employing only low-Z impurities, the dilution of the D-T fuel can be serious and may lead to a reduction of the fusion power and even to the end of the burning plasma.

The problem of seeded impurities for the purpose of radiation cooling adds to those coming from intrinsic impurities eroded from the wall and, most critically, to the He-ash generated by the fusion process. For an effective He-removal time $\tau_{He} / \tau_E = 10$, as foreseen in the ITER design, and assuming 3% of Be in the plasma centre, the feasibility of a radiative edge with seeded impurities appears to be marginal. The uncertainties in the predictions on impurity transport do not allow a precise answer to the question, whether a cold radiative plasma mantle is feasible under these conditions.

Therefore, any measure for optimization is of major importance. A figure of merit, which is to be minimized, is the ratio of $\Delta Z_{eff} / \Delta P_{rad}$ - i.e. the increase in Z_{eff} one has to accept for a given increase of the radiated power from the plasma edge. In this respect various aspects play a role : the choice of impurities, operation at high densities and low edge temperatures, He-exhaust efficiencies and the confinement properties of impurities. The latter can be influenced significantly by *ergodizing* the plasma boundary.

In an ergodic plasma boundary the radial transport of particles is enhanced due to the radial components of the magnetic field. This has been demonstrated in experiments on TORE SUPRA with a static ergodic divertor. The level of the intrinsic carbon impurity has been reduced by a factor of 3. At the same time the radiation level has been enhanced by a factor of 1.5, thus the radiation efficiency of the impurities is improved, or in other words the figure of merit $\Delta Z_{eff} / \Delta P_{rad}$ is significantly reduced.

An analysis of this behaviour has been performed with the transport code RITM, which can treat the transport of impurities and the background plasma self-consistently (indispensable for a high radiation level). It is shown that with a shorter life time of the impurities in the plasma (particle confinement) the population of the lower ionization stages is enhanced, in particular the Li- and Be-like stages, which contribute the dominant fraction to the total radiation. This explains the strong increase in radiation efficiency. With respect to a reactor this improvement would be beneficial and could provide just that margin for intrinsic impurities (incl. helium) required for the compatibility of a cold radiative plasma mantle and the conditions for a burning fusion plasma.

In the context of the TEXTOR 94 programme - devoted to the study of "*Advanced Concepts for Energy- and Particle-Transport and -Exhaust and their Control in Fusion Reactors*" - the possibility for ergodizing the plasma boundary would be an outstanding element. It is expected that a coherent treatment of all aspects of particle and heat transport leads to a deeper understanding and to solutions for optimization. The results will not only be applicable to tokamaks. Also in stellarators, where "steady state" is the primary aim, power exhaust via radiation can be indispensable. In this respect the various possibilities to ergodize a stellarator plasma will be helpful.

15. Particle, in Particular Helium Removal Experiments

K.H. Finken

Institut für Plasmaphysik, Forschungszentrum Jülich, Association EURATOM-KFA

The magnetic confinement studies on plasmas aim on achieving a burning plasma with long pulse reactor operation. A prerequisit for obtaining stationary conditions are both continuous fuelling of the burning gas and removal of the helium ash, impurities and working gas e.g. for density control. On the average, the working gas has to be removed from the discharge at the gas injection rate. During the start-up phase the situation can be delicate if gas is released from the walls e.g. during heating up of the structural materials. Therefore particle and in particular helium removal studies have been performed on TEXTOR and continue to be a critical issue. The helium removal must be sufficient efficient such that the central helium concentration remains below 10%; otherwise the fusion process is strongly deteriorated by dilution. It has been shown[1], that the helium has to be extracted from the reactor in a time of at most 15 energy confinement times ($\tau_{He}{}^{*}/\tau_E \leq 15$) for an otherwise clean plasma. If the plasma contains other impurities than helium, this ratio is progressively reduced with higher contamination levels. Present day experiments fulfill the requirement on the helium exhaust only barely and for selected discharge conditions only. Any possible improvement should be investigated and therefore the dynamic ergodic divertor will be thoroughly studied on this aspect.

TEXTOR is one of the experiments, which has pioneered the question of helium removal. The device is in particular suited for these investigations, because it is equipped with an efficient particle removal system, the toroidal pump limiter ALT-II; this system removes all gases and not preferentially hydrogen isotopes as getter pumps or cryo pumps do in other devices. A poloidal cross section including the pumping system is shown in Fig. 1.

The exhaust efficiency of a pump limiter is the product of the collection efficiency and the removal efficiency[2,3] . The collection efficiency is the propability for particles leaving the plasma to be intercepted by the pump limiter scoop entrance. The removal efficiency equals the probability of the intercepted particles to be pumped away. In the very simplest approximation the the collection efficiency is determined by the width of the pump limiter blade relative to the decay length of the scrape off layer and the removal efficiency by the conductances in the pump limiter. For this case they were estimated to be 15% - 20% (collection efficiency), 50% (removal efficiency) and 5% - 10% exhaust efficiency. The interaction of the flux towards the pumps with the background plasma, however, changes the values and makes them dependend on the plasma density and temperature in and in front of the scoops. Thus the actual exhaust efficiency is modified to 2% - 10%.

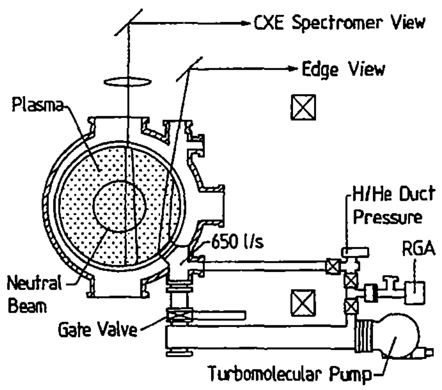

Abb. 1: Cross section through TEXTOR including one pumping line of the pump limiter ALT-II

For the helium removal experiments, small quantities of He-gas (typically less than 10% of D; puff length $\propto$ 10 ms) are injected in a short puff during the discharge. The decay of the helium density is observed by charge exchange spectroscopy (CXS) in the central plasma, by emission spectroscopy of recycling helium on the front surface of the ALT-II limiter and by a modified Penning discharge[4] in the exhaust line of ALT-II. For studies on energetic helium confinement[5,6], He-ions have been injected by a specially prepared neutral beam injector with an energy of 40 - 50 keV.

15.1 Helium Exhaust Measurements

In ohmic discharges or in discharges with neutral beam heating a small puff of helium is injected into the discharge[7,8,9]. Fig. 2 shows the electron density for two consecutive discharges; in # 38810 the gate valves to the ALT-II turbo pumps are open while in # 38811 they are closed. The helium is injected at the end of the density ramp-up phase and is seen in the density signal as a change of the slope. About 50 ms after the He-puff, the neutral beam injector is switched on. Just after the onset of the beam, the electron density increases and then decays. The decay from 0.8 s to 1.2 s is mostly due to the implantation of deuterium in the TEXTOR walls. If the valves are closed, the density soon reaches a stationary value and decays further when pumping with ALT-II.

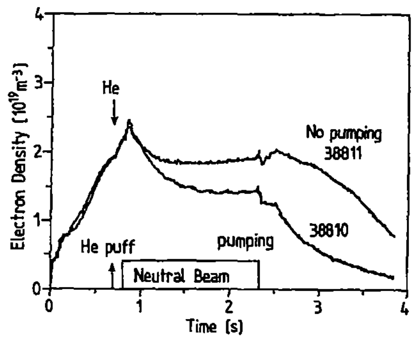

Abb. 2: Electron density for two consecutive discharges with neutral beam injection. Top curve: ALT pumps closed, bottom ones pumps open.

The helium signal from the core recorded by charge exchange spectroscopy is shown in fig. 3. The data can only be obtained as long as the neutral beam is switched on as source for charge exchange processes. Shortly after the injection, the helium signal shows a small maximum. When the gate valves to ALT-II are closed, the signal stays constant during the rest of the discharge. In case of open gate valves ALT-II pumps the helium away. In L-mode discharges the e-folding time is about 0.6 s while in the ohmic case it is about 3 s. The higher removal rate in the L-mode is caused by the reduced particle confinement time during the L-mode and is related to an enhanced removal efficiency for the helium. The figure of merit in a reactor τ_{He}^{*}/τ_E for L-mode discharges is in the range of 10 - 30. The lowest values are valid for high density discharges and would just be sufficient for the continuous operation of the fusion reactor.

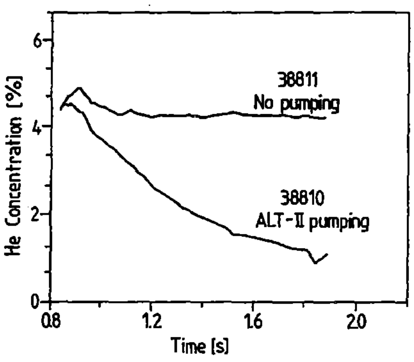

Abb. 3: Core helium concentration from CXS for the same discharges as in Fig. 2.

For a comparison with other fusion devices the determination of the transport coefficients is necessary. The experiments performed are analyzed with respect to the quasi-stationary He-decay phase and there the electron profile is given by the balance of the inward pinch and the diffusion term:

$$n_e \cdot v_p = D_A \cdot dn_e/dr.$$

To derive the transport coefficients for He (MIST Code), the right hand side of this equation is multiplied by C_v. The quantity C_v describes the enhancement of the He-diffusion coefficient relative to the electron diffusion coefficient. The analysis has shown, that the He-diffusion coefficient is slightly increased for low density discharges (C_v = 1.5 - 2.5) while for high density discharges it is close to the electron value (C_v = 0.65 - 1.5).

15.2 The Role of a Dynamic Ergodic Divertor

Unfortunately, the extrapolation of results of an ergodic divertor gained on other machines to the particle removal on TEXTOR is not straightforward: The geometry on the location of the perturbation coils inside the machines is different from TEXTOR and the toroidal belt pump limiter of TEXTOR is unique also. To estimate, nevertheless, the removal rate of the ergodized plasma boundary, it may be assumped that the diffusion coefficient of the plasma boundary by about a factor of five as discussed in §3.

Scaling the scrape off layer width δ according to $\delta^2 = (D \cdot L)/c_s$ results in an increase of δ by a factor of about 2.24, provided that the edge temperature, connection length and recycling remains constant. The collection efficiency of the pump limiter is estimated as $\varepsilon_{coll} = [\exp(-x1/\delta) - \exp(-x2/\delta)]$ where x1 and x2 are the distance between the last closed flux surface to of the scoop entrance and scoop back and δ is the decay length of the flux. For the "old" ALT-II graphite tile configuration with a radial thickness of 17 mm it increases from 20% to 36% for the ergodized case and for the "new" tiles with a thickness of 20 mm to 30%. If this assumption is applicable the particle removal rate by the ALT-II pump limiter would nearly double with the ergodic limiter.

A more complete modelling effort is under way in which the magnetic field lines hitting the pump limiter blades and scoop entrance are traced back into the plasma. From the average connection length of these field lines and their distance from the last closed flux surface the particle fluxes to the neutralizer plates of ALT-II will be estimated. This work will be presented at a given time.

References

1. D. Reiter, G.H. Wolf, H. Kever, Nucl. Fusion **30** (1990) 2141
2. W.J. Corbett, R.W. Conn, D.M. Goebel et al., Nucl. Fusion, **31** (1991) 1067
3. D.S. Gray, K.H. Dippel, K.H. Finken et al., J. Nucl. Mater., **176 - 177** (1990) 810
4. K.H. Finken, K.H. Dippel, W.Y. Baek, A. Hardtke, Rev. Sci. Instrum., **63** (1992) 1
5. K.H. Finken, R. Koch, H. Euringer et al., Phys. Rev. Lett., **73** (1994) 436
6. R. Koch, A.M. Messiaen, J. Ongena et al., Fusion Engineering and Design, **26** (1995) 103
7. D.L. Hillis, J.T. Hogan, L.D. Horton et al., "Helium Removal and Transport Studies in TEXTOR" To be published in: Plasma Physics and Contr. Fus. Research (Proceedings of the 13th Intern. Conf.), IAEA-**CN-53/G-II-8**, p. III. (1990) 597 Vienna
8. D.L. Hillis, K.H. Finken, J.T. Hogan et al., Phys. Rev. Lett., **65** (1990) 2382
9. K.H. Finken, D.L. Hillis, K.H. Dippel et al., J. Nucl. Mater., **176 - 177** (1990) 816

FORSCHUNGSZENTRUM JÜLICH GmbH

Jül-3285
September 1996
ISSN 0944-2952